OPEN ACCESS

University of BRISTOL

This electronic thesis or dissertation has been downloaded from Explore Bristol Research, http://research-information.bristol.ac.uk

Author:
Song, Jie

Title:
Uncertainty Quantification of Tsunami Catastrophe Modelling

General rights
Access to the thesis is subject to the Creative Commons Attribution - NonCommercial-No Derivatives 4.0 International Public License. A copy of this may be found at https://creativecommons.org/licenses/by-nc-nd/4.0/legalcode This license sets out your rights and the restrictions that apply to your access to the thesis so it is important you read this before proceeding.

Take down policy
Some pages of this thesis may have been removed for copyright restrictions prior to having it been deposited in Explore Bristol Research. However, if you have discovered material within the thesis that you consider to be unlawful e.g. breaches of copyright (either yours or that of a third party) or any other law, including but not limited to those relating to patent, trademark, confidentiality, data protection, obscenity, defamation, libel, then please contact collections-metadata@bristol.ac.uk and include the following information in your message:

• Your contact details
• Bibliographic details for the item, including a URL
• An outline nature of the complaint

Your claim will be investigated and, where appropriate, the item in question will be removed from public view as soon as possible.

Uncertainty Quantification of Tsunami Catastrophe Modelling

Jie Song

Department of Civil Engineering
University of Bristol

A dissertation submitted to the University of Bristol in accordance with the requirements of the degree of Doctor of Philosophy in the Faculty of Engineering.

October 2019

Dedicated to my parents and my late grandma.

Declaration

I declare that the work in this dissertation was carried out in accordance with the regulations of the University of Bristol. The work is original except where indicated by special reference in the text and no part of the dissertation has been submitted for any other degree.

Any views expressed in the dissertation are those of the author and in no way represent those of the University of Bristol.

The dissertation has not been presented to any other University for examination either in the United Kingdom or overseas.

Signed:
Dated:

Jie Song
October 2019

Acknowledgements

Firstly, I would like to express my greatest gratitude to my supervisor Dr Katsuichiro Goda for his constant support in every way even after he moved to Canada. Without his patience, understanding, and encouragement, I would not have made it through those difficult times and come to the end of my PhD. It is the best decision in my life to have been his student, always so understanding, patient. Doing my PhD with him is the best decision I made and he is also a role model I will always look upto. I really miss the cherish the interesting discussions and the camaraderie that we had.

I would also like to thank Dr Raffaele De Risi for his extensive knowledge and offering technical support during my research and my second supervisor Dr Nick Alexander for his support especially after my primary supervisor left Bristol.

Many thanks to my lovely friends who left me beautiful memories during my PhD life. I am particularly grateful to Elham, Reza, Irina, Shoba, and Delwyn, who always stood by my side and supported me. I will miss you all.

At last but not least, I would like to thank my parents, my uncle and my brothers for your unconditional love and support as always. I love you!

Jie Song
Bristol, 30th of April 2019

Abstract

Recent earthquake-triggered tsunamis, such as the 2004 Indian Ocean tsunami and the 2011 Tohoku Japan tsunami, have caused tremendous economic losses, which emphasised the necessity of tsunami risk assessment. The development of financial risk transfer instruments for tsunamis requires catastrophe modelling which typically consists of hazard, vulnerability, exposure, and financial modules; among these elements, the hazard modelling is a major source of uncertainty. The current tsunami risk assessment, which is based on one or a few selected earthquake rupture scenarios, is not capable of considering all situations for tsunami hazard. The 2011 Tohoku tsunami revealed the great uncertainty in tsunami hazard assessment by exceeding the hazard level predicted by scenario-based tsunami hazard maps for the Tohoku region. To deal with the uncertainty in earthquake source characterisation, an innovative stochastic tsunami risk assessment framework is developed to take into a wide range of possible tsunami scenarios. This method allows the generation of a large number of stochastic slip distributions by using new scaling relationships for the tsunamigenic earthquakes.

This thesis aims to characterise and quantify major sources of uncertainty in the tsunami catastrophe model. Based on the stochastic tsunami risk assessment framework, the influences of various aspects on tsunami loss estimation are investigated, including resolution of elevation data, selection of tsunami intensity measure, building location (coastal topography, distance from the sea, and land elevation), and earthquake recurrence model. The results showed the importance of these aspects quantitatively, which facilitate the decision-making of different stakeholders for tsunami risk management. A multi-hazard earthquake-tsunami insurance rate-making method is proposed and applied to consider the missing link between earthquake and tsunami catastrophe models. Using the new multi-hazard tool, the pure premium rates for tsunami insurance are differentiated for fair pricing by considering structural and location attributes.

Table of contents

List of figures

List of tables

Chapter 1

Introduction

1.1 Introduction

A tsunami is a series of travelling waves of long wave-length and period, which is initiated by the sudden deformation of sea-floor. (Kanamori, 1972; Okada, 1985; Tanioka and Satake, 1996; Synolakis et al., 1997; Titov et al., 2005; Fujii and Satake, 2007). The most common cause of tsunamis is the rupture of an earthquake. Other triggers include volcanoes, landslides, and high-energy atmospheric disturbances (Grezio et al., 2017). The displaced water column by the sea-floor deformation gives a rise to the change of water surface and generates the tsunami waves. The wave height increases significantly when the wave travels from deep sea to shallow water. A tsunami triggered by an extremely large subduction earthquake can cause tremendous damage to coastal communities. Two recent examples are the catastrophic 2004 Indian Ocean tsunami (Borrero, 2005; Murata et al., 2010) and the 2011 Great East Japan (Tohoku) tsunami (Fraser et al., 2013). The direct economic loss of the 2011 Tohoku earthquake and tsunami was 211 billion USD, exceeding the losses of the 1995 Kobe earthquake and the record-breaking Hurricane Katrina (Kajitani et al., 2013), which revealed the necessity of tsunami risk mitigation and management.

Tsunami risk assessment offers the essential information for tsunami risk management, and the tsunami risk assessment can be performed using a tsunami catastrophe model. The tsunami risk is calculated by integrating four main components of a tsunami catastrophe model: hazard (i.e. earthquake source characterisation, tsunami propagation and inundation), tsunami vulnerability, exposure, and financial analysis. The accuracy of tsunami risk assessment for a tsunami-prone area has a direct influence on the

preparedness and mitigation of tsunami risk in terms of both physical measures and financial measures. Physical measures include enhancing resistance of infrastructures (e.g. structure retrofitting) and mitigating the hazard intensity (e.g. breakwaters, levees and seawalls). Financial risk management is mainly referred to risk transfer measures (e.g. insurance, reinsurance and insurance linked securities (ILS)), which is mainly concerned with the loss estimation.

Within a catastrophe model, the event generation is considered as the primary source of uncertainty, whereas local intensity, exposure data, damage estimation and incurred loss estimation are considered the secondary sources of uncertainty (Mitchell-Wallace et al., 2017). The primary source of uncertainty related to tsunami hazard modelling can be attributed to the source characterisation of future tsunamigenic earthquakes, such as magnitude, location, fault geometry and slip distribution (Geist, 2002; Løvholt et al., 2012; Fukutani et al., 2015; Mueller et al., 2015; Goda et al., 2016). There are mainly two approaches for tsunami hazard modelling: deterministic/scenario-based tsunami hazard assessment (Geist and Parsons, 2006; González et al., 2009; Heidarzadeh and Kijko, 2011) and probabilistic tsunami hazard assessment (PTHA) (Parsons and Geist, 2008; Davies et al., 2015; Mueller et al., 2015; Goda and De Risi, 2017). The scenario-based approach is mainly concerned with tsunami hazard parameters that correspond to a single scenario on a single fault or several selected slip models based on expert opinions using a logic-tree method, without considering the uncertainty in earthquake source characterisation (i.e. the variability of geometric and statistical source parameters). As a result, the scenario-based tsunami hazard prediction is unable to take into account all potential risks (i.e. financial losses and casualties) in different situations, especially extreme events of high consequence but low probability. The 2011 Tohoku tsunami has revealed the insufficiency of the scenario-based approach since the inundation scale along the Tohoku coast in Japan was beyond the hazard level predicted by the tsunami hazard map which was prepared based on the largest historical event, although Tohoku was thought as a region of high tsunami risk and was well prepared against tsunamis (Mori et al., 2011). As a consequence, the preparation turned out to be significantly insufficient, with a high proportion of tsunami barriers severely damaged and thus could not serve their functions.

PTHA is advantageous because it allows the consideration of a large number of various possible tsunami hazard situations based on stochastic earthquake source models (Power et al., 2007; Goda et al., 2016). The stochastic slip models with varied

earthquake source parameters can be generated based on spectral analysis of slip heterogeneity of an inverted source model and spectral synthesis of slip random fields (Mai and Beroza, 2002; Lavallée et al., 2006; Goda et al., 2014a). The stochastic tsunami hazard modelling approach also enables the quantification of epidemic uncertainty associated with tsunami hazard modelling. Therefore, to evaluate a wide range of tsunami risk situations, a stochastic probabilistic tsunami loss estimation method is proposed (Chapter 3) by employing scaling relationships for tsunamigenic earthquakes (Goda et al., 2016). By conducting Monte Carlo tsunami simulation and integrating with the vulnerability component, probabilistic tsunami risk analysis (PTRA) or tsunami catastrophe model can provide a set of hazard and risk information including: stochastic tsunami hazard or risk maps (e.g. inundation depth, loss, damage probability spatial distribution), the tsunami risk curves (i.e. probability exceeding a certain a loss level) at different scales (i.e. a building, a community, or a region). Such quantitative estimation of potential tsunami hazard and risk information is valuable for different stakeholders in making various tsunami risk management decisions over a variety of temporal and spatial scales. The novelty of this framework is that the primary uncertainty in the tsunami catastrophe model is taken into account and quantified for tsunami loss estimation. In other words, PTRA through stochastic source modelling with Monte Carlo tsunami simulation offers various new ways of presenting and visualising tsunami hazard and risk results.

Enhancing the accuracy of tsunami hazard and risk assessment is the fundamental solution to effective tsunami risk management. In addition to the uncertainties associated with tsunami event generation, the secondary sources of uncertainty also have a significant influence on tsunami risk results. These sources of uncertainty include modelling resolution of tsunami propagation and run-up, the selection of intensity measure (IM), building attributes (e.g. structural type and location), and earthquake recurrence model. The quantification of these uncertainties in the tsunami catastrophe model informs tsunami modellers/analysts of the relative importance of the key modelling options and improves the understanding of uncertainty in tsunami risk results, especially when available data are limited and is not of satisfying quality.

Similar to flood modelling which is sensitive to spatial resolution (Fewtrell et al., 2008; Sangati and Borga, 2009), resolutions of bathymetry and digital elevation model (DEM) represent the ability of reflecting the local geographical features and make a significant difference to local tsunami intensity (Griffin et al., 2015; Schäfer and Wenzel, 2017; Muhammad and Goda, 2018). Unlike seismic risk, the influenced area

by tsunamis is significantly smaller, limited to coastal areas less than 5 km (mostly less than 3 km) from the sea, and the local tsunami intensity largely depends on the location of buildings as well. The seismic intensity is similar in the tsunami inundated area, while the tsunami intensity varies significantly at different locations. The resolution of DEM represents its ability of reflecting geophysical and geographical features of different locations. Therefore, local tsunami risk is sensitive to the location attributes and thus significantly depends on the resolution of DEM.

One source of uncertainty associated with damage estimation can be attributed to the use of appropriate intensity measure (IM). Inundation depth has been widely used as tsunami IM because it is the most available data from post-event surveys. However, it cannot solely represent the tsunami effect on structures, especially for damage caused by hydrodynamic, impulsive, and debris impact forces which are more influenced by flow velocity (Yeh et al., 2013, 2014). Therefore, the probabilistic tsunami loss considering other tsunami IMs (i.e. flow velocity and momentum flux) help understand the suitability of using inundation depth for loss estimation and the importance of considering additional/other tsunami IMs.

Another major source of uncertainty in a tsunami catastrophe model is the occurrence rate prediction for mega-subduction earthquakes (Chapter 5). Tsunamis are triggered by large subduction earthquakes which have a long return period. This means there are far less historical events than smaller crustal earthquakes that occur more frequently. A Gutenberg-Richter (GR) magnitude-occurrence rate relationship is commonly used for crustal earthquakes, which is typically combined with a memoryless Poisson process with a constant occurrence rate over time. However, it has been commonly accepted that time-dependent recurrence models are more suitable for subduction earthquakes, and the Poisson process tends to overestimate the occurrence rate, unless the fault rupture is overdue (Ellsworth et al., 1999; Cramer et al., 2000; Gomberg et al., 2005; Sykes and Menke, 2006; Abaimov et al., 2008; Geist and Parsons, 2011; Fitzenz and Nyst, 2015). A time-dependent recurrence model is a quasi-periodic process; its inter-arrival time distribution is expressed by a certain probability distribution (Anagnos and Kiremidjian, 1988; Matthews et al., 2002; Garavaglia et al., 2010; Parsons et al., 2012). The lack of historical data results in uncertainty in tsunami recurrence models. Since no consensus has been reached with regard to the most suitable earthquake recurrence model, the comparison of multiple models with various reasonable model parameters improves the understanding of uncertainty related to tsunami recurrence.

The tsunami losses using different recurrence models imply how the uncertainty in recurrence models propagates into tsunami risk.

For disastrous hazards like tsunamis which result in tremendous economic losses, financial risk transfer tools are necessary for earthquakes and hurricanes. Tsunamis have been gaining its weight as one of the low-probability high-consequence natural perils in the insurance market after the devastating 2011 Tohoku tsunami. Similar to earthquakes and tropical cyclones, the tsunami risk is ceded through multiple layers of insurance risk transfer instruments; the pricing of insurance risk transfer instruments is typically conducted through catastrophe modelling (Mitchell-Wallace et al., 2017). In the insurance risk sharing system, the first layer is tsunami insurance which is a policy issued between property owners and an the insurance company. The current-state-of-practice earthquake and tsunami insurance rate making are based on independent catastrophe models. However, realistically, tsunamis are secondary hazards triggered by mega-subduction earthquakes, and thus they share the same hazard source and occurrence rate. For portfolios affected by both hazards, the accumulation of earthquake risk and tsunami risk involves great uncertainty because they are essentially a series of events. To bridge the missing link between the tsunamis and triggering earthquakes, a multi-hazard earthquake-tsunami risk model is developed and is applied to insurance rate making (Chapter 5). Similar to earthquake insurance, structural attributes should be reflected, resulting in different tsunami insurance rates due to structural vulnerability of different structure types. Importantly, tsunami risk is more sensitive to the location attributes than seismic risk at a smaller scale; seismic intensity at a community scale may be regarded as almost uniform, while tsunami intensity can vary significantly, depending on location attributes, such as coastal topography (i.e. plain coast or ria coast), distance from the sea, and land elevation. According to location attributes and structural attributes, the tsunami pure premium rates are differentiated by structural material, distance from the sea, and land elevation.

1.2 Scope and objectives

A novel stochastic tsunami risk assessment framework is proposed in this thesis, which entails key uncertainties of hazard, vulnerability, and exposure comprehensively. This stochastic PTRA method takes into account a wide range of possible tsunami scenarios and corresponding consequences to enrich the risk information related to potential con-

sequences of buildings in coastal areas, which facilitates the tsunami risk management decisions by different stakeholders. Based on this PTRA framework, the thesis intends to quantify the several sources of uncertainty in tsunami catastrophe modelling and investigates how the uncertainty propagates into tsunami loss and influences insurance rate making.

Different sources of uncertainty are investigated, including earthquake source characterisation, the influence of DEM resolution, the selection of tsunami intensity measures, the effects of location attributes of buildings (i.e. coastal topography, distance to the sea, and elevation), and the impact of tsunami recurrence modelling. The research is carried out by focusing upon on a case study in Sendai and Onagawa, Miyagi Prefecture, Japan. The relative importance of these uncertainties is useful for informing stakeholders who are concerned by tsunami risk, such as parametrising tsunami risk for insurance portfolio diversification, particularly when given data of poor quality (e.g. DEM of low resolution and a lack of historical data).

Reflecting the findings for the above mentioned uncertainties in the tsunami catastrophe model, an earthquake-tsunami insurance rate making method is proposed by taking into account tsunamis and triggering earthquakes as a series of events. Besides, the insurance rate is differentiated considering the structure type, coastal topography, distance to the sea, and land elevation.

1.3 Structure of the thesis

Chapter 2 reviews the methods of tsunami catastrophe modelling. A literature review is carried out by covering all main components of a tsunami catastrophe model and identifies different sources of uncertainty which need to be better understood and characterised with the focus on tsunami loss. In addition to tsunami risk assessment, the importance of tsunami catastrophe modelling for the insurance financial risk transfer and its role in facilitating the development of risk transfer instruments are reviewed as well.

A comprehensive computational stochastic tsunami risk assessment framework is proposed in Chapter 3 based on a stochastic tsunami hazard modelling method. The stochastic tsunami risk assessment method is implemented and explained through a

case study of the 2011 Tohoku tsunami. Through novel earthquake source modelling combined with Monte Carlo tsunami simulation, tsunami hazard and risk for the case study region are evaluated by considering hundreds of different tsunami scenarios and probabilities, and are presented by employing various visualisation methods (e.g. stochastic tsunami hazard maps using different IMs and tsunami loss curves at different scales). In particular, the influence of DEM resolution is investigated by comparing tsunami losses at calculated based on DEMs of four resolutions different scales .

The stochastic risk assessment framework developed in Chapter 3 is extended in Chapter 4 to consider tsunami flow velocity and momentum flux in addition to the commonly used inundation depth as tsunami IMs. The updated loss estimation method is referred as bivariate-IM method. For the fair comparison and due to the lack of momentum-flux-based tsunami fragility models, a new set of tsunami fragility functions considering momentum flux are developed using a multinomial regression approach, which is the same method that was adopted by De Risi et al. (2017) in developing the flow-velocity-based fragility functions. The importance of flow velocity and momentum flux is discussed by comparing tsunami loss estimations based on inundation depth only and losses considering the additional IM.

Chapter 5 develops a multi-hazard catastrophe model considering earthquakes and tsunamis as coupled events and proposes a new multi-hazard insurance rate making method considering the dependency between tsunamis and earthquakes. The uncertainty of tsunami occurrence rate is explored by considering multiple time-dependent earthquake recurrence models that are characterised by different probability distributions and model parameters. In addition, to differentiate premium rates for fair pricing, the influence of structural attribute (i.e. structure type) and location attributes (coastal topography, distance from the sea and elevation) are investigated.

The major conclusions and suggestions for future works are presented in the Chapter 6. The findings of this research promote the understanding of uncertainties in the tsunami catastrophe model and thus facilitate the decision-making of different stakeholders for tsunami risk management.

1.4 Research outputs

The work presented in this thesis have been submitted or published in the following publications.

Song, J. and Goda, K. (2019). Influence of elevation data resolution on tsunami loss estimation and insurance rate-making. *Frontiers in Earth Science*, 7(246).

Song, J. and Goda, K. (2019). Insurance rate differentiation of multi-hazard shaking-tsunami loss coverage for subduction earthquakes. In *13th International Conference on Application of Statistics and Probability in Civil Engineering*, Seoul, South Korea.

Goda, K., Franco, G., Song, J., and Radu, A. (2019). Parametric Catastrophe Bonds for Tsunamis: CAT-in-a-Box Trigger and Intensity-based Index Trigger Methods. *Earthquake Spectra*, 35(1), 113–136.

Song, J., De Risi, R., and Goda, K. (2018). Probabilistic tsunami loss estimation using momentum flux-based tsunami fragility functions. In *16th European Conference of Earthquake Engineering*, Thessaloniki, Greece.

Song, J., De Risi, R., and Goda, K. (2017). Influence of flow velocity on tsunami loss estimation. *Geosciences*, 7(4).

Goda, K. and Song, J. (2016). Uncertainty modeling and visualization for tsunami hazard and risk mapping: a case study for the 2011 Tohoku earthquake. *Stochastic Environmental Research and Risk Assessment*, 10(8):2271-2285.

Song, J. and Goda, K. (2015). Sensitivity of probabilistic tsunami loss estimation to stochastic tsunami modelling. In *The 13th International Probabilistic Workshop*, Liverpool, UK.

Chapter 2

Background of Tsunami Catastrophe Modelling

This chapter reviews the tsunami catastrophe modelling and identifies the research gaps in tsunami risk assessment. In a catastrophe model, uncertainties come from each catastrophe model component (i.e. hazard, vulnerability, exposure, and financial loss). They propagate and contribute to the uncertainty in loss and consequently influence the decision-making for tsunami risk management. In each model component, there are multiple sources of uncertainty, which have different levels of importance for tsunami risk assessment. For more accurate tsunami risk assessment, the uncertainties in the tsunami catastrophe model need to be better understood. Therefore, this chapter identifies different sources of uncertainties in the tsunami catastrophe model and reviews the existing research with regard to each aspect (Section 2.2 and Section 2.3).

A comprehensive dataset used in this study is demonstrated in Section 2.4, since the uncertainties in the tsunami catastrophe model are investigated through a case study based on the Miyagi Prefecture, Japan, which was severely inundate during the 2011 Tohoku tsunami. Given the tremendous loss caused by tsunamis, the primary financial risk management method to transfer the tsunami risk through insurance risk transfer instruments (e.g. insurance, reinsurance, and CAT bonds), which are developed based on catastrophe modelling. Section 2.5 reviews the role and importance of catastrophe modelling for developing financial risk transfer tools. Tsunami loss has only attracted the attention in the insurance market since the the devastating 2011 Tohoku tsunami, and the current tsunami catastrophe model in practice needs improvement by better understanding of uncertainty in the tsunami catastrophe model. In addition, Section 2.5.3

also reviews the current-state-of-practice tsunami catastrophe model for Japan and the corresponding issues.

2.1 Catastrophe modelling

This section reviews the importance of catastrophe modelling for financial risk management through insurance risk transfer instruments. Catastrophe risks are more threatening than non-catastrophic risks due to their high consequences and regional concentrations. Extreme events, such as the 2011 Tohoku earthquake and the 2005 Hurricane Katrina, caused a direct economic loss of 211 billion USD and 125 billion USD, respectively (Kajitani et al., 2013). Even for the well-known catastrophe-prone areas, such as the Tohoku region before the 2011 event, the protection measures may turn out to be insufficient due to uncertainty in natural disasters. For example, the tsunami inundation scale of the 2011 Tohoku region was beyond the hazard level predicted by the then hazard map in practice which was prepared based on the worst historical event without considering other possible scenarios; more than 120,000 buildings were completely damaged, and more than 230,000 buildings were partially damaged (Mori et al., 2013). For risk management, catastrophe modelling is necessary, which facilitates the quantitative estimation of potential financial losses from extreme natural or man-made perils (Grossi and Kunreuther, 2005; Mitchell-Wallace et al., 2017). The catastrophe modelling typically referred in the insurance industry essentially corresponds to quantitative risk assessments in academic fields.

A general catastrophe model incorporates four main components: hazard, exposure, vulnerability, and financial loss, as depicted in Figure 2.1. The hazard module includes a physical model which characterises the mechanics of natural hazard processes as well as the spatial distribution of the physical impact over a geographical area at risk. For example, a tsunami is modelled by simulating triggering earthquake rupture and wave propagation. An earthquake source can be represented by earthquake magnitude and source parameters, such as fault geometry (i.e. width, length, and area) and rupture characteristics (e.g. slip, dip, and strike) (Somerville et al., 1999; Mai and Beroza, 2002; Satake et al., 2013; Goda et al., 2014a; Goda et al., 2016). The deformation of the sea floor due to earthquake rupture induces the displacement of water columns, which initiates the rise of water surface. The tsunami propagation and inundation can be modelled by evaluating non-linear shallow water equations (Goto et al., 1997), and

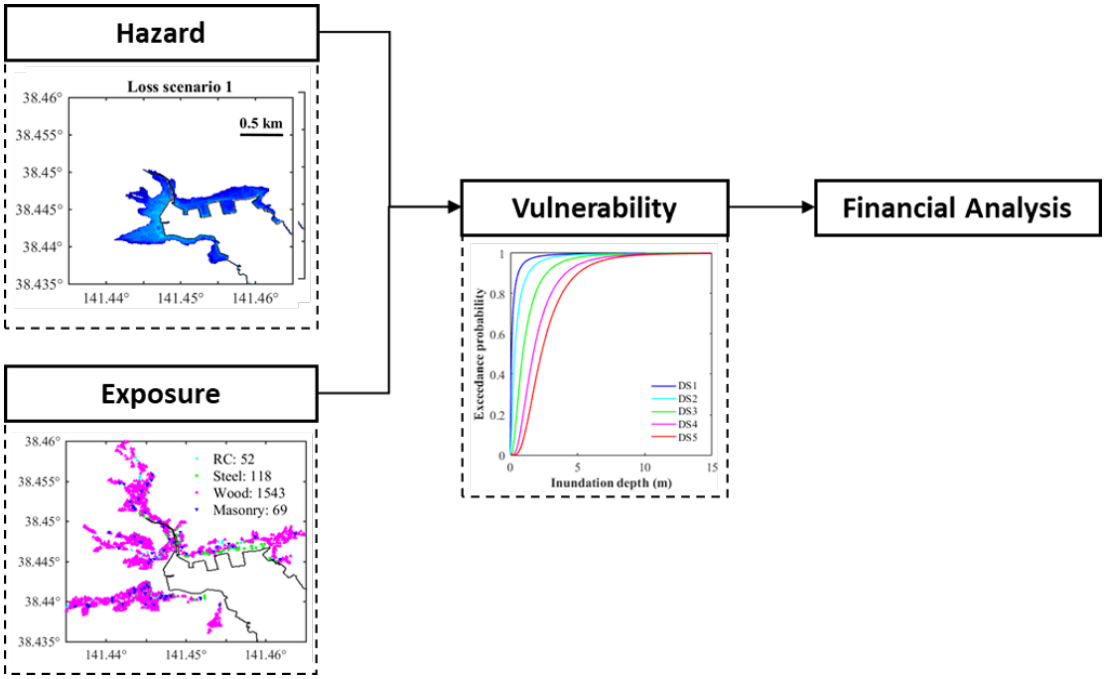

Figure 2.1 Structure of a tsunami catastrophe model.

inundation height/depth is commonly used to represent the tsunami intensity at a given location.

The exposure or inventory refers to assets at risk (e.g. insurance portfolio). The building inventory provides information of each structure of the building portfolio. Typical inventory attributes include building location and structure type (Grossi and Kunreuther, 2005). Taking tsunamis as an example, buildings closer to the sea tend to have higher tsunami risk and wood structures are more vulnerable than RC structures. The extended inventory database may include built year, number of floors, and whether or not retrofitted, which have influences on the resistance of structures. Given an insurance portfolio of buildings, the hazard module quantifies the hazard intensity at building locations.

The vulnerability module is the key to link the physical impact to the structural damage through fragility functions which provide the relationships between intensity measures (IM) and attained probabilities exceeding different damage states (Nielson and DesRoches, 2007; Sfahani et al., 2015; Charvet et al., 2017). The vulnerability of structure is commonly represented by fragility curves, such as the tsunami fragility curves shown in the vulnerability module in Figure 2.1). The last module of financial

loss estimation that translates the structural damage into probabilistic loss is the essential information for developing financial risk transfer instruments such as insurance policies and catastrophe bonds. For tsunami insurance rate-making, the catastrophe tsunami model can be regarded as a practical application of the probabilistic tsunami risk assessment (PTRA).

2.2 Tsunami hazard modelling

The recent disastrous tsunamis, including the 2004 Indian Ocean Tsunami, the 2011 Great East Japan (Tohoku) tsunami, and the most recent 2018 Sulawesi tsunami caused tremendous economic losses and casualties (Fujii and Satake, 2007; Le Billon and Waizenegger, 2007; Fraser et al., 2013; Kajitani et al., 2013; Heidarzadeh et al., 2018). A tsunami hazard assessment is the fundamental information to take tsunami mitigation measures, and one of the important results is the tsunami inundation map which predicts the spatial distribution of tsunami intensity. Due to the tremendous loss, an essential financial risk management method is to transfer the tsunami risk to the global market through insurance transfer instruments. To take either physical or financial protective measures for the tsunami-prone regions, one of the fundamentally important pieces of information is an accurate probabilistic tsunami hazard assessment (PTHA), which corresponds to the hazard module in a tsunami catastrophe model.

Large subduction earthquakes in the sea trigger tsunamis, and the tsunami hazard modelling consists of three components: i) earthquake occurrence, ii) earthquake source characterisation, and iii) tsunami propagation and inundation (Lynett and Liu, 2011). The physical process of tsunami generation and propagation has an significant influence on tsunami hazard and risk analysis, and tsunami risk mitigation measures that can be adopted proactively. Different stakeholders are keen on different hazard/risk information related to potential effects in coastal areas at varied temporal and spatial scales. The accuracy of tsunami hazard prediction directly influences the preparedness and mitigation of tsunami hazard in terms of both hard measures and soft measures.

2.2.1 Earthquake recurrence models

For catastrophe modelling of earthquakes and tsunamis, one of the primary sources of uncertainty is the occurrence rate of the events (Anagnos and Kiremidjian, 1988; Grezio et al., 2017; Kaczmarska et al., 2018). Probabilities of losses depend on the occurrence rate of earthquakes. The uncertainty in tsunami occurrence rate is even more significant because there are less historical data to constrain a recurrence model for tsunamigenic earthquakes which are usually triggered by large subduction earthquakes (i.e. greater than moment magnitude M_w 7.0). For probabilistic seismic risk assessment (PSRA), a standard model is a Poisson process that assumes the constant occurrence rate over time (Geist and Parsons, 2011). A standard practice in PSRA is to use a Gutenberg-Richter (GR) relationship between magnitude and occurrence rate (Gutenberg and Richter, 1956), which is a truncated exponential model. A GR magnitude-occurrence relationship is expressed as:

$$\log_{10} \lambda = a - bM \tag{2.1}$$

where λ is the occurrence rate of earthquakes with magnitudes greater or equal to M, the a-value reflects the level of seismicity, and the b-value is related to the rate decay of earthquakes with increasing magnitude. The b-value is typically close to 1 .

Recent studies have shown the time-dependency of earthquake occurrence rate particularly for large events, and the occurrence rate can be approximated by renewal recurrence models depending on the elapsed time since the last event (e.g. Ellsworth et al., 1999; Cramer et al., 2000; Gomberg et al., 2005; Sykes and Menke, 2006; Abaimov et al., 2008; Garavaglia et al., 2010; Geist and Parsons, 2011; Fitzenz and Nyst, 2015). Such findings are also applicable to PSTA since tsunamis are triggered by large earthquakes. A renewal model has the characteristics that inter-arrival times are independent and identically distributed random variables and the occurrence rate is updated after each event (Anagnos and Kiremidjian, 1988; Matthews et al., 2002; Garavaglia et al., 2010; Parsons et al., 2012). The occurrence rate increases with the elapsed time since the last event of the given fault, and the inter-event times follow a particular probability distribution due to its quasi-periodicity feature (Cramer et al., 2000; Sykes and Menke, 2006; Garavaglia et al., 2010). Time-dependent earthquake recurrence models are generally characterised in a physical or statistical approach. The former method is based on physical experiment and/or field observations theoretically with certain assumptions and simplifications of real situations, while the latter uses

empirical data such as historical inter-event times, elapsed time since the last event, locations of the rupture, and earthquake magnitude.

Typically, a time-dependent recurrence model for a given fault is expressed by a particular probability distribution (e.g. lognormal and Weibull) in the form of hazard rate function $h(t)$ of inter-arrival times t. The hazard rate function is controlled by the probability density function $f(t)$ and the cumulative distribution function $F(t)$, and is expressed as:

$$h(t) = \frac{f(t))}{1 - F(t))} \tag{2.2}$$

Accounting for the elapsed time T_e since the last event, , the updated cumulative distribution function $F_{T_e}(t)$ is expressed as:

$$F_{T_e}(t) = \frac{F(T_e + t)) - F(T_e)}{1 - F(T_e))} \tag{2.3}$$

The inter-arrival time distribution is characterised by three key parameters: the mean return period μ_t, coefficient of variation *cov* which is the standard deviation of inter-event times divided by the mean return period, and the elapsed time T_e. The uncertainty also exists in the determination of mean return period and *cov* due to limited historical data. Therefore, in tsunami hazard and risk assessments, multiple earthquake recurrence models can be implemented by considering a range of possible values of mean return period and *cov* to investigate the uncertainty and risk range caused by different occurrence models. The exponential distribution can be treated as a special case of renewal models which leads to a Poisson process and has a constant occurrence rate with a *cov* value of 1. Three time-dependent renewal models have been widely used for PSHA: lognormal (e.g. Gomberg et al., 2005; González et al., 2006; Sykes and Menke, 2006), Weibull (e.g. Lee and Tsai, 2005; Sykes and Menke, 2006; Abaimov et al., 2008; Fitzenz and Nyst, 2015), and Brownian Passage-time (BPT) (e.g. Console et al., 2008; Nomura et al., 2011; Parsons et al., 2012; Field and Jordan, 2015; Fitzenz and Nyst, 2015)). The lognormal distribution has been extensively used in engineering design to model specific types of data; the Weibull distribution is widely used for reliability and life data analysis of various components and phenomena; and the BPT distribution model characterises the earthquake rupture as a Brownian relaxation oscillator which is a loading and unloading process (Matthews et al., 2002). The $f(t)$ and $F(t)$ required for the hazard rate functions of the four occurrence models are:

Exponential

$$f(t) = \frac{\exp\left(-\frac{t}{\mu_t}\right)}{\mu_t} \tag{2.4}$$

$$F(t) = 1 - \exp\left(-\frac{t}{\mu_t}\right) \tag{2.5}$$

Lognormal

$$f(t) = \frac{1}{\sqrt{2\pi}\sigma_t t} \exp\left(-\frac{(\ln t - \mu_t)^2}{2\sigma_t^2}\right) \tag{2.6}$$

$$F(t) = \Phi\left(\frac{\ln t - \ln \mu_t + \ln(1+cov^2)/2}{\sqrt{\ln(1+cov^2)}}\right) \tag{2.7}$$

where μ_t and σ_t are the mean and standard deviation of lognormal distribution; and Φ^{-1} is the inverse of the standard normal cumulative distribution.

Weibull

$$f(t) = \frac{\kappa}{\zeta}\left(\frac{t}{\zeta}\right)^{\kappa-1} \exp\left(-\frac{t}{\zeta}\right)^{\kappa} \tag{2.8}$$

$$F(t) = 1 - \exp\left(-\frac{t}{\zeta}\right)^{\kappa} \tag{2.9}$$

where ζ is the scale parameter and κ is the shape parameter of Weibull distribution; $\zeta = \mu_t/\Gamma(1+1/\kappa)$; $cov = \sqrt{\Gamma(1+1/\kappa)/\Gamma(1+1/\kappa)^2 - 1}$.

BPT (Matthews et al., 2002)

$$f(t) = \sqrt{\frac{\mu_t}{2\pi cov^2 t^3}} \exp\left(-\frac{(t-\mu_t)^2}{2\mu_t cov^2 t}\right) \tag{2.10}$$

$$F(t) = \Phi\left[\frac{1}{cov}\left(\sqrt{\frac{t}{\mu_t}} - \sqrt{\frac{\mu_t}{t}}\right)\right] + e^{\frac{2}{cov^2}}\Phi\left[-\frac{1}{cov}\left(\sqrt{\frac{t}{\mu_t}} + \sqrt{\frac{\mu_t}{t}}\right)\right] \tag{2.11}$$

Different recurrence models result in significantly different hazard rates, which is further investigated in Chapter 5. The exponential distribution has a constant hazard rate equal to $1/\mu_t$; the lognormal distribution has a hazard rate reaching 0 at a long

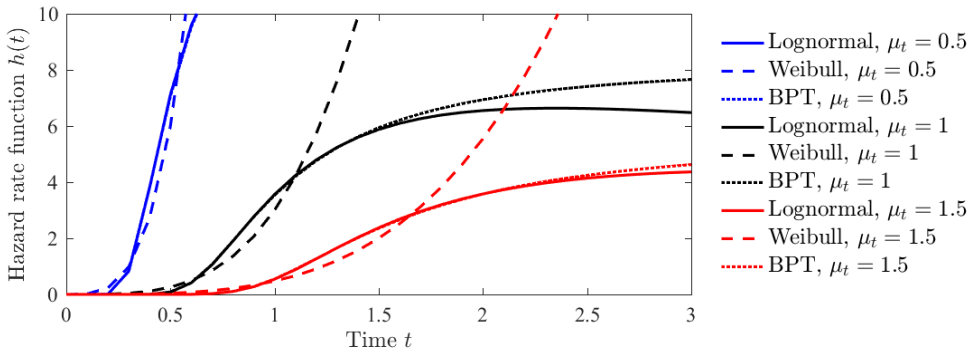

(a) Hazard rate functions with different values of μ_t and $cov = 0.25$

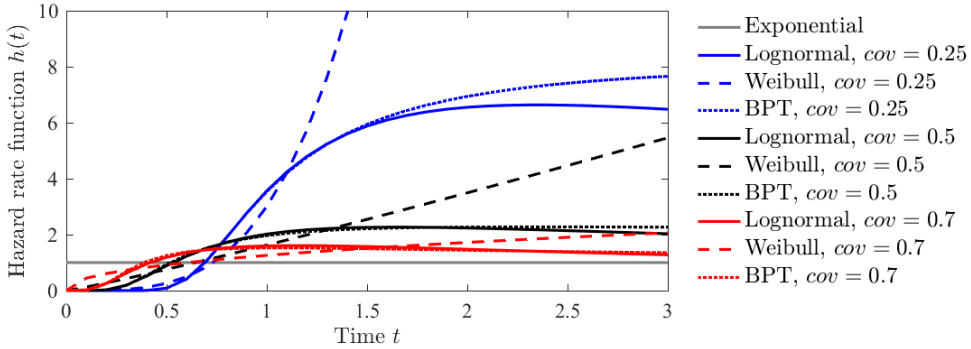

(b) Hazard rate functions with different values of cov and $\mu_t = 1$

Figure 2.2 Hazard rate functions of different renewal models.

elapsed time; the Weibull distribution with $\kappa > 1$ has a monotonically increasing hazard rate; and the hazard rate of the BPT distribution tends to be constant with the increase of elapsed time (Fitzenz and Nyst, 2015). The values of μ_t and cov can derived based on historical data, however, for large events like the 2011 Tohoku earthquake and tsunami, there is great uncertainty in determining the model parameters due to limited historical events. Figure 2.2 shows the hazard rate functions using four recurrence models (exponential, lognormal, Weibull, and BPT) given different values of μ_t and cov. The line types distinguish different renewal models and the line colours represent different parameters (either cov or μ_t). In Figure 2.2a, the cov is set equal to 0.25 and three values of μ_t (= 0.5, 1.0, and 1.5) are compared, while Figure 2.2b shows the results for three values of cov (= 0.25, 0.5 and 0.7) and $\mu_t = 1$. In Figure 2.2a, with the increase of μ_t the hazard rate functions increase rapidly in time, while the rate becomes lower for the time after μ_t. Figure 2.2b shows a constant hazard rate for the exponential model, and indicates that the hazard rate curves of time-dependent models become steeper when cov is smaller.

Currently, it is difficult to justify which renewal occurrence model is the best given the limitation of historical statistics as well as the nature of earthquakes, but a memoryless Poisson process is often considered to be unrealistic and less suitable for large subduction events (Anagnos and Kiremidjian, 1988; Ellsworth et al., 1999; Garavaglia et al., 2010; Fitzenz and Nyst, 2015). As seen in Figure 2.2, the calculated occurrence rates from different occurrence models differ significantly. To deal with the uncertainties in recurrence model and parameters, some studies implement multiple recurrence models in a logic-tree approach (Annaka et al., 2007; Field et al., 2009; Fukutani et al., 2015), but the weight of each case is based on expert opinions (i.e. assumed without physical evidence).

In Japan, the BPT inter-arrival time distribution is a preferred model (Fukutani et al., 2015; Nomura et al., 2011). For the 2011 Tohoku-type earthquake, the Japan Seismic Hazard Information Station (J-SHIS) (http://www.j-shis.bosai.go.jp/en/) and the Earthquake Research Committee (ERC) of Japan typically adopt a mean recurrence return period of 600 years and *cov* of 0.24 while estimating the return period to be between 300 to 800 years with wide variability. The BPT model is favoured by the ERC because the BPT model is considered to be physically compatible to the tectonic stress accumulating and releasing of an earthquake fault (Nomura et al., 2011) and the nearly constant hazard rate with a long elapsed time (Fitzenz and Nyst, 2015). Substantial uncertainty is involved by such assumptions and has a great impact on seismic and tsunami hazard assessments. It is important to mention that earthquake occurrence models for the Tohoku-like events consider only one characteristic magnitude of M_w 9.0, and do not consider any intermediate magnitudes between M_w 8.2 and M_w 9.0 (note: M_w 8.2 is the maximum magnitude considered for interface events that exclude the Tohoku-like events). Because it has been eight years since the 2011 Tohoku event (very short compared to the mean recurrence period), the 30-year and 50-year probabilities for the Tohoku-type characteristic earthquake predicted by the BPT model are nearly negligible, given the return period of 600 years and *cov* of 0.24. Consequently, the contribution of possible M_w 9.0 mega-thrust events to the probabilistic seismic hazard curves is evaluated as negligible. A different *cov* value may be more suitable, especially for the cases where the underlying inter-event time data for large subduction earthquakes are scarce (Nomura et al., 2011). It is important to point out that the *cov* values for global subduction earthquakes are in the range of 0.5 ± 0.2 (Sykes and Menke, 2006). Moreover, different renewal models with different model parameters can lead to a wide range of predictions with regard to the occurrence probability of major tsunamigenic

earthquakes as shown in Figure 2.2.

2.2.2 Tsunami source models

Major sources of uncertainty in predicting tsunami inundation intensity and extent can be attributed to source characteristics of future tsunamigenic earthquakes, such as location, magnitude, geometry, and slip distribution (Geist, 2002; McCloskey et al., 2008; Fraser et al., 2014; Goda et al., 2014a; Wiebe and Cox, 2014). The earthquake slip distribution has a significant influence on the triggered tsunami in terms of wave propagation and inundation extent. The primary source of uncertainty in tsunami hazard comes from earthquake source modelling. For a predictive purpose, considering an earthquake of a given magnitude, there are many combinations of the key source characteristics (e.g. size of the fault plain, strike, rake and dip).

The regional tsunami hazard maps in practice are prepared based on tsunami hazard parameters corresponding to a single tsunami scenario on a single fault or a few selected tsunami scenarios given different weights according to expert opinions. These deterministic approaches do not take into account the possible variation in the tsunami source model, and thus unable to reflect the variability of tsunami hazard situations (e.g. inundation area and tsunami intensity). The scenario-based or deterministic hazard analyses fail to take into account the uncertainty involved in tsunami hazard prediction and consequently users of scenario-based tsunami hazard maps are unable to assess the tsunami risk in different possible situations. The drawback of the scenario-based tsunami hazard assessment is highlighted by the 2011 Tohoku tsunami. The underestimated tsunami hazard for the coastal areas in the Tohoku region prior to the 2011 Tohoku earthquake and tsunami revealed the deep uncertainty and potential bias in some of the key assumptions in the assessment (e.g. the maximum largest earthquake in the offshore region of Tohoku). Note that Tohoku had been a well-identified region with high seismic and tsunami risk where protective countermeasures (e.g. breakwaters and seawalls) had been already in place, however, they turned out insufficient when the 2011 Tohoku tsunami struck Japan (Mori et al., 2011; Fraser et al., 2013). During the 2011 Tohoku tsunami, the experienced tsunami was significantly more than anticipated and the tsunami protection was overwhelmed; more than 65% of all fatalities in Kamaishi, Iwate Prefecture, Japan, were caused outside identified major inundation zones in public tsunami hazard maps presented before 2005. The tsunami hazard maps prepared based

on historical events/scenarios may underestimate the tsunami risk, which is the reason why the tsunami inundation extent due to the 2011 Tohoku event was beyond the hazard level in the 2005 hazard map.

The 2011 Tohoku tsunami, which was triggered by a M_w 9.0 earthquake off the north-east coast of Japan, was the most devastating tsunami in recent decades (Mori et al., 2011). The 2011 Tohoku tsunami provides a valuable opportunity with various types of data and information for tsunami modelling. Goda et al. (2014a) summarised 11 earthquake source models for the 2011 Tohoku tsunami, which were developed using different types of data (i.e. tsunami/teleseismic/geodetic) having different geometry parameters. In their study, it was shown that the variability of predicted tsunami wave profiles at buoys stations based on various source models compared to the observations leads to significant uncertainty associated with tsunami inundation due to uncertainty in earthquake source characterisation. To take into account a wide range of possible earthquake ruptures with different slips distributions and fault geometries, stochastic earthquake source modelling methods have been developed based on spectral analysis of slip heterogeneity of a tsunami inverted source model and spectral synthesis of slip random fields (Mai and Beroza, 2002; Lavallée et al., 2006). They facilitate the generation of possible tsunami scenarios triggered by different earthquake slips and fault geometries. However, these methods are only applicable to non-tsunamigenic earthquakes up to M_w 8.0.

Subsequently Goda et al. (2016) extended the stochastic earthquake source methods to include subduction earthquakes larger than M_w 8.0 by developing new scaling relationships which link earthquake source parameters (e.g. geometry, slip statistics, and spatial slip distribution) of a fault rupture with earthquake magnitude and also distinguish tsunamigenic and non-tsunamigenic earthquakes. Although a handful existing earthquake scaling relationships can be found in the literature which relate moment magnitude to different source parameters (e.g. Wells and Coppersmith, 1994; Somerville et al., 1999; Mai and Beroza, 2002; Blaser et al., 2010; Strasser et al., 2010), they are either developed for crustal earthquakes or not for tsunamigenic subduction earthquakes. For earthquake slip models with the same geometry and magnitude, different slip distributions can result in significant tsunami inundation consequences (Goda et al., 2014a). Therefore, the scaling relationships without considering more comprehensive slip parameters (e.g. mean and maximum slip) and spatial slip distribution, are not able to reflect the variability in the resulted tsunami inundation. For a particular tsunami

event of interest, the inversion-based rupture model can be referred to in the SRCMOD database (Mai and Thingbaijam, 2014) which contains 350 inverted finite-fault source models. The parameters derived from the spectral analysis are used in a spectral synthesis approach to generate random fields that represent earthquake slip with statistical properties equivalent to the reference slip model. Given the complexity and uncertainty of the rupture process of mega-thrust subduction earthquakes, details of the slip distribution and fault geometry of different inversion models vary significantly due to different sources of data (e.g. strong ground motion data, tsunami data, tele-seismic data and geodetic measurements) and modelling methods. The stochastic approach allows the inclusion of epistemic uncertainty related to earthquake source characterisation by considering multiple slip models (Goda et al., 2014a). A set of stochastic tsunami inundation hazard maps can be obtained through a large number of Monte Carlo simulations considering the uncertainty in the tsunami source, which promote the informed decision making regarding tsunami risk by showing a full range of different tsunami scenarios.

2.2.3 Tsunami propagation and inundation

Similar to quantifying the effects of earthquake ground motions, for which probabilistic seismic hazard assessment (PSHA) is carried out for the prediction of an earthquake intensity measure (e.g. peak ground acceleration *pga*), in PTHA the physical impact of tsunami is commonly characterised by tsunami inundation depth and flow velocity. Although a tsunami and the triggering earthquake share the same hazard source, PSHA adopts ground motion prediction equations (GMPE) which estimate the ground motion intensity given the earthquake magnitude, source-site distance, and soil condition (García et al., 2012; Douglas and Edwards, 2016; Montalva et al., 2017), whereas PTHA is typically based on tsunami propagation and run-up models (Goto et al., 1997; Geist and Parsons, 2006). The empirical method is suitable for a region with relatively abundant tsunami data (Geist and Parsons, 2006; Burbidge et al., 2008) and the analytical method is applicable for areas without extensive tsunami data (Power et al., 2007; Parsons and Geist, 2008).

Tsunami waves are initiated by the sudden deformation of sea-floor caused by the earthquake rupture (Okada, 1985). The initial water displacement depends on the sea-floor deformation, and the initial rise of water level is assumed to be identical to

the vertical displacement of the sea-floor in tsunami simulation. Besides the vertical effect, the horizontal displacement of the tsunami source has a significant influence on the tsunami wave profiles as well, particularly for earthquakes on a steep ocean slope (Tanioka and Satake, 1996). Therefore, given the earthquake source model, the initial water surface elevation can be calculated by using the analytical formulae of Okada (1985) and Tanioka and Satake (1996) as a joint effect of vertical displacement and horizontal displacement of the ocean bottom (Goda, 2015a).

The tsunami wave propagation can be approximated by evaluating the shallow water equations because the water depth is fractional compared to the tsunami wave-length (i.e. 10-500 km) (Kawahara et al., 1978; Shuto, 1991; Satake, 1995; Grezio et al., 2017; Schäfer and Wenzel, 2017). Under the shallow water theory, it is assumed that the vertical acceleration of water particles is neglected and the horizontal velocity is vertically uniform (Goto et al., 1997). Goto et al. (1997) developed a well-tested numerical code that simulates off-shore tsunami propagation and run-up processes by discretising the shallow water equations based on a leap-frog staggered-grid finite difference scheme. The Goto et al. (1997) code has been widely implemented for tsunami simulation in various tsunami studies (Sugawara et al., 2014; Goda, 2015b; Griffin et al., 2015). The drawbacks of the Goto et al. (1997) code are that it does not consider the effects of Coriolis force, spherical coordinates, and dispersion, and that the tidal force is not incorporated in the momentum equation. However, given the distance between the earthquake source and the coast of the 2011 Tohoku tsunami, these effects are sufficiently small to be neglected (Dao and Tkalich, 2007) for the specific source region.

The tsunami run-up is significantly influenced by the coastal topography (Mori et al., 2012; Leelawat et al., 2015). In terms of spatial inundation scale, plain areas (i.e. with greater inundation distance and moderate flow depth) tend to have a larger area inundated (i.e. with greater inundation distance and moderate flow depth) than higher terrain and river area (Charvet et al., 2014b). The influence of local geophysical features depends on the resolution of the bathymetry and digital elevation model (DEM). Tsunami modelling results are sensitive to DEM resolution (Satake, 1995; Tang et al., 2009; Schäfer and Wenzel, 2017). The tsunami inundation maps obtained by Griffin et al. (2015) and Muhammad and Goda (2018) have shown notable differences caused by DEM resolution and the importance of modelling with a high resolution. De Risi et al. (2017) demonstrated the sensitivity of tsunami hazard to DEM resolution for

evaluating the influence of flow velocity in the context of tsunami fragility modelling by comparing tsunami simulation results for the Tohoku region of Japan based on 10-m and 50-m DEM resolutions. However, it remains unknown if the conclusion is still valid when a coarser DEM is implemented (in the order of several hundreds of metres).

2.3 Tsunami fragility and damage estimation

2.3.1 Uncertainty of tsunami fragility functions

Tsunami fragility curves convert the hazard intensity of the tsunami waves on structures into the extent of physical damage. Similar to PSRA, tsunami fragility is an important component of PTRA. Unlike earthquake fragility curves which have been extensively developed for various structural types in different seismic regions, a limited number of tsunami fragility functions have been developed so far. The development of empirical fragility curves relies on availability of post-tsunami damage data, which is limited to specific regions where significant tsunamis had occurred and building damage surveys had been conducted. These fragility functions need to be developed on a regional basis as similar types of structures in different regions can have very different vulnerability given the same tsunami intensity (Suppasri et al., 2013).

The tsunami wave effects on structures are generally classified as different types of forces to facilitate engineering application: i) hydrodynamic forces, ii) hydrostatic forces, iii) impulsive forces, iv) buoyant forces, and v) debris impact and damming forces (Yeh, 2007; FEMA, 2012). The hydrostatic force is as calculated as a triangular pressure distribution increasing with tsunami depth h; the hydrodynamic force is a function of both inundation depth h and flow velocity v, which collectively is defined as momentum flux m ($= hv^2$), as a uniform load over the depth of tsunami wave; and the impulsive force is essentially the initial surging water on the structure, which is higher than the hydrodynamic forces (Yeh et al., 2014). In addition to water acting on structures, the mixture of floating debris can also cause major damage to structures (Fraser et al., 2013). However, the debris impact is not well understood and is not considered for tsunami structural design due to the difficulty of predicting such effects accurately (FEMA, 2012; Naito et al., 2013). It is commonly approximated as an impulsive force acting on the structure at the elevation of water surface, which is mainly controlled by the debris flow velocity and mass of the debris (FEMA, 2012; Yeh et al.,

2014).

Because of the complex composition of tsunami loading, various tsunami intensity measures (IM) have been used to represent the tsunami effect. In the literature, a consensus about which IM is the most representative for tsunami damage estimation has not been reached. The inundation depth h, which is equivalent to the maximum depth, is the most common tsunami IM, because it is the most measurable and accessible quantity in post-event surveys and also the essential information to calculate tsunami forces. The majority of the tsunami fragility functions are developed using inundation depth h as IM, based on empirical data of the past major tsunami events (e.g. the 2004 Indian Ocean tsunami and the 2011 Tohoku tsunami; Dias et al., 2009; Koshimura and Kayaba, 2010; Reese et al., 2011; Suppasri et al., 2011; Hayashi et al., 2013; Suppasri et al., 2013; Charvet et al., 2014a; Narita and Koshimura, 2015; De Risi et al., 2017). However, inundation depth cannot be taken as the sole representation of tsunami impact on structures, especially for damage caused by hydrodynamic and debris impact forces that are influenced by flow velocity v as well.

Although flow velocity is measurable from particle image velocimetry analysis of videos of survivors (Fritz et al., 2006; Hayashi and Koshimura, 2013), coastal oceanographic radar tsunami system (Lipa et al., 2012), and satellite altimetry (Song et al., 2012), these methods have their limitations in obtaining sufficient amount of data. The influence of flow velocity on tsunami fragility has been demonstrated by several studies (Charvet et al., 2015; Macabuag et al., 2016; Park et al., 2017), but the importance of velocity for tsunami loss has not been explored yet. Existing velocity-based fragility functions (Koshimura et al., 2009; Maruyama et al., 2013) offer an option to use either inundation depth or flow velocity, which enables the comparison of two intensity measures in tsunami risk assessment. However, such comparisons cannot be directly applied to evaluate the differences made by flow velocity in addition to inundation depth, since these models are developed for tsunami hazard parameters individually. Hybrid tsunami fragility functions considering inundation depth and flow velocity simultaneously have been developed based on observed inundation depth and simulated flow velocity, in a multinomial regression analysis approach (Charvet et al., 2015; De Risi et al., 2017). Results from the advanced statistical fragility analysis carried out by Charvet et al. (2014a) implied that inundation depth estimates low damage states reasonably well but does not have a satisfactory performance for high damage states, which indicated the inefficiency of inundation depth as tsunami IM and the influence of other factors, such

as debris impact and flow velocity. There is a knowledge gap between the importance of flow velocity for tsunami fragility model development and its influence on tsunami loss estimation; the latter may be more relevant for risk managers who are concerned with the financial impact of tsunami disasters. Although the simulation-based approach has a limitation in that simulated flow velocity values are associated with significant uncertainty and cannot be fully verified, such fragility functions considering multiple IMs allow the quantification of differences made by the inclusion of IM in addition to inundation depth.

In the context of efficient tsunami IM, the momentum flux hv^2 is often considered to be a superior hazard indicator for tsunami damage estimation because it captures both inundation h and flow velocity v (Tanaka et al., 2015; Macabuag et al., 2016; Park and Cox, 2016; Park et al., 2017). The integration of inundation depth and flow velocity also reduces the uncertainty of using the maximum value of h and v, because h_{max} and v_{max} do not necessarily happen at the same time and $h_{max}v_{max}^2$ is not equivalent to $(hv^2)_{max}$. Taking the maximum values of inundation depth and flow velocity can cause an overestimation of momentum flux up to 260% (Park et al., 2013). The momentum flux can be regarded as equivalent to hydrodynamic force since the hydrodynamic force is essentially a function of momentum flux. Several tsunami fragility functions have been developed using hydrodynamic force as IM (Suppasri et al., 2011; Hayashi et al., 2013). However, the observation of momentum flux or tsunami force is almost impossible in post-tsunami damage surveys, and hence, the tsunami fragility modelling based on momentum flux needs to solely rely on numerical simulations without calibration against actual data – this is a major drawback.

2.3.2 Influential factors of tsunami damage

Tsunami damage is largely dependent on building location and environment (Yeh et al., 2013). A quantitative assessment on influential factors of tsunami building damage carried out by Leelawat et al. (2014) indicates that inundation depth, building function (i.e. residential, commercial, public facility or transport facility), coastal topography, and building material can significantly affect the damage scale of buildings; for wood structures which are the main building material for residential houses in Japan, the number of floors is another significant variable. However, the influence of geographical features, such as distance from the sea and land elevation, has not been quantitatively explored.

Given the importance of these explanatory factors which were proved predominant on tsunami damage (Suppasri et al., 2012, 2013; Leelawat et al., 2015), tsunami fragility curves used for damage prediction are associated with a high degree of uncertainty.

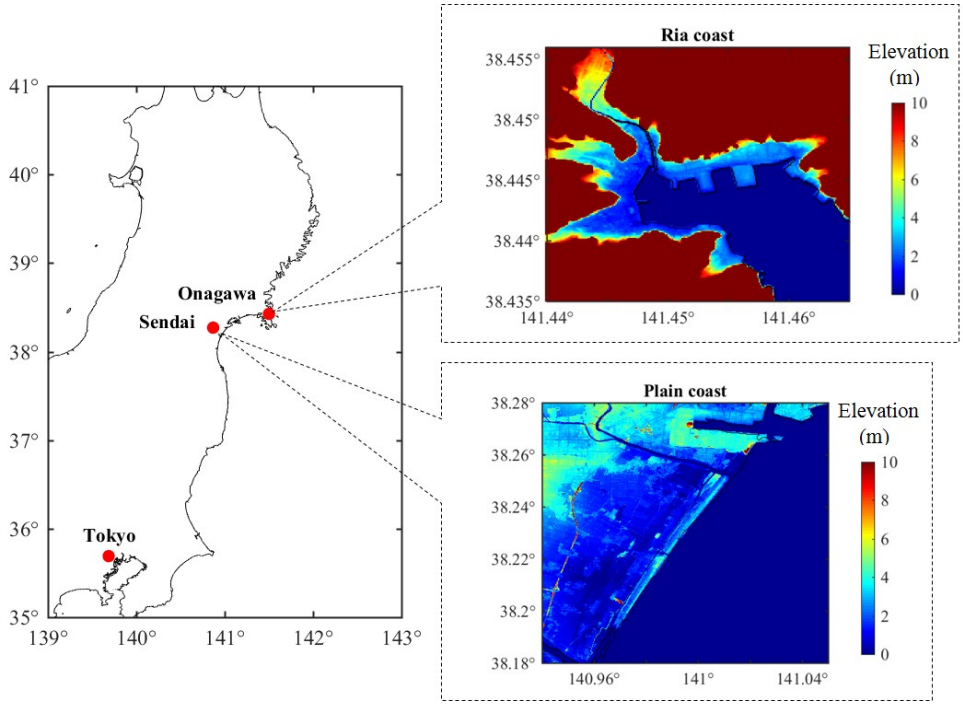

Figure 2.3 Plain coast and ria coast in the Tohoku region of Japan.

The coastal topography in Miyagi Prefecture, Japan can be broadly classified as plain coast and ria coast. As shown in Figure 2.3, a plain coast has a relatively flat terrain (e.g. the Sendai Plain), while the ria coast is located on rising terrain with steep and narrow bays (e.g. Onagawa). Coastal topography has been found important in characterising inundation situations during the 2011 Tohoku tsunami (Mori et al., 2012; Suppasri et al., 2012). The V-shape bays of ria coast can induce resonance of tsunami waves and thus amplifies tsunami effect. A plain coast tends to experience tsunami waves with much farther travelling distance (Suppasri et al., 2012). For example, during the 2011 Tohoku event, the highest tsunami run-up occurred at regions featuring a ria coast; the maximum tsunami inundation heights at Otsuchi were more than two times higher than those of the Sendai Plain (Mori et al., 2013). The tsunami fragility curves developed by Suppasri et al. (2013) that use inundation depth as IM and distinguish coastal topography also indicate that structures along ria coast are significantly more vulnerable than those on plain coast. Besides, the local topography can also dramatically influence the maximum tsunami height and flow velocity (Mori et al., 2013; Charvet

et al., 2014b; Suppasri et al., 2015).

2.4 Dataset for the 2011 Tohoku tsunami

Compared to existing databases for other tsunami-prone regions around the world, an extensive dataset is available for the 2011 Tohoku tsunami, which provides a unique opportunity for tsunami studies. The bathymetry/elevation data, roughness data, information of coastal defence structures for the Tohoku region are obtained from the Miyagi Prefecture Government. The damage data of buildings in the inundated area during the 2011 event are provided in the MLIT (2014) database. The key features of the available information are described below.

2.4.1 Bathymetry and elevation data

A complete set of bathymetry/elevation data , surface roughness data and coastal/riverside structures (e.g. breakwater and levees) is obtained from the Miyagi Prefecture Government. The bathymetry and elevation data are provided in five grid resolutions: 1350-m, 450-m, 150-m, 50-m, and 10-m. The ocean bathymetry data are based on the 1:50,000 bathymetric charts and digital database developed by Japan Hydrographic Association based on the nautical charts developed by the Japan Coastal Guard. The land elevation data are included in the DEM developed by the Geospatial Information Authority of Japan and the raw elevation data were obtained through airborne laser surveys and aerial photographic surveys. The measurement errors of the data are less than 1.0 m horizontally and 0.3 m to 0.7 m vertically (as standard deviation).

The elevation data of the coastal/riverside structures with dimensions less than 10 m are provided by municipalities in Miyagi Prefecture, because those with dimensions larger than 10 m are included in the DEM data. In tsunami simulations, the coastal/riverside structures are represented by a vertical wall at one or two sides of the computational cells. To evaluate the volume of water that overpasses these walls, Homma's overflowing formulae are employed.

2.4.2 MLIT database

The database provided by the MLIT contains more than 200,000 buildings across the area affected by the 2011 Tohoku tsunami. Information given for a building entry include: structural type (i.e. building material), number of storeys, damage state, inundation depth the building experienced, and location. The structural types are categorised as reinforced concrete (RC), steel, wood, and masonry, noting that the tsunami capacities for RC, steel, wood, and masonry buildings differ significantly (Koshimura et al., 2009; Suppasri et al., 2013). The damage state is defined as six damage classes: (1) minor damage DS1, (2) moderate damage DS2, (3) major damage DS3, (4) complete damage DS4, (5) collapse DS5 and (6) washed-away DS6. The classification details for each damage state is summarised in Table 2.1.

Table 2.1 Definition of damage states.

	Damage State	Description[1]	Condition[2]
DS1	Minor	No significant structural or non-structural damage	Possible to be used immediately after minor floor and wall clean
DS2	Moderate	Slight damage to non-structural components	Possible to be used after moderate repair
DS3	Major	Heavy damage to some walls but no damage in columns	Possible to be used after major repair
DS4	Complete	Heavy damage to several walls and some columns	Possible to be used after a complete repair and retrofitting
DS5	Collapse	Destructive damage to walls (more than half of wall density) and several columns (bend or destroyed)	Lost functionality (system collapse). Non-repairable or great cost for retrofitting
DS6	Washed-away	Washed away, only foundation remained, total overturned	Non-repairable, requires total reconstruction

[1]Descriptions from Japan Cabinet Office (2013)

[2]Conditions are from Suppasri et al. (2013)

Because both DS5 and DS6 will result in a full replacement of buildings, for the purpose of tsunami loss estimation DS5 can be re-defined as collapse and washed-away in this study and six damage states are reduced to five. RC and wood structures are further classified by the number of storeys as one storey, two storeys, and higher than

two storeys. The MLIT database also allows the investigation into coastal topographical effects, since the inundated buildings in Miyagi Prefecture are spatially distributed on both plain coast and ria coast.

2.5 Financial risk management

2.5.1 Catastrophe risk transfer system

Given the catastrophic losses of natural hazards, the individual property owners can hardly bear the loss of their houses and belongings, and catastrophe modelling has emerged to assist the insurance industry in transferring the catastrophe risk from the property owners who directly face the losses of catastrophes to the global market which has a much greater capacity and capital. Consequently, the catastrophe risk is shared and diversified among different stakeholders to reduce the chances of insolvency. The risk-sharing and diversification can be in forms of insurance/reinsurance and retrocession as well as insurance-linked securities (Dong and Grossi, 2005; Mitchell-Wallace et al., 2017). The catastrophe risks are insurable because the nature of natural disasters is highly uncertain. In the context of catastrophe losses, an insurance risk transfer instrument is essentially a financial compensation sold for future losses due to a particular type of natural peril, which may or may not happen during the policy term time (i.e. the period of time covered). A brief risk sharing diagram is shown in Figure 2.4. This involves policy holders, insurers, reinsurers, and investors in the capital market. A deductible is the amount of losses the insurer does not cover, which helps mitigate the moral hazard. In other words, the loss expenses not reaching the deductible are incurred by the policyholders. The insurance limit/cap limits the insurer's liability against huge losses, such as catastrophe losses (Cummins and Mahul, 2004). The co-insurance factor specifies the risk shared by the insurer proportionally for a loss exceeding the deductible but less than the limit. The excessive loss that the insurer is unable to bear needs to be transferred to the re-insurer and/or the capital market.

The incurred loss for the insurer, which is also the claims paid to the policyholders, is determined by the arrangements of three insurance parameters for risk transfer: deductible D, limit/cap C, and co-insurance factor η. The payout I_P of an insurance policy is commonly expressed as:

$$I_P = \begin{cases} 0 & L \leq D \\ \eta(L-D) & D < L < C \\ \eta(C-D) & L \geq C \end{cases} \tag{2.12}$$

In Figure 2.4, the loss not exceeding the deductible is sustained by the policyholders who pay premiums to the insurer. The loss between the deductible and limit is covered by the insurer and the reinsurer; the loss between the deductible and the attachment point is covered by the insurer while the excess of loss is shared between the insurer and the reinsurer proportionally by applying the coinsurance factor. The insurer pays premiums to the reinsurer to transfer the excess of risk. The high layer of risk which exceeds the limit is hedged in the capital market by insurance linked securities (ILS) such as CAT bonds (Cummins, 2008; Lakdawalla and Zanjani, 2012; Mariani and Amoruso, 2016). The high catastrophe risks are eventually transferred to the global capital market through various risk transfer instruments, and the rate-making for all kinds of premiums depends on the loss estimation from catastrophe modelling. The better the insurer/reinsurer understand the risk of its exposure to the catastrophe, the lesser amount of capital they need to reserve for such catastrophe risks (Gibson et al., 2014).

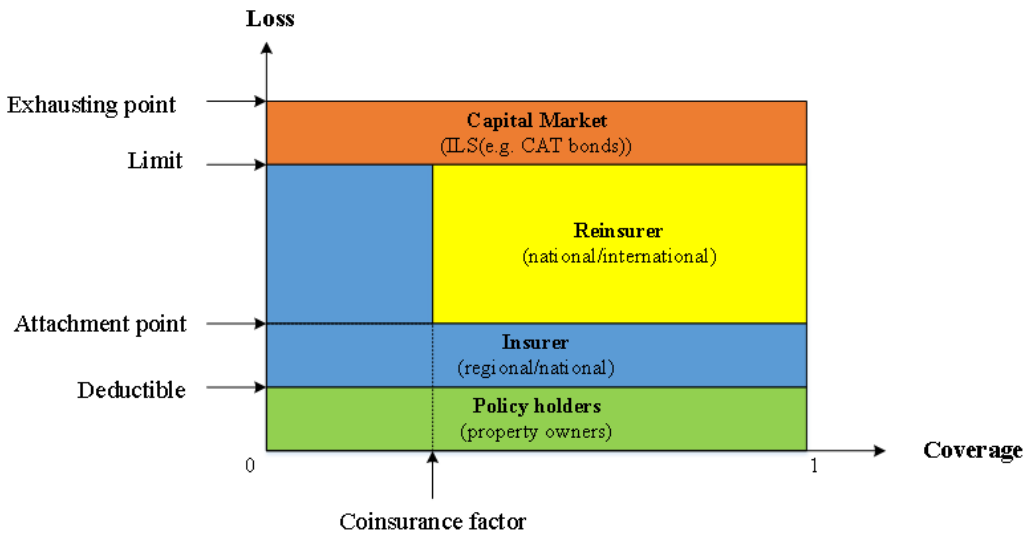

Figure 2.4 Insurance risk sharing diagram.

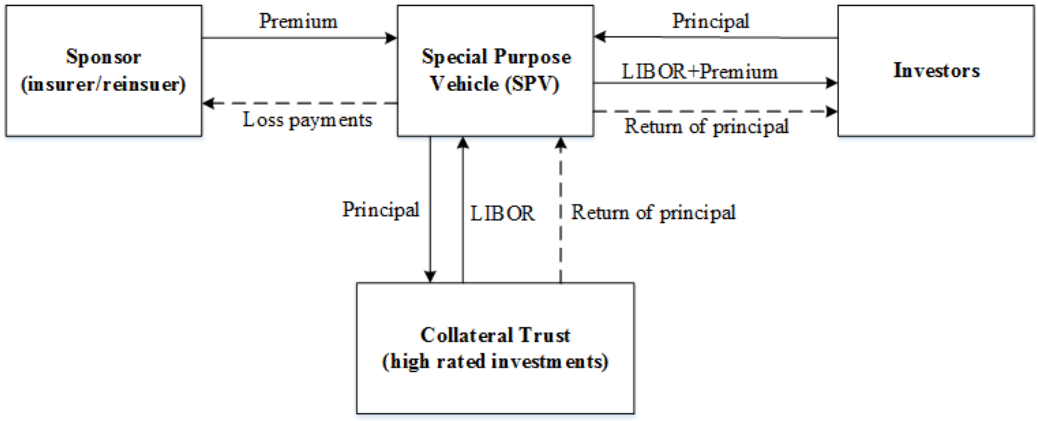

Figure 2.5 Structure of a CAT bond (Lalonde, 2005; Cummins, 2008).

The catastrophe risk of insurers and reinsurers that is transferred from property owners may be too high. The extremely high risk needs to be further transferred to the capital market which has a high capacity and is equipped with financial instruments for risk diversification, such as insurance linked securities such as CAT bonds. A CAT bond is one of the standardised event-linked securities which makes regular payments to the investors but the principal will be paid to the insurers/reinsurers when a specified natural catastrophe occurs, as demonstrated in Figure 2.5 (Cummins, 2008; Lakdawalla and Zanjani, 2012; Braun, 2016). CAT bonds have gained popularity in the global investment market to hedge the high risks of natural catastrophes (Cummins and Weiss, 2009; Lakdawalla and Zanjani, 2012). Compared to the conventional insurance risk transfer instruments, the remarkable role of CAT bonds is that it transfers the catastrophic risks from the property owners who are exposed to the disastrous losses to the global capital market where the risks are diversified (Franco, 2010).

A typical structure of a CAT bond is shown in Figure 2.5. There are mainly two stakeholders when issuing a CAT bond: the sponsor which is normally the insurer/reinsurer who wants to cede their excess of risk, and investors who offer the principal to cover the potential loss of a catastrophic event. The sponsor and investors do not have transactions directly but through the third-party entity called special purpose vehicle (SPV). SPV sells insurance contracts to the sponsor and collects investment principal from the investor (Braun, 2016). The agreement between the sponsor and SPV is similar to insurance policies. The fund collected from the two parties is held in a collateral trust account and invested with high-rated short-term securities which give steady returns at a risk free rate, such as London InterBank Offered Rate (LIBOR) (Cummins, 2008;

Braun, 2016). When the cat bond is not triggered, the investors receive LIBOR plus the premium, while if the bond is triggered, the investors lose their principal which will be paid to the sponsor to cover the loss of the event.

The selection of CAT bonds in terms of the trigger mechanism faces a dilemma between basis risk (i.e. the difference between the payout and the actual loss) and transparency, because the former is important for the sponsor while the latter is important for the investors, and a CAT bond with low basis risk and high transparency is preferred (Cummins, 2008; RMS, 2012). Compared to other types of CAT bonds of the different trigger mechanism, the parametric trigger has its advantage due to a good trade-off between the two concerns. The parametric CAT bonds are normally designed through catastrophe modelling for a certain natural peril, based on several physical characterising parameters which are measurable right after the event (Goda, 2015b). The parametric is beneficial to investors because it is easy for them to validate the parameters and the sponsors do not have much potential to influence the performance of the bond (Hagendorff et al., 2014). It has the highest transparency compared to other types of CAT bonds, but the payment to sponsors may not be able to cover all the losses, which poses basis risk to the issuer. Although indemnity trigger gives the lowest basis risk, which is favoured by the sponsors, it is disadvantageous to the investors given the low transparency and moral hazard involved. Another advantage of parametric CAT bonds is that the transactions are settled quickly after the event and thus the risk of bond extension is minimised.

2.5.2 Catastrophe insurance

For insurance decision-making, the loss is typically interpreted by exceedance probability (EP) curves, which demonstrate the annual probability of exceeding a certain loss level. From the EP curves, various risk metrics can be derived to aid the insurance decision-making: average annual loss (AAL), probable maximum loss (PML), value at risk (VaR), conditional value at risk (CVaR), and ruin probability (Goda et al., 2014b). AAL is the fundamental component of insurance premium calculation, taken as the pure premium (Straub, 1988; Grossi and Kunreuther, 2005). However, AAL is unable to capture the heavy tail by the low-probability high-consequence events, while the PML can, at least partially. VaR indicates the loss at a considered cumulative probability level, while CVaR takes the conditional expectation of loss exceeding a certain probability

level. The ruin probability is equal to the probability when the loss exceeds the insurer's reserve. In capturing the upper-tail loss characteristics, CVaR and ruin probability are generally more suitable.

The insurance premium is typically composed of pure premium P_{pure}, risk premium P_{risk}, and transaction fees $P_{expense}$, as shown in Equation (2.13) (Kuzak and Larsen, 2005; Gray and Pitts, 2012; Goda et al., 2014b):

$$P_{total} = P_{pure} + P_{risk} + P_{expense} \tag{2.13}$$

The risk premium is determined by the pure premium and various risk factors for insurers (e.g. insurers' capital reserve, transaction fees, and rate regularity requirement). The transaction fees reflect the administrative costs involved in issuing the insurance policy, which include marketing, premium taxes, and processing fees. P_{risk} and $P_{expense}$ are not negligible, but are difficult to evaluate. On the other hand, P_{pure} should be determined based on valid catastrophe modelling, which has been discussed throughout this thesis. Therefore, the pure premium is mainly focused upon in this thesis.

For fair insurance pricing, multiple attributes have been applied in some countries such as the US and Mexico when selling catastrophe insurance policies. Two critical factors are the structural attributes and location attributes of the insured properties (Kuzak and Larsen, 2005). The insurance premium rate varies given these attributes of the insured properties.

Structural attributes include features related to the resistance of structures in a hazard event, such as built year (i.e. what codes are enforced), structural type, number of storeys, and whether any structural retrofitting has been done. For example, wood structures are generally thought to be more seismic resistant, while they are more vulnerable to tsunami inundation than other building materials (Suppasri et al., 2013). The structural vulnerability can be reduced with some protective measures such as structural strengthening and better codes enforcement, however, many people often do not voluntarily adopt such protective measures before the event occurs (Kunreuther, 1996). In some countries such as the United States, an incentive scheme is devised for retrofitted buildings by offering discounted premium rates.

The location attributes reflect how susceptible the building is to a hazard of interest (Kuzak and Larsen, 2005). Taking seismic hazard as an example, the seismic intensity at a given site is a function of distance from the earthquake source and earthquake magnitude by using GMPEs and is also related to the local soil condition (Bommer et al., 2010; Barani and Spallarossa, 2017). For tsunami, the inundation risk of a building in a coastal region is closely related to its distance from the coast. Compared to seismic risk, tsunami risk is more sensitive to location attributes because the inundation distance is usually is no more than 3 km inland from the coast (Fraser et al., 2013), and even the disastrous 2011 Tohoku tsunami extended up to 5 km from the shoreline (Mori et al., 2012). Another location attribute that is important for the local tsunami hazard is the elevation. The inundation depth is the tsunami wave height minus the land elevation, and thus a higher elevation directly results in a lower inundation depth. The difference that elevation makes on local tsunami intensity eventually contributes to the tsunami loss estimation. There is a lack of literature in quantifying how the land elevation influences the tsunami risk.

Therefore, the uncertainty in the catastrophe modelling needs to be understood and quantified, which is beneficial for all stakeholders in the insurance risk transfer system. For insurers and reinsurers who sell insurance policies, a more accurate loss estimation help minimise their basis risk. The property owners want to have a fair insurance policy which is parametrised considering different attributes of properties. The influence of those attributes needs to be quantified and included in the catastrophe model for pricing depending on the importance.

2.5.3 Tsunami insurance

The tsunami risk did not draw the attention of the insurance market until the 2011 Tohoku tsunami because the large-scale tsunami did not occur in recent years and the tsunami risk was generally underestimated (AIR, 2013). Although the majority of the tsunamis are secondary hazards of earthquakes, currently the tsunami risk and earthquake risk are underwritten based on losses estimated by independent earthquake and tsunami catastrophe models without considering the dependency of tsunamis on subduction earthquakes.

A unique characteristic of tsunami damage is that buildings have experienced the ground shaking before tsunami waves, so the final damage of a structure is actually an accumulation of damage due to both the main-shock and tsunami waves in sequence. Currently the catastrophe modelling is carried out on a hazard-by-hazard basis (e.g. earthquakes, flooding, and tsunamis, respectively) based on substantial assumptions. However, realistically a tsunami cannot be isolated from the triggering earthquake. In other words, the earthquake is the cause of a series of following hazards including ground shaking, aftershock tremors, tsunami, fire, and landslides, and thus the final physical damage of a building is an accumulation of multiple cascading hazards. The coastal area inundated tsunami is threatened by high seismic risk at the same time. Therefore, tsunami vulnerability of structures should be analysed within a multi-hazard framework by considering the damage contribution of both strong ground motions and tsunami waves.

It remains a challenge to investigate the damage contribution of earthquake and tsunami in the same event, because it is difficult to distinguish the source of structural damage from observations in the post-event survey. For example, some buildings collapsed or were washed away during the tsunami and it is impossible to find out the damage caused by earthquake before the building was hit by tsunami waves. In this regard, Park et al. (2012) made an attempt to take into account the interaction of main-shock and subsequent tsunami and developed tsunami collapse probability curves. Their study indicated that there is a substantial difference which cannot be neglected with and without initial earthquake impact, however, only the collapse damage state was considered in their research and there is still no tsunami fragility functions that consider earthquake and tsunami at the same time. It remains to investigate how important the consideration of the two-phase loading (i.e. seismic loading and tsunami loading) is to tsunami fragility derivation and how sensitive the tsunami loss estimation is to this difference. Goda and De Risi (2018) developed a multi-hazard loss estimation method for shaking and tsunami using stochastic earthquake models as the source of both ground shaking and triggered tsunami. Their methodology takes into account the dependency of two hazards and a wide range possible earthquake slip distributions, which allows the consideration of tsunamigenic earthquakes and tsunamis as coupled events.

The current state-of-the-practice tsunami catastrophe model for Japan is one of the most advanced in the world. It takes into account the complexity of earthquake slip

model by using the kinematic slip distributions generation approach by Melgar et al. (2016) which was extended from the static slip distributions using Karhunen-Loève (K-L) expansion method (Woessner et al., 2018). Their approach allows stochastic tsunami source modelling but is not comprehensive because earthquake source is characterised by only magnitude and fault geometry parameters (i.e. width, length, and moment magnitude), while the new scaling relationships by Goda et al. (2016) characterise the earthquake source also by slip parameters (e.g. mean and max slips) and spatial slip distribution parameters (e.g. correlation lengths along the dip and strike directions). In the Japan tsunami catastrophe model, the earthquake sources are defined using a segmented method and their corresponding seismicities are consistent with the J-SHIS. The uncertainty in earthquake magnitude is considered as $M_w \pm 0.1$ with subjective weights based on the historical magnitude, but wider range of possible magnitudes are not considered. The J-SHIS treated the 2011 Tohoku event separately with a mean return period of 600 years and the BPT recurrence model, which does not belong to the segmented source zones. This leads to an occurrence probability of nearly zero for the time being, while the magnitudes of earthquakes in the segmented subduction zones defined by the J-SHIS which overlap with the 2011 Tohoku-type source zone do not exceed M_w 8.4. Due to the lack of historical events, there is great uncertainty in the occurrence rate and the associated magnitude, which is not adequately considered in the Japan tsunami catastrophe model (see Section 2.2.1). In the tsunami catastrophe model for Japan, 50-m DEM is used as the highest resolution which is not necessarily sufficient to reflect the variation of local tsunami risk. In addition, the tsunami damage is estimated using inundation depth-based tsunami fragility functions, which does not account the uncertainty of intensity measure as other IM such as flow velocity has a significantly influence on structures as well.

Chapter 3

Stochastic Tsunami Risk Assessment Framework

Publications resulting from this chapter:
Song, J. and Goda, K. (2019). Influence of elevation data resolution on tsunami loss estimation and insurance rate-making. *Frontiers in Earth Science*, 7(246).

Goda, K. and Song, J. (2016). Uncertainty modeling and visualization for tsunami hazard and risk mapping: a case study for the 2011 Tohoku earthquake. *Stochastic Environmental Research and Risk Assessment*, 10(8):2271-2285.

Song, J. and Goda, K. (2015). Sensitivity of probabilistic tsunami loss estimation to stochastic tsunami modelling. In *The 13th International Probabilistic Workshop*, Liverpool, UK.

3.1 Introduction

The most recent devastating tsunami that struck the Tohoku region of Japan in 2011 caused a tremendous economic loss (Kajitani et al., 2013). An extreme event, such as the 2011 Tohoku tsunami, has revealed the underestimation of tsunami hazard and insufficient tsunami countermeasures already in place before the event which were based on scenario-based tsunami hazard assessment according to historical events (Mori et al., 2011; Fraser et al., 2013). The underestimated tsunami hazard for the coastal areas in Tohoku prior to the event highlighted deep uncertainty and potential bias in

some of the key assumptions in the assessment (e.g. largest earthquake in the offshore region of Tohoku). The recent advancement of catastrophe modelling research has facilitated catastrophe risk management by providing more accurate estimates of the potential loss. All stakeholders who are involved in risk management are concerned about the scale of disasters, and a catastrophe model serves as a decision-support tool to manage their risk exposures more effectively. The 2011 M_w 9.0 Tohoku, Japan tsunami was an example that the exiting preparation turned out to be insufficient, although major countermeasures had been already in place (Mori et al., 2011). This highlights the importance of accurate hazard and risk assessments for extreme events. One of the reasons for this underestimation is that tsunami hazard maps serving at that time were prepared by considering tsunami hazard parameters that correspond to a single scenario on a single fault, and thus failed to assess uncertainty related to hazard predictions. As a result, deterministic tsunami hazard maps according to historical events were unable to incorporate all potential risks (i.e. tsunami loss) in different situations. Therefore, a set of tsunami hazard maps, representing various possible tsunami scenarios and consequences, will help understand the full picture of tsunami risk.

A strategy to address this issue is to consider possible scenarios comprehensively in tsunami hazard assessment. Based on the predicted hazard level, physical protective measures (e.g. breakwaters, sea walls, and sea dikes) can be taken to mitigate the tsunami impact, and evacuation plans can be made (Imamura et al., 2012; Strusińska-Correia, 2017). The uncertainty in the hazard propagates into the risk assessment, being transformed into tsunami impact parameters (i.e. economic loss). In addition to hard measures, a risk assessment of natural catastrophes is essential for achieving effective financial risk management to deal with the low-probability high-consequence events among stakeholders as well (Lakdawalla and Zanjani, 2012; Gibson et al., 2014; Mitchell-Wallace et al., 2017). Tsunami is one of such natural disasters, and thus the improved accuracy of tsunami loss estimation can help insurance/re-insurance underwriters to better understand their exposure to catastrophe risks. It is also beneficial for the profitable design of risk transfer instruments (Yoshikawa and Goda, 2013; Hagendorff et al., 2014; Goda, 2015b).

The physical processes of tsunami generation, propagation, and inundation have crucial influences on how hazard analysis is formulated and conducted, and what mitigation measures are adopted to protect our society and assets. Different stakeholders require different tsunami hazard/risk information related to potential effects on coastal commu-

nities and infrastructure over a variety of temporal and spatial scales. Understanding the meaning of hazard estimates with regard to epistemic uncertainty of hazard modelling processes is an essential part of probabilistic hazard analysis and thus visualisation of the outcomes of an uncertainty assessment has become increasingly important. Major sources of uncertainty in predicting tsunami inundation intensity and extent can be attributed to source characteristics of future tsunamigenic earthquakes, such as location, magnitude, geometry, and slip distribution (Geist, 2002; McCloskey et al., 2008; Fraser et al., 2014; Goda et al., 2014a; Wiebe and Cox, 2014). The methods for developing stochastic earthquake source models, based on spectral analysis of slip heterogeneity of an inverted tsunami source model (Mai and Beroza, 2002), facilitate the generation of possible tsunami scenarios triggered by different earthquake slips and fault geometry. For a predictive purpose, considering an earthquake of a given magnitude, there are many combinations of the key source characteristics (e.g. size of the fault plane, strike, rake and dip). To take into account tsunami risks in all situations, a large number of stochastic slip models are generated based on the parameters derived from spectral analysis of numerous inversion-based source models (Goda et al., 2016).

A comprehensive and extensive computational framework of tsunami hazard and risk assessment, which is based on stochastic tsunami modelling using scaling laws, is developed in this chapter. The stochastic tsunami loss estimation framework is generally composed of four major components:

- Earthquake occurrence
- Stochastic earthquake source modelling
- Tsunami inundation modelling
- Tsunami damage assessment and loss estimation

Resolutions of bathymetry and digital elevation model (DEM) used for tsunami modelling play a vital role in simulating tsunami propagation and inundation. In particular, tsunami inundation is sensitive to DEM resolution and leads to significantly different results (Satake, 1995; Tang et al., 2009). Besides, local tsunami hazard also depends on the location of buildings (Ioualalen et al., 2007). The uncertainty in these two aspects has a significant influence on tsunami hazard assessments (Griffin et al., 2015; Muhammad and Goda, 2018). However, the impact of the uncertainty to probabilistic tsunami loss estimation has not been investigated and quantified extensively. The

relative sensitivity of tsunami loss at different scales and the resulting spatial variability of the loss needs further investigation.

Compared to earthquakes, an area impacted by a tsunami is smaller and tsunami run-up and inundation can vary spatially within a small region (e.g. within 2 km from the sea). Moreover, the local tsunami intensity is sensitive to the resolution of land elevation data, especially for ria-coast areas with irregular-shaped shorelines. Although finer bathymetry and elevation data produce more accurate tsunami risk results, the elevation data of high resolution may not be available universally. Understanding the differences caused by adopting elevation data of a range of high and low resolutions is useful for understanding of the uncertainty in tsunami loss from elevation data resolution. For example, given the tsunami loss based on available DEM, such results answer the questions such as how much improvement can be made if a finer DEM is used and whether it is necessary to implement the finest DEM which dramatically increases the computation time.

The properties of key variables of tsunami hazard and data have a significant impact on the selection of visualisation methods. The variables may be multi-dimensional, and may be dependent spatially and temporally (e.g. tsunami depths at different locations, and losses given by different tsunami scenarios for the same location). The probabilistic characteristics of the variables can differ significantly (e.g. Gaussian variable versus non-Gaussian variable with heavy right tail). In these cases, simple metrics, such as mean and standard deviation (statistical moments), are not sufficient to convey the underlying uncertainty of the hazard and risk estimates, and some higher-order statistics as well as probability distribution may be presented graphically (Potter et al., 2010). For representing uncertainty of spatially varying quantities (e.g. tsunami inundation map), visual parameter cues, such as colour, texture, transparency, clarity, and size, can be varied in a cartographic graphical system (MacEachren et al., 2005; Kunz et al., 2011).

Within the stochastic tsunami risk assessment framework, this chapter investigates the influences of elevation data resolution on tsunami hazard estimates (e.g. inundation depth and flow velocity). The framework is not only able to present stochastic hazard and risk maps using based on multiple tsunami intensity measures, but also capable of generating probabilistic tsunami risk curves at different scales (i.e. single building, and a building portfolio). More specifically, the objectives of this chapter are to quantify how sensitive tsunami loss estimation is to DEM resolution at different scales: i) regional

(e.g. whole Sendai), ii) a local scale (e.g. a coastal community), and iii) a single location. The sensitivity of tsunami hazard intensity to DEM resolution is also important for evaluating the influence of flow velocity in tsunami simulations. Compared to tsunami loss obtained based on a fine-resolution DEM, if the simulated inundation depth and flow velocity based on a coarse-resolution DEM and not accurate, the tsunami loss would be significantly different as well. The inaccurate tsunami hazard intensity estimated by using coarse DEM directly results in underestimation or overestimation of tsunami loss, which adds uncertainty in tsunami risk management.

Sendai and Onagawa in Miyagi Prefecture, Japan, are selected as the representative sites of plain coast and ria coast, respectively. In addition to the M_w 9.0 events (the magnitude of the 2011 Tohoku tsunami), multiple possible magnitudes (i.e. M_w 7.6, M_w 7.8, M_w 8.0, M_w 8.2, M_w 8.4, M_w 8.6, M_w 8.8, and M_w 9.0) are considered. It was found that 300 simulations are sufficient to keep the median tsunami height stable, which is in agreement with other preliminary test results (De Risi and Goda, 2016). In total, 9600 tsunami simulations are conducted for each location by considering four grid resolutions of DEM (i.e. 10-m, 50-m, 150-m, and 450-m) and eight earthquake magnitudes. For each combination of the above (e.g. 10-m DEM and M_w 9.0 scenario for Sendai), 300 tsunami simulations are carried out.

3.2 Stochastic tsunami loss estimation framework

To consider multiple discrete earthquake magnitudes of the tsunamigenic earthquakes represented by f_{M_w}, a stochastic probabilistic tsunami risk can be expressed as:

$$\nu(L \geq l) = \frac{1}{\mu_t} \int \sum_{k=1}^{n} [p_{Mk} \cdot P(L \geq l | m_k)] \tag{3.1}$$

where $\nu(L \geq l)$ is the annual exceedance probability that the tsunami loss L exceeds certain loss threshold l, μ_t is the mean return period of earthquakes equal or greater than magnitude M_{min}, p_{Mk} denotes the probability mass for a given magnitude range which is represented by the kth magnitude m_k, and n is the number of magnitudes. For example, given a magnitude interval of 0.2, M_w 8.8 represents the magnitude range between 8.7 and 8.9. The conditional loss exceedance function $P(L \geq l | m_k)$ is given by:

$$P(L \geq l|m_k) = \int P(L \geq l|ds) f_{DS|IM}(ds|im) f_{IM|EQS}(im|eqs) \times f_{EQS|M_w}(eqs|m_w) |\mathrm{d}ds||\mathrm{d}im||\mathrm{d}eqs| \quad (3.2)$$

where $P(L \geq l|ds)$ is the tsunami loss function in terms of damage state variable (DS), $f_{DS|IM}$ is the tsunami fragility function in terms of intensity measure IM, $f_{IM|EQS}$ is the probability density function of IM given a particular earthquake slip model EQS which also corresponds to the induced tsunami scenario, $f_{EQS|M_w}$ is the probability density function of EQS given M_w, and f_{M_w} is the conditional probability distribution of $M_w \geq M_{min}$. Note that DS is often defined in a discrete manner; in such cases, integration for DS in can be replaced by summation. A typical IM is the inundation depth, which is often used as an input parameter for tsunami fragility modelling (i.e. $f_{DS|IM}$). $f_{IM|EQS}$ is obtained through numerical evaluations of governing equations for tsunami waves and inundation/run-up (e.g. solving the non-linear shallow water equations for given initial boundary conditions). The uncertainty associated with variable earthquake source characteristics is captured by f_{EQS}.

Given an earthquake magnitude and stochastic tsunami scenarios, Equation (3.2) can be calculated by:

$$P(L \geq l|m_k) = \frac{1}{n_{EQS}} \sum_{i=1}^{n_{EQS}} I_{m_k}(L_i \geq l|m_k) \quad (3.3)$$

where n_{EQS} is the number of earthquake/tsunami scenarios generated through stochastic source modelling. $I_{m_k}(L_i \geq l|m_k)$ is the count of scenarios which result in losses greater or equal to l.

3.2.1 Tsunami occurrence rate

As discussed in Section 2.2.1, the occurrence rate is critical for PTRA, which corresponds to $1/\mu_t$ in Equation (3.1) and has a direct influence on the probabilistic tsunami loss estimation. A standard occurrence model for earthquakes of an identified fault or source zone is a memory-less Poisson process with a Gutenberg-Richter (GR) relationship (Gutenberg and Richter, 1956). It should be noted that there is substantial uncertainty associated with the occurrence rate for earthquakes with a long return period

given the lack of historical data (Kagan and Jackson, 2013; Kaczmarska et al., 2018). The Poisson process is thought equivalent to the exponential recurrence model which has a constant occurrence rate. The Poisson-GR relationship may result in conservative loss estimation because the constant hazard rate of the Possion model is higher than that indicated by the renewal models at the early stage of strain accumulation (Goda and De Risi, 2018). It has been commonly accepted that time-dependent models are more suitable for mega-thrust subduction earthquakes (Ellsworth et al., 1999; Cramer et al., 2000; Gomberg et al., 2005; Geist and Parsons, 2011; Fitzenz and Nyst, 2015), but the consideration of renewal recurrence models is not the focus of this chapter which is discussed in Chapter 5.

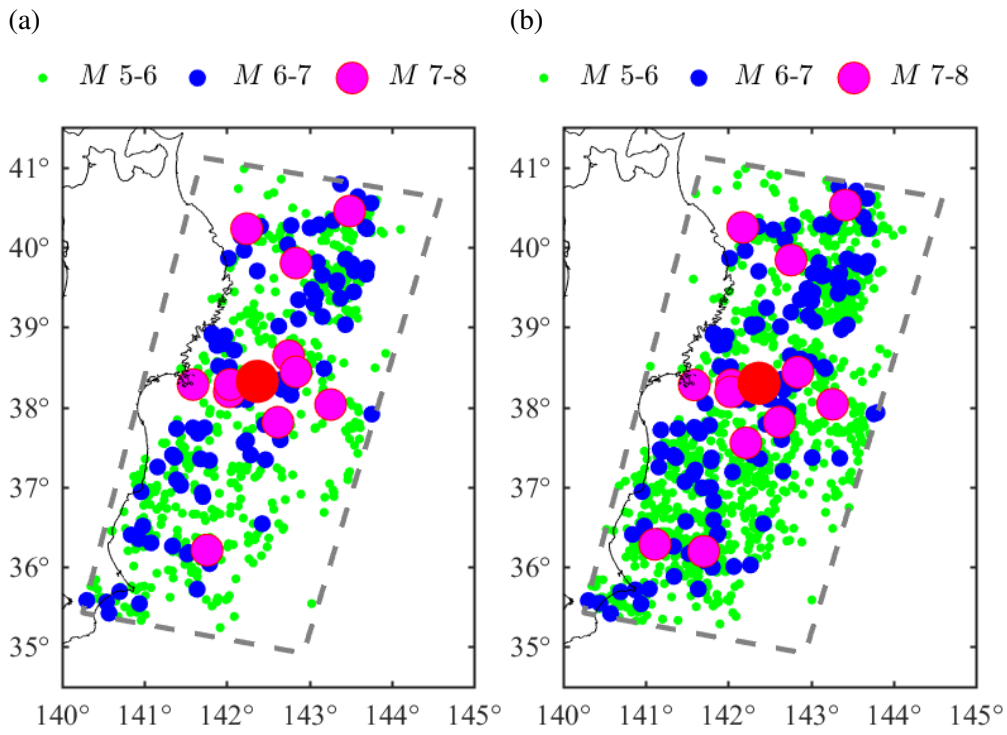

Figure 3.1 Harvard CMT and the NEIC catalogues: (a) Harvard CMT and (b) NEIC.

In this chapter, a Poisson process with a regional GR relationship is applied by considering tsunamigenic earthquake magnitudes between 7.5 and 9.1 with a 0.2 interval. The GR relationships for off-shore Tohoku region (the grey box in dashed line in Figure 3.1) are obtained using historical events from the Harvard CMT catalogue (http://www.globalcmt.org/CMTsearch.html) and the NEIC catalogue (http://seisan.ird.nc/USGS/mirror/neic.usgs.gov/neis/epic/code_catalog.html). The re-

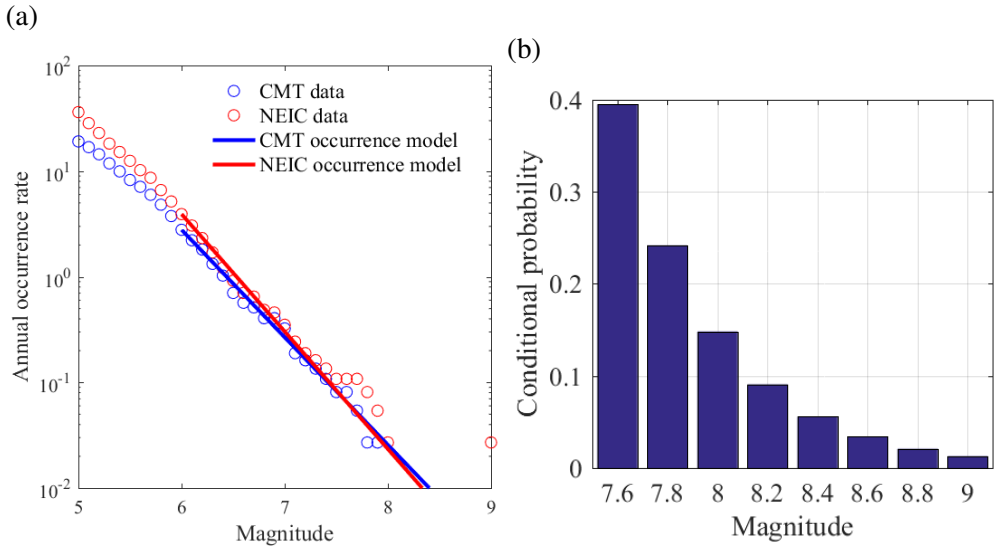

Figure 3.2 Seismicity of the off-Tohoku region: (a) GR relationships for the off-shore Tohoku region based on Harvard CMT and the NEIC catalogues, and (b) conditional distribution of earthquake magnitudes $\geq M_w$ 7.5.

gional seismicity in the Tohoku region based on these two catalogues can be found in Figure 3.1a and Figure 3.1b, respectively. This setup is consistent with the segmented subduction zones by the Japan Seismic Hazard Information Station (J-SHIS) which roughly correspond to the off-shore source zone for the Tohoku-type earthquakes as defined in Figure 3.1. The fitted GR occurrence models shown in Figure 3.2a are similar to that employed by the Headquarters for Earthquake Research Promotion (HERP) (2013), which adopted the catalogue of the Japan meteorological Agency. Figure 3.2a indicates that the annual occurrence rate of earthquakes larger than M_w 7.5 and M_w 8.1 is approximately 0.08 and 0.02, respectively. Based on the fitted GR occurrence model, the probability mass function (i.e. p_{M_k}) of a range of discrete magnitudes (e.g. 7.5 to 9.1) can be achieved, as shown in Figure 3.2b.

3.2.2 Stochastic tsunami source models

The current state-of-the-practice tsunami hazard maps which are prepared based on the hazard parameters of a single scenario on a single fault cannot deal with the potential risks in different situations. A method of stochastic earthquake slip modelling targeted for large mega-thrust subduction earthquakes, such as the 2011 Tohoku earthquake, is employed. The uncertainty of earthquake rupture characterisation is taken into account by using new scaling relationships (Goda et al., 2016) and stochastic slip synthesis

(Goda et al., 2014a). This is an extension of the earthquake slip modelling method developed by Mai and Beroza (2002) based on the spectral synthesis of random field, which is originally targeted for M_w 6-8 crustal earthquakes. For predictive purposes, the post-event evaluation for relevant source models is not applicable. Therefore, it is reasonable to take into account a wide range of possible slip distributions that are encompassed by the scaling relationships, and the resulting variability in tsunami hazard prediction can be interpreted to include epistemic uncertainty. This step of earthquake slip model generation corresponds to $f_{EQS}|M_w$ in Equation (3.2).

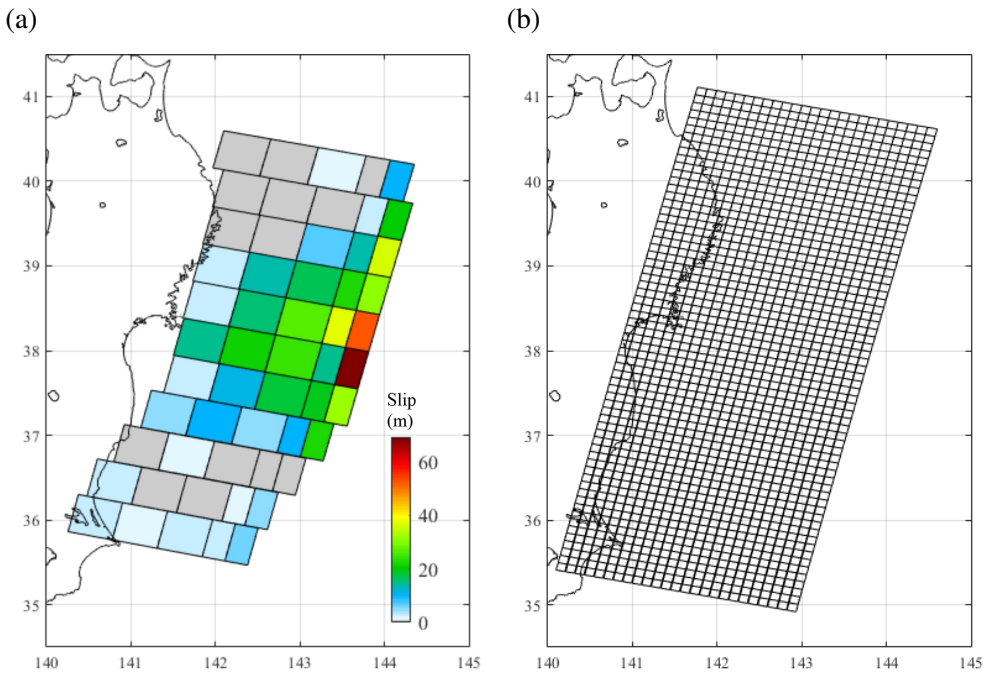

Figure 3.3 Earthquake source model: (a) earthquake source model by Satake et al. (2013), and (b) re-defined off-Tohoku tsunami source region.

Given the 2011 Tohoku tsunami, a seismic source zone, which is sufficiently large to accommodate a M_W 9.0 event, is defined as 650 km along the strike direction and 250 km along the dip direction (Figure 3.3) off the Tohoku region of Japan (Goda et al., 2016). To apply the stochastic synthesis method for generating slip distributions, the fault plane is discretised with sub-faults of 10 km$\times$10 km which have a constant strike of 193° and variable dip angles gradually steepening from 8° to 16° along the down-dip direction, based on the source model by Satake et al. (2013). The reasons for selecting the Satake et al. (2013) source model as reference are: i) it gives the best performance among the eleven inverted source models for the 2011 Tohoku event

(Goda et al., 2014a), ii) it was developed using tsunami data and kinematic rupture processes were considered, and iii) the tsunami simulation codes used in this thesis and the tsunami computation method adopted by Satake et al. (2013) are similar. The asperity zone corresponds to a smaller sub-region where a set of sub-faults have slip values greater than a threshold value and it is typically two to three times the average slip. The size and location of asperity zones of different magnitudes are different.

The fault rupture (i.e. geometry and slip distribution) is characterised through earthquake source models by multiple earthquake source parameters which vary and are obtained by applying scaling relationships given the magnitude (Goda et al., 2016). Three types of seismic source parameters are required for the stochastic tsunami simulation: i) geometry parameters including the fault width W, fault length L and fault area S, ii) slip parameters including the mean slip D_a, maximum slip D_m and Box-Cox power B, and iii) spatial slip distribution parameters including the correlation lengths along dip and strike directions A_z and A_x, and the Hurst number H.

The first step of stochastic source modelling is to obtain the geometry and key slip parameters (mean and maximum slips). For the 2011 Tohoku earthquake, the dimension of the fault plane is determined by fault width W and length L, which is obtained by the following scaling relationships (Goda et al., 2016):

$$\log_{10} W = -0.4877 + 0.3125 M_w + 0.1464 \varepsilon_W \tag{3.4}$$

$$\log_{10} L = -0.1.5021 + 0.4669 M_w + 0.1717 \varepsilon_L \tag{3.5}$$

where the ε terms are regression residuals of the corresponding source parameters. The fault plane is randomly located within the whole pre-defined source region. The equations for D_a and D_m are given below:

$$\log_{10} D_a = -5.7933 + 0.7420 M_w + 0.2502 \varepsilon_{D_a} \tag{3.6}$$

$$\log_{10} D_m = -4.5761 + 0.6681 M_w + 0.2249 \varepsilon_{D_m} \tag{3.7}$$

In addition, the heavy right tail feature of the slip distribution is modelled via Box-Cox transformation:

$$Y = \frac{X^B - 1}{B} (B \neq 0) \tag{3.8}$$

where B is the Box-Cox power parameter, Y is the transformed slip and X is the original slip (note: when $B = 0$, $Y = \log(X)$). The Box-Cox analysis is necessary because for the 2011 Tohoku earthquake, very large slip values (e.g. exceeding 40 m) are obtained for a small number of sub-faults and thus the distribution of earthquake slip significantly deviates from a normal distribution with the same slip statistics (Goda et al., 2014a). An optimal Box-Cox parameter can be estimated by evaluating the linear correlation coefficient of the standard normal variable and the transformed variable of the slip values. The slip distribution is further adjusted to achieve a target mean slip D_a and a maximum slip D_m to avoid very large slip values exceeding the target maximum slip.

Secondly, the spatial characteristics of the power spectra are expressed as wave-number spectra in down-dip and along-strike directions. The wave number spectra are based on a von Karman auto-correlation function:

$$P(k) \propto \frac{A_x A_z}{(1 + k^2)^{H+1}} \tag{3.9}$$

where k is the wave-number, $k = \left({A_z}^2 {k_z}^2 + {A_x}^2 {k_x}^2\right)^{0.5}$, A_z and A_x are the correlation lengths for the down-dip and along-strike directions, respectively, which are determined by Equation (3.10) and Equation (3.11).

$$\log_{10} A_x = -1.9844 + 0.4520 M_w + 0.2204 \varepsilon_{A_x} \tag{3.10}$$

$$\log_{10} A_z = -1.0644 + 0.3039 M_w + 0.1592 \varepsilon_{A_z} \tag{3.11}$$

A_x and A_z control the absolute level of the power spectrum in the low wave-number range (i.e. $k \ll 1$) and capture the anisotropic spectral features of the slip distribution. H is the Hurst number, which determines the slope of the power spectral decay in the high wave-number range and is theoretically constrained to fall between 0 and 1. It is given a value of 0.99 with a probability of 0.43 and a sampled value from the normal distribution with mean of 0.714 and a standard deviation of 0.172 with a probability of 0.27 (Goda et al., 2016).

Subsequently, multiple realisations of slip distributions with desired stochastic properties are generated using a Fourier integral method (Pardo-Igúzquiza and Chica-

Table 3.1 Linear correlation coefficients of regression residuals of six source parameters (Goda et al., 2016).

Variable	ε_W	ε_L	ε_{D_a}	ε_{D_m}	ε_{A_z}	ε_{A_x}
ε_W	1.000	0.139	-0.680	-0.545	0.826	0.035
ε_L	0.139	1.000	-0.595	-0.516	0.249	0.734
ε_{D_a}	-0.680	-0.595	1.000	0.835	-0.620	-0.374
ε_{D_m}	-0.545	-0.516	0.835	1.000	-0.564	-0.337
ε_{A_z}	0.826	0.249	-0.620	-0.564	1.000	0.288
ε_{A_x}	0.035	0.734	-0.374	-0.337	0.288	1.000

Olmo, 1993). The amplitude spectrum of the target slip distribution is specified by the theoretical power spectrum with the estimated correlation lengths and Hurst number, while the phase spectrum is represented by a random phase matrix. The constructed complex Fourier coefficients are transformed into the spatial domain via 2D inverse Fast Fourier Transform (FFT). The synthesised slip distribution is converted via Box–Cox transformation to achieve realistic heavy right-tail features of the slip distribution. An acceptable slip distribution is expected to have its maximum slip patch and similar slip concentration within the asperity zone of the original distribution.

It should be noted that the regression residuals of six source parameters (i.e. W, L, D_a, D_m, A_x and A_z) are distributed according to a multivariate normal distribution (Goda et al., 2016). The linear correlation coefficients of the six regression residuals are given in Table 3.1.

Several constraints are implemented prior to accepting a candidate stochastic source model to ensure that the synthesised slip distribution is consistent with the seismotectonic characteristics of the region of interest according to Goda et al. (2016). The ratio of asperity area over fault area S_a/S, where S_a is defined as the asperity area of sub-faults with slips greater than 1.5 times mean slip (Murotani et al., 2013), is modelled as a normal variable with a mean of 0.240 and a standard deviation of 0.046 and should typically fall between 0.2 and 0.3 (Goda et al., 2016). A high concentration of seismic slip in the shallow segment of the seismic region has been suggested by multiple inversion studies (McCloskey et al., 2008; Lay et al., 2011; Goda et al., 2014a; Davies et al., 2015). Therefore, a slip distribution, which is the percentage of total slip in the asperity region of the total slip across the whole fault plane, is constrained between 50% and 80% in this study assuming the simulated slip is higher in the designated

asperity region. Furthermore, the correlation length A_z along dip direction normalised by the fault width A_z/W needs to fall between 0.15 and 0.45, and the correlation length A_x along strike direction normalised by the fault length A_x/L is constrained within the range of 0.15 to 0.6. Figure 3.4 shows three examples of synthesised earthquake source models for the M_w 9.0 Tohoku event.

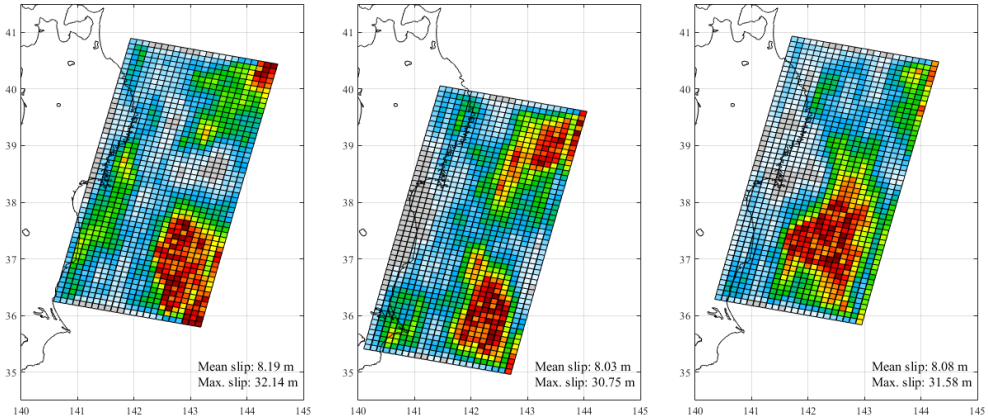

(a) Realisation 1 (b) Realisation 2 (c) Realisation 3

Figure 3.4 Three synthesised earthquake source models for the 2011 Tohoku earthquake

3.2.3 Monte Carlo tsunami simulation

Tsunami modelling is carried out using a well-tested numerical code (Goto et al., 1997) which is capable of generating off-shore tsunami propagation and inundation profiles by evaluating non-linear shallow water equations with run-up using a leap-frog staggered-grid finite difference scheme. The run-up calculation is performed by a moving boundary approach, where a dry or wet condition of a computational cell is determined by comparing the total water depth with its elevation. The computational domains are nested at five resolutions (i.e. 1450-m, 450-m, 150-m, 50-m, and 10-m domains). Computational cells include those on land, and coastal defence structures are taken into account using overflowing formulae as a sub-grid model.

In tsunami simulation, the initial water surface elevation is evaluated based on formulae by Okada (1985) and Tanioka and Satake (1996). The latter equation accounts for the effects of horizontal sea-floor movements in case of steep sea-floor, inducing additional vertical water dislocation. Although the sea-floor deformations are obtained

for the same event, spatial characteristics of the sea-floor displacements vary significantly among the models, leading to different tsunami wave profiles at various locations along the Tohoku coast (Goda et al., 2014a). The fault rupture is assumed to occur instantaneously, and numerical tsunami calculation is performed for duration of 2 hours. The tidal fluctuation is not taken into account in this thesis.

Table 3.2 Manning's coefficients of different types of land use ($m^{-1/3}s$).

Agricultural	Ocean/water	Forest vegetation	Low-density residential	Moderate density residential	High-density residential
0.02	0.025	0.03	0.04	0.06	0.08

The tsunami flow resistance is parametrised by Manning's roughness coefficient in the shallow water equations. The bottom friction is evaluated through Manning's formula according to the national land use standard in Japan by considering six types of land use, as shown in Table 3.2. The assigned roughness coefficients are a crude representation of the actual situation and depend on the resolution of the available DEM . Consequently, a more detailed roughness condition is applied when a DEM of finer resolution is used, which gives more reliable tsunami intensity measure prediction (Kaiser et al., 2011; Griffin et al., 2015). Although the actual surface roughness is influenced by multiple factors (e.g. building density and slope) and thus the friction may be spatially variable within the same type of land use, a constant and uniform Manning's roughness coefficient is applied for each type of land use since the influence of surface roughness is not the main focus of this study.

During a tsunami simulation, the peak water height and peak flow velocity in two horizontal directions are saved for each grid. As water height and flow velocity are calculated, the momentum flux which is a function of inundation depth and velocity, can be calculated by modifying Goto et al.'s code. Water heights are converted into inundation depth by subtracting elevation data. Integrating with the MLIT damage database, the simulated inundation depth and flow velocity for each building in the selected portfolio are obtained. Subsequently, the inundation depth/height distribution maps as well as the velocity distribution maps for the region of interest are produced.

Due to the substantial computation of a large number of tsunami simulations, all simulations are done by using the high-performance computer (HPC) BlueCrystal of the University of Bristol. Each simulation runs as one job on one node of a processor, and hundreds of jobs can be submitted to the BlueCrystal's job submission queue. The advantage of using the job array for Monte Carlo tsunami simulations is that the queueing time is relatively short as the jobs can be dispatched to different processors and be performed when they become available. In this way, hundreds of simulations can be executed in parallel.

3.2.4 Tsunami fragility

Seismic fragility functions, as an essential element for earthquake damage estimation and prediction, has been well developed for different kinds of building types and different regions all over the world. Similarly, tsunami fragility models provide relationships between the exceedance probability attaining a certain damage state and tsunami intensity, which are generated based on damage statistics from post-event surveys or computational simulations (Koshimura and Kayaba, 2010; Suppasri et al., 2011; Hayashi et al., 2013; Charvet et al., 2015; Suppasri et al., 2013; Macabuag et al., 2016; De Risi et al., 2017). Mathematically, the fragility is commonly modelled by the lognormal distribution, which is expressed as:

$$F_R(x) = \Phi\left(\frac{\ln(x) - \mu_x}{\sigma_x}\right) \tag{3.12}$$

where Φ is the cumulative distribution function of the standard normal variate; x is the IM, and tsunami inundation depth/height is most commonly used because the measurement is relatively straightforward; μ_x and σ_x are median (in units that are dimensionally consistent with demand $\ln(x)$) and logarithmic standard deviation of damage state capacity in terms of *IM*, respectively. Six discrete damage states are defined consistently with damage states classified in Table 2.1: DS0 no damage, DS1 minor damage, DS2 moderate damage, DS3 major damage, DS4 complete damage, and DS5 collapse & washed-away. Therefore, the exceedance probability P of damage state ds_i for a given im value is expressed as:

$$P(DS \geq ds_i|im) = \Phi\left(\frac{\ln(im) - \ln(\mu_{IM|DS_i})}{\ln(\sigma_{IM|DS_i})}\right) \tag{3.13}$$

For mutually exclusive damage states that are defined in a discrete manner, the probability $P(ds_i|im)$ of damage state ds_i for a given IM can be obtained as:

$$P(ds_i|im) = P(DS \geq ds_i|im) - P(DS \geq ds_{i+1}|im) \tag{3.14}$$

It should be noted that despite its advantage of convenient measurement, inundation depth is not necessarily most efficient IM for tsunami fragility, because inundation depth cannot solely represent tsunami impact on structures, especially for structural damage caused by hydrodynamic forces and impact forces (Suppasri et al., 2011; Hayashi et al., 2013; Yeh et al., 2014). Thus, the importance of other tsunami IMs (i.e. flow velocity and momentum flux) are investigated in Chapter 4. Because the resistance of buildings are strongly related to the structure type, some tsunami fragility functions are developed by distinguishing different major structural materials (i.e. RC, steel, wood, and masonry) as well (Suppasri et al., 2013; De Risi et al., 2017).

Although the tsunami fragility curves by Suppasri et al. (2013) are more widely used for PTSA, empirical fragility curves by De Risi et al. (2017) are adopted in this study for tsunami loss estimation. The main reasons for selecting these tsunami fragility functions are:

- Such models are derived in a multinomial regression analysis approach, which allows the consideration of flow velocity as additional IM and facilitate the investigation of importance of flow velocity in Chapter 4.
- The models are built on the same database as implemented in this thesis (Section 2.4), which helps maintain the consistency of momentum-flux-based fragility functions developed in Chapter 4 and allows fair comparison.

Figure 3.5 shows fragility curves for RC, wood, masonry, and masonry structures, respectively, noting the fragility model was referred to as M3 in De Risi et al. (2017). Wood structures are most vulnerable to tsunamis, followed by masonry, steel and RC buildings. For example, for wood structures. The tsunami impact is critical when the inundation depth is 5 m with collapse&washed-away probability of more than 90%, while that for RC structures is less than 40%.

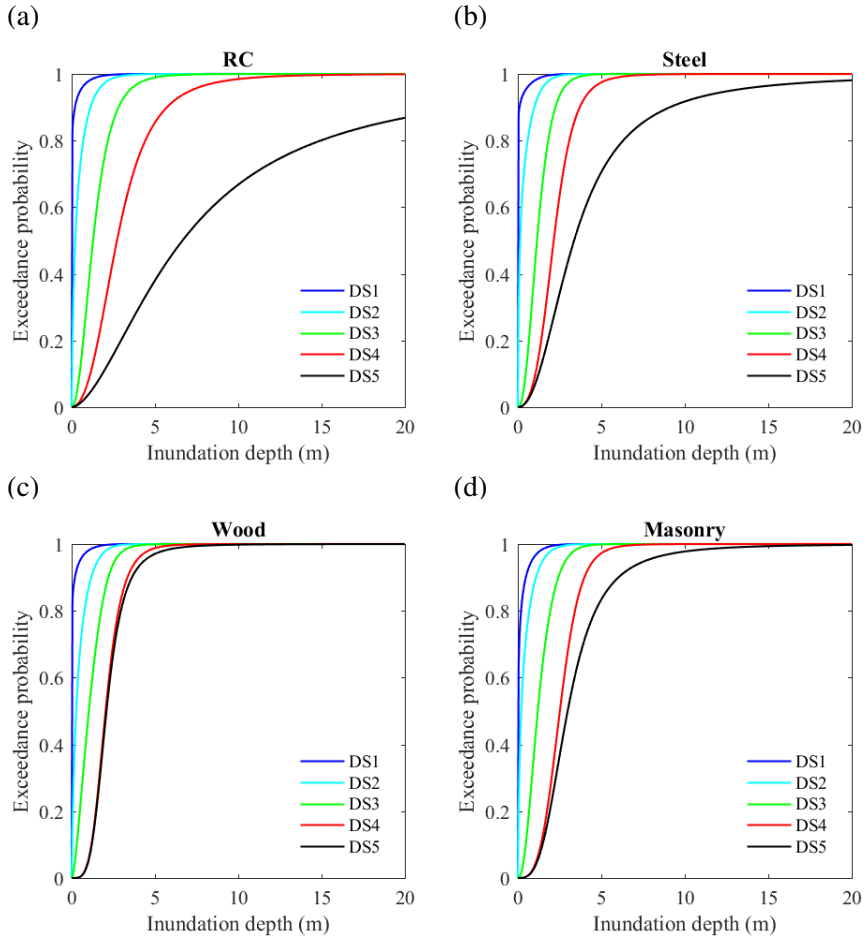

Figure 3.5 Fragility neglecting velocity for four structural types: (a) RC, (b) steel, (c) wood and (d) masonry.

3.2.5 Financial loss estimation

Based on the Monte Carlo tsunami simulation results, stochastic tsunami hazard maps for a given region can be obtained for any selected probability levels (see examples in Section 3.3). The spatial tsunami intensity distribution can be displayed for multiple tsunami hazard parameters, which are inundation height, inundation depth, flow velocity, and momentum flux. To move from hazard to building damage assessment, probabilities of attaining a particular damage state can be estimated for each building and for each earthquake scenario, by using tsunami fragility curves (see Equation (3.13)). The stochastic tsunami loss estimation methodology produces results including a set of tsunami hazard maps (i.e. tsunami height, inundation depth, flow velocity, and momentum flux) corresponding to different scenarios as well as different probability levels, and tsunami loss curves at different scales (i.e. single building, community level,

or regional level). For instance, spatial distribution of tsunami damage probability at representative percentiles (e.g. 50th and 10th/90th percentiles) can be displayed on a map to show the relative likelihood of tsunami damage occurrence at different locations.

Moreover, the calculated values of tsunami damage probability can be used in Monte Carlo sampling to generate realisations of individual damage states for the buildings. Subsequently, by incorporating damage cost models for different buildings, the tsunami damage information can be transformed into tsunami loss information for individual buildings as well as building portfolios. The loss/damage ratio represents the percentage of replacement cost of a building. In this chapter, a uniform damage ratio scheme is applied to account for the uncertainty in damage cost, which is assigned as: 0.0 for DS0 (no damage), 0.03-0.1 for DS1 (minor), 0.1-0.3 for DS2 (moderate), 0.3-0.5 for DS3 (major), 0.5-1.0 for DS4 (complete) and 1.0 for DS5 (collapse & washed-away). Using the damage state probability $p(ds)$ and the loss ratio $R_L(ds)$, tsunami damage cost for a given tsunami hazard intensity can be calculated as:

$$L = C_R \sum_{i=0}^{5} p(ds_i) \times R_L(ds_i) \tag{3.15}$$

where C_R is the replacement cost of a building. An advantage of using loss metrics, instead of damage probability or the number of damaged buildings, is that the consequences due to tsunami damage in coastal cities/towns can be aggregated for the entire building portfolio. Moreover, calculated values of tsunami damage probability can be used in Monte Carlo sampling to generate realisations of individual damage states for the buildings. This re-sampling facilitates the development of exceedance probability curves (EP) which are the fundamental information to achieve various tsunami risk metrics, such as AAL and VaR.

Since the MLIT database does not provide occupancy information for individual buildings, the buildings are broadly classified based on building materials into residential houses (i.e. wood houses) and commercial buildings (i.e. RC, steel, and masonry structures) according to the Japanese building cost information handbook published by the Construction Research Institute (2011). The replacement cost is modeled by lognormal distribution. Moreover, typical floor areas of wood-frame houses and store/offices are determined based on the Japan's national construction statistics maintained by the MLIT (http://www.mlit.go.jp/toukejouhou/chojou/stat-e.htm). The cost information including mean unit cost, coefficient of variation, and mean total floor area of the

two types of buildings is shown in Table 3.3. Therefore, the mean replacement cost of a residential house and commercial property is $1600 \times 130 = 208000$ USD and $1500 \times 540 = 810000$ USD.

Table 3.3 Building cost information for residential and commercial buildings

	Mean unit cost USD/m^2	Coefficient of variation	Mean floor area (m^2)
Residential	1600	0.320	130
Commercial	1500	0.318	540

Note:1 USD = 100 yen

3.3 Influence of elevation data resolution

Land elevation has a direct influence on tsunami run-up and inundation and is crucial for evaluating tsunami damage and loss. Buildings close to one another but at different elevations can incur significantly different tsunami risks locally. For buildings located near the shore and those located on a slope, a coarse DEM can result in an inaccurate assignment of elevation data at building locations. To understand and quantify the influence caused by DEM resolution, four DEMs of different resolutions are obtained from the Miyagi Prefectural Government, which are 10-m, 50-m, 150-m, and 450-m.

3.3.1 Building portfolio

The building portfolios of Sendai and Onagawa are focused upon in this thesis, as shown in Figure 3.6. These two locations are selected because Sendai is located on a plain coast while Onagawa is located on a ria coast. A building portfolio in Sendai consists of 223 RC structures, 570 steel structures, 7,022 wood structures, and 840 masonry structures. A building portfolio in Onagawa contains 52 RC, 118 steel, 1,543 wood, and 69 masonry structures.

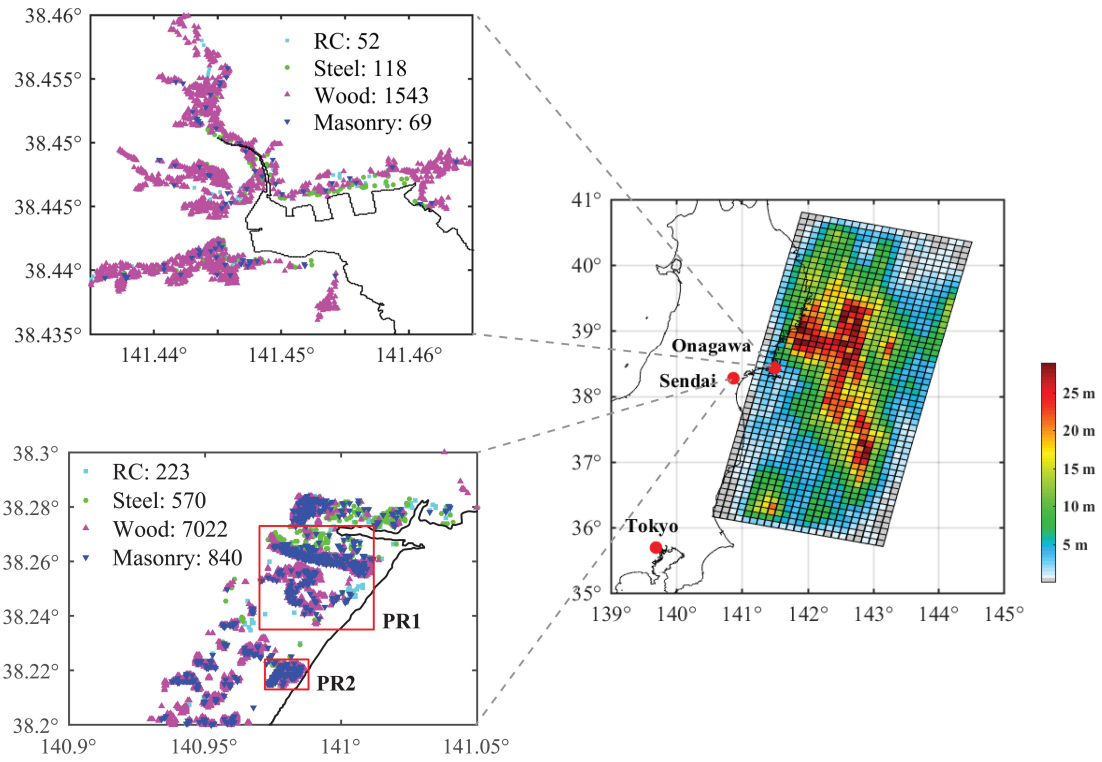

Figure 3.6 Building portfolio of Sendai and Onagawa.

3.3.2 Plain coast

Hazard assessment

To visualise the spatial tsunami hazard variation, two smaller regions PR1 and PR2 are selected for demonstration. There are 3,679 buildings in PR1, containing 89 RC, 316 steel, 2,920 wood, and 354 masonry structures, whereas there are 1,070 buildings in region PR2, including 27 RC, 17 steel, 911 wood, and 115 masonry structures. These two small regions both have a concentration of buildings, and structures in PR1 have different distances from the sea while the buildings in PR2 is located within 1 km from the coastline.

The elevation maps for PR1 are shown in Figure 3.7 to explain the differences caused by DEM resolutions. Because the coastal area of Sendai is relatively low and flat, the elevation range shown in Figure 3.7 is limited to 8 m to focus on the variation in the lower elevations. The coarse resolution tends to reduce the spatial variation in elevation, particularly for places with abrupt changes of elevation. For example, there is a red patch at the top of the 10-m map with elevations higher than 8 m, while the 150-m and 450-m maps fail to reflect this accurately. The high-elevation area at the top of the

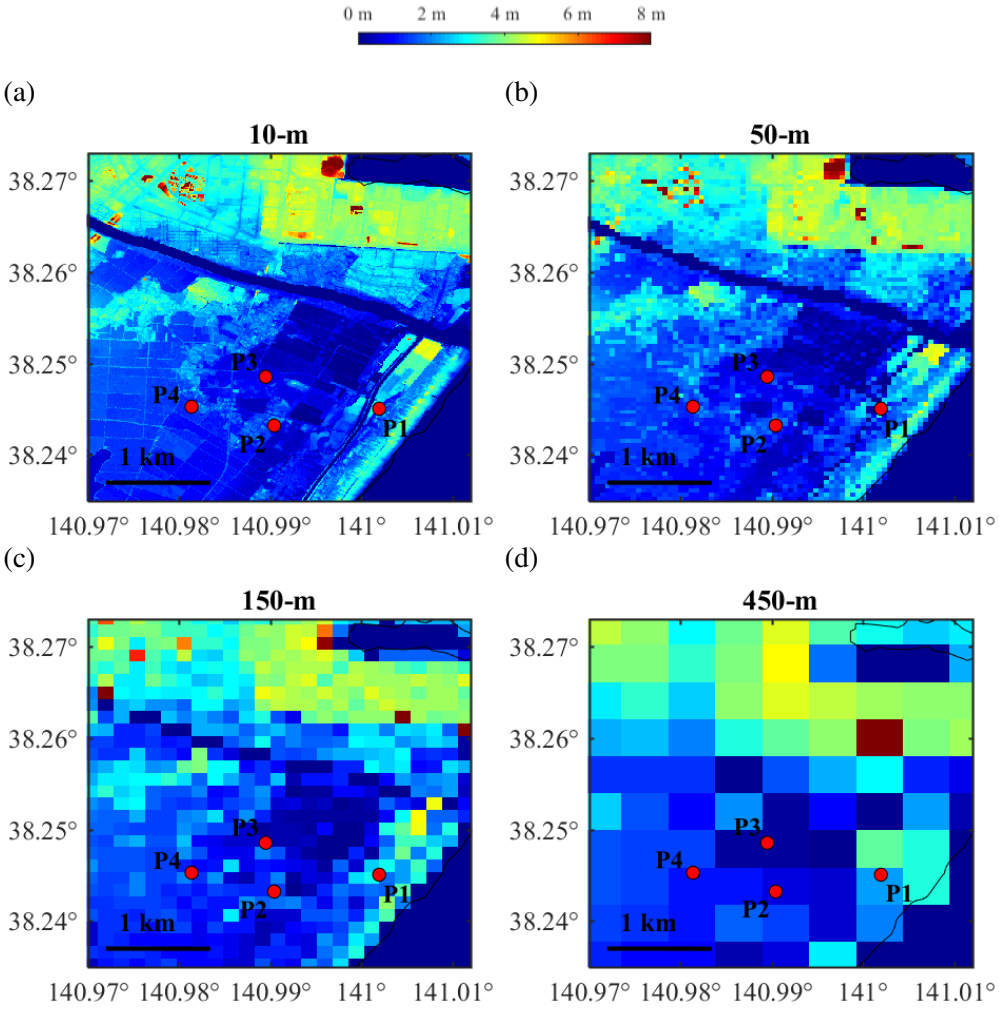

Figure 3.7 Elevation maps for region PR1 in Sendai of different resolutions.

10-m map is completely missed out in the 450-m map. In other words, the assignment of elevation results in loss of accuracy with the decrease in resolution. Four locations P1, P2, P3, and P4 are selected to examine the differences in local tsunami risk caused by DEM resolution. In the 10-m map, the elevations of these four locations are similar, which are around 2 m above the mean sea level, while the corresponding elevations given by the coarser DEMs are different from this value, as shown in Table 3.4. The elevations of P3 given by the 150-m DEM and those of P3 and P4 given by the 450-m DEM indicate substantial errors although the elevations at other locations do not show such discrepancy. The finer 50-m resolution gives a better estimation for all four locations than the 150-m and 450-m maps, although the elevation at P1 is still more than 50% higher than that of 10-m resolution.

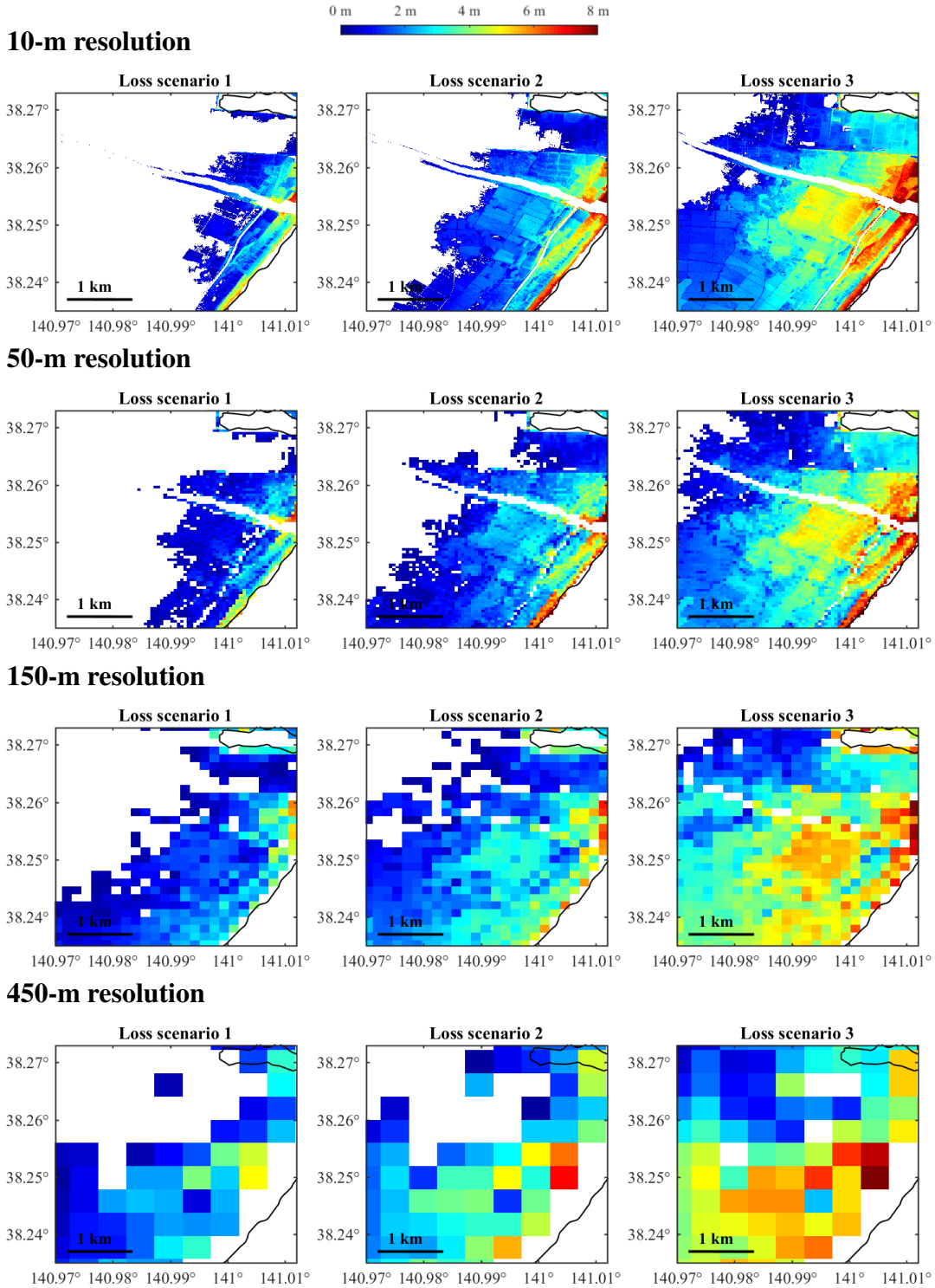

Figure 3.8 Inundation depth maps of M_w 9.0 events for region PR1 in Sendai by considering different DEM resolutions.

Table 3.4 Elevations of P1 to P4 in PR1 using DEM of different resolutions (m).

Location	10 m	50 m	150 m	450 m
P1	2.00	3.11	3.03	2.13
P2	1.99	1.59	1.41	0.71
P3	1.99	1.39	0.50	0.20
P4	1.98	2.38	1.99	1.09

The inundation maps for PR1 based on four resolutions of DEM are shown in Figure 3.8, given three slip models. The three slip models are chosen from 300 stochastic source models for M_w 9.0 events by ranking the total tsunami loss of Sendai using the 10-m DEM, noting that the M_w 9.0 events have the highest contribution to total tsunami loss. The selected loss scenarios aim to show the rare cases (i.e. 10th and 90th percentiles) and the median case (i.e. 50th percentile). The loss scenarios 1 to 3 correspond to the model which gives tsunami loss ranked 10th percentile, 50th percentile, and 90th percentile, respectively. For each loss scenario, the slip model is the same while the losses are affected by different resolutions of the DEMs. Because of the variation in tsunami inundation caused by DEM resolution, the same slip models do not necessarily result in the same rank of tsunami loss at different resolutions, and it is mainly intended to demonstrate the variation at different inundation scales.

Generally, a coarser DEM is less capable of reflecting the variation of inundation depth locally and thus makes the inundation depth more uniform at a local scale, as shown in Figure 3.8. For example, there is a strip of area along the coastline with the highest tsunami depth, and the maximum inundation depth becomes higher than 6 m for the loss scenario 3 of 10-m resolution. This red-coloured area gradually start to disappear as the resolution becomes coarser from 10 m to 450 m. The 50-m DEM is more capable of capturing the spatial variation of inundation depth than the 150-m and 450-m DEMs, but sill loses the detail in abrupt changes of inundation depth. For the 10-m resolution, the inundation depth decreases rapidly with increasing distance from the coastline, while with the increase in grid size, the decrease of tsunami intensity becomes more gradual spatially. On the other hand, a coarser resolution tends to underestimate the tsunami intensity for areas right beside the coast while tends to overestimate the hazard for areas at the far end of the inundated area. It can be seen that the places of the highest tsunami intensity of 50-m, 150-m, and 450-m resolution are not consistent with that of 10-m resolution. In other words, a coarse DEM may not be able to capture the

spatial variability of tsunami intensity accurately. The coarse resolutions are unable to evaluate (locally) high inundation depths accurately, and they tend to result in larger inundation areas. The inundation results based on the 450-m resolution data are highly inconsistent with those based on finer resolutions in terms of inundation amplitude, spatial distribution and inundation area.

The influence of DEM resolution is also significant for flow velocity. Figure 3.9 shows the flow velocity maps which are obtained based on different resolutions for the three loss scenarios (same as Figure 3.8). The flow velocity does not drop as rapidly as inundation depth, and the strip of area right along the coast will experience the highest flow velocity (greater than 5 m/s for the 10-m resolution cases). However, the increase in grid size leads to not only the decrease in flow velocity amplitude in these areas but also smaller impacted areas. For the loss scenario 1, there is an about 200-m wide area having a red colour for the 10-m resolution case. The velocity in this area decreases to lighter red colour for the 50-m resolution case, while this red-coloured area almost disappears in the 150-m and 450-m resolution cases. For more intense inundation (i.e. loss scenarios 2 and 3), the 150-m resolution results in larger red areas with high flow velocity (i.e. greater than 4 m/s), and higher flow velocity for those places farther from the coast. The 50-m resolution can roughly capture the spatial variation of flow velocity as indicated by 10-m resolution while the 150-m and 450-m resolution cases cannot.

To investigate the local spatial variation of tsunami hazard further, inundation depth and flow velocity maps for PR2, which is within 500 m from the sea, are shown in Figure 3.11 and Figure 3.12, respectively. Note that the loss scenarios selected for PR2 are consistent with those for PR1. Due to the higher elevation within 250 m from the sea (see Figure 3.10), the inundation depth and flow velocity drop dramatically, while the 150-m and 450-m maps are unable to show such features, resulting in tsunami waves travel farther inland. Even the 50-m maps cannot show the spatial variation accurately, especially for higher inundation cases (i.e. loss scenarios 2 and 3). The 150-m and 450-m DEM cases fail to capture the highest inundation depth and flow velocity but give higher estimation of the hazard values for the rest of the area. Taking the loss scenario 3 for example, in the 10-m depth map there is a strip of area which experiences inundation depth higher than 7 m (coloured red), while in the 150-m and 450-m maps, the inundation depth is not higher than 6 m. There are some areas with 5 m inundation depth (coloured yellow) in the 10-m map, which do not appear in the 50-m map where inundation depth is lower than 4 m. In terms of flow velocity, within 250 m from the

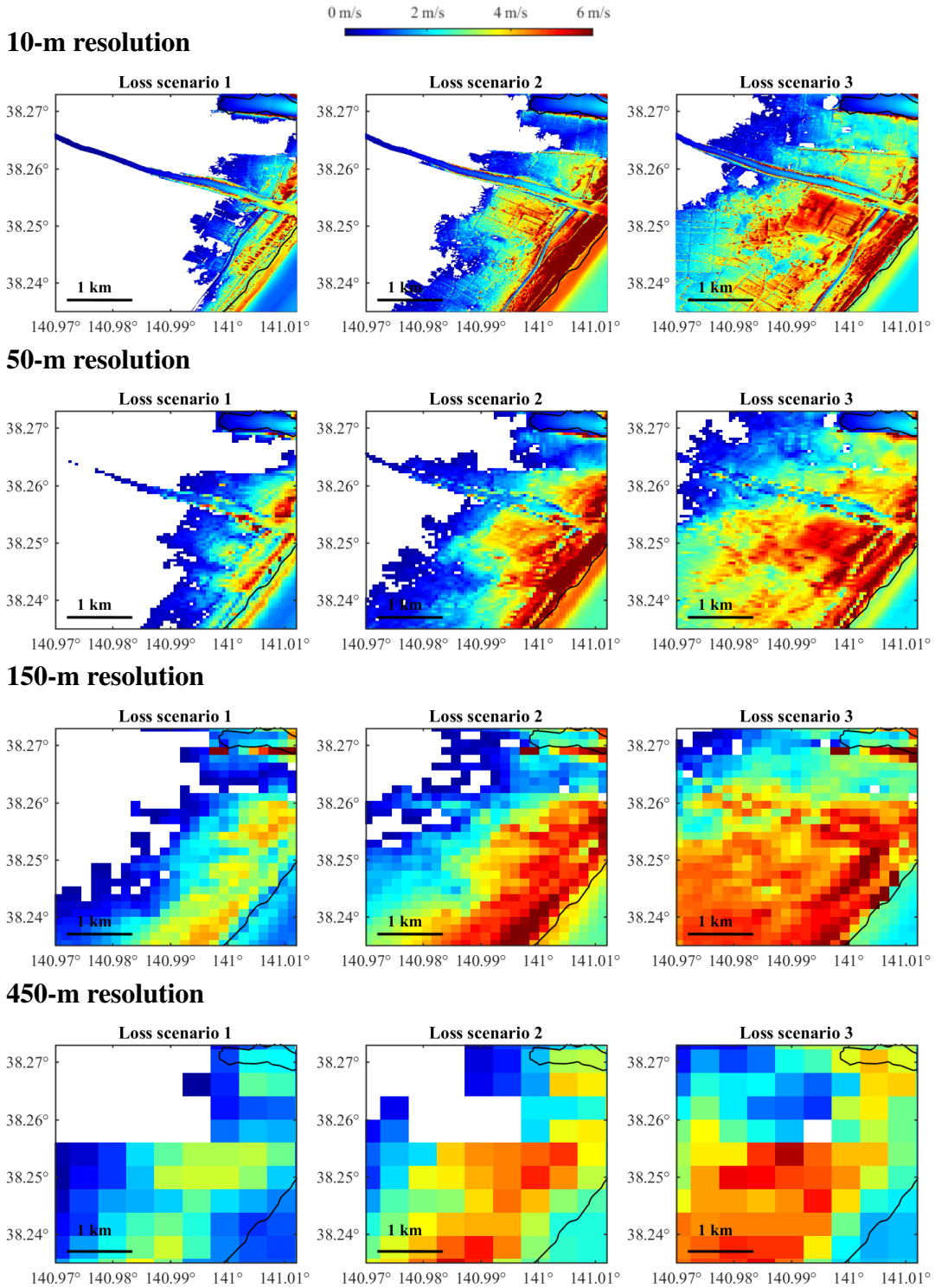

Figure 3.9 Flow velocity maps of M_w 9.0 events for region PR1 in Sendai by considering different DEM resolutions.

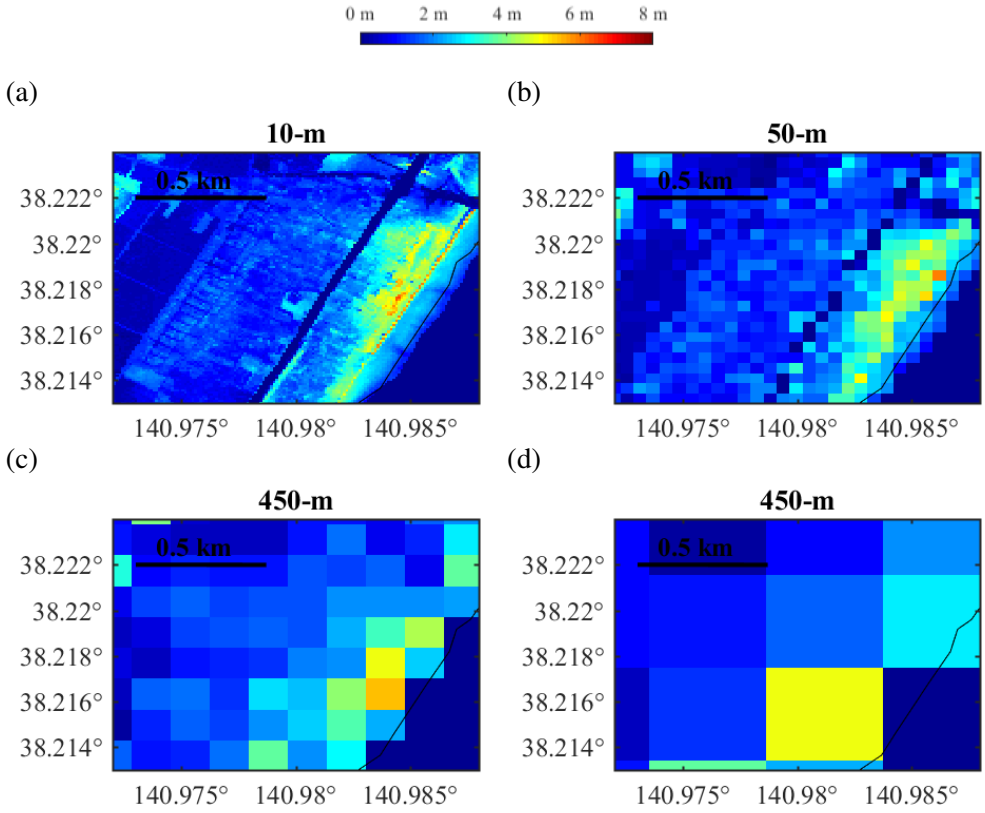

Figure 3.10 Elevation maps for PR2 in Sendai by considering different DEM resolutions.

coast, there is an area in the 10-m map with significantly lower velocities less than 3 m/s (coloured blue-green), while flow velocity in those places is higher than 5 m/s (coloured red) in the 50-m map. Besides, for areas farther than 250 m from the coastline, the 50-m map overestimates the flow velocity and does not show the higher velocity at some particular locations. The differences between the loss scenarios 2 and 3 become smaller with the decrease of DEM resolution. The DEM resolutions of 150 m and 450 m are too coarse for the size of PR2, which give significantly different inundation results in terms of both inundation area and inundation intensity.

Loss estimation

Given the stochastic inundation depths for the building portfolio in Sendai, the annual EP curves for tsunami loss are shown in Figure 3.13 for the whole Sendai, PR1, and PR2. The tsunami losses are calculated based on the method explained in Section 3.2 considering the possibility of eight magnitudes (i.e. M_w 7.6, M_w 7.8, M_w 8.0, M_w 8.2, M_w 8.4, M_w 8.6, M_w 8.8, and M_w 9.0). The structural damage is estimated using

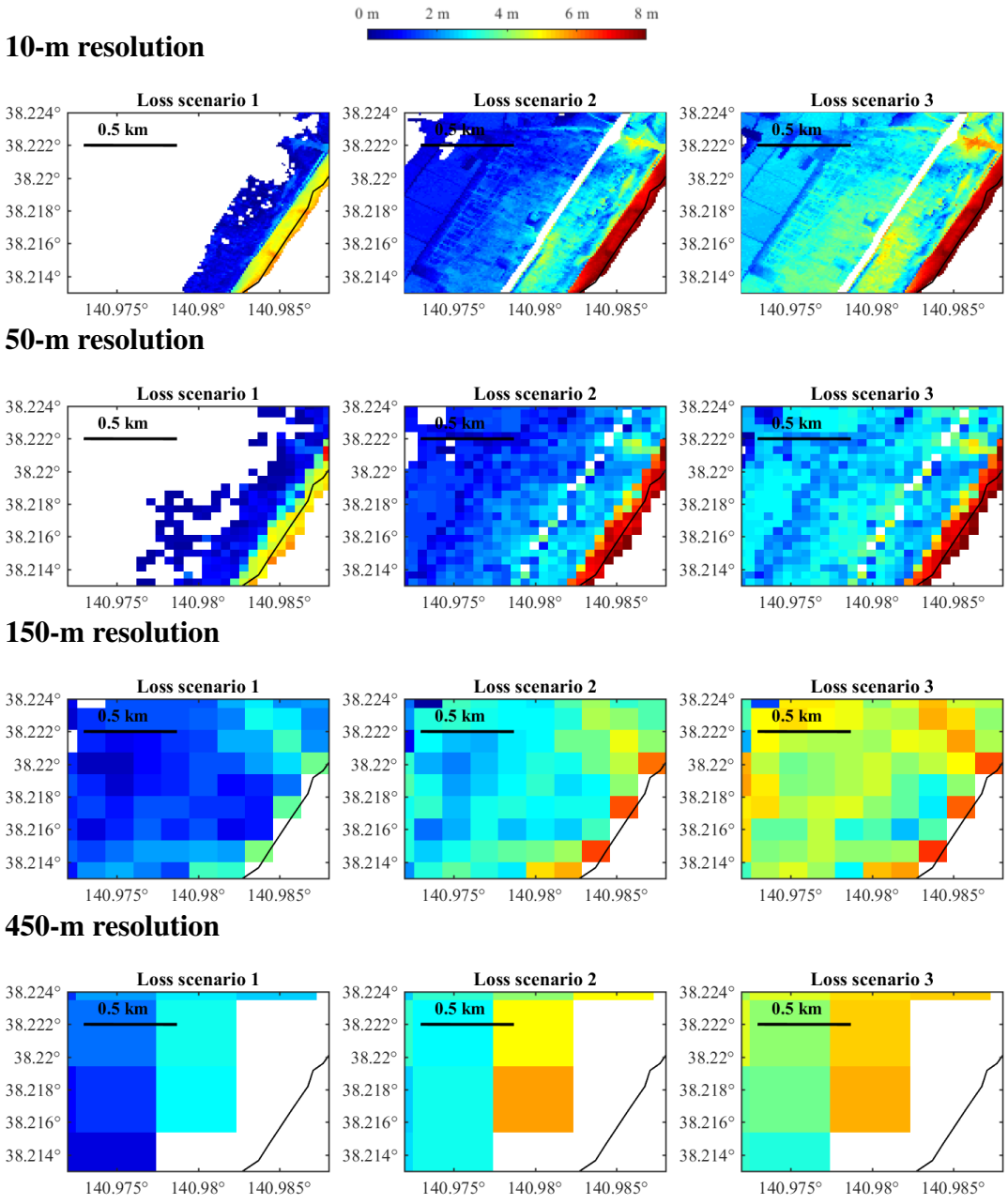

Figure 3.11 Inundation depth maps of M_w 9.0 events for PR2 in Sendai by considering different DEM resolutions.

inundation depth-based tsunami fragility curves developed by De Risi et al. (2017). It needs to be mentioned that the 450-m DEM results in negative values of elevations for a large number of buildings close to the coast, which means those buildings are located below the mean sea level and it is not true. In tsunami loss calculations, the elevations of those buildings are set to 0. Consequently, this modification reduces the differences of tsunami loss at different locations. For example, if elevations of 1 m and -5 m (some

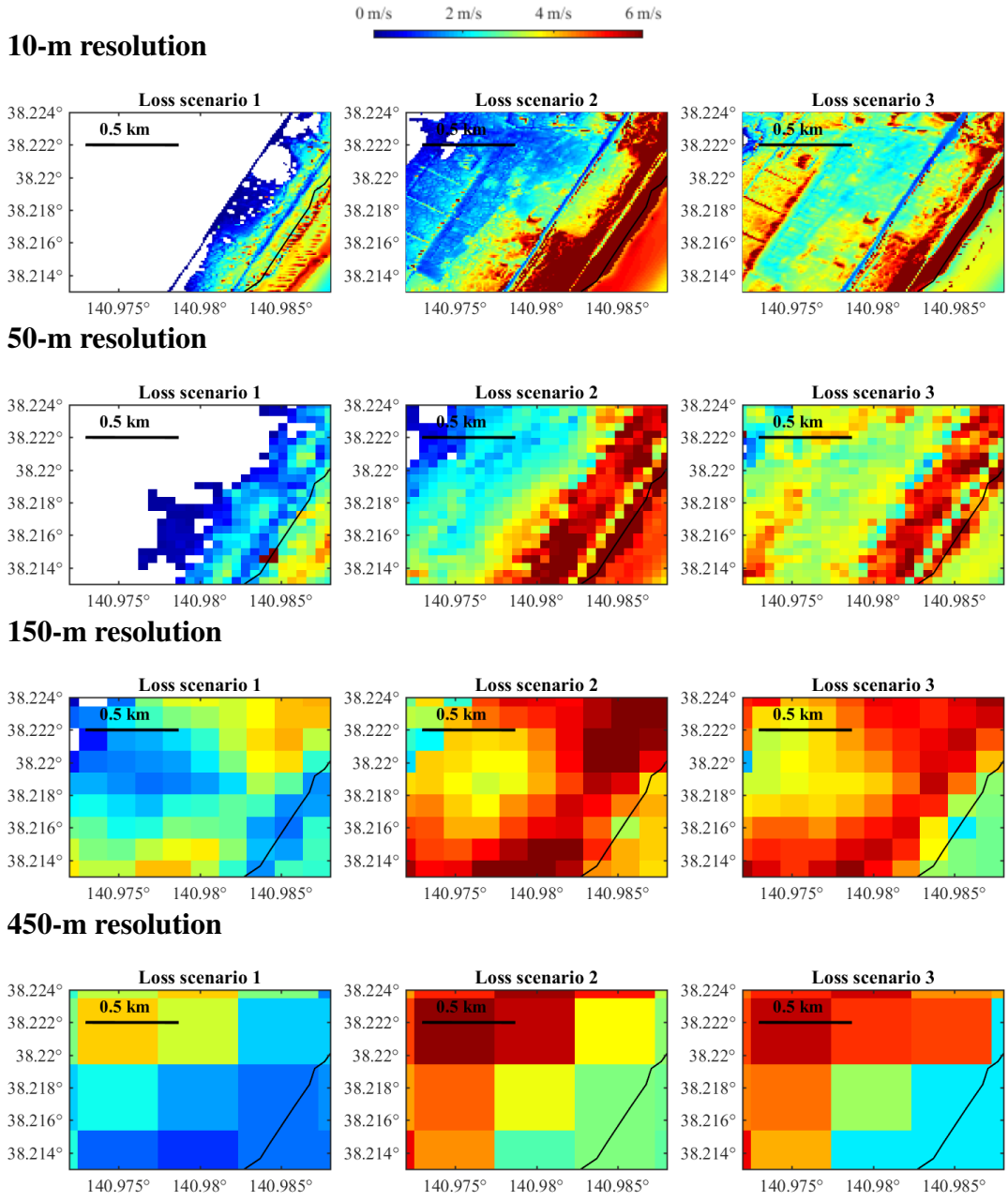

Figure 3.12 Flow velocity maps of M_w 9.0 events for PR2 in Sendai by consdering different DEM resolutions.

locations close to the sea are allocated an elevations below sea level by 450-m DEM) are assigned to two buildings A and B based on the 450-m DEM, assuming they experience the same inundation height, there would be a difference of 6 m in inundation depth but the different is reduced to only 1 m if -5 m is corrected to zero. These errors are due to the inappropriateness of 450-m DEM in assigning accurate elevations. For the 10-m, 50-m, and 150-m cases, a small number of data points which are assigned negative

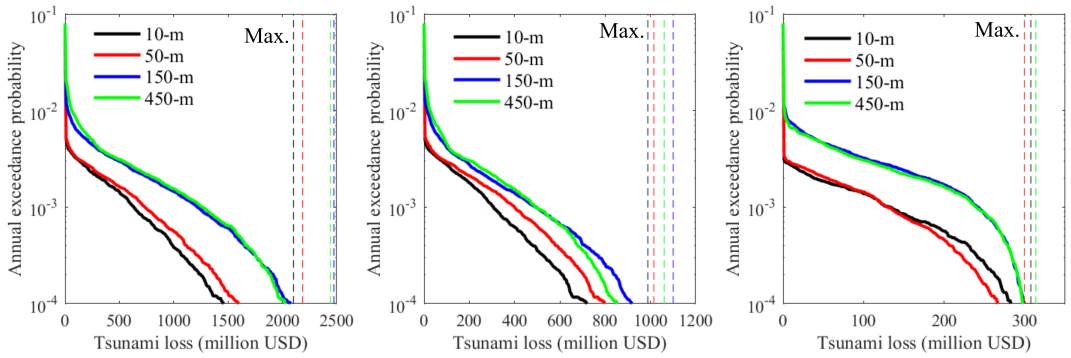

(a) Whole Sendai (b) Region PR1 (c) Region PR2

Figure 3.13 Tsunami loss curves in Sendai: (a) tsunami loss curves for whole Sendai, (b) tsunami loss curves for PR1, and (c) tsunami loss curves for PR2.

elevations are removed.

From the results, the 150-m and 450-m DEM cases lead to more than 30% higher tsunami losses, especially for more frequent events. For the whole Sendai, the 10-m resolution case results in the smallest estimated loss, followed by the 50-m, 150-m, and 450-m resolution cases. The 10-m and 50-m resolution cases are similar in terms of total tsunami loss. One of the risk metrics to assess the risk at a certain probability level is VaR, which is the risk value at a selected probability level. The $\text{VaR}_{0.999}$ for the 10-m resolution case is about 700 million USD, while that for the 150-m resolution case is about 1,500 million USD, which almost twice as large as that of the 10-m resolution case. The comparisons of the tsunami loss distributions and the corresponding risk metrics for different grid resolution cases highlight the importance of the elevation data resolution to the accurate estimation of the potential financial impact due to catastrophic tsunamis.

A coarser DEM tends to underestimate the tsunami hazard closer to the sea and overestimate it at farther places. Therefore, the resulted difference in total tsunami loss from different DEM resolutions depends on the spatial distribution of buildings as well. For example, the difference between the case of 10-m and 150-m/450-m case is greater for the whole Sendai than PR1. This is because the whole Sendai includes more buildings farther from the coast which are inundated for the cases of 150-m and 450-m resolution, but not inundated for the cases of 10-m and 50-m resolution. The $\text{VaR}_{0.999}$ for the 150-m resolution case is reduced to about 40% higher than that of 10-m resolution. The tsunami loss for the 150-m resolution case is similar to that for 450-m resolution for

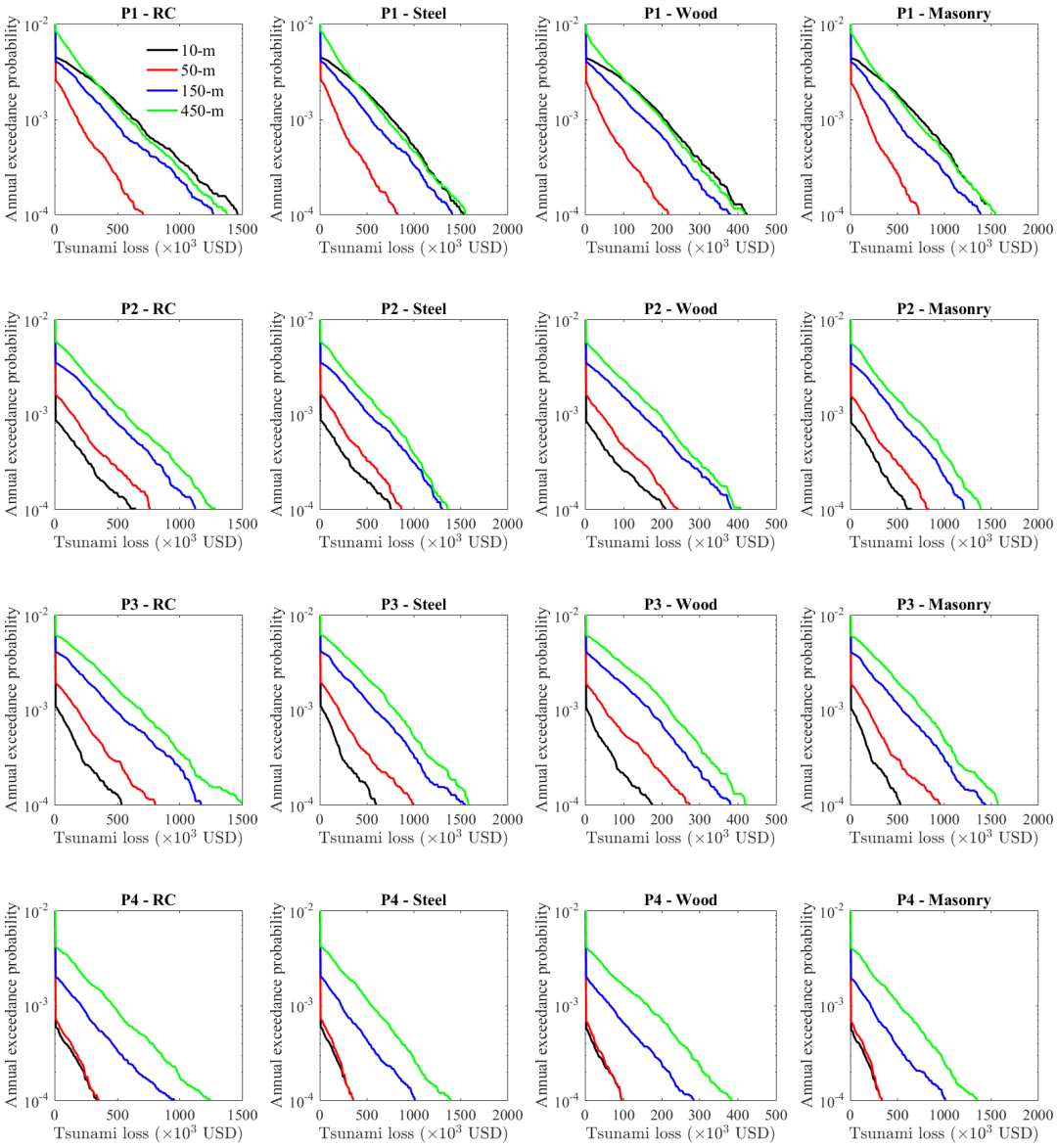

Figure 3.14 Tsunami loss EP curves at different locations in Sendai.

more frequent events but lower for extreme events with longer return periods. As seen in Figure 3.8, the 450-m DEM case leads to some areas not inundated but are inundated in the 150-m inundation maps. For PR2 which has a smaller area size and is closer to the sea, the tsunami losses for the 150-m and 450-m resolution cases are dramatically higher than those for the 10-m and 50-m resolution cases due to the overall overestimation of inundation depth based on the 150-m and 450-m DEMs, particularly for areas farther from the coast. Although the differences of $VaR_{0.9999}$ are within 20%, $VaR_{0.999}$ for the 150-m

and 450-m resolution cases are almost twice as large as that for the 10-m resolution case.

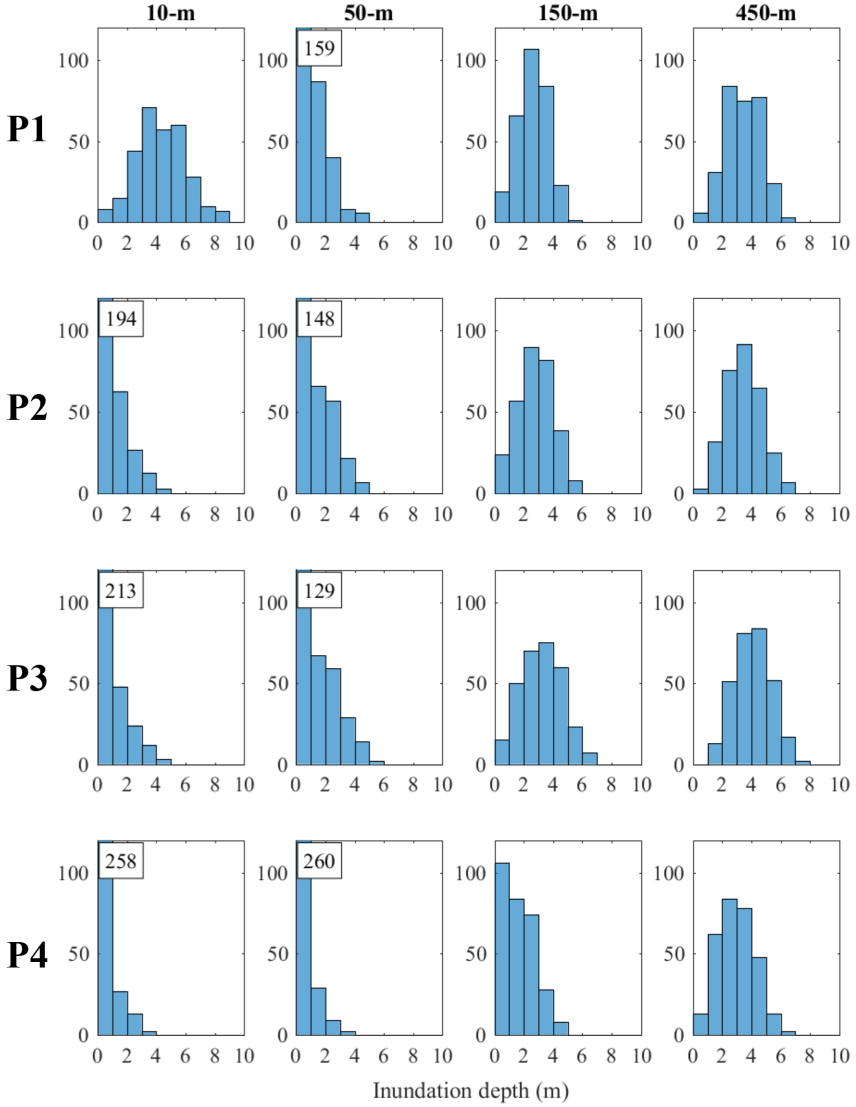

Figure 3.15 Inundation depth distribution at four locations in Sendai for the M_w 9.0 events by considering different DEM resolutions (The counts exceeds the y axis limit are numbered in a box).

As seen in the tsunami hazard maps for different DEM resolutions, how the tsunami intensity is weakened when waves travelling inland is significantly affected by DEM resolution. In Sendai, with low-lying flat topography, an increasing distance from the coast reduces the tsunami hazard level, however, the coarse DEM is less capable of reflecting the difference. To investigate such effects, the tsunami loss curves of a single structure at P1, P2, P3, and P4 in PR1 are compared in Figure 3.14 by distinguishing different DEM

resolution cases and structural types. These locations all have an elevation of around 2 m (Table 3.4) and have an increasing distance from the coast, which are roughly 0.5 km, 1.2 km, 1.5 km, and 2 km. The corresponding inundation depth distributions from the 300 simulations of the M_w 9.0 events are shown in Figure 3.15, noting that the M_w 9.0 events have the highest contribution to total tsunami loss. Although it has been found in Figure 3.13 that tsunami loss for the 50-m resolution case is relatively close to that for the 10-m resolution case, the estimated local risks at P1 for the two resolution cases are different. Around P1, a rapid change of elevation occurs, which makes the coarser DEMs likely to assign an elevation with error. The 50-m DEM assigns an elevation more than 3 m to P1. In the 10-m elevation map, P1 is located in the front of an area with increased elevation, while in the 50-m elevation map P1 is located on the farther side of the area with an increase of elevation due to the reduced resolution. Consequently, for the 10-m case tsunami waves are weakened after arriving P1 due to a sudden increase of elevation, while for the 50-m case the wave height has been reduced before arriving P1. Compared to the 10-m resolution case, which is taken as the most reliable case, more than 80% of the depths given by the 50-m DEM are less than 2 m and no depth is greater than 5 m, while using the 10-m DEM more than half of the depths are higher than 4 m. As seen in Figure 3.8 that the inundation depths in the 50-m maps are lower than those in the 10-m maps before tsunami waves arrive at P1, and with a higher elevation given by the 50-m case, consequently the inundation intensity at P1 estimated by the 50-m DEM is significantly lower than that by the 10-m DEM. Although the 150-m and 450-m resolution cases do not generate depths higher than 7 m as the 10-m resolution case does, there are more cases where depths between 2 m and 6 m occur, compared with the 10-m resolution case. This eventually makes the tsunami loss curves at P1 similar for the 10-m, 150-m and 450-m resolution cases.

For other three locations, where the elevations given by the 50-m DEM are relatively close to that for the 10-m resolution case, the tsunami loss curves for the 50-m resolution case are similar to the 10-m resolution case but higher for P2 and P3 due to lower elevations assigned by the 50-m DEM. It can be seen in Figure 3.15 that the 150-m and 450-m resolution cases significantly overestimate the inundation depths at P2, P3 and P4. The tsunami losses at P2 for the 150-m and 450-m resolution cases are twice as large as that of the 10-m resolution case. It is interesting to notice that although the loss curves for the 150 m and 450 m resolution cases are similar at P2, the elevation based on the 150-m DEM is 1.41 m while that based on the 450-m DEM is only 0.71 m (Table 3.4). It implies that local risk is affected not only by the assigned

elevation but also by other factors. Consequently, for some cases, it would be difficult to determine the relative tsunami risk solely from elevations without conducting tsunami simulations. The differences of the loss curves between finer resolution and coarser resolution cases increase at P3 and P4. This indicates that for local tsunami risk assessment at a particular location, using the 150-m and 450-m DEM can be highly unreliable. The elevations of P3 based on the 150-m and 450-m DEM are only 0.50 m and 0.20 m, respectively, and thus the loss results are almost three times greater than those for the 10-m resolution case. At P4, the tsunami losses for the 150-m and 450-m resolution cases are significantly higher than the other two cases. The risk decreases significantly from P1 to P4 with tsunami loss curves for the 10-m DEM, but for the 150-m and 450-m resolution cases, the differences between risks at four locations are substantially small.

3.3.3 Ria coast

The tsunami risk in Onagawa is expected to be more sensitive to DEM resolution, because Onagawa is surrounded by terrain with rapidly rising elevations due to a valley-like coastline. The elevation maps of Onagawa for four resolutions are shown in Figure 3.16. The elevation range in Figure 3.16 is limited to 8 m to show the elevation variation at the low-elevation area where the majority of buildings are located. Buildings are concentrated in a flat and confined area close to the sea. As a result, nearby buildings that are located relatively close to hill sides can have significantly different elevations when different resolutions of DEM are adopted, which results in varying levels of tsunami risk.

Table 3.5 Elevations in Onagawa using DEM of different resolutions (m).

Location	10 m	50 m	150 m	450 m
R1	2.06	1.28	1.51	0.00
R2	3.81	1.92	1.24	0.00
R3	6.00	3.26	0.73	0.00

To examine the differences in local tsunami risk caused by DEM resolution, three locations R1, R2, and R3 are selected. The locations R1, R2, and R3 are fairly close with a similar distance of about 300 m from the sea, but have different elevations which are about 2 m, 4 m, and 6 m, respectively, according to the 10-m DEM. The elevations

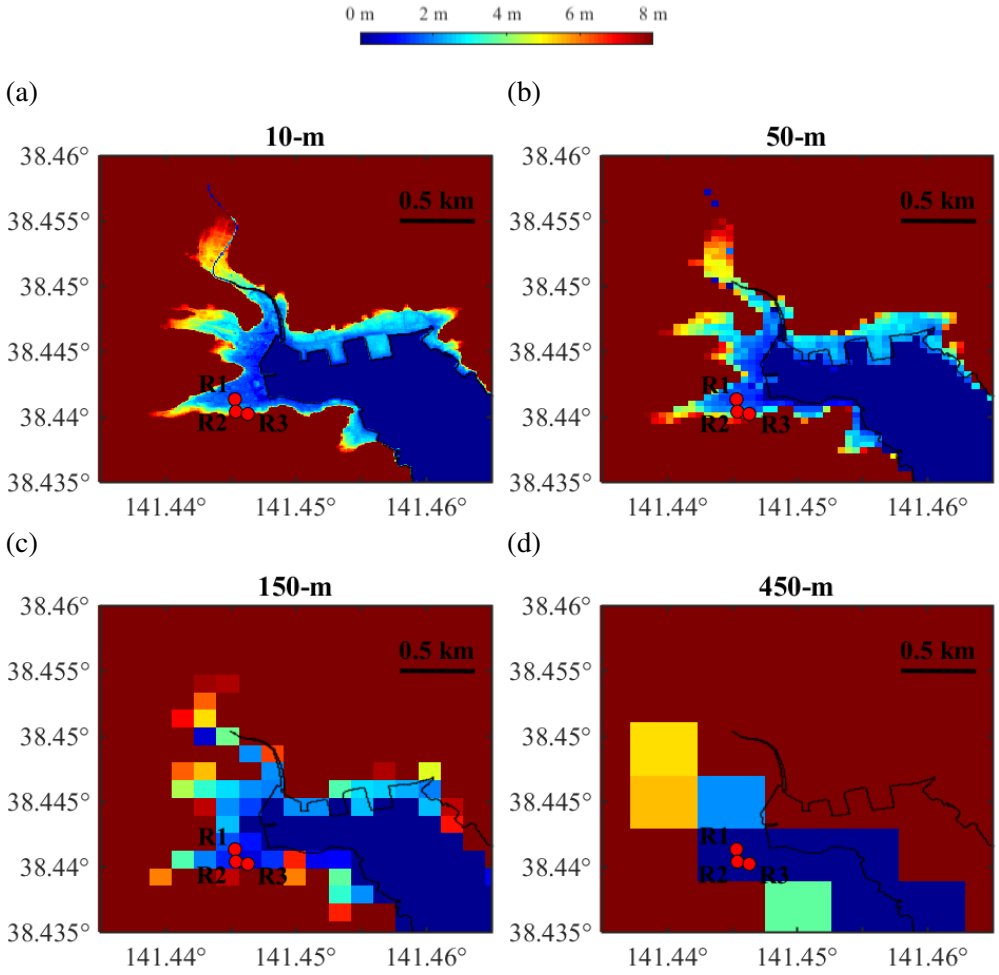

Figure 3.16 Elevation maps for Onagawa of different resolutions.

assigned to these three locations based on different DEMs are summarised in Table 3.5. The 450-m DEM is regarded as unsuitable for representing topographic features of Onagawa realistically, which made the three locations below the mean sea level. The 50-m and 150-m DEMs still show the changes of elevation but are not well resolved to distinguish different elevations within small areas. The 50-m DEM, which is acceptable to represent elevations for Sendai, is not suitable and assigns inaccurate elevations to all three locations. With the increase of grid size, the assigned elevations tend to become lower.

Hazard assessment

The unrealistic representation of elevation using coarser DEMs results in substantially inaccurate spatial distribution of tsunami intensity measures. The inundation depth

and flow velocity maps are shown in Figure 3.17 and Figure 3.18, respectively, by considering three loss scenarios. The loss scenarios are selected by ranking the tsunami loss of 300 tsunami simulations for the M_w 9.0 of Onagawa using the 10-m DEM, and thus they are not the same slip models for Sendai. Increase in inundation depth and flow velocity can be observed for the different loss scenarios. Although the 50-m DEM case can broadly capture the inundation area, the spatial extent of inundation is visually smaller. Besides, the 50-m DEM case cannot account for the change of tsunami intensity at places near steep hills/slopes.

The 150-m and 450-m DEMs do not generate realistic tsunami simulation results for Onagawa. More specifically, the 150-m DEM is not capable of obtaining neither the correct inundated area nor the correct tsunami intensity, whereas the 450-m DEM can hardly capture the reasonable inundated areas, with flooded areas which should not be inundated and the unflooded areas which should be inundated. Besides, some areas turned out to be unflooded for the 450-m resolution case because they are below the mean sea level according to the 450-m elevation data.

Loss estimation

The total tsunami loss curves for Onagawa are shown in Figure 3.19 by considering DEMs of different resolutions. The loss curve of the 50-m resolution case is close to the loss curve of the 10-m resolution case but is about 10% lower for the extreme cases. The loss results based on the 150-m and 450-m resolution cases are judged to be unreliable, generating significantly higher losses for the high-frequency scenarios while underestimating losses for the extreme events. The DEMs of low resolution (i.e. 150 m and 450 m) tend to overestimate the inundation area but underestimate the tsunami intensity for those critical areas. As shown in Figure 3.17 that tsunami hazard intensity distribution in Onagawa is highly sensitive to DEM resolution and local tsunami intensity varies significantly. The influences of DEM resolution on regional tsunami loss in Figure 3.19 are not necessarily consistent with the influences on local tsunami risks in Figure 3.20, because the coarse DEM overestimate the hazard intensity for some locations while underestimating it for other locations. In other words, for an area with rapidly changing elevation, the influence of DEM resolution on regional tsunami loss is not able to imply which DEM will result in higher or lower loss for individual locations without tsunami simulations. In terms of regional losses, the 10-m

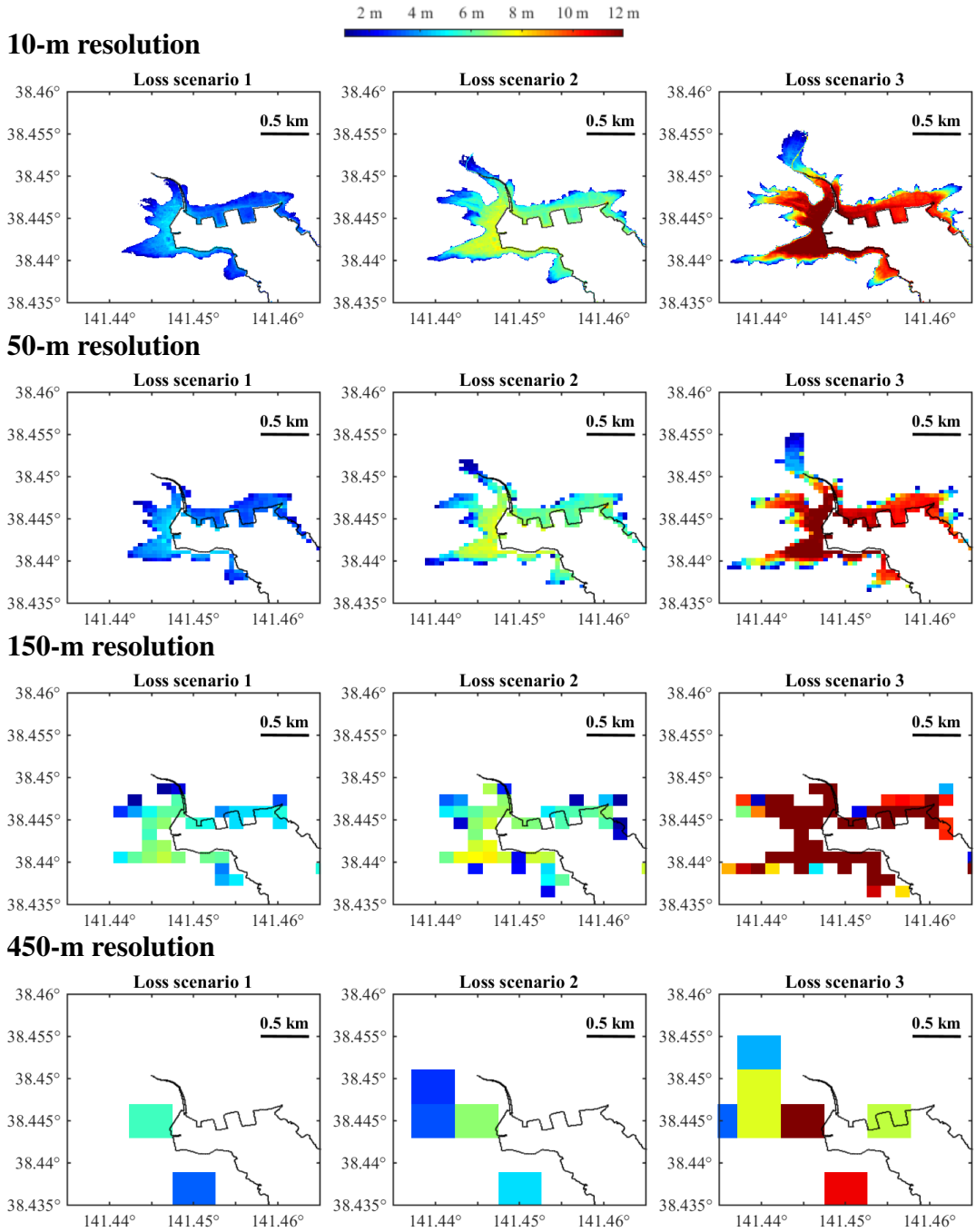

Figure 3.17 Inundation depth maps of M_w 9.0 events for Onagawa by considering different DEM resolutions.

and 50-m DEMs can be used, while 150-m and 450-m DEMs cannot be relied on.

The local tsunami risks at R1, R2, and R3 are consistent with the assigned elevations in Table 3.5. It can be seen in Figure 3.20 that the tsunami risk decreases from R1 to R3

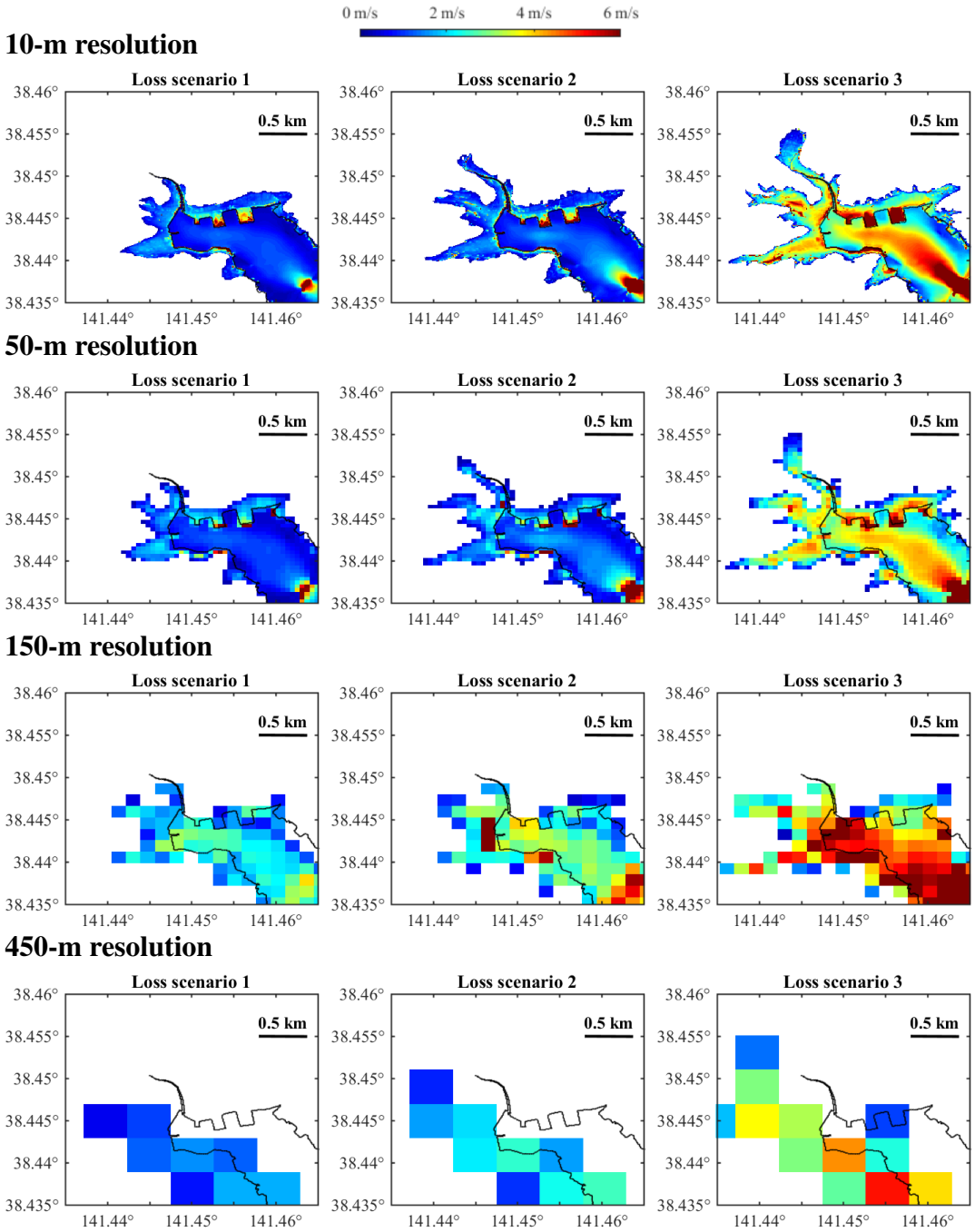

Figure 3.18 Flow velocity maps of M_w 9.0 events for Onagawa by considering different DEM resolutions.

with the increase of elevation according to results of the 10-m resolution case. The 10-m resolution case has the smallest tsunami loss for all three locations, followed by the 50-m, 150-m, and 450-m resolution cases. The differences caused by DEM resolution increase with the crudeness of elevation resolution. Referring to the histograms of

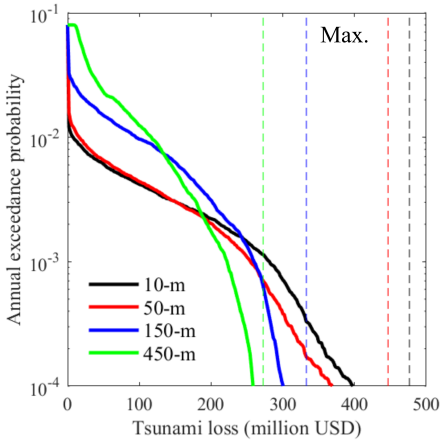

Figure 3.19 Tsunami loss curves in Onagawa.

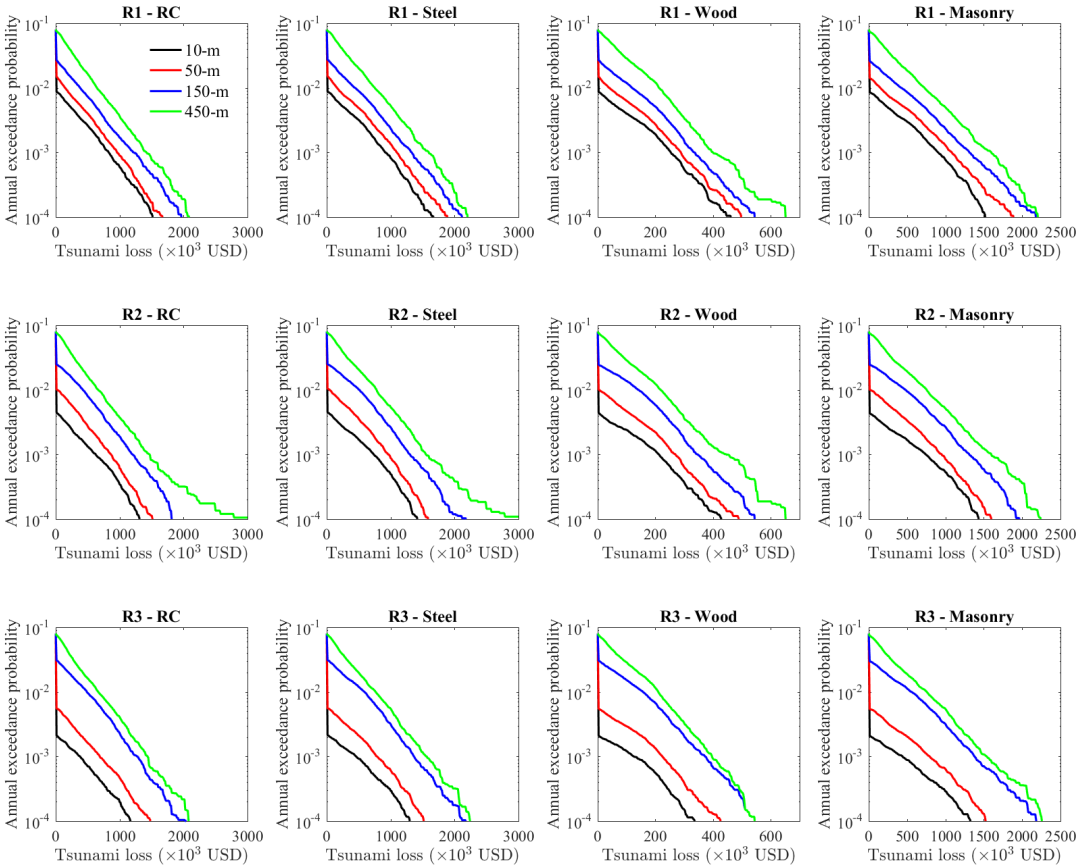

Figure 3.20 Tsunami loss curves at three locations in Onagawa.

inundation depth for the M_w 9.0 events in Figure 3.21, it can be seen that generally the coarser DEMs tend to cause higher inundation depth. The distribution for the 50-m resolution case at R1 is similar to that for the 10-m resolution case, and thus the loss

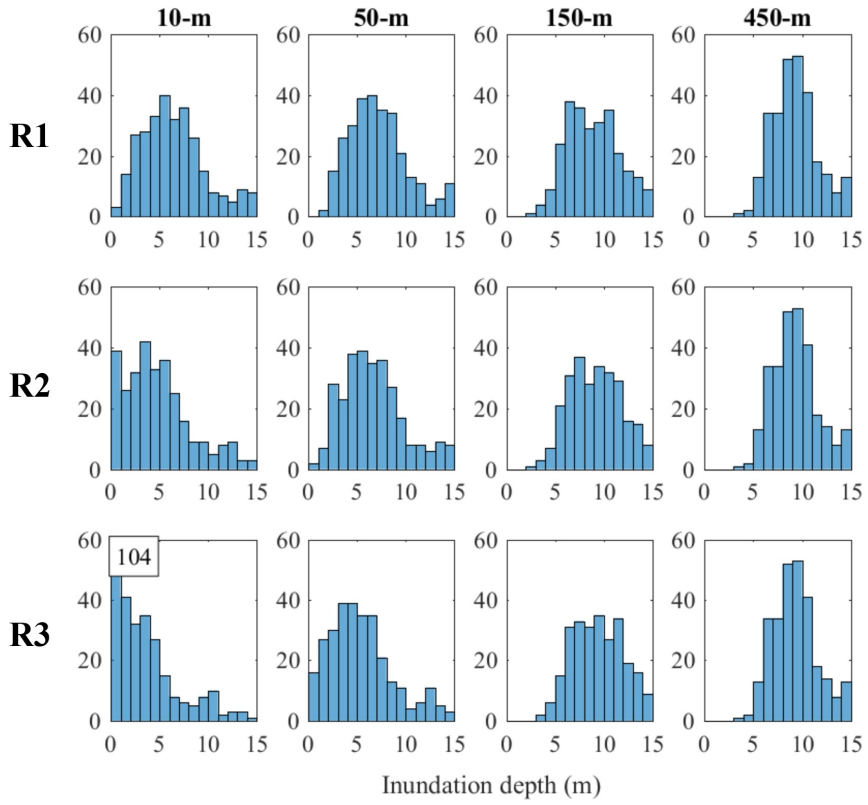

Figure 3.21 Inundation depth distribution at three locations in Onagawa for the M_w 9.0 events by considering different DEM resolutions (The counts exceeds the y axis limit are numbered in a box).

curves of the 10-m resolution case and the 50-m resolution case are similar at R1. Because the elevation is not the sole parameter for determining the local tsunami, the tsunami loss given by 150-m DEM is higher although the assigned elevation at R1 is higher than that for the 50-m resolution case. At R2, the loss for the 50-m resolution case is about 20% higher than that for the 10-m resolution case because of the lower elevation assigned. When the elevation rises to 6 m at R3, the tsunami losses of the 150-m and the 450-m resolution case are more than 80% greater than that of the 10-m resolution case, while the losses given by the 50-m DEM are more than 20% higher. In Figure 3.21, the inundation depth distribution is similar using the 450-m DEM for three locations, which shows significantly higher inundation depths than those for the 10-m resolution case for these locations.

To summarise, tsunami risk is very sensitive to DEM resolution because of the topographic features of Onagawa. For tsunami risk at specific locations, the realistic representation of elevation is vitally important. The 50-m DEM, which is the finest

DEM apart from the 10-m one, still cannot ensure the accurate representation of elevation and can cause significant differences in estimated loss.

3.4 Summary and conclusions

A comprehensive computational framework of probabilistic tsunami hazard and risk assessments for coastal areas was developed by evaluating the uncertainty in earthquake source characterisation. The methodology was implemented for the Tohoku-type earthquake and tsunami, focusing on two real building portfolios of Miyagi Prefecture, Japan to distinguish two coastal topography types and four structural types. The uncertainty of earthquake source modelling was quantified by taking into all possible tsunami scenarios. The hazard and risk predictions were obtained from Monte Carlo tsunami simulations taking into account the uncertainty related to earthquake rupture process using scaling relationships for the key source parameters and stochastic spectral synthesis method for spatial slip distributions. The uncertainty propagation from tsunami hazard to tsunami risk was evaluated by integrating tsunami fragility functions and damage cost models, and subsequently the influence of tsunami modelling resolution on tsunami loss prediction was explored. For a given subduction zone, the possible tsunami inundation situations (e.g. inundation depth and flow velocity) for the adjacent coastal regions were highly variable. In addition to stochastic tsunami hazard maps, the resulting stochastic tsunami damage and loss distribution maps by considering tsunami vulnerability of structures were useful for developing tsunami emergency response plans for local communities. The complete set of results from the stochastic tsunami risk assessment method enables quantification and visualisation of the uncertainty in tsunami hazard prediction through various tsunami intensity measures and can provide risk managers with rich information about the tsunami risk of their portfolios in tsunami-prone regions in terms of total aggregate loss and loss distribution.

Based on the stochastic tsunami loss estimation framework, the uncertainty in tsunami risk caused by different DEM resolutions was investigated. To consider different coastal topography, Sendai (coastal plain) and Onagawa (ria coast) were focused upon. The differences on tsunami loss estimation were evaluated at a regional scale as well as for single locations. The main findings are:

- The DEM resolution has a significant influence on tsunami loss estimation, especially for local tsunami risk assessment. It is noteworthy that the coarser DEM tends to underestimate the tsunami intensity at some places while overestimating it at some other places. Therefore, the accuracy of resulted tsunami loss depends on the location of buildings as well. When there is more variation in land elevation at a regional scale, a greater difference is caused by using a coarser DEM. For a plain terrain of Sendai, the 50-m DEM can still produce a loss estimation similar to that of the 10-m DEM, but the 150-m and 450-m DEMs tend to overestimate the total tsunami loss dramatically. Using a coarser DEM tends to underestimate the tsunami loss for the most risky areas but tends to overestimate it for the least risky areas. The 150-m and 450-m DEMs are not able to give a reasonable tsunami loss estimation for both Sendai and Onagawa, particularly for single locations; the $\mathrm{VaR}_{0.999}$ for by these two DEMs are twice higher than that by 10-m case for whole Sendai, while for Onagawa they overestimate the loss at high probability levels (probability greater than 0.002) and underestimate at low probability levels (probability lower than 0.002).

- The tsunami risk at single locations is more sensitive to DEM resolution than regional tsunami losses. For local tsunami risk, DEM resolution controls the accuracy of assigned elevations, which determines the accuracy of local tsunami loss estimation. Even for Sendai, the 50-m resolution is likely to result in significant bias in estimated tsunami losses for single locations with respect to those based on the 10-m DEM. In Onagawa, only 10-m DEM is capable of producing accurate tsunami loss estimation at single locations.

The findings of the influence of DEM resolution have major implications for tsunami insurance rate differentiation by considering the location attributes. Because of the smaller influenced area by tsunamis (only several kilometres from the coast) than earthquakes, elevation data of low resolution like 150 m and 450 m are not capable of simulating the realistic inundation scales. For both regional and local tsunami risk assessments, 150-m and 450-m DEMs are not recommended for use, which can cause substantial errors. For regional tsunami loss, the 50-m DEM is acceptable, which gives a less than 20% difference in comparison to that for the 10-m resolution. The location of buildings makes a significant difference to local tsunami risk, which includes the distance from the coast and elevation. However, the difference caused by building locations largely depends on the elevation data resolution. A coarser DEM will lead to more uniform tsunami risk at different locations. The effects of the location attributes (i.e.

distance from the sea and elevation) on insurance premium pricing will be investigated in Chapter 5.

Chapter 4

Influence of Flow Velocity and Momentum Flux to Tsunami Loss Estimation

Publications resulting from this chapter:
Song, J., De Risi, R., and Goda, K. (2018). Probabilistic tsunami loss estimation using momentum flux-based tsunami fragility functions. In *16th European Conference of Earthquake Engineering*, Thessaloniki, Greece.

Song, J., De Risi, R., and Goda, K. (2017). Influence of flow velocity on tsunami loss estimation. *Geosciences*, 7(4).

4.1 Introduction

Tsunami fragility is a key component of a tsunami risk assessment, which relates the physical severity of tsunamis to probabilistic damage of structures. Due to different geographical features and tsunami propagation paths, tsunami hazard varies within inundated areas significantly (Chapter 3). Multiple intensity measures (IM) that describe the extent of tsunami inundation have been proposed, including inundation depth, flow velocity, and momentum flux (Gibson et al., 2014; Macabuag et al., 2016; Park et al., 2017). Although inundation depth is the most observable intensity measure in post-tsunami situations and the most common IM in tsunami risk assessment (Suppasri et al., 2013; Charvet et al., 2014a; Narita and Koshimura, 2015; De Risi et al., 2017), it

cannot be taken as the sole representation of tsunami impact on structures especially for damage caused by hydrodynamic and debris impact forces which are mainly determined by flow velocity (Yeh et al., 2014, 2013). During tsunami events, flow velocity can be obtained by multiple methods including particle image velocimetry analysis of videos of survivors (Fritz et al., 2006; Hayashi and Koshimura, 2013), coastal oceanographic radar tsunami system (Lipa et al., 2012), and satellite altimetry (Song et al., 2012). Therefore, when validated and supplemented by accurate numerical tsunami simulations, reliable estimates of flow velocity can be obtained; they can be used for developing velocity-based tsunami fragility functions. The influence of flow velocity on tsunami fragility has been demonstrated by several studies (Charvet et al., 2015; Macabuag et al., 2016; Park et al., 2017), but the importance of flow velocity for tsunami loss has not been explored yet. Existing velocity-based fragility functions (Koshimura et al., 2009; Maruyama et al., 2013) offer an option to use either inundation depth or flow velocity, which enables the comparison of two intensity measures in risk assessment. However, such comparisons cannot be directly made to evaluate the differences due to flow velocity in addition to inundation depth, since these models are developed individually. There is a knowledge gap between the importance of flow velocity for developing tsunami fragility models and its influence on tsunami loss estimation; the latter may be more relevant for risk managers who are concerned with the financial consequence of tsunamis.

Moreover, in the context of efficient tsunami IM, momentum flux m ($= hv^2$) is often considered to be a superior hazard indicator for tsunami damage estimation because it captures two fundamental characteristics of tsunami waves, i.e. inundation h and flow velocity v at the same time (Tanaka et al., 2015; Macabuag et al., 2016; Park and Cox, 2016; Park et al., 2017). However, its observation is almost impossible in post-tsunami damage surveys, and hence, the tsunami fragility modelling based on momentum flux needs to solely rely on numerical simulations without calibration against actual data, which is a major drawback. Given the benefit and limitation of momentum flux, it is worth understanding the influence of it on tsunami loss estimation compared to the use of inundation depth. Besides, the differences made by momentum flux compared to inundation depth in probabilistic tsunami loss estimation cannot appropriately represent the differences made by v because momentum flux is proportional to hv^2. Therefore, the influences of flow velocity and momentum need to be investigated respectively.

This chapter extends the stochastic tsunami risk assessment framework (Chapter 3) and develops a new stochastic bivariate-IM tsunami loss estimation method by integrating stochastic tsunami hazard simulations with tsunami fragility functions which enable the consideration of flow velocity or momentum flux in addition to inundation depth. The bivariate-IM fragility functions facilitate the investigations of how and when flow velocity is important for tsunami loss estimation in addition to inundation depth, and will shed light on whether it is necessary to use more complex terms, such as momentum flux and hydrodynamic forces, for tsunami risk assessment (Macabuag et al., 2016; Petrone et al., 2017). Targeting on probabilistic tsunami loss estimation of a large number of buildings due to numerous different tsunami scenarios, flow velocity is generated through stochastic tsunami simulation (Goto et al., 1997; Goda et al., 2014a). Scaling relationships, which link earthquake source parameters (e.g. geometry, slip statistics and spatial slip distribution) of a fault rupture with earthquake magnitude, are employed to generate stochastic source models corresponding to a M_w 9.0 earthquake (Goda et al., 2016). Subsequently, inundation depth and flow velocity are obtained from Monte Carlo tsunami simulation, and are integrated with depth-based fragility and depth-and-velocity-based fragility derived by De Risi et al. (2017), respectively, to calculate tsunami loss. The tsunami scenarios are ranked by the total tsunami losses for the given building portfolio. Scenarios corresponding to pre-defined loss percentiles (e.g. 10th, 50th, and 90th) obtained considering and neglecting the flow velocity are compared both in terms of probability distribution and spatial distribution of tsunami loss. These results provide insight regarding where and when flow velocity is important, and facilitate accurate risk prediction given a specific building portfolio. It has been found in Chapter 3 that tsunami simulation is sensitive to DEM resolution, and thus the inaccurate estimation of velocity leads to a loss of capability of illuminating the influence of velocity on tsunami loss estimation realistically.

To investigate the importance of momentum flux, tsunami fragility models using momentum flux are developed based on the damage data of the 2011 Tohoku tsunami by conducting a multinomial regression analysis, and are compared with those using inundation depth and flow velocity that are developed based on the same dataset. Because of the lack of recorded flow velocity, flow velocity and momentum flux at building locations are simulated based on the inverted source model of the 2011 Tohoku tsunami by Satake et al. (2013). Aiming at investigating the effects of different IMs for tsunami loss estimation, tsunami loss is calculated by considering three tsunami fragility models that adopt different tsunami intensity measures (i.e. inundation depth, flow velocity, and

momentum flux), for numerous possible slip distributions. Tsunami loss estimated using momentum flux as additional IM is compared with those based on inundation depth and flow velocity. Finally, the results from probabilistic tsunami loss estimation using different IMs will provide insight regarding an optimal IM for tsunami risk assessment in different situations.

To reflect the physical features of two coastal topographical types, Sendai and Onagawa are selected as representative sites for plain coast and ria coast, respectively. In total, 300 tsunami simulations for the M_W 9.0 events were carried out for each location using the 10-m DEM. Finally, the tsunami risk (i.e. economic loss) is analysed in term of probabilistic total loss and spatial distribution for the given building portfolios.

Analyses are carried out at three geographical levels: i) municipal scale, ii) community scale, and iii) single building (e.g. local) scale. To consider the potential intensity amplification due to the coastal topography, two coastal types are investigated: plain type and ria type, respectively. Moreover, to reflect typical buildings in the case study areas, four building typologies are considered: reinforced concrete (RC), steel, wood and masonry. Building portfolios of Sendai and Onagawa in Miyagi Prefecture as representative sites for plain coast and ria coast, respectively, are focused on. Tsunami scenarios generated within the source zone, which correspond to M_w 9.0 Tohoku-type earthquakes, are adopted.

4.2 Influence of flow velocity on tsunami loss estimation

4.2.1 Methodology

The probabilistic tsunami loss is calculated according to the stochastic tsunami risk assessment framework (Chapter 3; Goda and Song, 2016), by accommodating a method of stochastic tsunami modelling targeted for large mega-thrust subduction earthquakes to take into account the uncertainty in earthquake rupture characterisation (Mai and Beroza, 2002; Goda et al., 2014a, 2016). Using probabilistic scaling relationships which predict earthquake source parameters (Goda et al., 2016), stochastic earthquake slip models are generated within the seismic source zone, given the moment magnitude of

an earthquake. For a seismic source zone of interest, relevant inversion-based rupture models can be found in the SRCMOD database (Mai and Thingbaijam, 2014). In this chapter, 300 possible M_w 9.0 earthquakes source models that occur on a pre-defined fault plane are considered. The fault rupture area is large enough to accommodate a M_w 9.0 event off the Tohoku coast and is defined based on the source model developed by Satake et al. (2013) for the 2011 Tohoku tsunami (see Chapter 3). Tsunami propagation is carried out using a well-tested numerical code (Goto et al., 1997) as explained in Chapter 3. Coastal defence structures in place before the 2011 Tohoku event are considered in the tsunami simulations as vertical walls on the northern and/or eastern sides of computational cells, and their elevation data are provided by the Miyagi Prefectural Government. The volume of overflow over coastal defence structures is evaluated by Homma's formulae. The inundation profiles are saved as peak wave height and peak flow velocity. Inundation depth is then calculated by subtracting land elevation from wave height. Because the modelling resolution has a major influence on the accuracy of simulated velocity, two DEM resolutions (50 m and 10 m) are considered to investigate the relative importance of velocity given the spatial grid resolution. Integrating with the building information for the 2011 Tohoku tsunami damage survey compiled by MLIT (2014), the simulated inundation depth and flow velocity are assigned to each building in the selected portfolio.

To reflect the physical features of two coastal topographical types, Sendai and Onagawa are selected as representative sites for plain coast and ria coast, respectively. In total, 1,200 tsunami simulations were carried out for four different cases (300 for each case) in terms of location and DEM resolution: Sendai with the 50-m DEM, Onagawa with the 50-m DEM, Sendai with the 10-m DEM, and Onagawa with the 10-m DEM. All cases are based on the same set of 300 stochastic slip models of M_w 9.0 earthquakes.

4.2.2 Bivariate-IM tsunami loss estimation

Empirical fragility models developed by (De Risi et al., 2017) are adopted for tsunami loss assessment. The models considering and neglecting tsunami flow velocity in addition to inundation depth are built based on the same damage data of the 2011 Tohoku tsunami; therefore, they can be used to estimate tsunami loss for both cases. Both fragility models take into account four structural types (i.e. RC, steel, wood, and masonry), and different coastal topographical effects (i.e. plain coast and ria coast)

are further considered by the bivariate-IM fragility model. Six damage states (DS) are considered: no damage (DS0), minor damage (DS1), moderate damage (DS2), major damage (DS3), complete damage (DS4), and collapse & washed-away (DS5). Unlike single-IM tsunami fragility models, the damage probabilities of a building are expressed as a function of both inundation depth and velocity.

Consider that the damage state takes one of the six discrete values (i.e. ds_0, ds_1, ..., ds_5), and let

$$p_{ij} = P(DS_i = ds_j) \tag{4.1}$$

where p_{ij} denotes the probability that the ith observation falls in the jth category. All damage states are mutually exclusive and completely exhaustive; the sum of probabilities of all five damage states is 1. The probability that buildings of the ith bin fall in each damage state ds_j is determined by the multinomial probability distribution shown in Equation (4.2), which represents the random component of the model and describes the distribution of the response around the central value.

$$P(DS_{i0} = ds_0, ..., DS_{i5} = ds_5) = \frac{m_i!}{\prod_{j=0}^{5} y_{ij}!} \prod_{j=0}^{5} p_{ij}^{y_{ij}} \tag{4.2}$$

where m_i is the total number of buildings corresponding to the ith bin and y_{ij} denotes the number of structures in the ith bin attaining the jth damage state d_j.

The relationship between the probability p_{ij} and a vector of explanatory variables x is represented by a link function $f(p_{ij})$, which usually is a linear function of explanatory variables.

$$f(p_{ij}) = \theta_{j,0} + \sum_{k=i}^{n_e} \theta_{j,k} \cdot x_k \tag{4.3}$$

where θ denotes the vector of the model parameters $\theta_{j,k}$ and determines the shape of a curve for each damage state, and n_e denotes the number of explanatory variables. The logit model is adopted as a link function (Equation (4.4)), and thus commonly known as multinomial logit regression (Hosmer et al., 2013).

$$f(p_{ij}) = \ln\left(\frac{p_{ij}}{1-\Sigma_{k=1}^{j} p_{ik}}\right) \tag{4.4}$$

The point estimates for the regression parameters are obtained based on the maximum likelihood estimation (MLE) method, by calculating the first and second derivatives of the likelihood function that is expressed in Equation (4.5).

$$L(\theta|x,y) = \prod_{i=1}^{n}\prod_{j=0}^{5} p^{y_{ij}} \tag{4.5}$$

The fragility function based on inundation depth only is shown in Equation (4.6), and the fragility function considering velocity v_i is expressed in Equation (4.7). Both take into account four structural types and interaction between inundation depth and structural typology.

$$\begin{aligned} f(p_{ij}) = \theta_{j,0} + \theta_{j,1}\ln(h_i) + \theta_{j,2}\cdot d_W + \theta_{j,3}\cdot d_M + \theta_{j,4}\cdot d_S \\ + \theta_{j,5}\ln(h_i)d_W + \theta_{j,6}\ln(h_i)d_M + \theta_{j,7}\ln(h_i)d_S \end{aligned} \tag{4.6}$$

$$\begin{aligned} f(p_{ij}) = \theta_{j,0} + \theta_{j,1}\ln(h_i) + \theta_{j,2}\cdot d_W + \theta_{j,3}\cdot d_M + \theta_{j,4}\cdot d_S \\ + \theta_{j,5}\ln(h_i)d_W + \theta_{j,6}\ln(h_i)d_M + \theta_{j,7}\ln(h_i)d_S + \theta_{j,8}\ln(v_i) \end{aligned} \tag{4.7}$$

where d_W, d_M, and d_S are the dummy variables for wooden, masonry, and steel buildings, respectively, and take a value of 1 when a building belongs to this material typology. For example, for wood structure,s d_W equals 1, and both d_M and d_S are equal to 0. There are only three dummy variables instead of four to avoid over-parametrisation.

The regression parameters for the depth-based fragility according to Equation (4.6) are shown in Table 4.1. Regression parameters for the bivariate-IM fragility according to Equation (4.7) for plain coast and ria coast are listed in Table 4.2; this fragility function was referred to as M4 in De Risi et al. (2017). Figure 4.1 shows an example of bivariate-IM fragility surfaces for RC structures by distinguishing plain and ria coast types. It can be observed that at severer damage states, the fragility curves are more sensitive to the change of flow velocity. In other words, due to the inclusion of flow velocity, the shapes of fragility curves are affected by the velocity. The differences by

Table 4.1 Regression parameters of single-IM tsunami fragility neglecting flow velocity (De Risi et al., 2017).

Parameter	DS1	DS2	DS3	DS4	DS5
θ_0	1.540	1.430	-0.904	-3.462	-3.722
θ_1	0.105	0.924	1.650	2.299	1.557
θ_2	0.186	-0.375	0.768	-2.255	0.738
θ_3	-0.845	0.023	0.437	-1.989	0.215
θ_4	-0.186	0.169	0.213	-0.417	0.696
θ_5	0.058	-0.019	-0.257	0.906	2.023
θ_6	0.108	-0.010	0.27	1.486	1.16
θ_7	-0.118	-0.122	0.319	0.878	0.354

Table 4.2 Regression parameters of bivariate-IM tsunami fragility considering flow velocity (De Risi et al., 2017).

Parameter	Plain coast					Ria coast				
	DS1	DS2	DS3	DS4	DS5	DS1	DS2	DS3	DS4	DS5
θ_0	1.795	1.742	-1.283	-3.346	-3.826	81.396	1.685	-0.195	-2.294	-2.758
θ_1	0.307	1.355	1.925	1.564	1.701	1.638	0.827	0.458	1.774	1.063
θ_2	-0.159	-0.803	1.105	-3.300	0.548	-76.758	-0.867	0.459	-3.692	0.432
θ_3	-1.352	-0.196	0.754	-1.679	0.144	105.544	-0.606	0.767	-2.403	1.039
θ_4	-0.696	-0.089	0.406	-0.697	0.589	21.370	0.223	0.486	-2.618	0.849
θ_5	-0.051	-0.499	-0.819	1.415	2.001	-2.677	0.052	0.976	1.470	2.491
θ_6	-0.088	-0.343	-0.271	0.375	1.263	-110.334	0.088	0.808	2.090	0.595
θ_7	-0.332	-0.576	-0.212	1.152	0.296	-1.709	0.776	0.702	1.730	0.304
θ_8	-0.211	-0.037	0.782	1.604	0.850	-0.974	0.004	0.767	0.234	0.773

the consideration of velocity are increasing with worsening damage, particularly for DS5 where buildings had collapsed or had been washed away. Similar fragility surfaces can be obtained for steel, wood, and masonry structures.

Based on the Monte Carlo tsunami simulation results, tsunami risk for a given region can be obtained for any selected probability levels (the details see Chapter 3). The loss ratios in terms of the replacement cost of a building for the six damage levels (i.e. from *no damage* to *collapse & washed-away*) can be assigned as: 0.0, 0.05, 0.2, 0.4, 0.6, and 1.0 (MLIT, 2014). Note that fixed damage ratios are used for given damage states to assess the differences made by the consideration of flow velocity, which is different from the uniform damage ratio scheme used in Chapter 3. Moreover, to reflect the influence of using different tsunami intensity measures, uncertainty in the cost model is not considered and a mean unit cost and floor area are applied for all buildings. The

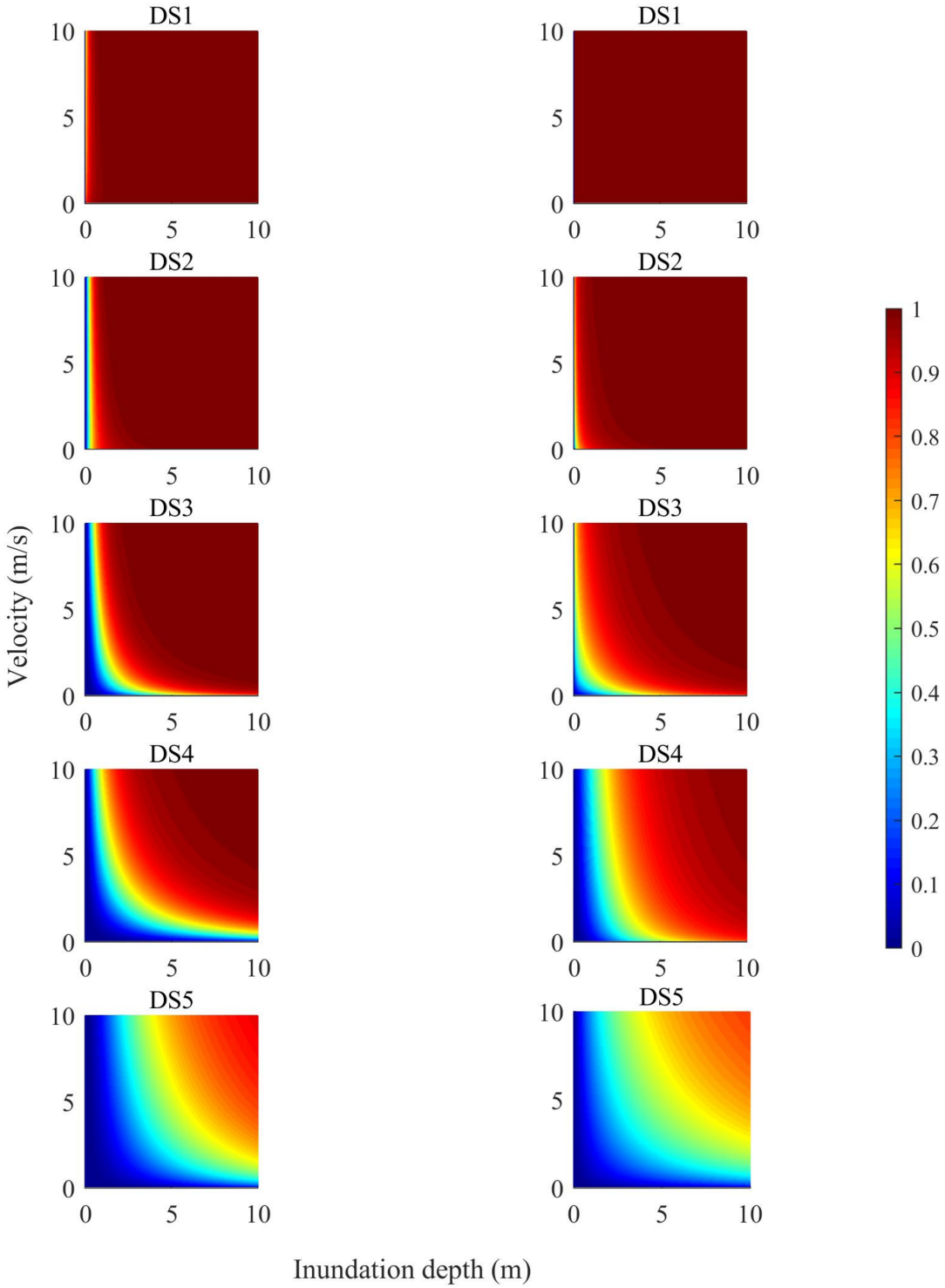

Figure 4.1 Fragility considering velocity for RC structures (the left are fragility surfaces for plain coast and the right are fragility surfaces for ria coast).

cost information is given in Section 3.2.5.

4.2.3 Influence of flow velocity on tsunami loss

To consider two tsunami intensity measures in tsunami fragility, the tsunami loss is evaluated as a function of both inundation depth and flow velocity. The differences in the estimated tsunami loss considering and neglecting flow velocity in terms of all possible combinations of depth and velocity, are presented in Figure 4.2 as the percentage of complete replacement cost, by distinguishing four building materials and two topographical types. For example, -10% of loss difference means that the loss considering flow velocity is less than neglecting flow velocity by 10% of the mean building replacement cost. The range of the differences is distinguished by colours (e.g. orange colour corresponds to 10% - 20%). The loss is calculated based on the corresponding bivariate-IM fragility of each structural type for single building and is not related to tsunami hazard results at specific locations. The coloured contour graphs indicate that importance of flow velocity for the loss estimate largely depends on the combination of local inundation depth and flow velocity of a building.

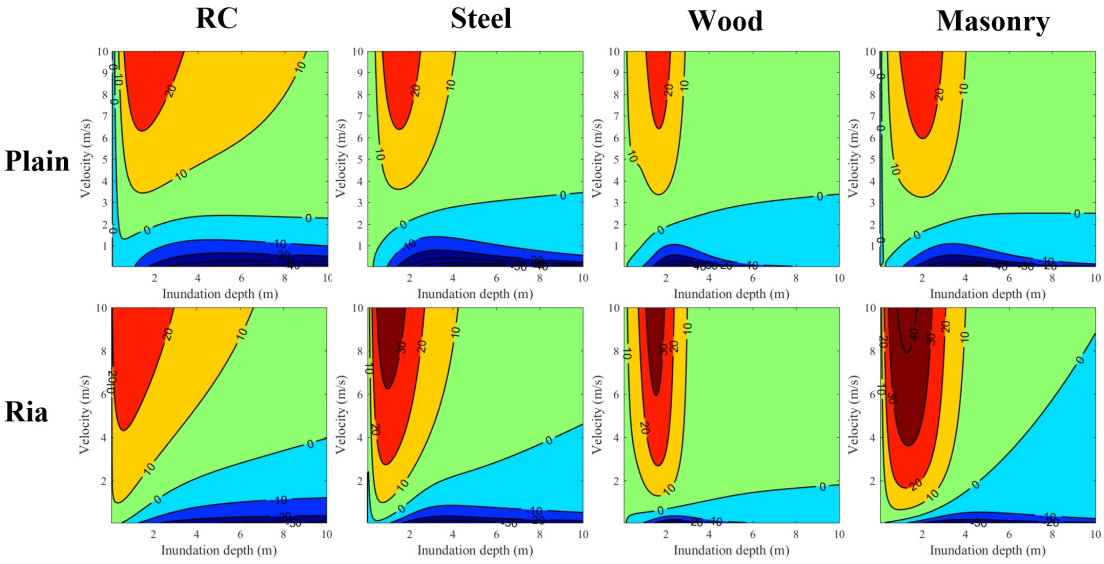

Figure 4.2 Percentage of loss difference considering and neglecting velocity.

For both types of coastal topography, when flow velocity is very small the consideration of velocity can result in an underestimation of tsunami loss. It is noteworthy that top left corners of the contour graphs are less meaningful because it is rare that

a location experiences a low inundation depth and high flow velocity (e.g. 1 m inundation depth with 8 m/s velocity). For the areas where depth-based loss is less than depth-velocity-based loss (i.e. red), the most loss occurs in a range of low inundation depth less than 3 m. Although red-coloured and orange-coloured areas for all four structural types are roughly a wedge shape which extends with the increase of flow velocity, some combinations of inundation and flow velocity in these areas (e.g. 2-m depth and 8-m/s flow velocity) are highly unlikely to happen. Moreover, RC structures are the most sensitive to flow velocity with larger areas in red and orange, which cover the combination of an inundation depth higher than 2 m and flow velocity faster than 3 m/s. In other words, for an area that is severely inundated where high flow velocities and high inundation depths are expected, the consideration flow velocity does not make a significant difference compared to a less destructive tsunami.

However, the distributions of tsunami loss considering and neglecting flow velocity for plain coast and ria coast are still different for certain depth-velocity combinations. Firstly, focusing on the most sensitive RC structures, there is a wider gap of green and blue along the velocity axis of the graph of plain coast than ria especially at the left bottom corner, which represents less than 10% difference, as seen in Figure 4.2. This means flow velocity is not important when tsunami hazard intensity falls in the range of inundation depth less than 1 m and velocity less than 2.5 m/s. This characteristic is not reflected for ria coast shown in Figure 4.2. For ria coast, the bivariate-IM fragility produces greater tsunami loss from a velocity value as low as 1 m/s, while this number for plain coast is about 4 m/s. Similar features are found for steel and masonry structures. Secondly, although the region corresponding to a difference between 5% and 30% for RC is roughly the same for plain coast and ria coast, a positive difference for ria coast is found from lower velocity and inundation depth, while that for plain coast occurs only when inundation depth is greater than approximately 2 m and velocity is larger than about 4 m/s. Generally speaking, the positive difference for plain coast covers a range of higher inundation depth than ria coast.

For all structural types, the consideration of velocity results in more tsunami loss from lower velocity values for ria coast than plain coast. For both topographic types, the loss differences of more than 20% caused by the consideration of velocity mainly occur when inundation depth is lower than 3 m, and it increases with the rise of velocity. Except for RC structures, ria coast has a larger region of difference ratio over 30% than plain coast, particularly for steel and masonry structures. For instance, for steel, when

inundation depth falls between 1 m and 2 m and flow velocity ranges between 4 m/s and 6 m/s, the differences for plain coast are about 5% to 10%, while those for ria coast are mainly 20% to 30%. Judging from the areas of loss difference ratio, RC is the most sensitive to the consideration of flow velocity, followed by steel and masonry structures, and wood structures are the least sensitive. This is consistent with general observations of tsunami fragility of wood structures that when the inundation depth reaches a certain value, it tends to be critical regardless of flow velocity. Overall, the importance of flow velocity increases with the increase of flow velocity, however, it is only true for a certain range of inundation depth values.

4.2.4 Importance of flow velocity for tsunami loss estimation at different scales

Sendai and Onagawa in Miyagi Prefecture are selected as representative locations for plain and ria coast, respectively. Tsunami losses considering and neglecting velocity are compared at three scales: (i) the whole city, (ii) a small community, and (iii) within 1 km from the coastline. The influence of DEM resolution is also investigated.

Plain coast

A building portfolio in Sendai consists of 337 RC structures, 695 steel structures, 7,488 wood structures, and 1,097 masonry structures (Figure 4.3a), which is larger than that in Chapter 3 to investigate the influence of flow velocity at different spatial scales. The probabilistic tsunami loss curves for the entire portfolio in Sendai shown in Figure 4.4a indicate that velocity is not important at a city scale. However, this is due to the fact that the majority of buildings considered are wood structures which are least sensitive to flow velocity. The DEM resolution makes larger differences than the consideration of flow velocity for the whole Sendai, with the 50-m DEM resulting in more than 20% overestimation in comparison with the 10-m resolution. The reason is that in plain coastal areas the coarse resolution is unable to reflect the rapid drop of tsunami waves travelling inland realistically (see Chapter 3).

To look into the loss differences more closely, the spatial distribution of the differences in tsunami loss due to the flow velocity is examined for a smaller region PR1 (consistent with Chapter 3) for tsunami scenarios corresponding to 10th, 50th and 90th

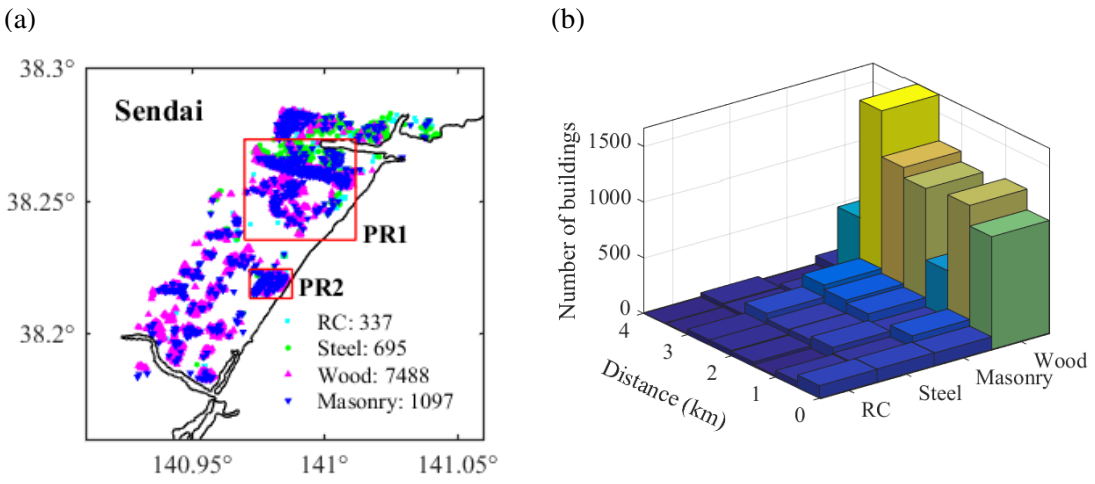

Figure 4.3 Building portfolio of Sendai: (a) building distribution; and (b) number of buildings by distance from the coastline.

percentiles of total tsunami loss (Figures 4.5a to 4.5c). RC structures are taken for illustration as they are the most sensitive structural type to flow velocity as found in Section 4.2.3. A positive loss ratio means that flow velocity gives higher loss and a negative one means the opposite. The largest difference occurs at buildings closest to the sea (i.e. within 1 km from the coastline) which experience much faster tsunami flow than the rest of the buildings. It is noteworthy that the difference for this small group of buildings at 50th percentile is larger than those at the 10th percentile and 90th percentile. The reason is that the corresponding inundation depths for those buildings at 90th percentile of total tsunami loss are higher than those at 50th percentile, while velocities at 50th percentile are larger than those at 90th percentile. In addition, the loss difference becomes smaller when inundation depth becomes higher and flow velocity becomes lower, as shown in Figure 4.2. Such features that the largest difference for certain buildings does not necessarily occur at the high percentiles are caused by tsunami propagation path of specific scenarios and the location of buildings. To put in another way, the tsunami loss of a small coastal community cannot represent the damage scale of the whole city. Moreover, minor underestimation of bivariate-IM loss is observed at the far end of the building stock. Because both depth and velocity decrease when tsunami waves travel further inland, the combination of the two intensity measures make those buildings fall into the blue area in Figure 4.2 which indicates that the consideration of velocity generates lower tsunami loss than neglecting it.

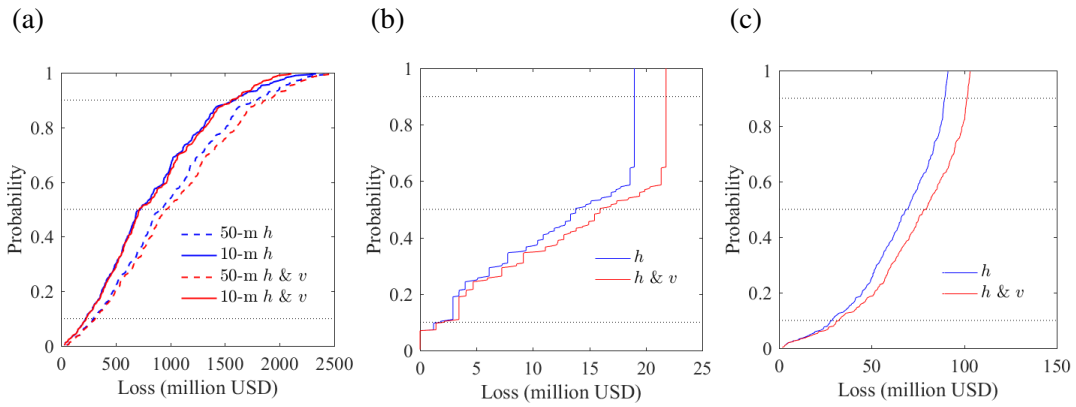

Figure 4.4 Cumulative distribution functions of tsunami losses in Sendai: (a) whole Sendai, (b) RC in region PR2, and (c) RC within 1 km from the coastline.

Given the tsunami losses of all buildings considering and neglecting flow velocity, the percentage of loss difference (i.e. loss considering velocity minus loss neglecting velocity over total replacement cost) is calculated (Figure 4.4). Since the loss difference distribution in PR1 indicates that buildings located close to the coastline tend to be more sensitive to flow velocity, a small region PR2, which is a community located within 1 km from the sea, is focused on, as shown in Figure 4.3a. Similar features as found in region PR1 in terms of largest difference can be seen in region PR2 (Figures 4.5d to 4.5f). Referring to the inundation depth and velocity contour maps in Figure 4.6, the inundation depth is consistent with the rank of total loss, while higher velocity occurs at 50th percentile rather than the 90th percentile. It means that for the same location, a higher inundation does not necessarily come with a higher velocity for different tsunami scenarios. This also explains why larger differences are found at 50th percentile than 90th percentile. As a result, the actual tsunami propagation inland can make a significant difference in total tsunami loss. Besides, in region PR2, no significant underestimation of loss by the consideration of velocity is found. Therefore, the importance of flow velocity for tsunami loss estimation in Sendai largely depends on the combination of inundation depth and flow velocity of the specific tsunami scenario and is also related to the building location. The depth-velocity distributions of region PR2 at three percentile levels shown in Figure 4.7 indicate that at all three percentiles the majority of inundated buildings fall in the green area which represents a difference less than 10%, and a few of them fall into the orange area which corresponds to a difference of 10% to 20%. Overall, the differences decrease with the increasing distance from the shoreline.

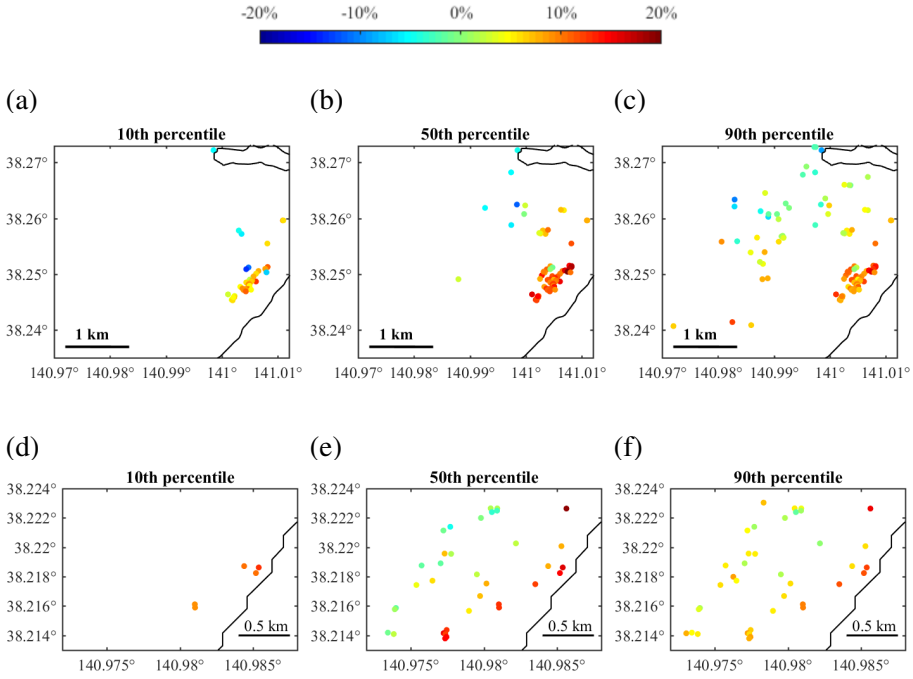

Figure 4.5 Distribution of loss difference ratio for RC structures in small regions PR1 and PR2 of Sendai: (a-c) PR1 and (d-f) PR2.

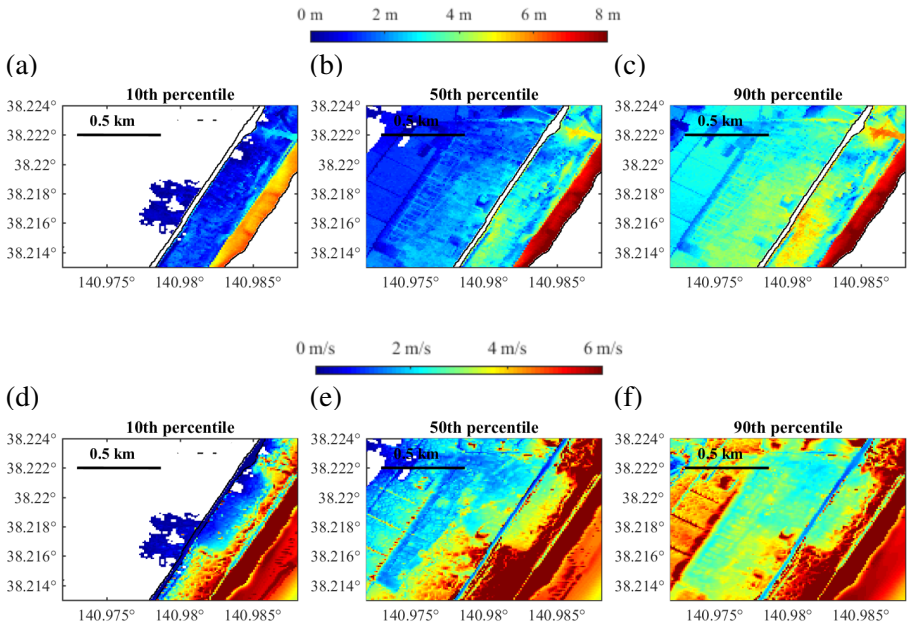

Figure 4.6 Stochastic tsunami hazard maps for PR2 in Sendai: (a-c) inundation depth, and (d-f) velocity

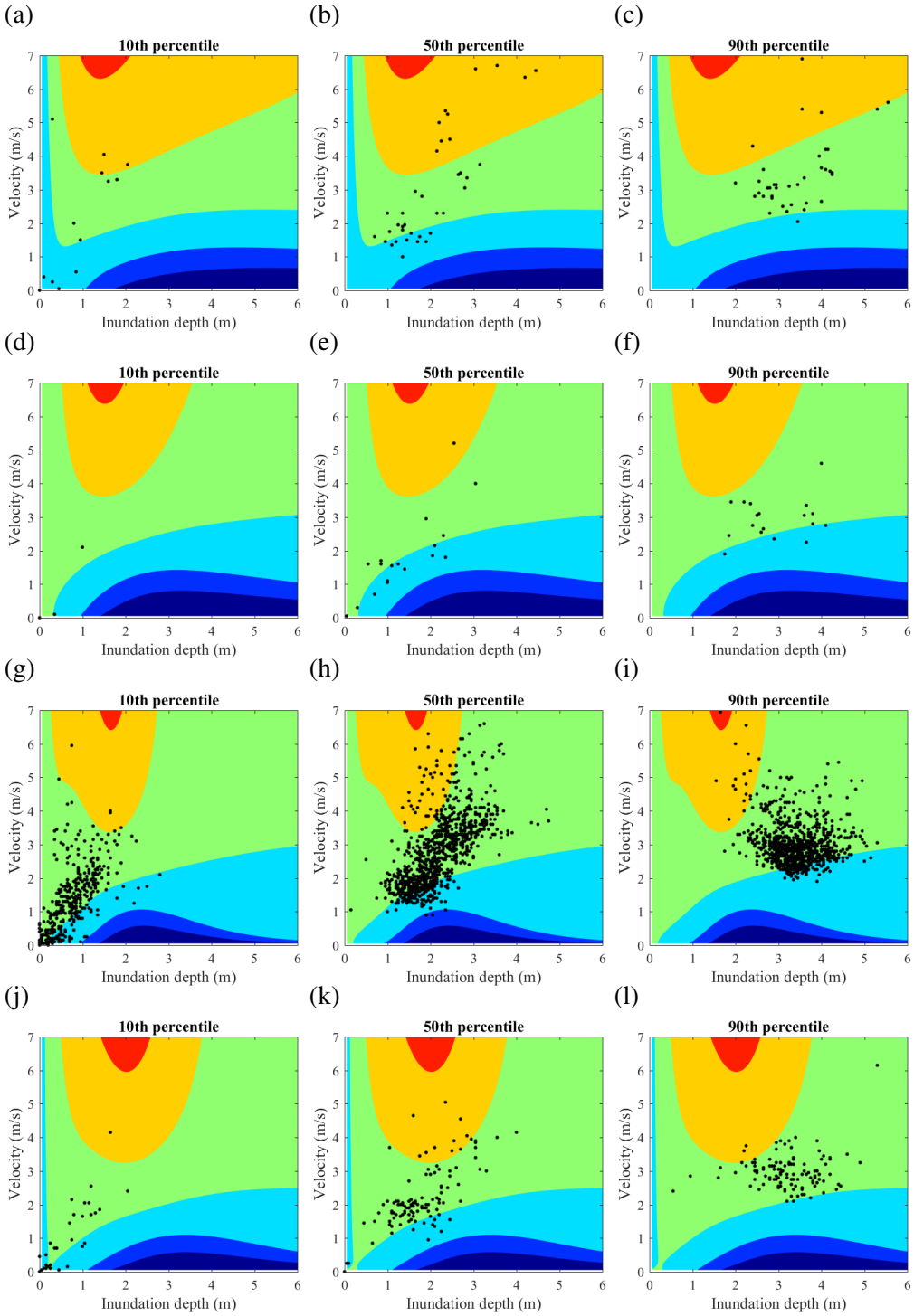

Figure 4.7 Distribution inundation depth and flow velocity for PR2 in Sendai (green for 0∼10%, orange for 10%∼20%, red for 20%∼30%, sky blue for -10%∼0%, sapphire for -20%∼-10%, and midnight blue for -30%∼-20%): (a-c) RC, (d-f) steel, (g-i) wood, and (j-l) masonry.

The sensitivity of RC structures to velocity PR2 is consistent with the findings in PR1. The loss curves for RC buildings in PR2 (Figure 4.4b) show a more than 10% loss increase by the consideration of flow velocity, which is due to the high proportion of RC buildings located close to the shoreline (i.e. less than 0.5 km). Another noteworthy feature of tsunami loss curves in PR2 is that the curves start to become steeper after about 60th percentile. Given the location of PR2 as a small community, when the hazard intensity reaches a certain level, the majority of buildings will collapse or be washed away, and thus the increase of tsunami intensity will significantly increase the tsunami loss. This information not only provides potential economic loss for a given building portfolio considering all possible situations, but also indicates the area from which the greatest loss comes. For the purpose of exploring the difference caused by flow velocity, the difference of losses caused by the bivariate-IM method compared to the single-IM method is computed and discussed below.

Based on the findings above, tsunami risks of buildings located within 1 km from the coastline are most sensitive to the inclusion of flow velocity. The tsunami loss curves in Figure 4.4c show that a loss of up to 15% more is caused by the consideration of velocity for RC buildings within 1 km from the coastline. Although velocity hardly has any influence on tsunami loss of the whole Sendai, it does not mean it is not important at the local scale. For this specific situation of Sendai, the majority of buildings are wood structures, and most buildings are located farther than 1 km from the coastline, as presented in Figure 4.3b. Therefore, the importance of velocity for loss estimation depends on the locations of buildings and composition of building materials.

Ria coast

The buildings in Onagawa are distributed long the dendritic shoreline, consisting 163 RC structures, 270 steel structures, 2,836 wood structures, and 140 masonry structures. Most buildings are concentrated in the region RR1 (the portfolio considered in Chapter 3), as shown in Figure 4.8a. A notable feature of the building composition in Onagawa is that most buildings are located within 1 km from the coastline where the land is relatively flat (Figure 4.8b). Therefore, to reflect the influence of flow velocity at different scales, in addition to the total tsunami loss in whole Onagawa (Figure 4.9a), RC buildings in the smaller region RR1 and within 1 km are further considered (Figures 4.9b and 4.9c) as RC has been found most sensitive to the inclusion of flow velocity

in Section 4.2.3.

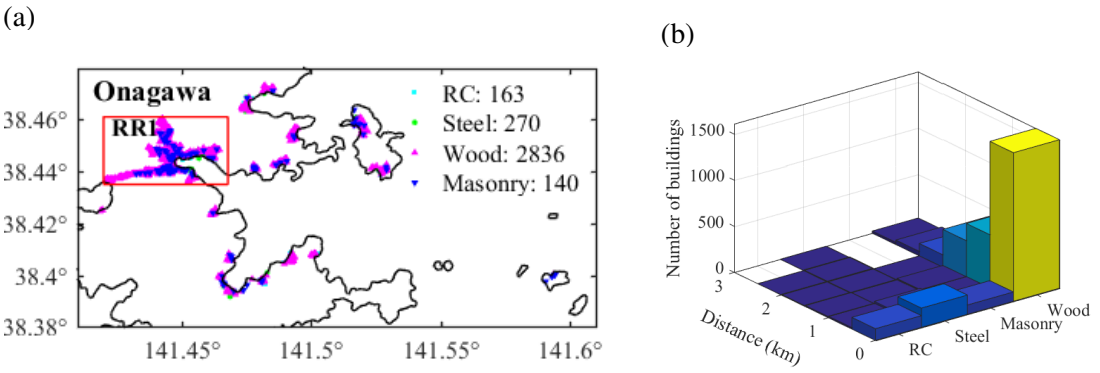

Figure 4.8 Building portfolio of Onagawa: (a) building distribution and (b) number of buildings by distance from the coastline.

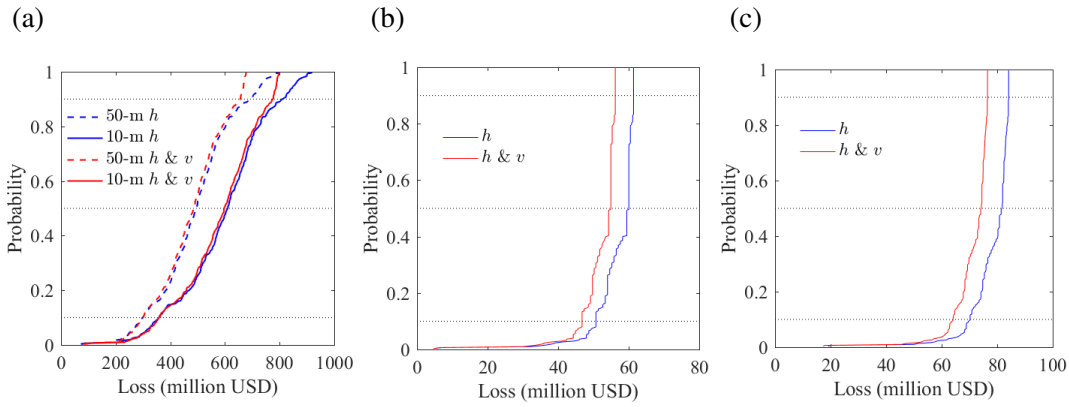

Figure 4.9 Cumulative distribution functions of tsunami losses in Onagawa: (a) whole Onagawa, (b) RC in region RR1, and (c) RC within 1 km from the coastline.

An opposite finding compared to the results in Sendai in terms of the influence of DEM resolution is that the coarser resolution tends to underestimate tsunami loss in Onagawa (Figure 4.9a). This is due to the rising elevation of Onagawa, and the DEM of coarse resolution cannot accurately simulate the tsunami intensity at locations where the elevation changes abruptly (see Chapter 3). Although the low importance of velocity at a town scale agrees with the findings in Sendai, a deviation is seen above 90th percentile that the consideration of velocity leads to smaller tsunami loss. Another contrasting trend of tsunami loss curves of Onagawa compared to those of Sendai is that tsunami loss considering velocity is slightly lower than that neglecting velocity although the difference is fairly small. The different increases to about 10% for RC structures in

RR1 and RC structures within 1 km from the coastline (Figure 4.9b and Figure 4.9c), which are consistent with the findings in Sendai that that the buildings close to the coastline are more sensitive to consideration of velocity but the consideration of flow velocity produces lower tsunami losses. This is true for these two scales in Onagawa only because the land is flat for areas close to the coastline, and thus may not apply to other cities and towns along ria coast where the features of land elevation are different. Similarly to Sendai, the consideration of velocity does not make a significant difference in tsunami loss for the whole Onagawa, due to the dominance of wood structures.

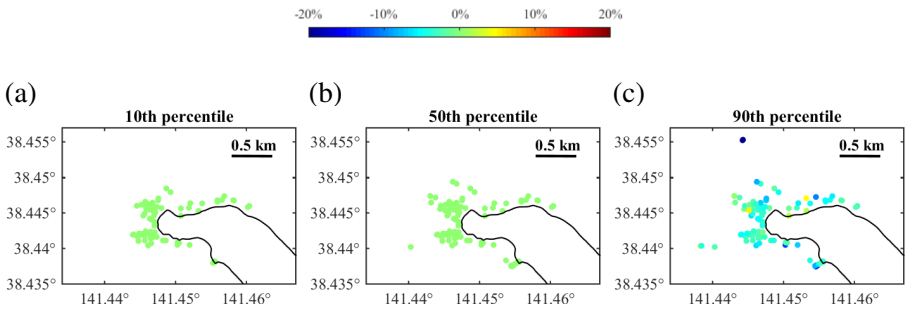

Figure 4.10 Distribution of loss difference for RC structures in Onagawa

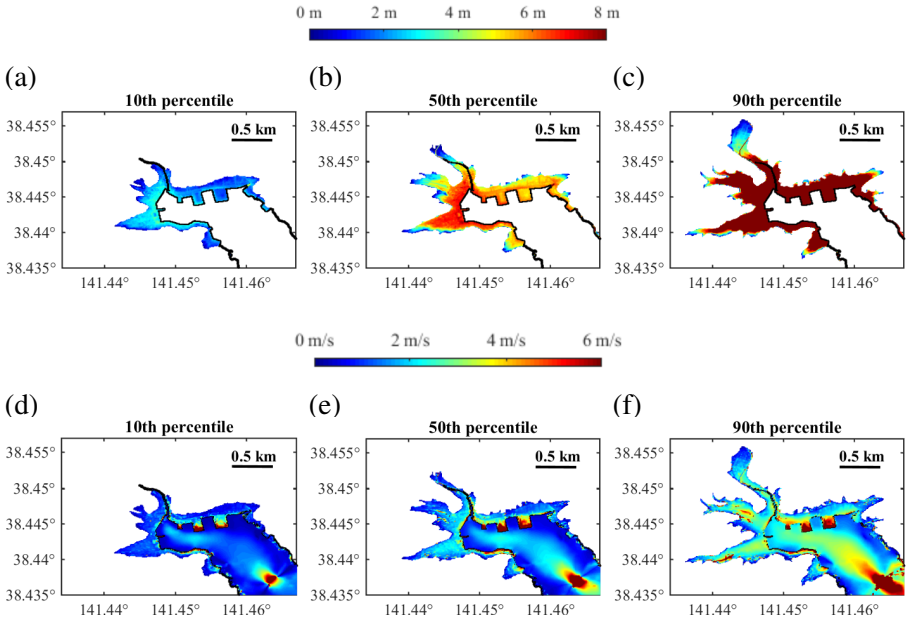

Figure 4.11 Stochastic tsunami hazard maps for RR1 in Onagawa: (a-c) inundation depth; and (d-f) flow velocity.

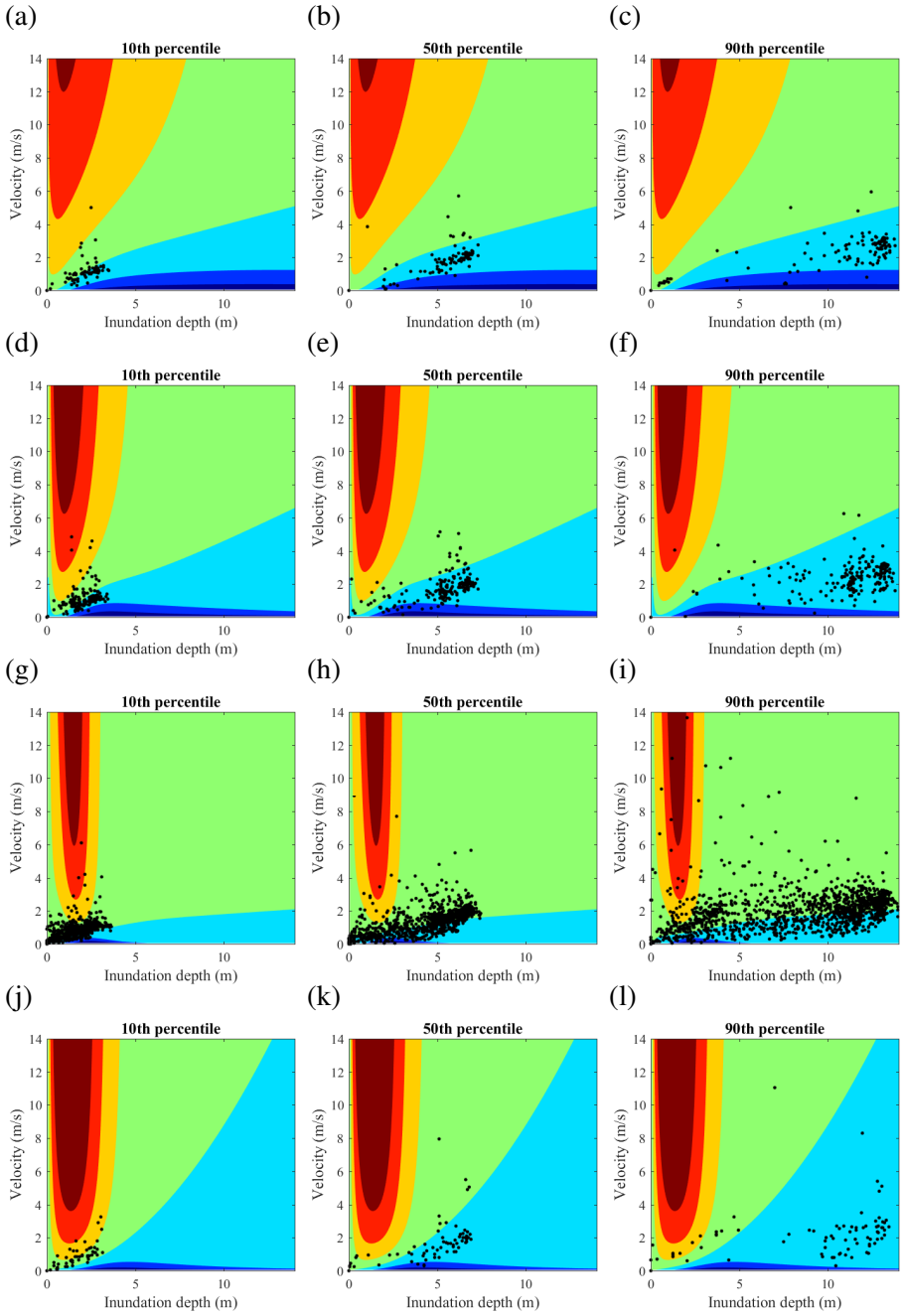

Figure 4.12 Distribution inundation depth and flow velocity for RC structures of region RR1 in Onagawa: (green for 0∼10%, orange for 10%∼20%, red for 20%∼30%, dark red for 30%∼40%, sky blue for -10%∼0%, sapphire for -20%∼-10%, and midnight blue for -30%∼-20%): (a-c) RC, (d-f) steel, (g-i) wood, and (j-l) masonry.

Focusing on RR1 which is the identical building portfolio considered in Chapter 3 and taking RC structures as an example, Figure 4.10 shows spatial distribution loss difference for RC structures in RR1, whereas Figure 4.11 shows inundation depth and

flow velocity maps for three probability levels. Figure 4.10 agrees with the loss curves that little difference is found for scenarios corresponding to 10th and 50th percentiles of total losses, whereas underestimation of less than 10% which is caused by flow velocity is seen at 90th percentile. Not many RC buildings experience flow velocity faster than 5 m/s and a concentration of points can be found with inundation depths higher than 10 m, which can also be seen from the inundation maps in Figure 4.11. However, for RC structures in RR1 approximately -10% differences still exist (Figure 4.9b), because the majority of RC structures in RR1 fall in the areas which represent -10% difference (see Figure 4.12). Figure 4.12 shows a significantly different features of inundation depth-velocity distribution compared to Sendai on plain coast (see Figure 4.7) that buildings in Onagawa tend to experience low flow velocity with high inundation depth, which agrees with observations by Latcharote et al. (2017). As shown in Figure 4.10, there are blue strips along the inundation depth axis, and the paired inundation depth and flow velocity in Onagawa make buildings fit into the green or blue areas which indicate less than 10% loss differences. For RC, steel, and masonry structures, most buildings fall in the range of -10%$\sim$0%, while most wood structure are in the range of -10%$\sim$10% concentrated along the zero difference line. These results show the predominant influence of inundation depth on estimated tsunami loss for M_w 9.0 tsunamis in Onagawa.

Another feature of tsunami loss for buildings in Onagawa is that the probabilistic loss curves become very steep after 10th percentile for RC, which means the inundation scale in RR1 in Onagawa is more extensive given the same set of tsunami scenarios. This implies that for tsunamis generated by earthquakes of lower magnitudes, the conclusion may be different because the combination of depth and velocity will be different. Assuming a tsunami of lower earthquake magnitude that generates lower inundation depth, the consideration of flow velocity may not result in less regional tsunami loss than neglecting it. In summary, the importance of flow velocity for ria coast is related to the inundation scale, land elevation, building distributions and building materials.

4.3 Tsunami fragility functions based on momentum flux

4.3.1 Tsunami fragility functions considering momentum flux

For a fair comparison with regard to the selection of IM for tsunami loss estimation, tsunami fragility models taking into account momentum flux are developed based on the tsunami damage data in Miyagi Prefecture during the 2011 Totoku tsunami in Japan. The fragility functions are developed via multinomial regression analysis, which is the same as the bivariate-IM tsunami fragility functions by De Risi et al. (2017). The damage data and tsunami simulations are consistent with the fragility models considering flow velocity in Section 4.2. There are more than 100,000 data points of building damage with supplementary information (i.e. damage scale, structure material, location, and observed inundation depth), which are distributed across the Miyagi Prefecture coast with different types of topography. The flow velocity and corresponding momentum flux at each building location during the 2011 Tohoku tsunami are simulated using the earthquake rupture model by Satake et al. (2013).

In total, ten different tsunami fragility models are investigated. Below FM is used to denote the tsunami fragility model variation. The considered cases include a depth-based model and a bivariate depth-velocity-based model that was considered in Section 4.2. In this section, these two models are referred to as FM1 and FM2. Models considering momentum flux m are classified as three categories: models considering momentum flux only, models considering both inundation depth and momentum, and models considering both flow velocity and momentum flux. FM3 considers momentum flux only, whereas FM4 considers interaction between structural type and momentum flux as well.

FM 3:

$$f(p_{ij}) = \theta_{j,0} + \theta_{j,1}\ln(m_i) + \theta_{j,2}\cdot d_W + \theta_{j,3}\cdot d_M + \theta_{j,4}\cdot d_S \tag{4.8}$$

FM 4:

$$f(p_{ij}) = \theta_{j,0} + \theta_{j,1}\ln(m_i) + \theta_{j,2}\cdot d_W + \theta_{j,3}\cdot d_M + \theta_{j,4}\cdot d_S + \theta_{j,5}\ln(m_i)d_W + \theta_{j,6}\ln(m_i)d_M + \theta_{j,7}\ln(m_i)d_S \tag{4.9}$$

FM5, FM6, and FM7 consider momentum flux in addition to inundation depth. FM6 considers interaction between inundation depth and structural topology, and FM7 considers interaction between structural typology and both inundation depth and momentum flux.

FM 5:

$$f(p_{ij}) = \theta_{j,0} + \theta_{j,1}\ln(h_i) + \theta_{j,2}\cdot d_W + \theta_{j,3}\cdot d_M + \theta_{j,4}\cdot d_S + \theta_{j,5}\ln(m_i) \tag{4.10}$$

FM 6:

$$\begin{aligned} f(p_{ij}) = \theta_{j,0} &+ \theta_{j,1}\ln(h_i) + \theta_{j,2}\cdot d_W + \theta_{j,3}\cdot d_M + \theta_{j,4}\cdot d_S \\ &+ \theta_{j,5}\ln(h_i)d_W + \theta_{j,6}\ln(h_i)d_M + \theta_{j,7}\ln(h_i)d_S + \theta_{j,8}\ln(m_i) \end{aligned} \tag{4.11}$$

FM 7:

$$\begin{aligned} f(p_{ij}) = \theta_{j,0} &+ \theta_{j,1}\ln(h_i) + \theta_{j,2}\cdot d_W + \theta_{j,3}\cdot d_M + \theta_{j,4}\cdot d_S \\ &+ \theta_{j,5}\ln(h_i)d_W + \theta_{j,6}\ln(h_i)d_M + \theta_{j,7}\ln(h_i)d_S + \theta_{j,8}\ln(m_i) \\ &+ \theta_{j,9}\ln(m_i)d_W + \theta_{j,10}\ln(m_i)d_M + \theta_{j,11}\ln(m_i)d_S \end{aligned} \tag{4.12}$$

FM8, FM9, and FM10 take into account flow velocity and momentum flux. FM9 further considers the interaction between flow velocity and structural typology, and FM10 accounts for the interaction between momentum flux and structural typology.

FM 8:

$$f(p_{ij}) = \theta_{j,0} + \theta_{j,1}\ln(v_i) + \theta_{j,2}\cdot d_W + \theta_{j,3}\cdot d_M + \theta_{j,4}\cdot d_S + \theta_{j,5}\ln(m_i) \tag{4.13}$$

FM 9:

$$\begin{aligned} f(p_{ij}) = \theta_{j,0} &+ \theta_{j,1}\ln(v_i) + \theta_{j,2}\cdot d_W + \theta_{j,3}\cdot d_M + \theta_{j,4}\cdot d_S \\ &+ \theta_{j,5}\ln(v_i)d_W + \theta_{j,6}\ln(v_i)d_M + \theta_{j,7}\ln(v_i)d_S + \theta_{j,8}\ln(m_i) \end{aligned} \tag{4.14}$$

FM 10:

$$\begin{aligned} f(p_{ij}) = \theta_{j,0} &+ \theta_{j,1}\ln(v_i) + \theta_{j,2}\cdot d_W + \theta_{j,3}\cdot d_M + \theta_{j,4}\cdot d_S \\ &+ \theta_{j,5}\ln(m_i)d_W + \theta_{j,6}\ln(m_i)d_M + \theta_{j,7}\ln(m_i)d_S + \theta_{j,8}\ln(m_i) \end{aligned} \tag{4.15}$$

4.3.2 Model selection

The performances of the ten tsunami fragility models are evaluated by their goodness-of-fit scores according to three diagnostic criteria: i) the Bayesian Information Criterion (BIC) (Schwarz, 1978) (Equation (4.16)), ii) the Akaike Information Criterion (AIC)

(Akaike, 1974) (Equation (4.17)), and iii) the residual deviance G^2, which compares the proposed model (i.e. a model with a small number of parameters) with a saturated model (i.e. a model with parameters equal to the number of observations), as shown in Equation (4.18).

$$BIC = -2\ln[L(x,y|\theta)] + r\ln n \tag{4.16}$$

$$AIC = -2\ln[L(x,y|\theta)] + 2r \tag{4.17}$$

$$G^2 = 2\sum_{i=1}^{n}\sum_{j=0}^{5} y_{ij}\ln\frac{y_{ij}}{p_{ij}} \tag{4.18}$$

where $L(x,y|\theta)$ denotes the likelihood under the MLE of the evaluated model, r is the number of regression parameters, and n is the number of data points.

Table 4.3 Goodness-of-fit metrics for model evaluation.

Model	IM	Interaction terms with structural typology	Number of parameters	AIC	BIC	Deviance
FM1	h	h	40	132085	132461	132005
FM2	h, v	h	45	129760	130128	129616
FM3	m	None	25	172873	173107	172823
FM4	m	m	40	172775	173150	172695
FM5	h, m	None	30	129875	130157	129815
FM6	h, m	m	45	129331	129753	129241
FM7	h, m	h and m	60	129249	129812	129129
FM8	v, m	None	30	172667	172949	172607
FM9	v, m	v	45	172509	172932	172419
FM10	v, m	m	45	172571	172993	172481

For metrics of all three evaluation criteria, a model performs better if it has smaller values of AIC, BIC, and residual deviance. A model is considered of better performance in two situations: i) the model with better linear predictors (e.g. inundation depth and structural type) but the same link functions as others, and ii) the model with a better link function but the same linear predictors.

A summary of goodness-of-fit metrics for the ten tsunami fragility models is shown in Table 4.3. It can be observed that models perform significantly better when inundation depth h is considered, which means that inundation depth is the dominating IM for damage assessment. The results also indicate that models without considering

Table 4.4 Regression parameters for fragility model FM1 distinguishing coastal topography.

Parameter	Plain coast					Ria coast				
	DS1	DS2	DS3	DS4	DS5	DS1	DS2	DS3	DS4	DS5
θ_0	1.739	1.766	-1.199	-3.071	-3.675	85.321	2.098	0.191	-1.429	-2.602
θ_1	0.180	1.282	2.228	2.832	2.360	28.259	0.311	0.373	1.458	1.317
θ_2	-0.044	-1.216	0.994	-4.299	0.500	-81.674	-1.856	0.036	-3.438	1.424
θ_3	-0.413	-0.908	0.588	-2.255	0.489	17.244	-0.993	0.652	-2.904	0.863
θ_4	-0.571	-0.541	0.440	-0.457	0.595	17.244	-1.079	0.123	-2.212	1.204
θ_5	-0.217	-0.589	-1.141	1.825	1.888	-29.317	0.401	0.929	1.255	1.352
θ_6	0.351	-0.334	-1.275	0.623	0.934	-28.259	0.595	0.461	2.250	0.590
θ_7	-0.279	-0.279	-0.349	0.775	0.458	-28.259	0.453	0.405	1.471	0.045

Table 4.5 Regression parameters for fragility model FM2 distinguishing coastal topography.

Parameter	Plain coast					Ria coast				
	DS1	DS2	DS3	DS4	DS5	DS1	DS2	DS3	DS4	DS5
θ_0	1.723	1.765	-1.318	-3.759	-3.846	94.999	2.06	0.198	-1.397	-2.597
θ_1	0.304	1.308	1.623	1.546	1.917	6.936	0.467	0.363	1.391	1.107
θ_2	-0.151	-1.237	1.16	-3.903	0.728	-91.28	-1.777	0.027	-3.484	1.285
θ_3	-0.381	-0.91	0.611	-2.268	0.633	7.568	-1.071	0.652	-2.855	0.964
θ_4	-0.545	-0.537	0.426	-0.439	0.576	7.692	-1.053	0.113	-2.224	1.044
θ_5	-0.236	-0.586	-0.903	1.811	1.837	-7.922	0.298	0.936	1.302	1.487
θ_6	0.323	-0.329	-1.058	0.762	0.907	-6.898	0.457	0.467	2.22	0.537
θ_7	-0.244	-0.263	-0.275	0.833	0.494	-6.915	0.273	0.414	1.48	0.131

Table 4.6 Regression parameters for fragility model FM6 distinguishing coastal topography.

Parameter	Plain coast					Ria coast				
	DS1	DS2	DS3	DS4	DS5	DS1	DS2	DS3	DS4	DS5
θ_0	1.600	1.768	-1.253	-4.049	-3.839	93.430	1.958	0.241	-1.292	-2.413
θ_1	0.255	1.276	1.566	1.002	1.822	5.538	0.489	0.324	1.279	0.994
θ_2	-0.108	-1.212	1.202	-3.772	0.806	-89.783	-1.745	-0.006	-3.560	1.241
θ_3	-0.384	-0.906	0.671	-2.199	0.711	9.152	-1.075	0.648	-2.799	0.929
θ_4	-0.546	-0.542	0.429	-0.453	0.597	9.131	-1.015	0.071	-2.279	0.903
θ_5	-0.212	-0.589	-0.896	1.964	1.799	-6.613	0.287	0.967	1.409	1.534
θ_6	0.367	-0.334	-1.055	0.912	0.879	-5.541	0.437	0.487	2.183	0.540
θ_7	-0.214	-0.282	-0.305	0.802	0.460	-5.539	0.252	0.450	1.514	0.202

momentum flux (i.e. FM3, FM4, FM8, FM9, and FM10) are less preferred. For instance, comparing FM2 and FM6 which have the same number of regression parameters and the same functional forms, it can be seen that FM6 which considers momentum flux is slightly superior to FM2 which takes into account velocity instead. However, this

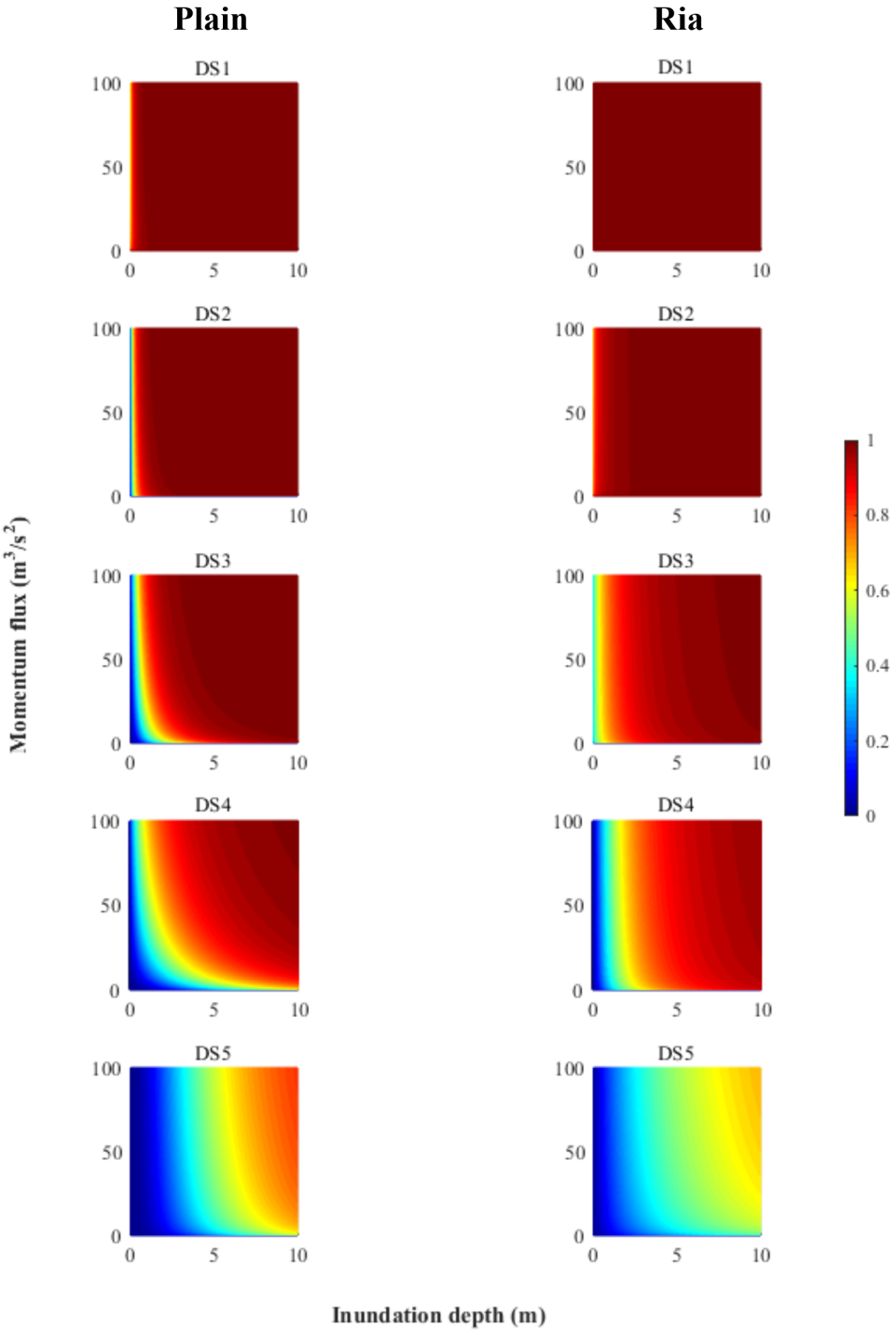

Figure 4.13 Tsunami fragility FM6 for RC structures (left for plain coast and right for ria coast).

improvement is not as significant as the difference between FM1 and FM2 (or between FM1 and FM6) when flow velocity (or momentum flux) is considered in addition to

inundation depth. In other words, the inclusion of flow velocity in addition to inundation depth improves the performance of tsunami fragility model, but the momentum flux term capturing the combined effects of inundation depth and flow velocity does not improve the model performance substantially in terms of model fitness. Among models considering both inundation depth and momentum flux, although FM7 is the best model with the lowest diagnosis metrics, FM6 may be a more preferred model because the difference of the metrics between FM6 and FM7 is less than 0.1%, whereas FM6 has 15 less parameters. Therefore, FM6 is selected as the best model that takes into account momentum flux.

To investigate the effects of adopting different intensity measures in tsunami fragility modelling on tsunami loss estimation, FM1, FM2, and FM6 are selected as representative models for inundation depth, depth-velocity, and depth-momentum flux, respectively. The corresponding regression parameters for these fragility curves are shown in Table 4.4, Table 4.5, and Table 4.6 by distinguishing plain coast and ria coast. Considering both inundation depth and momentum flux, FM6 is shown in Figure 4.13 as fragility surfaces for five damage states, for RC structures as an example by distinguishing plain and ria coast. It can be observed that momentum flux is more important for plain coast than ria coast.

4.3.3 Influence of momentum flux on tsunami loss

The importance of momentum flux in addition to inundation depth is investigated by comparing the tsunami loss of a single building of each structural material type (i.e. RC, steel, wood, and masonry). The influence of consideration of momentum flux in addition to inundation depth is compared to that of flow velocity, with regard to the percentage of difference of tsunami loss made by momentum or flow velocity over total replacement cost of a building. A positive value means that considering momentum flux gives higher tsunami loss and a negative value means the opposite. It should be noted that during tsunamis the maximum momentum flux does not necessarily happen at the same time with the maximum flow velocity, so that the momentum flux may not correspond to the same flow velocity.

Figure 4.14 shows the percentage of loss difference for plain coast by comparing the case when velocity (FM2) or momentum flux (FM6) is considered with respect

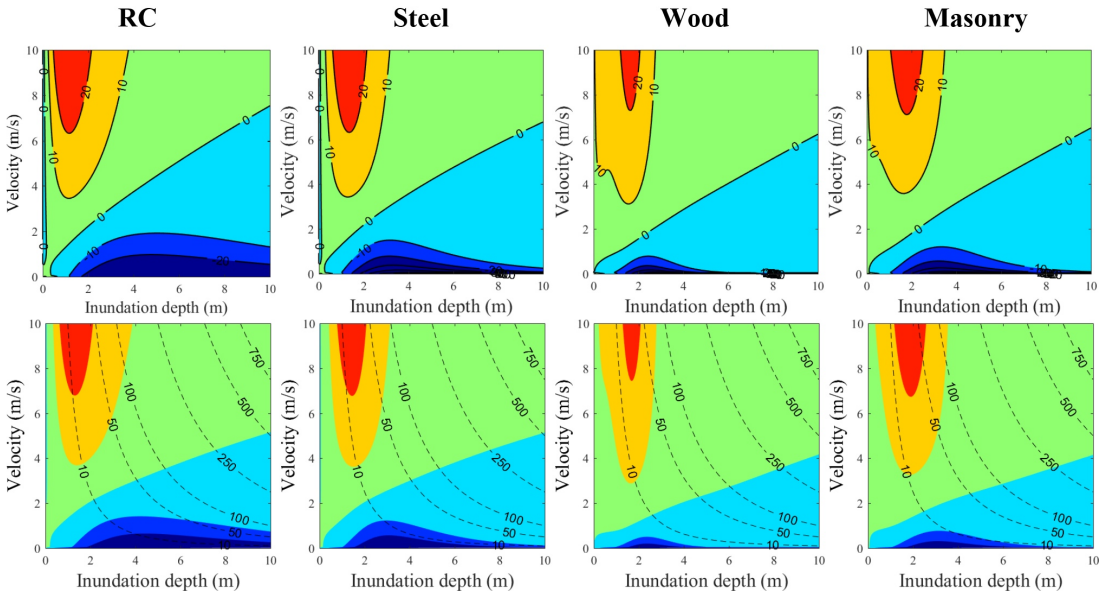

Figure 4.14 Percentage of loss difference for plain coast (top is whether velocity is considered, and bottom is whether momentum flux is considered; dashed curves are momentum flux).

to the case when inundation depth only is considered (FM1). To facilitate the direct comparison, the equivalent flow velocity (i.e. $v = \sqrt{m_{max}/h_{max}}$) is adopted for the case of momentum flux, and the corresponding momentum flux is shown by dashed curves. Note that for damage estimation the maximum value of the intensity measure is used, while in real tsunamis the maximum inundation depth, flow velocity, momentum flux do not necessarily happen at the same time ($m_{max} = (hv)^2_{max} \neq h_{max}v^2_{max}$). For all four types of structures, the areas that momentum flux generates smaller tsunami loss than using inundation depth only (bottom four graphs) are smaller than those of flow velocity (top four graphs). In other words, In other words, FM6 considering momentum flux is likely to cause a greater loss than FM2 considering flow velocity. Taking RC structures as an example, compared to FM1, at an inundation depth of 10 m FM2 generates higher tsunami loss when the flow velocity is faster than 7.5 m/s, while this value for FM6 is 5 m/s. In addition, there is a wider green gap along the velocity axis when momentum flux is used, which means momentum flux causes less differences than flow velocity when inundation depth is low (i.e. lower than 2 m). However, it is unlikely that tsunami waves come with low inundation depth and high flow velocity.

A similar comparison between momentum and flow velocity for ria coast is shown in Figure 4.15, where smaller loss differences are observed when momentum flux or

velocity is considered. Similar to plain coast, ria coast tends to experience smaller tsunami loss when momentum flux is used than flow velocity for a smaller range of velocity values, by green coloured areas covering lower velocities. For RC structures, the areas that momentum flux generates larger tsunami loss are larger than those of flow velocity, while slightly smaller differences are observed for steel, wood, and masonry structures when the flow velocity is high, which can be found by smaller areas representing for loss differences larger than 15%. This finding may not make a difference in tsunami loss estimation as ria coast tends to experience high inundation depth with low flow velocity.

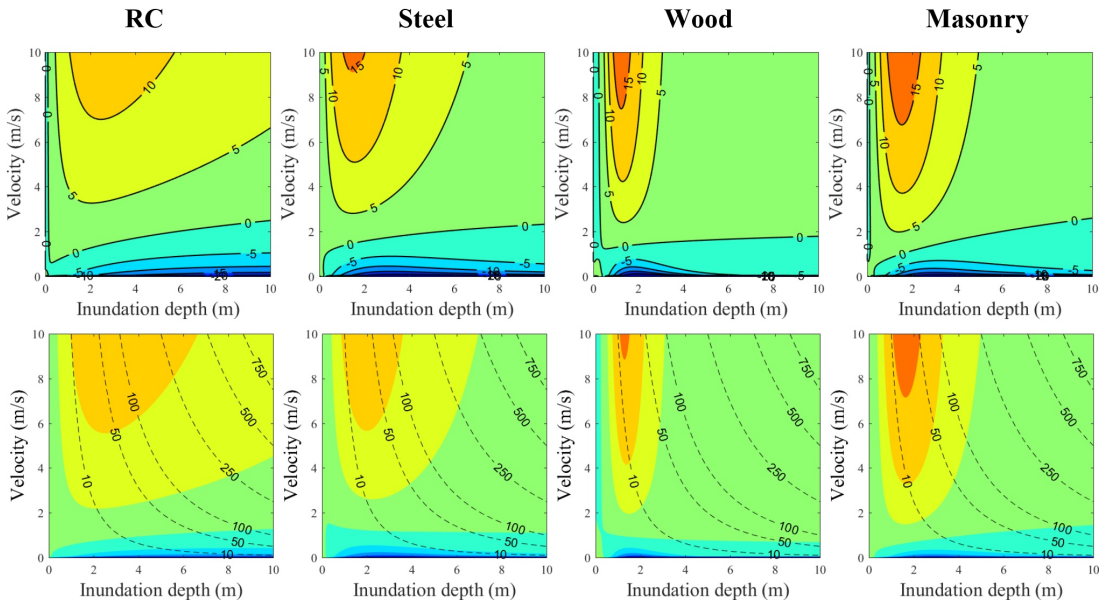

Figure 4.15 Percentage of loss difference for ria coast (top is whether velocity is considered, and bottom is whether momentum flux is considered; dashed curves are momentum flux).

4.3.4 Probabilistic tsunami loss based on different intensity measures

The probabilistic tsunami risk assessment is carried out by focusing on the Tohoku region in Japan as a case study given a M_w9.0 event. The setup is the same as Section 4.2. To evaluate the effects of considering different tsunami intensity measures on loss estimation, tsunami fragility models FM1, FM2, and FM6 are selected for loss calculation, which adopt inundation depth, inundation depth with flow velocity, and

inundation depth with momentum flux, respectively, as main tsunami hazard parameters. Tsunami fragility models distinguishing coastal topography are applied.

Sendai

Figure 4.16 shows the cumulative probability distribution function of stochastic tsunami loss, which is produced by ranking tsunami losses of 300 possible tsunami scenarios. It can be seen from the tsunami loss curves shown in Figure 4.16 that the consideration of momentum flux as IM leads to higher loss estimates, even though the consideration of flow velocity does not make a significant difference, which is consistent with the findings shown in Figure 4.14. For all buildings in Sendai, the tsunami loss considering momentum flux is more than 20% higher at 50th percentile than the other two cases when momentum flux is not taken into account. The difference decreases when a high percentile is considered (i.e. 0.8 to 1.0). The situations are different for RC buildings located in PR2 and within 1 km from the coastline that the difference increases with the increase of loss. For rare cases at 90th percentile, the consideration of momentum flux causes about 20% higher tsunami loss for RC within 1 km from the coastline than neglecting it. Besides, smaller differences of losses whether flow velocity is considered are seen for RC buildings in PR2 and buildings within 1 km from the sea compared to the same cases in Figure 4.4, because the depth-based fragility curves used in Figure 4.4 do not distinguish the coastal topography while Figure 4.16 uses fragility functions developed in Section 4.3.1 that all distinguish plain and ria coasts.

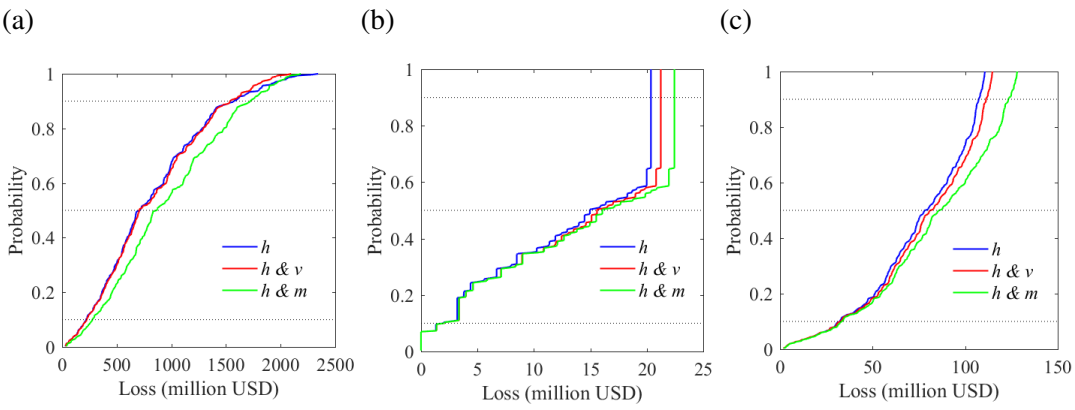

Figure 4.16 Cumulative probability distribution of tsunami losses in Sendai using different IMs : (a) whole Sendai, (b) RC in PR2, and (c) RC buildings within 1 km from the coastline.

Another finding in Figure 4.4 is that the difference made by flow velocity is smaller inundation depth-based fragility curves are distinguished by coastal topography that that in Figure 4.4. This highlights the importance of topographic effect on tsunami fragility curves particularly when flow velocity is not considered, because for tsunami waves with same height, plain coast and ria coast result in different flow velocities which are not reflected in fragility models using only inundation depth as IM.

Onagawa

Figure 4.17 shows cumulative probability distribution of tsunami losses at three different scales. Figure 4.17 agrees with the results in Section 4.2 that the consideration of flow velocity in addition to inundation depth does not make a significant difference for tsunami loss estimation in Onagawa on ria coast. However, FM6 which considers momentum flux generates a slightly larger tsunami loss. An interesting finding is that compared to inundation depth-based fragility model (FM1), the consideration of flow velocity (FM2) underestimates tsunami loss but the consideration of momentum flux (FM6) overestimates tsunami loss. However, this difference is insignificant, and as seen in Figure 4.15 that the position of zero lines are similar but not identical so that the points can fall above or below them. As can be seen in Figure 4.17, Onagawa tends to experience high inundation depth and low flow velocity, which makes hazard data of buildings fall into this sensitive area in Figure 4.15 where the loss difference may be positive or negative.

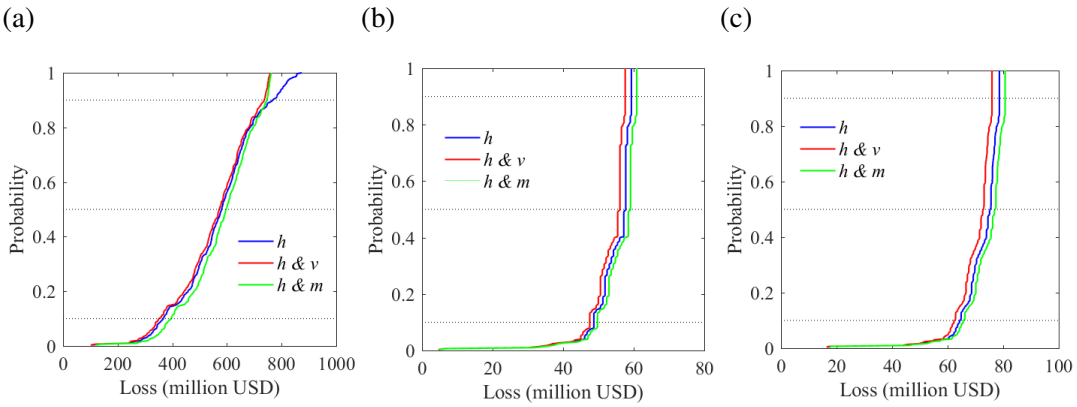

Figure 4.17 Cumulative probability distribution of tsunami losses in Onagawa: (a) whole Onagawa, (b) RC in RR1, and (c) RC structures within 1 km from the coastline.

In conclusion, when inundation depth is very large (e.g. Onagawa experiences +10 m tsunami for a M_w 9.0 tsunami), inundation depth is sufficient to represent the tsunami

intensity for loss estimation. In cases when inundation depth is dominant and flow velocity does not make a significant difference, the use of momentum flux does not improve the damage assessment either. The relative importance of inundation depth and flow velocity is related to the magnitude of events as well as site location and coastal topography.

4.4 Summary and conclusions

In this chapter, to investigate the importance of flow velocity and momentum flux for tsunami loss prediction, losses calculated by using bivariate-IM fragility function were compared with losses estimated by inundation-based fragility with respect to different total losses and spatial distributions. In addition, tsunami fragility functions using momentum flux as additional IM were developed based on the same dataset of the 2011 Tohoku tsunami in a multinomial regression approach, which allows a fair comparison of three IMs (inundation depth, flow velocity, and momentum flux) for tsunami loss estimation. The main conclusions in this chapter are:

- For both plain and ria coasts, RC buildings are the most sensitive structure type to flow velocity, followed by steel and masonry. Wood structures are not sensitive to consideration of velocity for tsunami loss estimation.
- The importance of flow velocity for tsunami mainly depends on the inundation depth and flow velocity combinations at buildings locations. Based on the case study for a M_w 9.0 Tohoku-type tsunami, flow velocity is more important for buildings located close to the sea (e.g. less than 1 km) where flow velocity tends to be higher. For M_w 9.0 tsunamis and buildings close to the sea, the consideration of flow velocity tends to result in higher losses for plain coast while producing slightly lower losses for ria coast.
- The influence of velocity for total tsunami loss at a municipal or community scale, depends on various factors, including spatial distribution of buildings, the main structural types, topography, land elevation, and inundation scale. For relatively low tsunami run-up (i.e. inundation less than 3 m and velocity less than 3 m/s) on plain coast, flow velocity is not important for steel, wood, and masonry structures. However, in certain cases where inundation depth is between 2 m to 5 m and flow

velocity is greater than 3 m/s, flow becomes important and greater differences are caused with the increase of flow velocity.

- The improvement by considering momentum flux is limited in terms of model performance of tsunami fragility function, compared to the inundation-depth-velocity based fragility model. However, for Sendai on plain coast, fragility models based on inundation depth and momentum flux result in more conservative tsunami loss estimation. For Onagawa on ria coast, neither flow velocity nor momentum flux make significant differences for regional tsunami losses. Given the small differences made by either flow velocity or momentum flux and the difficulty in recording them, inundation depth may be the suitable intensity measure for ria coast for a M_w 9.0 tsunami. It is noteworthy that the importance of momentum flux shown by the results in this study is limited to a M_w 9.0 tsunami for two specific building portfolios.

Chapter 5

Multi-Hazard Insurance for Earthquake and Tsunami

Publications resulting from this chapter:
Song, J. and Goda, K. (2019). Influence of elevation data resolution on tsunami loss estimation and insurance rate-making. *Frontiers in Earth Science*, 7(246).

Song, J. and Goda, K. (2019). Insurance rate differentiation of multi-hazard shaking-tsunami loss coverage for subduction earthquakes. In *13th International Conference on Application of Statistics and Probability in Civil Engineering*, Seoul, South Korea.

5.1 Introduction

Tsunamis in the recent decades have caused tremendous loss of lives and economic loss. The unprecedented 2011 Tohoku earthquake and tsunami resulted in more than 19,000 people dead or missing, 128,530 houses destroyed, and 240,332 buildings half-damaged (Kazama and Noda, 2012). The direct economic loss was estimated to be 211 billion USD, exceeding 125 billion USD loss of the Hurricane Katrina (Kajitani et al., 2013). The number of completely destroyed buildings in Miyagi Prefecture, Japan was more than four times those in Iwate Prefecture and Fukushima Prefecture, mainly due to the significantly higher inundation depths experienced in Miyagi Prefecture. The earthquake insurance payout of the 2011 Tohoku event was the largest in history, however, only 36.7 billion USD (about 17% of the total loss) was covered by insurance, which is a small fraction of the total damage cost (Kajitani et al., 2013). The earthquake risk has

been well characterised and quantified for earthquake insurance purposes for decades, while the tsunami risk only started to receive the attention in the insurance market following the devastating consequences of the 2011 Tohoku tsunami. Two of the issues in the current tsunami catastrophe models are: i) the great uncertainty of earthquake occurrence rate is not thoroughly incorporated; and ii) the tsunami catastrophe model is independent of the earthquake catastrophe model without considering the dependency of tsunamis on mega-thrust subduction earthquakes.

Earthquake occurrence is a critical element of probabilistic seismic hazard analysis (PSHA) and probabilistic tsunami hazard analysis (PTHA). Due to the high-consequence low-probability nature of tsunamigenic earthquakes, the recurrence rate has a significant influence on financial tsunami loss estimation. Particularly for mega-thrust subduction earthquakes, there is great uncertainty in the occurrence rate estimation due to the lack of historical inter-event data (Cramer et al., 2000; Abaimov et al., 2008; Garavaglia et al., 2010; Geist and Parsons, 2011; Fitzenz and Nyst, 2015). To characterise such occurrence, a large number of probabilistic earthquake recurrence models are available. The most common choice is a Poisson model. However, its applicability to mega-thrust subduction earthquakes is limited, because it does not account for the distinct physical mechanism and occurrence history of particular faults. In such cases, time-dependent renewal recurrence models are more suitable to large earthquakes originating from specific faults, which takes into account the occurrence history and quasi-periodic behaviour. Popular models for predicting the occurrence rate of future events are renewal processes, and inter-arrival times of recurrent events are often characterised by the exponential, lognormal, Weibull, and Brownian Passage Time (BPT) distributions (Anagnos and Kiremidjian, 1988; Matthews et al., 2002; Lee and Tsai, 2005; González et al., 2006; Sykes and Menke, 2006; see Section 2.2.1). However, due to our limited understanding of earthquake rupture processes, there has not been a consensus as to which model is the most suitable (Ellsworth et al., 1999; Garavaglia et al., 2010). In Japan, the BPT recurrence model is preferred which may underestimate the occurrence rate because it renders nearly zero probability given that the elapsed time is short compared with the mean recurrence period, while using a time-independent Poisson process together with a Gutenberg-Richter (GR) relationship may lead to overestimation of tsunami hazard and risk given that the major event occurred in 2011. In short, the selection of earthquake recurrence models poses great impact on the tsunami risk assessment for the Tohoku region.

Renewal recurrence models can be specified by three parameters: mean return period μ_t, coefficient of variation *cov* which is the standard deviation of inter-event times divided by the mean return period, and the elapsed time T_e. The uncertainty exists in the determination of mean return period and *cov* due to limited historical data. Therefore, to quantify the uncertainty of earthquake recurrence for tsunami risk assessment and the risk range caused by different recurrence models, multiple earthquake recurrence models may need to be implemented by considering a range of possible mean return periods and values of *cov*. With a set of time-dependent recurrence models covering a range of occurrence rates from low to high, this chapter aims to investigate the influence of tsunami occurrence on loss estimation and consequently insurance rate-making.

The consideration of possible earthquake recurrence models for large subduction earthquakes will result in non-zero occurrence rates for some cases. In such cases, seismic risk and tsunami risk for the coastal regions due to large subduction earthquakes cannot be neglected. The coastal region threatened by tsunamis is under seismic risk as well, since the tsunami is usually triggered by large earthquakes in the ocean and thus the ground shaking and tsunami affect the structures in sequence. To put it in another way, a tsunami and the triggering earthquake are coupled events occurring simultaneously, and the final damage should be determined by taking into account cumulative impact due to seismic damage and tsunami damage, rather than the sum of damage caused by ground shaking and tsunami separately (Park et al., 2012). Because a subduction earthquake may or may not trigger a tsunami, tsunamis are usually associated with a longer return period than earthquakes from the same source (Ozawa et al., 2011). Without integrating the effects due to ground shaking and the triggered tsunami as a sequence of events under a multi-hazard framework, the estimated damage and loss may be biased. Moreover, the risks originating from the same source may be evaluated twice separately, and the underlying data, source models, and methodology may not be consistent. This missing link between earthquakes and tsunamis for insurance coverage highlights the importance of integrating both hazards in the multi-hazard framework.

Currently, the tsunami loss is covered by earthquake insurance in Japan according to the General Insurance Rating Organisation of Japan (https://www.giroj.or.jp/ratemaking/earthquake/#kaitei), but buildings with similar seismic risks can have significantly different tsunami risks depending on their locations. Location attributes including distance from the coast, elevation, and topographical features have been demonstrated to have significant influences on local tsunami risk (Chapter 3). Compared to seismic risk,

tsunami risk is more sensitive to building locations in terms of elevation and site-to-coast distance. Besides the structural attributes (material types and structural systems) which have been implemented in some countries (e.g. Japan and the United States) for differentiating earthquake insurance premium rates, the location attributes are particularly important for fair pricing of tsunami insurance premium rates. location attributes are particularly important for fair pricing of tsunami insurance premium rates. Therefore, the effects of two location-specific attributes, site-to-coast distance and land elevation, should be investigated in determining tsunami insurance pure premium rates. Since these location-specific attributes are sensitive to the resolution of DEM (Chapter 3), the influence of DEM resolution on tsunami insurance rate-making shall be explored as well.

This chapter developed a multi-hazard earthquake-tsunami insurance rate-making method by considering ground shaking and the triggered tsunami as a sequence of environmental disturbances from the same event under a multi-hazard framework for earthquake and tsunami (Goda and De Risi, 2018) considering the uncertainty of occurrence rate. The developed method is innovative in two major aspects: i) time-dependent renewal models are adopted for characterising earthquake occurrence, which affect risks of both shaking and tsunami, and ii) for shaking, the effects due to both crustal earthquakes and subduction earthquakes are explicitly taken into account. Because of the novel approaches of the developed multi-hazard model, it can illuminate the relative importance of risk caused by crustal earthquakes, subduction earthquakes, and tsunamis. The latter aspect makes the model and investigations more comprehensive, and facilitates the discussion of determining pure insurance premiums for multi-hazard environments including earthquake-tsunami risks due to mega-thrust subduction earthquakes. To investigate the above mentioned problems, a case study is conducted by focusing on Sendai and Onagawa in Miyagi Prefecture, Japan. The setup for the case study is the same as Chapter 3, based on the same earthquake slip models and tsunami simulation results, with additional consideration of seismic risk.

5.2 Multi-hazard insurance rate-making methodology

To assess earthquake and tsunami risks jointly, three sources of individual hazards contributing to the combined risk are considered: i) non-tsunamigenic earthquakes including crustal earthquakes as well as subduction earthquakes, ii) tsunamigenic earthquakes, and iii) tsunamis . The previous chapters have mainly focused on iii), while the

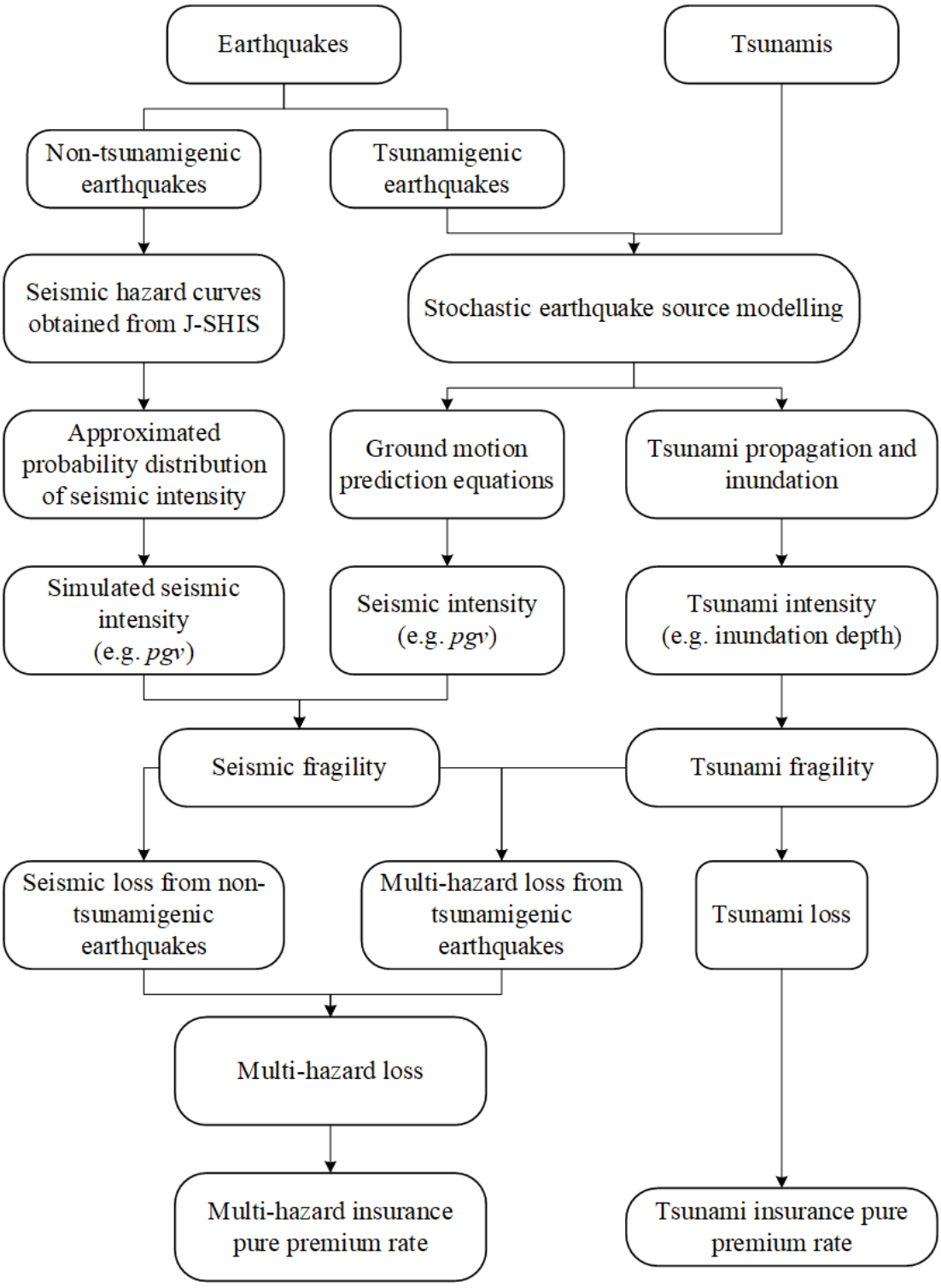

Figure 5.1 Multi-hazard insurance rate-making procedure.

multi-hazard risk method by Goda and De Risi (2018) can take into account ii) and iii), but not i). All three sources can have major influences on insurance premium rates. The

most fundamental composition of insurance premium is the annual average loss (AAL) (Straub, 1988; Grossi and Kunreuther, 2005; Mitchell-Wallace et al., 2017). In the context of insurance rate-making, including risks due to crustal earthquakes is important, especially for active seismic regions where major seismic hazard contributions come from this source.

This chapter extends the regional multi-hazard earthquake-tsunami impact by including all three sources mentioned above. Section 5.2.1 introduces the pure insurance premium rate-making in the context of earthquake and tsunami insurance in Japan. Subsequently, in Section 5.2.2 and Section 5.2.3, risk assessment methods for evaluating shaking-related risks due to non-tsunamigenic and tsunamigenic earthquakes, respectively, are described. The method for multi-hazard loss estimation is explained in Section 5.2.4. Based on the losses from three types of hazards above, the insurance rates can be made not only for earthquakes and tsunamis separately but also for earthquake-tsunami multi-hazard risk jointly. The multi-hazard insurance rate-making procedure is presented in Figure 5.1. In this chapter, the rate-making is carried out for low-rise wood structures because wood houses are the main structural type for residential buildings in Japan and there is a lack of suitable seismic fragility functions for other structure types in Japan.

5.2.1 Pure premium rate-making

Insurance premium is composed of pure premium P_{pure}, risk premium P_{risk}, and transaction fees $P_{expense}$, as shown in Equation (2.13) (Kuzak and Larsen, 2005; Gray and Pitts, 2012; Goda et al., 2014b), but pure premium is focused on in this chapter because it is the most essential component and its quantification relies on catastrophe modelling. P_{pure} is calculated by the annual expected loss:

$$AAL = \int L\nu(L)d\mathrm{L} \tag{5.1}$$

where L is the loss, and $\nu(L)$ is the exceedance probability function of L. In this chapter, P_{pure} is expressed as the rate per 1000 insured values, following industry convention.

According to the General Insurance Rating Organisation of Japan (https://www.giroj.or.jp/ratemaking/earthquake/), the earthquake insurance policy in Japan only covers building damage and loss exceeding 3% of the insured amount for seismic loss and

experiencing inundation depth higher than 45 cm for tsunami loss. Therefore, the deductible $D = 3\%$ is adopted for earthquakes and an inundation depth less than 45 cm is considered to cause no insurance loss for tsunamis (see Section 2.5 for for insurance structure arrangements in terms of deductible, cap, and limit). The value of the insured property is limited to the market value, and thus for typical wood houses, the limit is set to 208,000 USD taking the mean replacement cost as the market value. The coinsurance factor is assumed to be 1.

The current earthquake insurance policy does not differentiate properties having different tsunami risks. In this chapter, the premium rate differentiation for tsunami risks is considered based location attributes (i.e. coastal topography, distance to the coast, and elevation). For this purpose, realistic tsunami modelling is performed using 10-m DEM and stochastic tsunami simulations as the base case. Besides, the effects of DEM resolution (Chapter 3), structural types, and consideration of flow velocity (Chapter 4) on tsunami insurance rate-making are also investigated in this chapter.

5.2.2 Seismic hazard from non-tsunamigenic earthquakes

For integrated earthquake-tsunami risk assessments, crustal earthquakes and non-tsunamigenic subduction earthquakes can be grouped as non-tsunamigenic earthquakes. Since the probabilistic seismic hazard assessment of crustal earthquakes is not the main focus of this study, up-to-date earthquake hazard information, which is available from the Japan Seismic Hazard Information Station (J-SHIS) (http://www.j-shis.bosai.go.jp/en/), is considered. The J-SHIS provides national seismic hazard maps that are also used for determining the current earthquake insurance rates in Japan. This consideration allows us to make a fair comparison with the extended multi-hazard risk model that is developed in this chapter.

A wide range of earthquake information including earthquake occurrence models for rupture sources, site conditions, site-specific siemic hazard curves, and disaggregation results can be accessed from the J-SHIS. The hazard information is provided at 250-m resolution. The J-SHIS offers the options of expressing site-specific seismic hazard curves in terms of probability in 30 years or 50 years. The hazard curves can be converted to annual probability basis, which is more relevant for insurance premium calculations. A hazard curve obtained from the J-SHIS gives a relationship between

annual occurrence frequency and peak ground velocity v_b at basement/engineering bedrock. The site amplification factor is provided to obtain the peak ground velocity *pgv* on the ground surface. It is noted that in the J-SHIS there are multiple options for seismic IMs (e.g. peak ground acceleration, peak ground displacement, and spectral response acceleration). In this work, *pgv* is selected as the IM because it is commonly used in empirical seismic fragility curves in Japan (Yamaguchi and Yamazaki, 2001; Midorikawa et al., 2011; Wu et al., 2016). Since seismic hazard values calculated by the J-SHIS do not vary over short distances (less than a few kilometres), the coastal region of a city can be represented by a single seismic hazard curve. Therefore, representative seismic hazard curves are adopted from the J-SHIS database for the two locations in Sendai (latitude 38.23° and longitude 140.97°) and Onagawa (latitude 38.44° and longitude 141.45°). To adjust generic rock-site hazard curves to local site conditions, typical site simplification factors of 2 and 1.47 are applied for Sendai and Onagawa, respectively, according to the J-SHIS.

Although a full probabilistic seismic hazard assessment is preferred for given building portfolios, it is beyond the scope and focus of this chapter. Given the limitations, a random sampling is a valid approach if a hazard curve at a site of interest, which corresponds to long return period levels, can be represented by a theoretical probability distribution in the upper tail (e.g. extreme value distributions). The method uses a probability paper plot of a seismic hazard curve to identify a suitable probability distribution. Typical hazard curves of Sendai and Onagawa can be fitted using one of three types of probability distributions: lognormal, Gumbel, and Weibull. On the probability paper, the horizontal axis for the lognormal and Weibull distributions correspond to $\ln(v_b)$, while that for the Gumbel distributions is v_b, as expressed in Table 5.1.

Table 5.1 Probability distributions to fit J-SHIS seismic hazard curves.

	Probability distribution	x axis	y axis
Lognormal	$\ln v_b = \sigma\Phi^{-1}(1-P)+\mu$	$\ln v_b$	$\Phi^{-1}(1-P)$
Gumbel	$v_b = -\beta\ln(-\ln(1-P))+\gamma$	v_b	$\ln(-\ln(1-P))$
Weibull	$\ln(-\ln P) = \kappa\ln v_b - \kappa\ln\zeta$	$\ln v_b$	$\ln(-\ln P)$

In the table, P refers to exceedance probability; μ and σ are the mean and standard deviation, respectively; ζ and κ are the scale and shape parameters of the Weibull distribution, respectively; and β and γ are the scale and location parameters of the

Gumbel distribution, respectively.

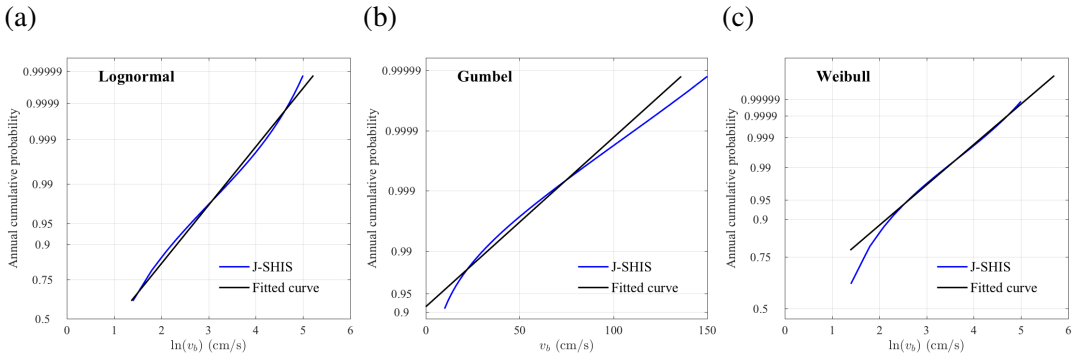

Figure 5.2 Probability paper plots of base-rock peak ground velocity v_b in Onagawa: (a) lognormal distribution, (b) Gumbel distribution, and (c) Weibull distribution.

To approximate the seismic hazard curves for non-tsunamigenic earthquakes, a suitable distribution with the best fitting is selected by focusing upon a velocity range between 50 cm/s and 150 cm/s (in natural logarithmic scale, they correspond to 3.91 cm/s and 5.01 cm/s). This range corresponds to the cases where major structural damage tend to be caused by ground shaking for Japanese buildings (Yamaguchi and Yamazaki, 2001; Midorikawa et al., 2011; Wu et al., 2016). A goodness-of-fit diagnostic analysis can be carried to select the best fitting, but in this case, the Weibull visually showed the best fitting without formal tests. Figure 5.2 shows the simulated base-rock *pgv* curves for three distribution models in comparison with the hazard curve for Onagawa obtained from the J-SHIS. Therefore, v_b for non-tsunamigenic earthquakes is simulated based on the Weibull distribution. The same fitting is carried out for a typical hazard curve for a coastal region in Sendai as well. Because Sendai and Onagawa are relatively close and affected by similar seismic sources, seismic hazard curves are similar for the two locations; the curve fitting is similar to Onagawa with the Weibull distribution as the best theoretical model. The obtained parameters for three distributions are listed in Table 5.2.

Table 5.2 Obtained parameters for the lognormal, Gumbel, and Weibull distributions to fit J-SHIS hazard curves.

	Lognormal	Gumbel	Weibull
Sendai	$\mu = 1.1574$; $\sigma = 0.8765$	$\beta = 12.9618$; $\gamma = -32.9917$	$\zeta = 1.7934$; $\kappa = 0.5735$
Onagawa	$\mu = 1.0595$; $\sigma = 0.9916$	$\beta = 15.4685$; $\gamma = -38.3174$	$\zeta = 1.8443$; $\kappa = 0.5421$

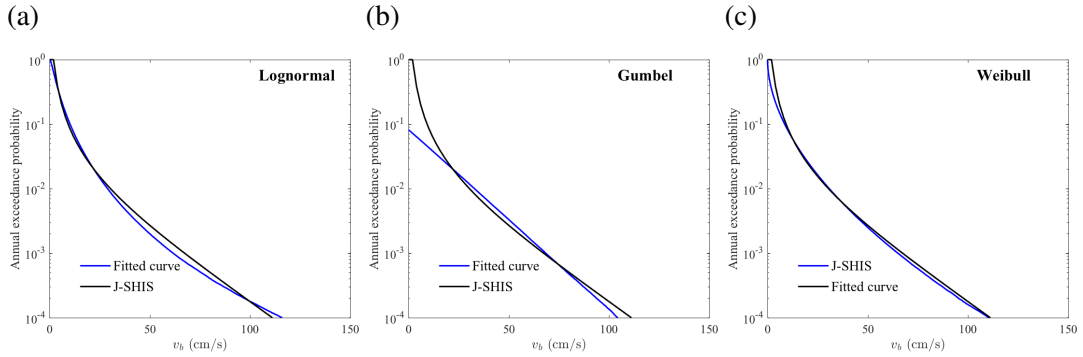

Figure 5.3 Simulated v_b in Onagawa fit to probability distributions: (a) simulated v_b fit to lognormal distribution, (b) simulated v_b fit to Gumbel distribution, and (c) simulated v_b fit to Weibull distribution.

5.2.3 Seismic hazard from tsunamigenic subduction earthquakes

The seismic hazard is assessed using stochastic earthquake source models, which predict earthquake rupture parameters based on scaling relationships given an earthquake magnitude. The method is the same as in Chapter 3. The stochastic source models take into account not only uncertainty in term of location and geometry of the fault plane but also uncertainty in spatial slip distribution. In Chapter 3, it has been demonstrated that the stochastic earthquake slip is of critical importance in performing tsunami risk assessments.

In this chapter, Tohoku-type earthquakes having multiple magnitudes ranging from 8.1 to 9.1 are considered, classified into 5 bins with an interval of 0.2 magnitude units, representing by M_w 8.2, M_w 8.4, M_w 8.6, M_w 8.8, and M_w 9.0 (as central values). It is important to note that in the J-SHIS seismic hazard curves (Section 5.2.2), earthquakes with magnitudes in this range are represented by the M_w 9.0 Tohoku-type earthquake but assigned occurrence models for these earthquakes are the BPT models with cov = 0.25; consequently, seismic hazard contributions from the large subduction events off the Tohoku coast are considered to be negligible (see Section 2.2.1).

The seismic intensity for tsunamigenic subduction earthquakes is simulated using ground motion prediction equations (GMPE) by Si and Midorikawa (1999) and Morikawa and Fujiwara (2013). The former is selected as it is commonly used for earthquake risk assessments in Japan; thus a fair comparison with the standard insurance rate in Japan can be made by using this GMPE. On the other hand, the latter is more suitable for interface subduction earthquakes, such as the 2011 Tohoku earthquake

because it was developed using the data from the 2011 Tohoku earthquake. The GMPE by Si and Midorikawa (1999) is given by Equation (5.2).

$$\log_{10}(pgv) = 0.58\min(M_w, 8.2) + 0.0038D - \log_{10}(R_{rup} + 0.0028 \times 10^{0.5\min(M_w,8.2)}) - 0.002R_{rup} - 1.31 + \varepsilon \quad (5.2)$$

where $\log_{10}$ is the base-10 logarithm, R_{rup} is the fault distance in km, D is the focal depth in km, and ε is the prediction error term with zero mean and a standard deviation of 0.23. No distinction of the predictor error term is made for intra-event and inter-event variability. The lack of underlying ground motion data for events having magnitudes greater than 8.2 leads to potential bias in applying this model to larger earthquakes. As a result, among different slip models having different magnitudes, pgv is mainly influenced by fault distance and focal depth. The GMPE by Si and Midorikawa (1999) was developed for stiff ground (engineering bedrock), and a site amplification factor AF was provided for soil ground as a function of average shear-wave velocity in the upper 30-m V_{s30}, as shown in Equation (5.3).

$$\log_{10}(AF) = 1.83 - 0.66\log_{10}(V_{s30}) \quad (5.3)$$

The values of V_{s30} at 250-m resolution are obtained from the J-SHIS. On the other hand, the GMPE by Morikawa and Fujiwara (2013) is expressed as:

$$\log_{10}(pgv) = -0.0325\left(\min(M_w, 8.2) - 16\right)^2 - 0.002408R_{rup} + 5.6026 - \log_{10}\left(R_{rup} + 0.002266 \times 10^{0.5\min(M_w,8.2)}\right) + G_d + G_s + AI + \varepsilon \quad (5.4)$$

where G_d, G_s, and AI are the site correction terms for amplification by deep sedimentary layers, amplification by shallow soft soils, and anomalous seismic intensity distribution, respectively. In this thesis, only G_s is considered, which is given by:

$$\log_{10}(G_s) = -0.5546\log_{10}\left(\frac{\min(V_{s30}, 1100)}{350}\right) \quad (5.5)$$

Due to the significant uncertainty in predicting the return period of infrequent large earthquakes, a preliminary comparison of non-tsunamigenic seismic hazard and tsunamigenic seismic hazard is based on the Poisson temporal process and the regional GR earthquake occurrence relationship for the Tohoku region (Chapter 3). The GR rela-

tionship indicates that the annual rate of earthquakes larger than M_w 8.1 is approximately 0.02, which is equivalent to a return period of 50 years. The occurrence rate estimated by the Poisson-GR model is more conservative than that given by time-dependent renewal occurrence models for the Tohoku region, because the constant occurrence rate given by the Poison model is higher than the rates predicted by the renewal models (note: the elapsed time since the last event in 2011 is short with respect to the mean recurrence period of the mega-thrust events in the Tohoku region; see Figure 2.2 for the comparison of different earthquake recurrence models).

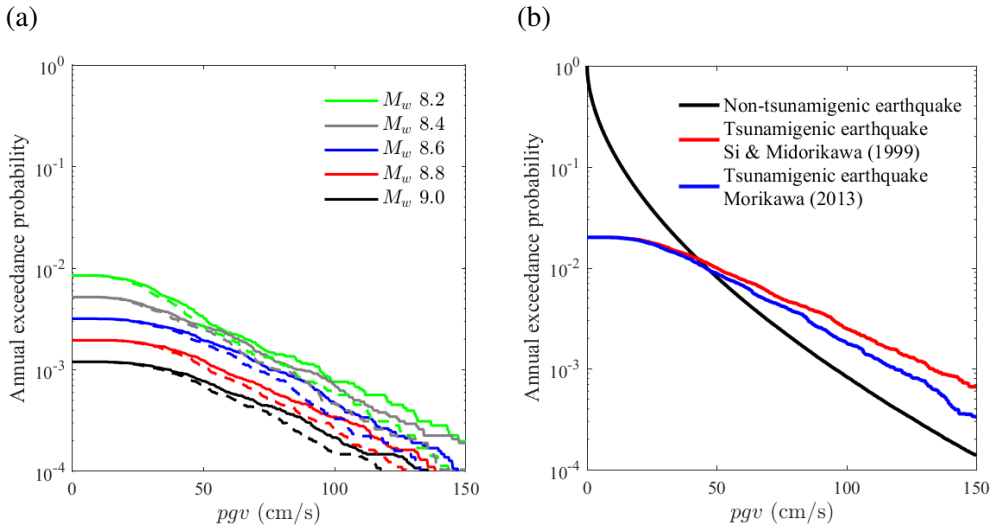

Figure 5.4 Seismic hazard curves of Onagawa: (a) Annual exceedance probability curves of *pgv* for different magnitudes using GMPEs by Si and Midorikawa (1999) (solid lines) and Morikawa and Fujiwara (2013) (dashed lines) and (b) Comparision of annual exceedance probablity curves of non-tsunamigenic earthquakes and tsunamigenic earthquakes.

Figure 5.4a shows *pgv* exceedance probability curves for different magnitude ranges and the corresponding annual probability using the occurrence rate for each magnitude range is obtained from the regional GR relationship (see Section 3.2.1). In comparing the seismic hazard curve for crustal earthquakes (obtained from the J-SHIS) and that for the subduction earthquakes, a critical return period can be identified as a point when the latter exceeds the former. It corresponds to *pgv* of about 50 cm/s or greater (see Figure 5.4). The hazard curves for large subduction events tend to exceed the hazards at higher *pgv* values. As can be seen in Figure 5.4a that the shapes of *pgv* curves of different magnitudes are similar (but starting at different probability levels). This is because the magnitude is capped at 8.2 due to the limitation of data used to develop

the GMPEs and magnitude saturation (see Equation (5.2) and Equation (5.4)). It is important to note that in the current J-SHIS hazard maps, the intermediate magnitudes between M_w 8.4 to M_w 8.9 are not considered and the Tohoku-type subduction earthquake is modelled as a characteristic event having the mean occurrence of 600 years with the BPT recurrence model. This leads to a small occurrence probability for M_w 9.0 events, and thus this scenario does not contribute to the overall hazard in Sendai and Onagawa. This highlights the importance of earthquake occurrence modelling.

However, seismotectonic conditions of the Tohoku region after the most recent 2011 event still may be in transition between strain relaxation and accumulation stages of a subduction cycle as the aftershocks are still active (Zakharova et al., 2017), and the duration of aftershocks influences the earthquake occurrence rates (Toda and Stein, 2018). Moreover, the recording period is generally short compared to the long return period of such mega-thrust subduction earthquakes, and the fitted magnitude-recurrence model should be considered carefully (Kagan and Jackson, 2013) Therefore, it is debatable which recurrence model is the most suitable for future mega-thrust subduction earthquakes off the Tohoku region. Under this working hypothesis, multiple earthquake occurrence models will be used to investigate the sensitivity of the seismic-tsunami hazard and risk assessments (Section 5.3). The investigation of the occurrence rate of the Tohoku-type mega-thrust subduction earthquakes is beyond the scope of this thesis.

5.2.4 Multi-hazard loss calculation

Losses caused by ground shaking and tsunamis are calculated by employing seismic fragility and tsunami fragility models, respectively. Tsunami damage and loss are calculated by fragility models developed by De Risi et al. (2017) which allow the consideration of flow velocity as tsunami intensity measure in addition to inundation depth. For shaking-related loss, three empirical seismic fragility models for low-rise wood buildings in Japan are applied, which are developed by Yamaguchi and Yamazaki (2001), Midorikawa et al. (2011), and Wu et al. (2016) and are shown in Figure 5.5. The first and the third models are based on damage data from the 1995 Kobe earthquake and the 2011 Tohoku earthquake, respectively, while the second one employs damage data of earthquakes that occurred between the two major events. *pgv* is used by all three models as seismic intensity measure. The damage states are defined as: partial damage (DS1), half collapse (DS2), and total collapse (DS3), which are consistent with

the standard post-earthquake damage survey procedure in Japan. Note the damage state definition for earthquakes is different from that for tsunamis (see Section 2.4). The corresponding damage ratios are assigned as: 0.03-0.2, 0.2-0.5, and 0.5-1.0 (Kusaka et al., 2015).

Given both seismic and tsunami hazard intensity parameters, the probabilistic earthquake-tsunami risk assessment can be expressed as an extension of Equation (3.1) in Chapter 3. Given the building portfolio, the probabilistic loss of the ith building/property is L_i. The seismic risk assessment and tsunami risk assessment are carried out given the same earthquake rupture source models, and the earthquake-tsunami risk is obtained by:

$$L_i = \max(SL_i, TL_i) \tag{5.6}$$

where SL_i and TL_i correspond to seismic loss and tsunami loss of the ith location, respectively.

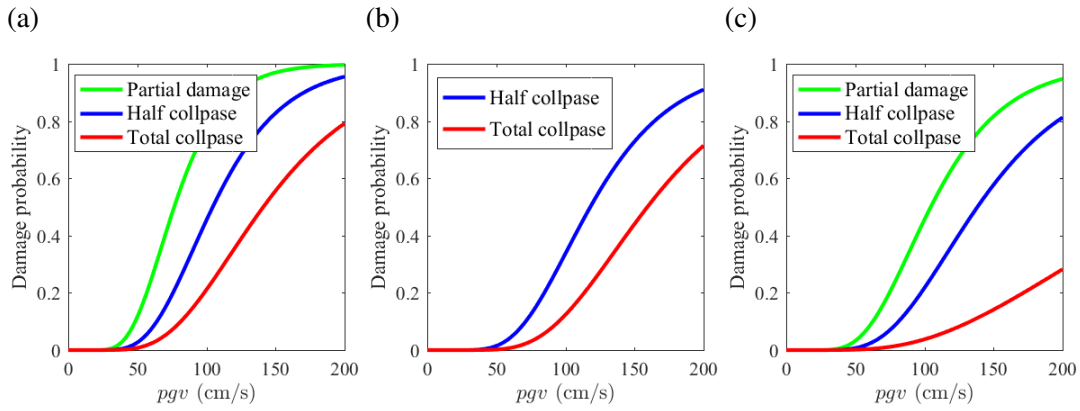

Figure 5.5 Seismic fragility curves: (a) Yamaguchi and Yamazaki (2001), (b) Midorikawa et al. (2011), and (c) Wu et al. (2016).

Table 5.3 Engineering damage ratios compared to insurance payout ratios.

Engineering damage	Actual loss	Payout	Modified payout
Partial damage: 0.03-0.2	Partial loss: 0.03-0.2	0.05	Partial loss: 0.05
Half collapse: 0.2-0.5	Small half loss: 0.2-0.4	0.3	Half loss: 0.45
	Large half loss: 0.4-0.5	0.6	
Total collapse: 0.5-1.0	Total loss: 0.5-1.0	1.0	Total loss: 1.0

The earthquake insurance claim/payout ratio (percentage of the insured amount) in Japan is different from the damage ratios that are based on engineering judgement of incurred structural damage, as shown in Table 5.3. For the payment of insurance claims that are related to the ratio of actual loss to the value of the property, there are four damage states (one more damage state than the engineering damage states): partial loss, small half loss, large half loss, and total loss, and the corresponding damage ratios are: 0.03-0.2, 0.2-0.4, 0.4-0.5, and 0.5-1.0, which are obtained from the Ministry of Finance, Japan (https://www.mof.go.jp/english/financial_system/earthquake_insurance/outline_of_earthquake_insurance.html#04). The corresponding payments for claims are 5%, 30%, 60%, and 100% of the insured amount which is limited to the market value, respectively. The damage state of an insured property is determined based on the actual loss ratio, and the insurance payout ratio is fixed for each damage state. To calculate the seismic loss using seismic fragility based on payout ratios and compare it to earthquake loss using engineering damage ratios, the damage states for small half loss and large half loss are combined as one damage state of half loss, with a damage ratio of 0.2-0.5, and the claim payment is set to 45% of the insured value (mean of the payout ratios these damage states). In this way, the damage ratios for insurance claims are consistent with the engineering damage states. In summary, a damage ratio of 0.03-0.2 corresponds to a payout ratio of 0.05; a damage ratio of 0.2-0.5 corresponds to a claim ratio of 0.45; and a damage ratio of 0.5-1.0 corresponds to a claim ratio of 1.0. Note that the claim payment ratios of DS2 and DS3 (i.e. 0.45 and 1.0) are higher than the mean engineering damage ratios (i.e. 0.35 and 0.75), while the claim payment ratio of DS1 (i.e. 0.05) is lower than the mean engineering damage ratio (i.e. 0.115).

A comparison of annual EP curves for a wood house at location P1 (see Section 3.3.2 and Figure 3.7) in Sendai using engineering damage ratios and insurance payout ratios can be found in Figure 5.6. The occurrence rates estimated by the GR relationships for the off-Tohoku region as obtained in Section 3.2.1 are used for tsunamigenic earthquakes. The differences of the two curves are related to how claim values are computed using the uniform damage ratio scheme or the fixed damage ratio scheme for the engineering damage and claim payment, respectively. Based on the results shown in Figure 5.6, the insurance pure premium rate for non-tsunamigenic earthquakes is calculated as 1.055 per 1000 insured value using the engineering damage ratios and is 0.9365 per 1000 insured value for the claim payment ratios; the rates for tsunamigenic earthquakes are 0.6655 and 0.6143 per 1000 insured values using the engineering damage ratios and claim payment ratios, respectively. The differences between the rates using the engineer-

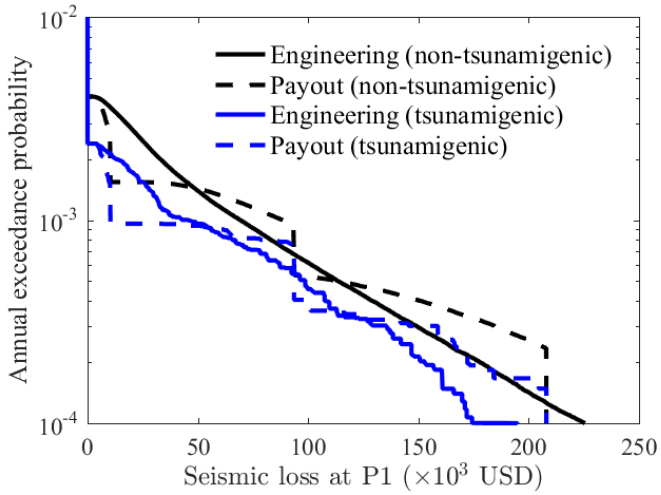

Figure 5.6 Seismic EP curve using engineering damage ratios and insurance claim ratios.

ing damage ratios and claim damage ratios are relatively small (around 10%). In this study, the engineering damage ratio is used. The calculated insurance rates are lower than the earthquake insurance standard rate for wood structures in Miyagi, Japan, which is 1.97 per 1000 value according to General Insurance Rating Organisation of Japan (https://www.giroj.or.jp/ratemaking/earthquake/pdf/201706_table.pdf#view=fitV), because risk premium and expenses are not included in the above-mentioned calculated rates. In this study and the seismic hazard assessment methods are not the same.

5.3 Influence of earthquake recurrence models

Estimating recurrence rates of mega-thrust subduction earthquakes involves significant uncertainty because the instrumental catalogues are usually too short to include more than a few large-magnitude events from a particular fault/zone (Fitzenz and Nyst, 2015). The recurrence rate makes significant differences in loss estimation. When estimating the recurrence rate of a specific event, a decision needs to be made with regard to whether to adopt a time-independent Poisson model or time-dependent renewal model. A Poisson temporal process assumes that earthquake events occur randomly in time and the occurrence of subsequent events is not influenced by previous events. Renewal recurrence models have been widely used to characterise the long-term recurrence behaviour for specific faults (Ellsworth et al., 1999; Cramer et al., 2000; Gomberg et al., 2005; Abaimov et al., 2008; Fitzenz and Nyst, 2015). There is substantial uncertainty

associated with the earthquake occurrence rate, and the occurrence rates predicted by different recurrence models are dramatically varied. This section intends to quantify the uncertainty due to selection of earthquake occurrence models and how they influence the relative importance of tsunamigenic events compared to non-tsunamigenic earthquakes. Subsequently, based on a set of earthquake recurrence models which give occurrence rates from low to high, the influence of recurrence model on tsunami loss estimation are investigated (Section 5.3.3 and Section 5.4).

5.3.1 Recurrence models considering multiple magnitudes

To explore various possibilities, four inter-arrival time distribution models (i.e. exponential, lognormal, Weibull, and BPT) are applied with different values of μ_T and *cov*, and a range of tsunamigenic earthquake magnitudes are considered. Although earthquakes of M_w 7.6 to 8.1 may cause tsunamis, it is considered that at regional scale inundation is relatively small and the loss is dominated by seismic loss (Goda and De Risi, 2018). Therefore, the tsunami loss due to subduction earthquakes smaller than M_w 8.1 is neglected off the Tohoku region. To account for the possibility of different earthquake magnitudes, five discrete magnitudes from 8.2 to 9.0 are considered with an interval of 0.2, i.e. 8.2, 8.4, 8.6, 8.8, and 9.0. To consider the uncertainty in recurrence models, six cases in terms of return period and probability of different magnitude are set up, as presented in Table 5.4. Cases 1 to 3 consider the characteristic-type magnitude model where only one extreme magnitude 9.0 is considered. In these three cases, the mean return periods of 400, 600, and 800 years are considered. Case 2 is consistent with the current J-SHIS model for the off-shore Tohoku mega-thrust subduction earthquakes. Cases 4 to 6 correspond to the GR-type magnitude model, which accommodate a range of magnitudes for the off-shore Tohoku region. The probability distributions of multiple-magnitude models for the off-shore Tohoku region are shown in Figure 5.7.

Three values of *cov* are considered for the characteristic magnitude cases: 0.25, 0.5, and 0.7. When the elapsed time is small (e.g. only 8 years after the 2011 Tohoku event), using a smaller μ_t and larger *cov* leads to a higher earthquake occurrence rate (see Figure 2.2). Note that the exponential distribution is a special case when $cov = 1$ for the Weibull distribution. For each case in Table 5.4, three values of *cov* are considered. Therefore, there are 6 cases for the exponential model, and 18 models for the log-normal,

Table 5.4 Cases given different combinations of return periods and magnitude conditional probabilities.

Case	μ_t (years)	Seismic moment release rate ($\times 10^{19}$ Nm/year)	Probability mass				
			M_w 8.2	M_w 8.4	M_w 8.6	M_w 8.8	M_w9.0
1	400	9.95	0	0	0	0	1
2	600	6.64	0	0	0	0	1
3	800	4.98	0	0	0	0	1
4	50	16.57	0.4241	0.2596	0.1590	0.0975	0.0598
5	75	11.45	0.4100	0.2587	0.1621	0.1030	0.0650
6	100	8.59	0.4100	0.2587	0.1590	0.1030	0.0650

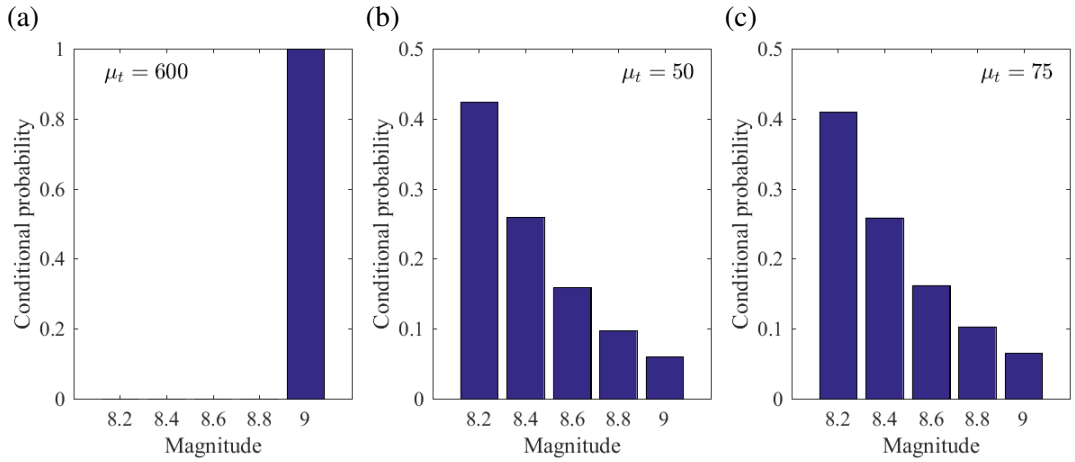

Figure 5.7 Conditional probability distribution of earthquake magnitude for the off-shore Tohoku region: (a) $\mu_t = 600$, (b) $\mu_t = 50$, (c) $\mu_t = 75$.

Weibull and BPT models, respectively.

To compare the energy release of different occurrence models, Table 5.4 also includes the seismic moment release rate for each model, which is the seismic moment over return period. (Frohlich and Wetzel, 2007). The seismic moment M_o (in dyn cm) is calculated by Equation (5.7) (Hanks and Kanamori, 1979):

$$\log M_o = 1.5M_w + 16.1 \tag{5.7}$$

Related to this, it is useful to mention that seismic moments of the 2011 Tohoku earthquake by different inversion-based slip models are estimated in a range of 3.6 - 5.8 $\times 10^{22}$ Nm (Ammon et al., 2011; Fujii et al., 2011; Hayes, 2011; Shao et al., 2011; Yamazaki et al., 2011; Gusman et al., 2012; Iinuma et al., 2012; Satake et al., 2013) . Assuming the return period is 600 years, it is equivalent to the seismic moment release

rate of 6.0 - 9.7 $\times 10^{19}$ Nm/year.

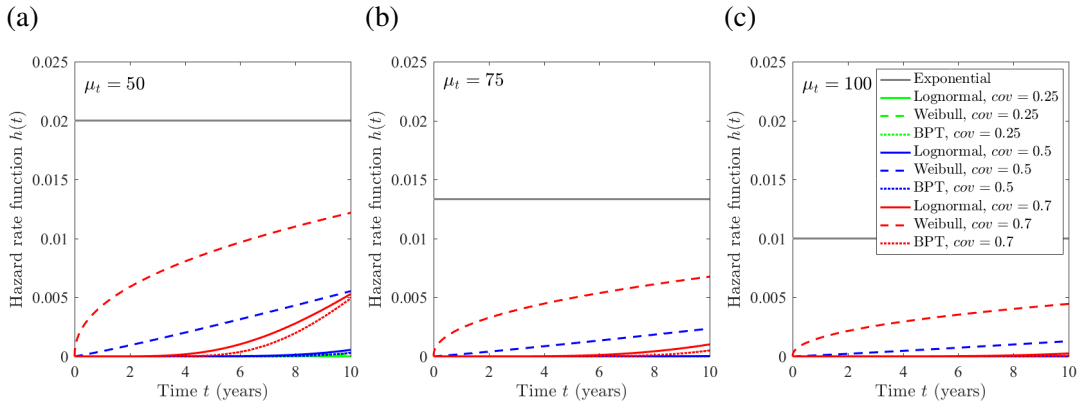

Figure 5.8 Hazard rate functions using different renewal models: (a) μ_t = 50, (b) μ_t = 75, and (c) μ_t = 100.

For the four considered recurrence models (i.e. exponential, lognormal, Weibull, and BPT), the hazard rates (see Section 2.2.1) when the mean return period is 50, 75, and 100 years, are compared in Figure 5.8. The hazard rates given by the exponential model is constant and significantly higher than those renewal models for the period range of less than 10 years. Given the same μ_t and *cov*, the BPT gives the lowest estimate of occurrence rates for a short elapsed time (e.g. 8 years). The rates obtained from the lognormal distribution is similar to those of the BPT but slightly higher, while the Weibull distribution gives significantly higher hazard rates. With the same return period, a higher *cov* results in higher rates in the early phase of therecurrence process. Given the short elapsed time after the 2011 Tohoku event, for any distribution model, a higher *cov* leads to a higher occurrence rate. Taking the Weibull distribution for example, for a situation of $\mu_t = 50$ and $T_e = 8$, the hazard rate based on $cov = 0.7$ is twice as large as the rate based on $cov = 0.5$.

5.3.2 Renewal earthquake occurrence simulation and time-dependent tsunami loss estimation

A procedure of simulating the inter-arrival times of earthquakes based on a renewal model is illustrated in Figure 5.9. Assume that the insurance term length is one year and the duration T_d is one year. The elapsed time T_e is set to 8 years. Given a renewal recurrence model, inter-arrival times can be simulated. The simulation is carried out for

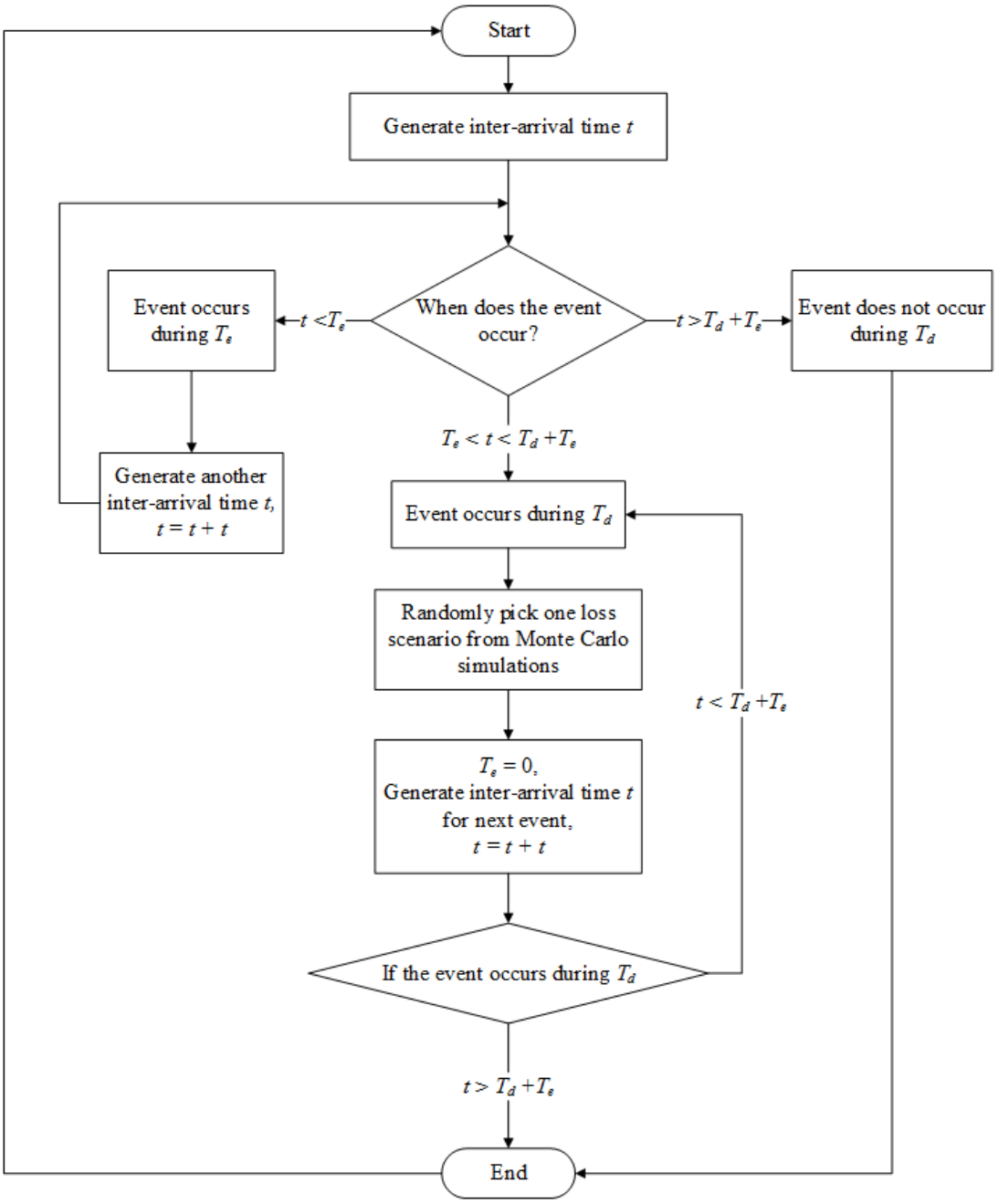

Figure 5.9 Procedures to simulate the occurrence time of earthquakes.

a sufficiently large number of times (e.g. 10^7 times). The inter-arrival time is generated and accumulated until it is longer than the elapsed time T_e. If the event occurs during the evaluation period of time T_d, a loss scenario is randomly picked from the results obtained from Monte Carlo simulations (applicable to both seismic and tsunami losses), and the generation of inter-arrival time is repeated until the accumulated time is longer than $T_e + T_d$. If the event occurs later than T_d, it means that it does not occur during T_d,

and the next simulation will start. The events after the first event occurring during T_d are simulated with the updated $T_e = 0$. If the event occurs during T_d, one earthquake scenario is picked randomly from the Monte Carlo simulations, which includes hazard and risk results of both earthquake and tsunami caused by this slip model. The simulated hazard/risk values are sorted to construct the annual exceeding probability (EP) curves.

The inter-arrival time to the next event by occurrence models of four probability distributions can be simulated by equations in Table 5.5 (see Section 2.2.1 for the probability density functions and cumulative distribution functions of the inter-arrival time models). u is a random sample from the standard uniform distribution; μ and σ are the mean and standard deviation of normal distribution of $\ln t$; $\sigma = \sqrt{\ln(1+cov^2)}$ and $\mu = \ln \mu_t - \sigma$; Φ^{-1} is the inverse of the standard normal cumulative distribution; ζ is the scale parameter and κ is the shape parameter of the Weibull distribution, i.e. $\zeta = \mu_t/\Gamma(1+1/\kappa)$, and $cov = \sqrt{\Gamma(1+1/\kappa)/\Gamma(1+1/\kappa)^2 - 1}$; and u_n is a random sample from the standard normal distribution.

Table 5.5 Inter-arrival time given by different probability distributions.

Exponential	$t = -\mu_t \ln(1-u)$
Lognormal	$t = \exp\left(\sigma\Phi^{-1}\left(F_{(T_e)} + u_{(0,1)}(1-F_{(T_e)})\right) + \mu_t\right) - T_e$
Weibull	$t = \zeta\left(-\ln(1-u_{(0,1)}(1-F_{(T_e)}) - F_{(T_e)})\right)^{\frac{1}{\kappa}} - T_e$
BPT	let $t_1 = \mu_t + \frac{1}{2}\mu_t cov^2 u_n^2 - \frac{covu_n}{2}\sqrt{4\mu_t^2 + \mu_t^2 cov^2 u_n^2}$
	$t = \begin{cases} t_1 - T_e & u < \frac{\mu_t}{\mu_t + t_1} \\ \mu_t^2/t_1 - T_e & u \geq \frac{\mu_t}{\mu_t + t_1} \end{cases}$

5.3.3 Evaluation of earthquake recurrence models

The earthquake recurrence model has a direct influence on the relative importance of tsunamigenic earthquakes compared to non-tsunamigenic earthquakes. Recurrence models based on four probability distributions with different values of μ_t and cov are applied to probabilistic seismic hazard assessment for tsunamigenic earthquakes. In evaluating the hazard levels given by different recurrence models, probabilistic hazard

curves at a representative location of the building portfolio with a typical site condition are compared with seismic hazard curves obtained from the J-SHIS. To facilitate the investigation about the influence of earthquake recurrence model on tsunami loss estimation, a set of recurrence models are applied which give a wide range of occurrence rates from low to high. These models are selected by evaluating the resulted seismic hazard from tsunamigenic earthquakes compared to that from non-tsunamigenic earthquakes. Note that probability of another Tohoku earthquake is nearly zero based on the J-SHIS by using the BPT distribution with $\mu_t = 600$ and $cov = 0.25$. Therefore, the hazard curves by the J-SHIS can be taken as for non-tsunamigenic earthquakes. Seismic hazard intensity due to subduction earthquakes are obtained from 300 stochastic earthquake simulations using GMPE by Morikawa and Fujiwara (2013), for M_w 8.2, M_w 8.4, M_w 8.6, M_w 8.8, and M_w 9.0, respectively. *pgv* is taken as the seismic intensity measure by both the J-SHIS and Morikawa and Fujiwara (2013).

The *pgv* curves for tsunamigenic earthquakes based on the four probability distributions considering different values of μ_t and *cov* are shown in Figure 5.10 and Figure 5.11 for Sendai and Onagawa, respectively, and are compared to the *pgv* curve of non-tsunamigenic earthquakes. Cases with different μ_t and magnitude distributions are distinguished by different colours and *cov* is represented by different types of lines. For the exponential model, the red line corresponding to the return period of 50 years is equivalent to using the regional GR relationship obtained in Section 5.3.1, which is too conservative as indicated by Figure 5.8. Cases of $cov = 0.7$ are not presented because the resulted seismic hazard is significantly higher than the cases of $cov = 0.5$, exceeding the hazard of non-tsunamigenc earthquakes. The curves move down with the increase of μ_t. For M_w 9.0 events only with μ_t of 400 to 800 years (Cases 1-3), the hazard curves lie below the hazard curve of nontsunamigenic earthquakes. The overestimation of seismic hazard by the exponential model is due to the significantly higher occurrence rates, as the *pgv* curves of tsunamigenic earthquakes still exceed that of non-tsunamigenic earthquakes for *pgv* greater than 50 cm/s, even when the return period of M_w 8.1+ events is 100 years (Case 6) for Onagawa. Given the exponential distribution and Case 6, the return period of M_w 9.0 is greater than 1500 years, which is longer than return periods estimated by seismological studies in Japan.

Sendai has lower seismic risk from subduction earthquakes than Onagawa, because it is farther from the fault plane. As a result, when the most conservative exponential models are used, the hazard curves for Sendai all fall below the curve of non-tsunamigenic

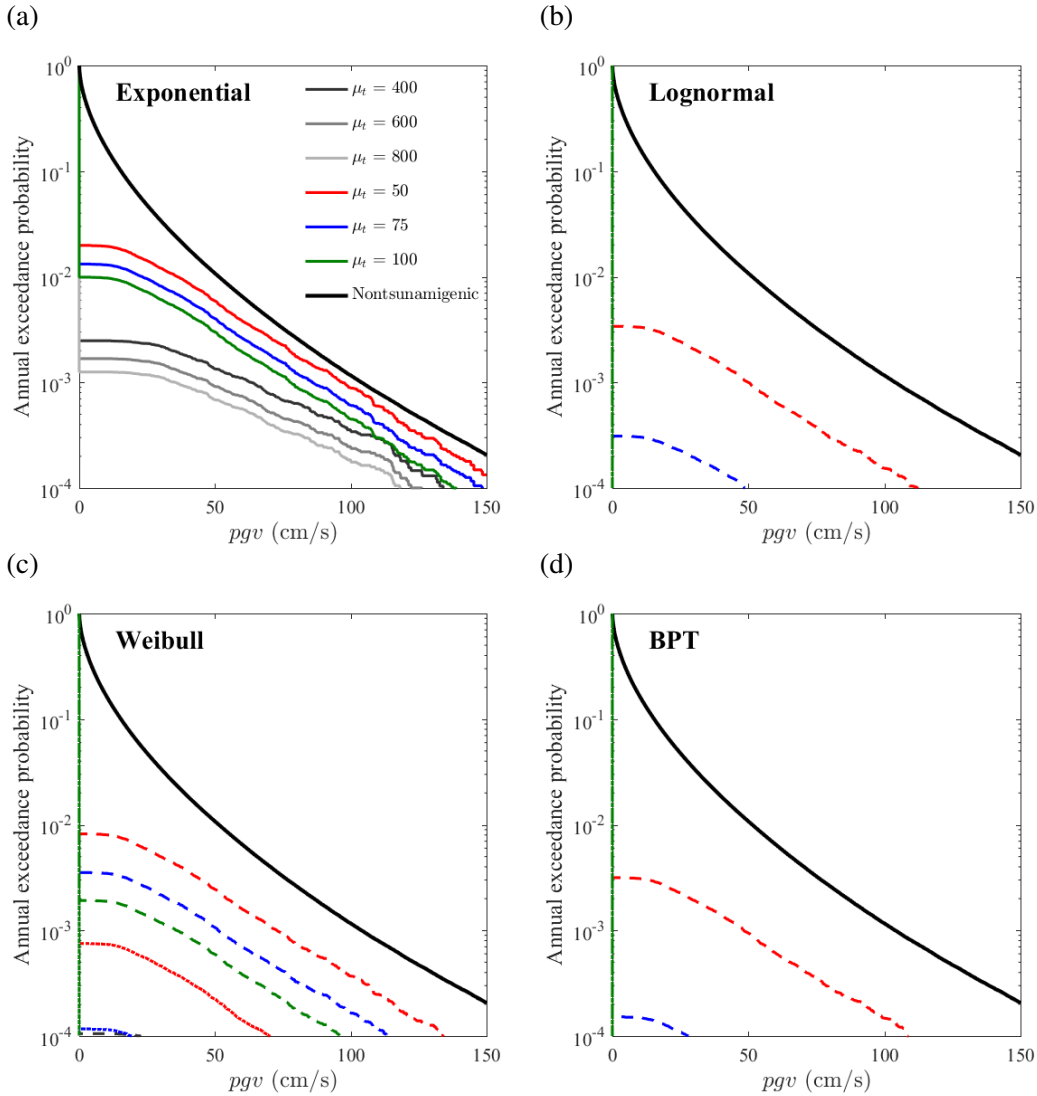

Figure 5.10 Seismic hazard curves of tsunamigenic earthquakes in Sendai based on different earthquake occurrence models using different cases of μ_t and *cov* combinations (dotted lines for $cov = 0.25$, dashed lines for $cov = 0.5$).

earthquakes, while the curves for Onagawa which consider the possibility of multiple magnitudes intersect with the non-tsunamigenic seismic hazard curve. When the mean return period is between 400 and 800 years and only M_w 9.0 events like the 2011 Tohoku earthquake are considered, the risk due to ground shaking is nearly zero using any of the three time-dependent models (lognormal, Weibull, and BPT). The *cov* of 0.25 results in the lowest risk, which leads to zero risk for the lognormal and BPT models. The Weibull distribution produces the highest occurrence rates among the three renewal distributions, and *cov* values of 0.5 and 0.7 result in non-negligible risk.

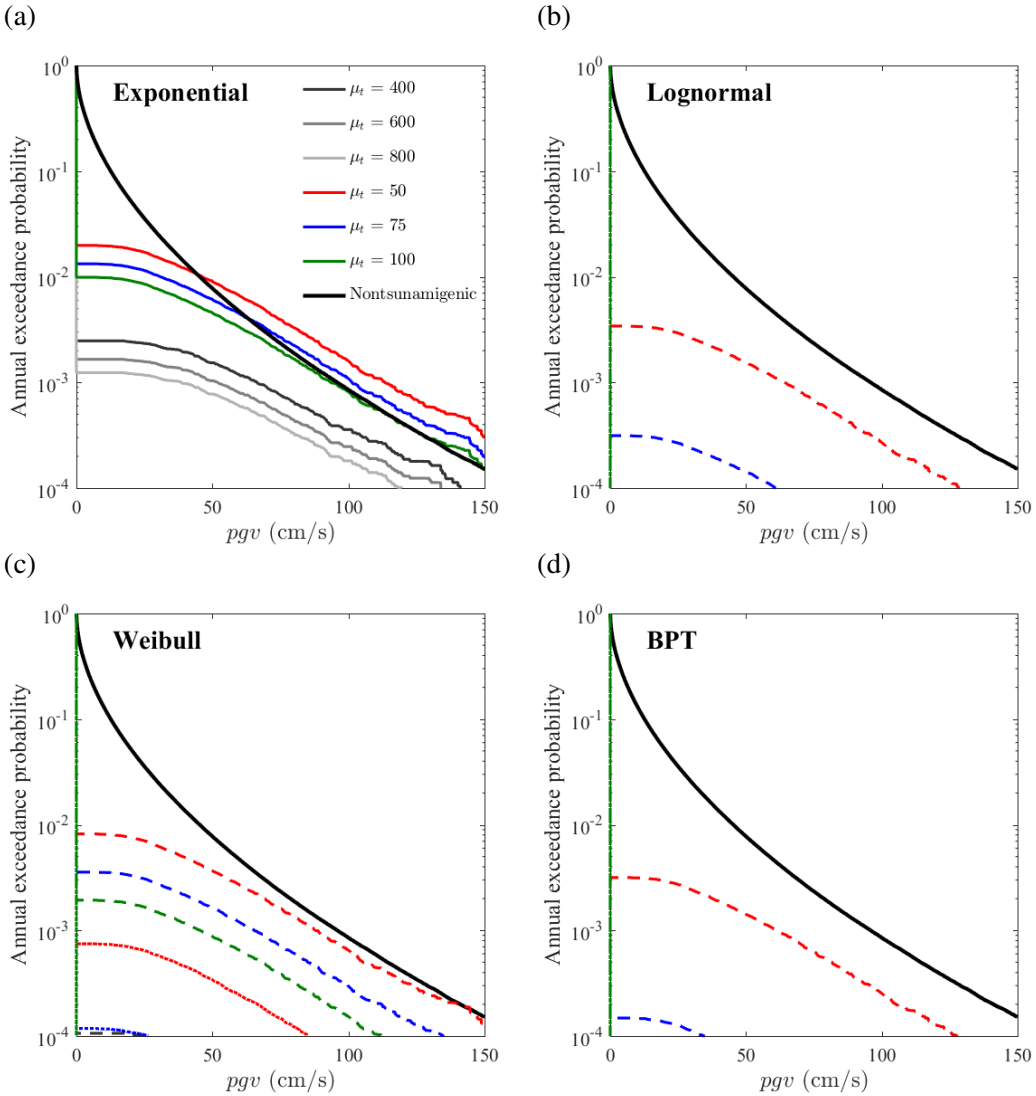

Figure 5.11 Seismic hazard curves of tsunamigenic earthquakes in Onagawa based on different earthquake occurrence models using different cases of μ_t and *cov* combinations (dotted lines for $cov = 0.25$, dashed lines for $cov = 0.5$).

The tsunami risk would be critical when the hazard curve of tsunamigenic earthquakes is just under or even crosses with that of nontsunamigenic earthquakes, because of its catastrophic nature, the underestimation of which would put the insurer under great risk. Using the BPT model tends to underestimate the occurrence rate for M_w 9.0 Tohoku-type earthquake given a short elapsed time of eight years compared to the other two time-dependent recurrence models (i.e. lognormal and Weibull). The comparison cannot determine which model is the most suitable one, but it shows the great variability of the calculated occurrence probabilities, especially given the situation that

the occurrence rate is not well constrained by the historical seismicity data for the region.

Table 5.6 Selected time-dependent earthquake occurrence models.

Case	Model	μ_t (years)	*cov*	Probability mass				
				M_w 8.2	M_w 8.4	M_w 8.6	M_w 8.8	M_w9.0
OM 1	Exponential	50	-	0.4241	0.2596	0.1590	0.0975	0.0598
OM 2	Exponential	600	-	0	0	0	0	1
OM 3	BPT	50	0.5	0.4241	0.2596	0.1590	0.0975	0.0598
OM 4	Weibull	50	0.25	0.4241	0.2596	0.1590	0.0975	0.0598
OM 5	BPT	75	0.5	0.4100	0.2587	0.1621	0.1030	0.0650

Among a wide range of possibilities given the uncertainty in earthquake occurrence prediction, five occurrence models (OM) are selected for risk calculation, as shown in Table 5.6, including a range of occurrences from low to high. These models are selected based on comparisons of the *pgv* curves of tsunamigenic earthquakes shown in Figure 5.10 and Figure 5.11. The *pgv* curves of the selected cases are below the *pgv* curve of non-tsunamigenic earthquakes, which reflect the current situation for the Tohoku region that the seismic risk of mega-thrust subduction earthquakes is not of imminent threat compared with the risk of more frequent non-tsunamigenic earthquakes. In the case where the *pgv* curve of tsunamigenic earthquakes is just under that of non-tsunamigenic earthquakes, the seismic risk from mega-thrust subduction earthquakes are comparable to that from crustal earthquakes and the tsunami risk is likely to exceed the seismic risk substantially. OM 1 is an exponential model considering the possibility of different magnitudes, with a return period of 50 years which is the same as the return period obtained for earthquakes larger than M_w 8.1 from the equivalent Poisson-GR occurrence relationship. OM 1 is taken as a reference case of non-renewal occurrence model, as used in the previous chapters. OM 2 is also a exponential model but only considers the M_w 9.0 events, with a return period of 600 years, which gives lower risk than OM 1. These return period and magnitude are the same as the model set-up adopted in the J-SHIS for this zone, while the J-SHIS used the BPT model gives a risk of almost zero at the moment. OM 3 is the BPT model with μ_t of 50 years and *cov* of 0.5. OM 4 is a Weibull model using $cov = 0.25$, as this value of *cov* is commonly used for earthquakes in Japan and only the Weibull distribution generates non-zero risk given this *cov*. OM 5 is the BPT model with a *cov* of 0.5, which produces the lowest occurrence but non-zero seismic hazard at the annual exceedance probability level of

10^{-4} .

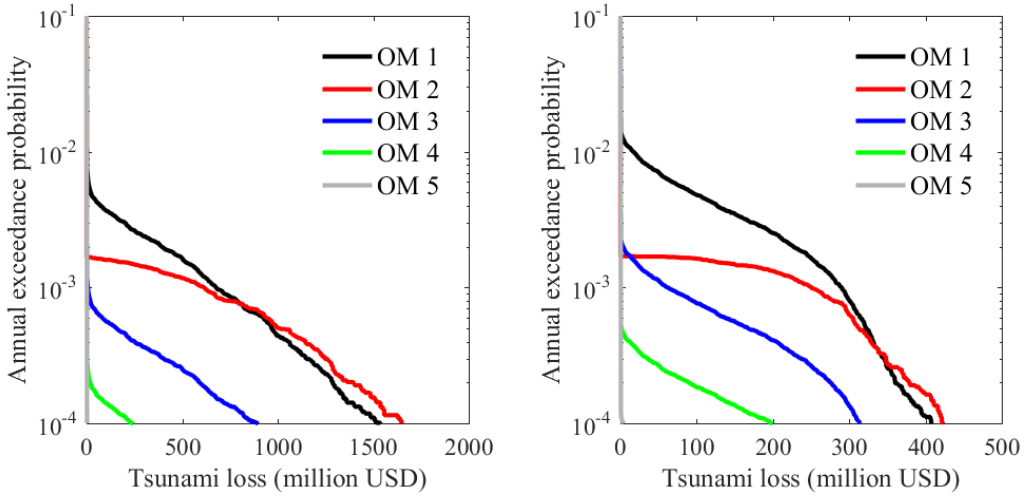

(a) Sendai (b) Onagawa

Figure 5.12 Tsunami loss curves based on different recurrence models.

Table 5.7 Average annual tsunami losses for Sendai and Onagawa given by different recurrence models (million USD).

	OM 1	OM 2	OM 3	OM 4	OM 5
Sendai	2.0676	1.3296	0.3182	0.0780	0.0151
Onagawa	1.3099	0.4542	0.2104	0.0503	0.0105

Figure 5.12 shows the differences of tsunami losses resulted from the selected earthquake recurrence models for Sendai and Onagawa. The results indicate the different consequences when different recurrence modes are used for tsunami loss estimation. OM 1 generally gives the highest loss but is exceeded by OM 2 for extreme situations, because OM 2 only considers the M_w 9.0 events with low occurrence rates. OM 1 and OM 2 are followed by OM 3 and OM 4, while the loss results from OM 5 are negligible for annual exceedance probability above 10^{-4}. For instance of Sendai, at a given probability level, the loss given by OM 1 is more than 70% higher than that of OM 3, and the loss of OM 3 is more than three times of the loss results given by OM 4. The corresponding AAL (see Equation (5.1)) given by OM 1-5 are shown in Table 5.7. Table 5.7 reveals the significant variability in AAL due to the selection of earthquake recurrence model. Taking Sendai as an example, the AAL for the middle case OM 3 is only 15% of that of OM 1 and is 4 times of the AAL for OM 4. Note that

the lowest case OM 5 is the BPT distribution with $cov = 0.5$, and if cov is 0.25 which is commonly used for mega-thrust subduction earthquakes in Japan, the AAL is almost zero because of the very small probability assigned to these extreme events.

5.4 Tsunami insurance rate-making and differentiation

Compared to ground shaking, tsunami hazard is more concentrated spatially, and its damage is more sensitive to the locations of buildings. Three important spatial factors are coastal topography, elevation, and distance from the sea. It can be expected that the higher the elevation and the farther from the coast, the less tsunami risk (Chapter 3), resulting in different insurance premium rates. Therefore, the determination of tsunami insurance rates is investigated by considering three location attributes: coastal topography, elevation, and site-coast distance. To distinguish these three location attributes, the tsunami insurance pure premium is calculated by considering two types coastal topography (i.e. plain coast and ria coast) and two different situations: i) similar elevations with different site-to-coast distances, and ii) similar site-to-coast distances with different elevations. Similarly to seismic vulnerability, the structural type has a major influence on the tsunami vulnerability of buildings (Suppasri et al., 2013; De Risi et al., 2017), while the other three location-related factors affect the insurance rate due to different local tsunami intensities. Note that a uniform damage ratio scheme is applied to account for the uncertainty in damage cost, which is assigned as: 0.03-0.1 for DS1 (minor), 0.1-0.3 for DS2 (moderate), 0.3-0.5 for DS3 (major), 0.5-1.0 for DS4 (complete) and 1.0 for DS5 (collapse & washed-away) (consistent with Chapter 3). These damage ratios are not the same as the fixed damage ratios applied in Chapter 4, and thus the loss estimation presented in this chapter can be higher due to a higher mean damage ratio for DS4.

Considering the uncertainty in tsunami recurrence, five time-dependent earthquake recurrence models covering the possible occurrence rates from low to high, are implemented to quantify the uncertainty in tsunami insurance rate caused by different recurrence models. It should be noted due to the sensitivity of tsunami risk to building location (see Chapter 3), the joint effect of location and uncertainty in recurrence model has significant influences on the relative importance of tsunami risk compared to seismic risk. The recurrence model of tsunamigenic earthquakes has a direct influence on the relative importance of tsunami hazard compared to crustal earthquakes. Besides, as

found in Chapter 4 that the consideration of flow velocity as intensity measure in addition to inundation depth can make substantial differences in tsunami loss estimation for local sites, the insurance rates considering and neglecting flow velocity are compared. Moreover, since a coarser DEM tends to result in more uniform tsunami risk at different locations (Chapter 3), the ability of different DEM resolutions in reflecting location attributes is investigated in the context of insurance rate-making.

Sendai is focused on to investigate the influence of distance from the coast because Sendai is on a plain coast, while Onagawa is considered to examine the influence of elevation because the buildings in Onagawa are located particularly close to the coastline with rapidly rising elevation (Chapter 3). More specifically, different locations in Sendai and Onagawa (i.e. P1 to P4 in Sendai and R1 to R3 in Onagawa; see Chapter 3) are considered to investigate the local tsunami risks on pure premiums for four types of structures (i.e. RC, steel, masonry, and wood). The variations of the grid resolutions are the same as those investigated in Chapter 3 (i.e. 10 m, 50 m, 150 m, and 450 m).

5.4.1 Sendai: influence of distance from the coastline

Sendai is on a plain coast and the elevation rises gradually. Within 2 km from the sea, the elevation is generally below 3 m. Many buildings in Sendai are at elevations between 1 m to 3 m. To investigate the influence of site-to-shore distance on tsunami insurance rate-making, four locations of 2 m elevation with different distances from the coastline are chosen: P1 of 0.5 km, P2 of 1.2 km, P3 of 1.5 km and P2 of 2 km, the local tsunami risks of which have been investigated in Chapter 3.

Influence of distance from coastline on tsunami risk

To compare the tsunami intensity at these four locations,300 Monte Carlo tsunami simulations are performed using the 10-m DEM; inundation depth distributions at different magnitudes are shown in Figure 5.13. Significant decreases of inundation depth can be observed with an increase of distance from the coastline. When the geographical environment (e.g. elevation, and land type) is similar, buildings within a 2 km distance would experience similar seismic intensity, but buildings located within 2 km from the sea are expected to have significantly different tsunami inundations. P1 is at the most critical location among the four. Although P2 is farther from the sea than P1 by 0.7

km only, both inundation depth and the inundation probability become lower. P2, P3, and P4 are almost unaffected by tsunamis with magnitudes lower than M_w 8.7. The inundation depth drops more quickly from 0.5 km to 1.2 km from the sea and the drop is much less significant when tsunami waves travel from 1.2 km to 1.5 km and 2 km. This drop of inundation depth with an increased distance from the coastline is smaller when more coarse resolution is used as found in Chapter 3. Consequently, the difference of tsunami premium rate caused by distance from the sea is smaller when a coarser DEM is used. Therefore, to distinguish the effect of distance from the sea, elevation data of high resolution are required.

Considering the five earthquake recurrence models selected in Section 5.3.3, Figure 5.14 shows the tsunami loss of a wood residential structure at the locations P1 to P4, using the DEM of 10-m resolution. The tsunami loss EP curves (solid lines) are compared with the seismic loss EP curves of tsunamigenic/subduction earthquakes (dashed lines) and non-tsunamigenic earthquakes (black solid lines). The tsunami loss is calculated by considering the variations of floor areas and unit costs of a wooden residential house, given a limit of 208,000 USD which is taken as the average cost of a wood house in Japan. The annual EP curves reveal great uncertainty when different earthquake occurrence models are used. The seismic EP curves have shown similar seismic risks at P1, P3, and P4, and the seismic risk of tsunamigenic earthquakes at P2 is lower than the other three locations because it is on a firmer site. A decreasing trend in tsunami risk can be seen from the location P1 to P4.

The earthquake recurrence model OM 1 gives the highest risk among the five selected models, followed by OM 2, OM 3, OM 4, and OM 5. The tsunami loss at P1 completely outweighs the seismic risk of the corresponding triggering earthquakes and non-tsunamigenic earthquakes, because P1 is closest to the coast. The differences between tsunami risk and seismic risk are reduced significantly when the distance from the coast is increased to 1.2 km at P2; seismic risk starts to outweigh tsunami risk at P3. At P4 when a building is 2 km far from the coastline, the tsunami risk has fallen below the seismic risk except for OM 2.

The seismic risks from tsunamigenic earthquakes are lower than those from non-tsunamigenic earthquakes for all four locations regardless of the recurrence model. Only OM 1 results in seismic risks from tsunamigenic earthquakes comparable but lower than those from non-tsunamigenic earthquakes, and the other four recurrence models

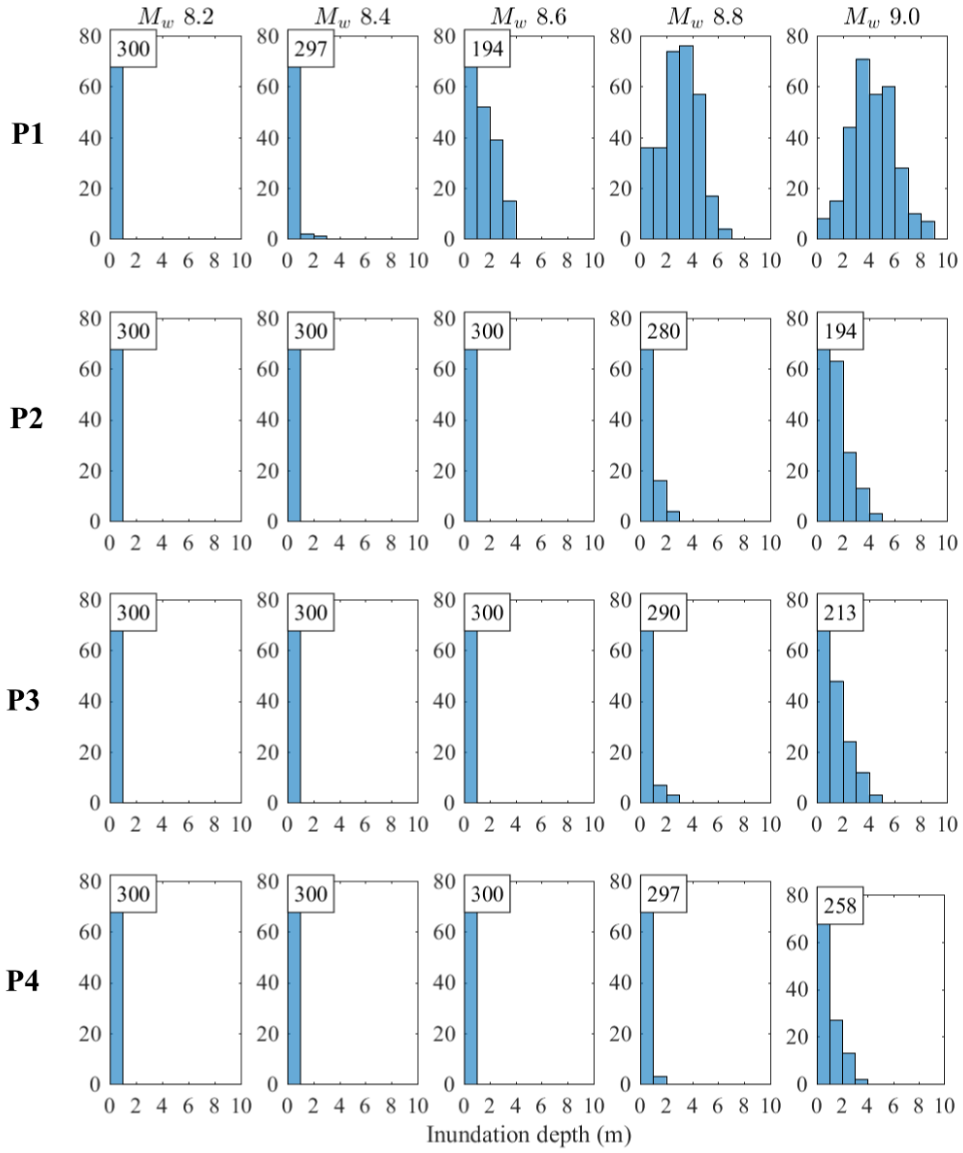

Figure 5.13 Inundation depth distribution of four locations in Sendai with different distances to the coastline.

give significantly lower risks for mega-thrust subduction earthquakes. Therefore, the selection of the recurrence model plays a dominant role in deciding the risk level of tsunamigenic earthquakes, while the relative importance of tsunami risk compared to seismic risk depends on both the distance from the sea and the recurrence model. At P1, tsunami risk is dominant for OM 1 and OM 2; using OM 3, the tsunami EP curve intercepts with the EP curve for non-tsunamigenic earthquakes; and when OM 4 and OM 5 are used, the seismic risk from non-tsunamigenic earthquakes becomes dominant. Due to the reduced tsunami risks at P2-P4, seismic risk from non-tsunamigenic

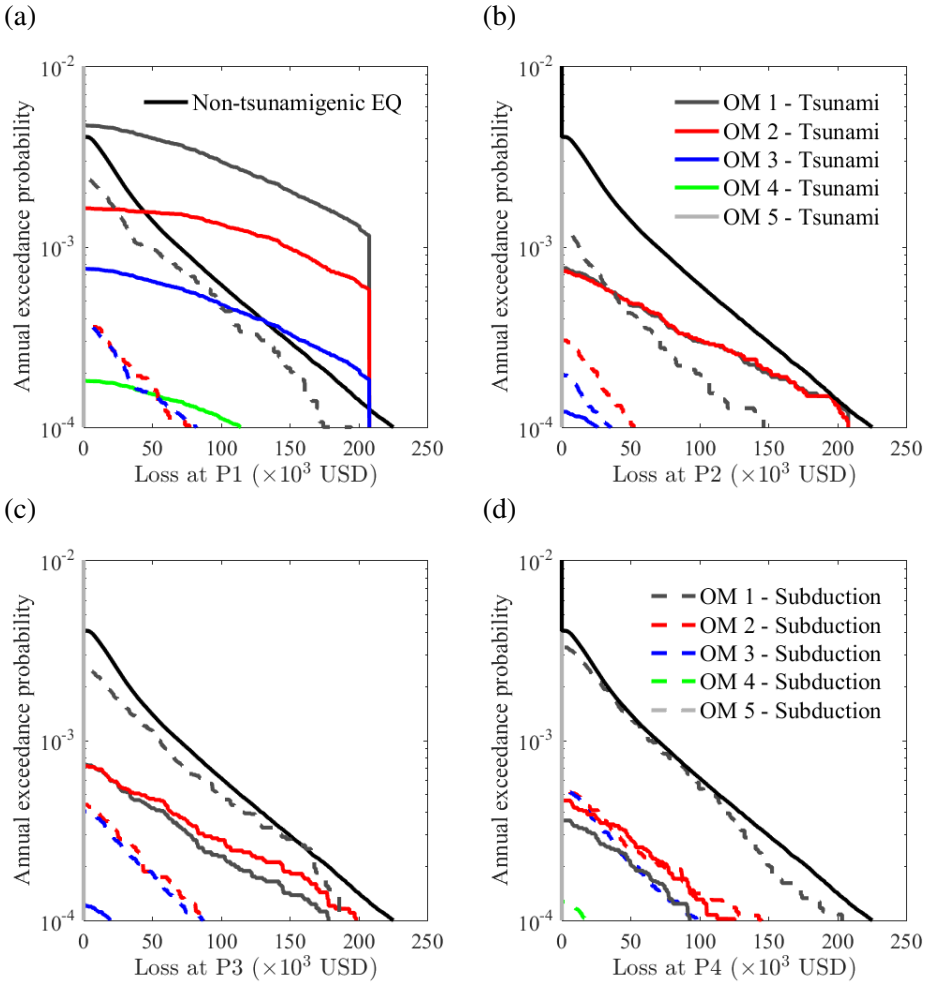

Figure 5.14 Annual EP curves for a residential wooden structure at different locations in Sendai using 10-m DEM: (a) P1, (b) P2, (c) P3, and (d) P4.

earthquakes is dominant for all five recurrence models, and the contribution of tsunamis is decreasing with the increase of distance from the sea. A significant reducuction of tsunami risk is seen from P1 to P2 for all recurrence models. For OM 2 which considers only the possibility of M_w 9.0 events, the tsunami risk outweighs seismic risk dramatically at P1-P3 and is similar to the seismic risk at P4. For OM 3, the tsunami risk is only dominant at P1 and tsunami loss is significantly greater than the seismic loss at P1. Using OM 3, OM 4, and OM 5, the risk of tsunamigenic earthquakes (both tsunami and seismic) is zero at all four locations. For OM 5 which gives the lowest recurrence rate among the five recurrence models, both seismic and tsunami risks for tsunamigenic earthquakes are negligible at all four locations.

The $VaR_{0.999}$ (i.e. the value at the cumulative probability of 0.999) of tsunami risk at P1 is capped by the limit for claim payout which is higher without the limit, while it drops to zero at P2. A significant reduction of tsunami risk is seen from P1 to P2, given any recurrence model. For OM 2 which considers only the possibility of M_w 9.0 events, the tsunami risk outweighs seismic risk dramatically at P1-P3 and is similar to seismic risk at P4. For OM 3, the tsunami risk is only dominant at P1 and tsunami loss is significantly greater than seismic loss at P1. Using OM 3, OM 4, and OM 5, the risk of tsunamigenic earthquakes (both tsunami and seismic) is zero at all four locations. Given OM 5 which gives the lowest recurrence rate among the five recurrence models, both seismic and tsunami risks for tsunamigenic earthquakes are negligible at all four locations.

The corresponding tsunami insurance pure premium rates at individual locations are summarised in Table 5.8. The rates are normalised by rates at P1 in Table 5.9 to show the reduced percentages of the rates with the increase of distance from the coastline. As expected, the insurance rate at P1 is significantly greater than other locations, regardless of which occurrence model is used. As OM 1 gives the highest occurrence rate and tends to overestimate the tsunami risk, the rate given by OM 1 at P1 is up to 2.9461 per 1000 insured value, which is more than twice as large as the rate given by OM 2, while the standard earthquake insurance rate in Miyagi Prefecture is only 1.97 for wood structures (note: the pure premium for this commercial rate in Japan is lower than the cited value). The rate drops significantly from P1 to P2, and mildly decreases from P2 to P3. Then the rate is almost halved from P3 to P4, with the distance increasing from 1.5 km to 2.0 km. Except for OM 2 which only considers the M_w 9.0 events, the rates at P2 and P3 are about 11% of the rates at P1, and the rates at P4 are only 4% of the rates at P1. When OM 2 is applied, the relative differences between rates at locations with different distances from the sea are smaller than other four recurrence models which consider multiple earthquake magnitudes. The differences between P1 and P4 by percentage are even smaller than those between P1 and P2 using the other four recurrence models. The comparison of the pure premium rates listed in Table 5.8 and Table 5.9 indicates that tsunami risk is very sensitive to site-to-coast distance, even within a distance as short as 2 km.

Table 5.8 Tsunami insurance pure premium rates for wood structures in Sendai with different distances to the coast by considering different earthquake occurrence models (per 1000 insured value).

Location	Distance	OM 1	OM 2	OM 3	OM 4	OM 5
P1	0.5 km	2.9461	1.2293	0.4752	0.1114	0.0226
P2	1.2 km	0.3500	0.3495	0.0555	0.0139	0.0025
P3	1.5 km	0.2839	0.3209	0.0482	0.0106	0.0029
P4	2.0 km	0.1315	0.1779	0.0206	0.0049	0.0012

Table 5.9 Tsunami insurance pure premium rates normalised by rates at P1 by considering different earthquake occurrence models.

Location	Distance	OM 1	OM 2	OM 3	OM 4	OM 5
P1	0.5 km	1.00	1.00	1.00	1.00	1.00
P2	1.2 km	0.11	0.28	0.11	0.12	0.11
P3	1.5 km	0.09	0.26	0.09	0.09	0.12
P4	2.0 km	0.04	0.14	0.04	0.04	0.05

Influence of structural types and flow velocity on tsunami insurance premium rate

It has been found in Chapter 4 that the consideration of flow velocity makes significant differences for local tsunami risk when a certain combination of inundation depth and flow velocity occurs, especially when a fine 10-m DEM is used (i.e. more accurate estimation of water flow). Taking OM 3 as the recurrence model which gives a middle-range occurrence rate, a comparison of tsunami pure premium rates for different structure types, considering and neglecting flow velocity is shown in Table 5.10, using the 10-m DEM. The differences by percentage are shown in Table 5.11. The rates distinguishing structural types indicate that wood structures have the highest rates and RC structures have the lowest rates, and steel and masonry structure have similar rates. The sensitivity of tsunami risk to consideration of flow velocity is different for these four structure types due to their different structural vulnerabilities (Chapter 4; Song et al., 2017). For non-wood structures, P1 and P4 are the least sensitive to the consideration of flow velocity (differences in rates within 11%), because in major events buildings locate closest to the coast are most likely to be heavily damaged in major events regardless of additional effects due to flow velocity, while at a distance of 2 km from the coastline the flow velocity is too low to cause any damage. Wood structures are least influenced by flow velocity at P1 and P4 as well but exhibit greater differences due to flow velocity

than non-wood structures.

Table 5.10 Tsunami insurance pure premium rate in Sendai based on OM 3 using different intensity measures (per 1000 insured value).

Location	IM - Depth				IM - Depth and Velocity			
	RC	Steel	Wood	Masonry	RC	Steel	Wood	Masonry
P1	0.3943	0.4479	0.4752	0.4366	0.3646	0.4193	0.4614	0.4193
P2	0.0451	0.0519	0.0555	0.0469	0.0519	0.0554	0.0603	0.0538
P3	0.0410	0.0451	0.0482	0.0415	0.0615	0.0625	0.0600	0.0568
P4	0.0183	0.0201	0.0206	0.0185	0.0204	0.0212	0.0226	0.0197

Table 5.11 Relative differences of rates neglecting and considering flow velocity in Table 5.10.

Location	RC	Steel	Wood	Masonry
P1	-0.07	-0.06	-0.02	-0.03
P2	0.15	0.06	0.08	0.14
P3	0.49	0.38	0.24	0.36
P4	0.11	0.05	0.09	0.06

RC is the most resistant structure. When tsunami waves travel from P1 to P3, inundation depth drops more than flow velocity. Taking one of the 300 simulations of M_w 9.0 events as an example, the inundation depth at P1 to P4 is 5.75 m, 2.15 m, 2.00 m, and 1.05 m, respectively, while the flow velocity is 3.1 m/s, 3.5 m/s, 6.4 m/s, and 2.75 m/s, respectively. As shown in Chapter 4 that when a location has relatively low inundation depth with high flow velocity, flow velocity plays a more important role in loss estimation and produces a higher loss. At P3, the inundation depth has dropped significantly, but the flow velocity is even higher than P1, and thus it makes a larger difference than other locations. At P2 where the flow velocity remains almost the same as P1, whereas inundation depth has dropped, flow velocity caused more than 14% differences for RC, wood, and masonry structures. The largest difference is found at P3 for all four structure types among the four locations, and a more than 24% difference is caused due to the significantly reduced inundation depth and high flow velocity. At P4, both inundation depth and flow velocity are weakened substantially and thus the importance of flow velocity becomes less important for non-wood structures, while flow velocity still causes 20% higher insurance rates for wood structures.

Influence of DEM resolution on tsunami insurance premium rate

Table 5.12 compares the tsunami insurance pure premium rates based on DEMs of different resolutions, using OM 3. As found in Chapter 3 that lower resolution DEM is less capable of reflecting the variability of local tsunami risk due to different distances from the coastline and different elevations, tsunami insurance pure premium rates at four locations in Sendai given by a coarser DEM are more uniform. As a result, the coarser DEMs tend to overestimate the rates at farther locations (i.e. P2, P3, and P4). Taking the rates using the 10-m DEM as the reference case, the coarser DEM tends to give more uniform rates at different locations. When the grid resolution is 450 m, the rates for the four locations are almost uniform, while the rates at P2, P3, and P4 are reduced to only 11%, 9%, and 4% of the rate at P1, when the finer 10-m resolution is considered. For the 10-m DEM, about 90% drop of the rate is seen from P1 to P2, while the rates at P1 and P2 are similar for the other three DEMs. Although the 50-m DEM, which is the second finest DEM, gives similar tsunami loss results as the 10-m DEM for the whole Sendai, it still cannot reflect the variability in local tsunami risk. The rate at P1 is only about one-fifth of that for the 10-m resolution case, while the rates at P2 and P3 are about twice the rates for the 10-m resolution case. At P2 and P3, the rates given by the 150-m DEM are as high as about 8 times of those given by the 10-m DEM. The cases of 450-m resolution is the most unreliable as there is a large discrepancy in rates, and the rates at P2, P3, and P4 are dramatically high as 7, 12, and 16 times of those given by the 10-m DEM. Therefore, the resolution of DEM has a tremendous impact on the accuracy of tsunami rate-making and the inaccurate elevation can lead to significant errors in the insurance rates, especially for individual locations.

Table 5.12 Tsunami insurance pure premium rate with different distances from the coastline based on OM 3 (per 1000 insured value).

Location	10 m	50 m	150m	450m
P1	0.4752	0.0973	0.3375	0.5029
P2	0.0555	0.1016	0.3041	0.4337
P3	0.0482	0.1241	0.3392	0.5708
P4	0.0206	0.0214	0.1309	0.3297

5.4.2 Onagawa: influence of land elevation

In Onagawa, buildings are surrounded by steep hills/mountains and the sea and concentrated in a small flat area close to the coast and the elevation rises rapidly towards inland. The majority of buildings in Onagawa are located within 1 km from the coastline, and about a half are located within 0.3 km from the sea. As seen in Chapter 3, nearby locations at similar distances from the coast can have various elevations. Three locations with distances of approximately 0.3 km from the coast and different elevations are selected: R1 of 2 m elevation, R2 of 4 m elevation, and R3 of 6 m elevation, which are the same locations as selected in Figure 3.16 in Chapter 3 for local tsunami risk comparison.

Influence of elevation on tsunami risk

The inundation depth distributions at three locations using the 10-m DEM shown in Figure 5.15 indicate the decrease of inundation depths with the increase of elevation. For instance, R1 with an elevation of 2 m may experience tsunami depths under 4 m during a M_w 8.4 event, while R2 and R3 with higher elevations are almost safe from tsunamis caused by earthquakes smaller than M_w 8.5 and M_w 8.7, respectively.

Figure 5.16 displays the annual EP curves for subduction earthquakes, non-tsunamigenic earthquakes, and tsunamis, for a wooden structure at R1, R2, and R3. For tsunamigenic events at all three locations, the tsunami risks are dominant for most cases, and the tsunami risk is higher than those in Sendai (Figure 5.14). One of the reasons that Onagawa has higher tsunami risk is that Onagawa is on a ria coast which would experience higher inundation depth than plain coast, as was observed during the 2011 Tohoku earthquake and tsunami (Mori et al., 2012; Fraser et al., 2013). Another reason is that in Onagawa most buildings are located in relatively flat areas close to the sea (i.e. within 0.5 km from the coastline), as Onagawa is surrounded by mountains. With similar site conditions, the seismic risks for three locations are similar.

Because the seismic risks at three locations are similar, the contributions of three types of hazards (i.e. tsunamigenic earthquakes, non-tsunamigenic earthquakes, and tsunamis) in Onagawa depend on the local tsunami risks and the recurrence model for tsunamigenic events. The elevation affects the local tsunami risk, and the recurrence model has a direct influence on both tsunamigenic events. When OM 1 is considered, the seismic risks from tsunamigenic earthquakes is high such that they exceed the

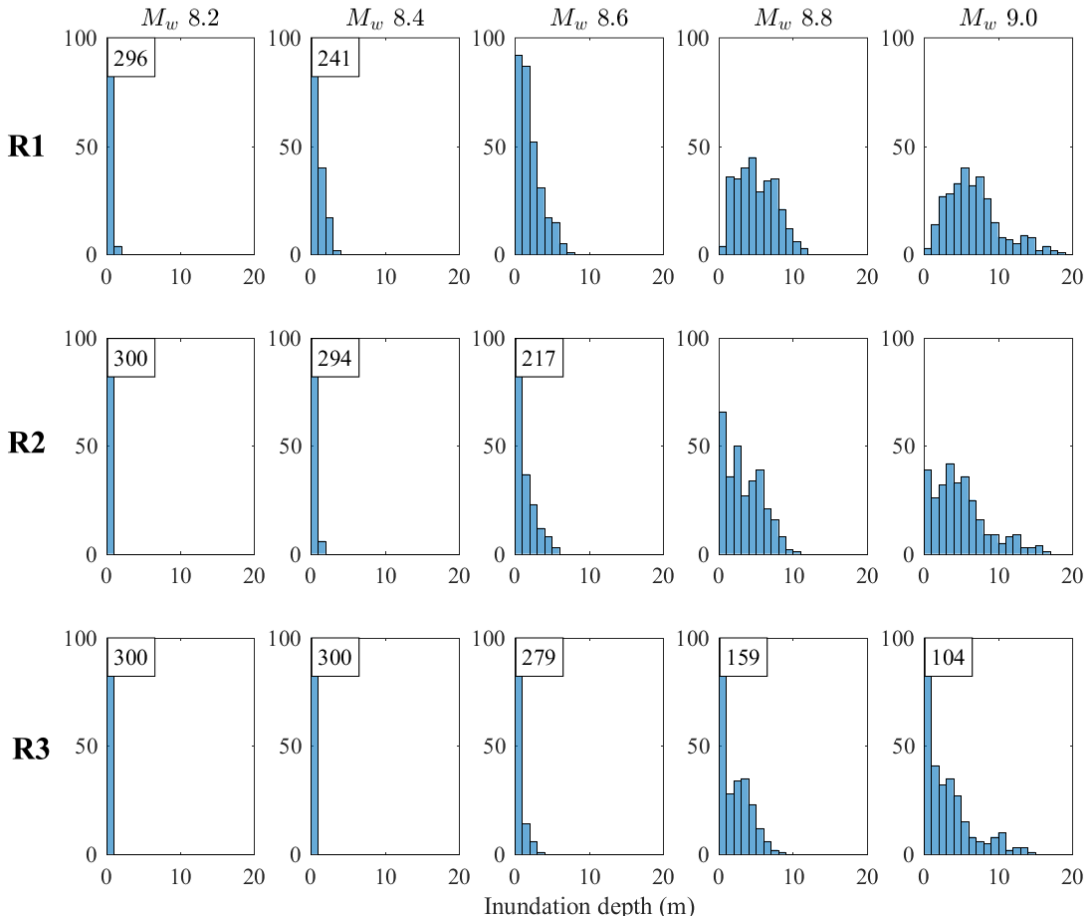

Figure 5.15 Inundation depths of three locations in Onagawa with different elevation.

seismic risk from non-tsunamigenic earthquakes at all three locations. This observation is not applicable when the other four recurrence models are considered such that tsunamigenic earthquakes have the least contribution and the corresponding risks are significantly lower than the risks from tsunamis and non-tsunamigenic earthquakes. For OM 1 and OM 2, tsunami risk is dominant at all three locations. However, seismic risk of tsunamigenic earthquakes is higher than that of non-tsunamigenic earthquakes given OM 1, while tsunamigenic earthquakes are estimated to cause significantly less losses than non-tsunamigenic earthquakes using OM 2. For the three locations, the reduction of tsunami risk by increased elevation is less than the difference made by different recurrence models.

Regarding the effects of earthquake occurrence modelling, OM 1, which tends to overestimate the tsunami hazard, causes greater differences in tsunami loss among three locations by giving a higher occurrence rate than the other four recurrence models. OM

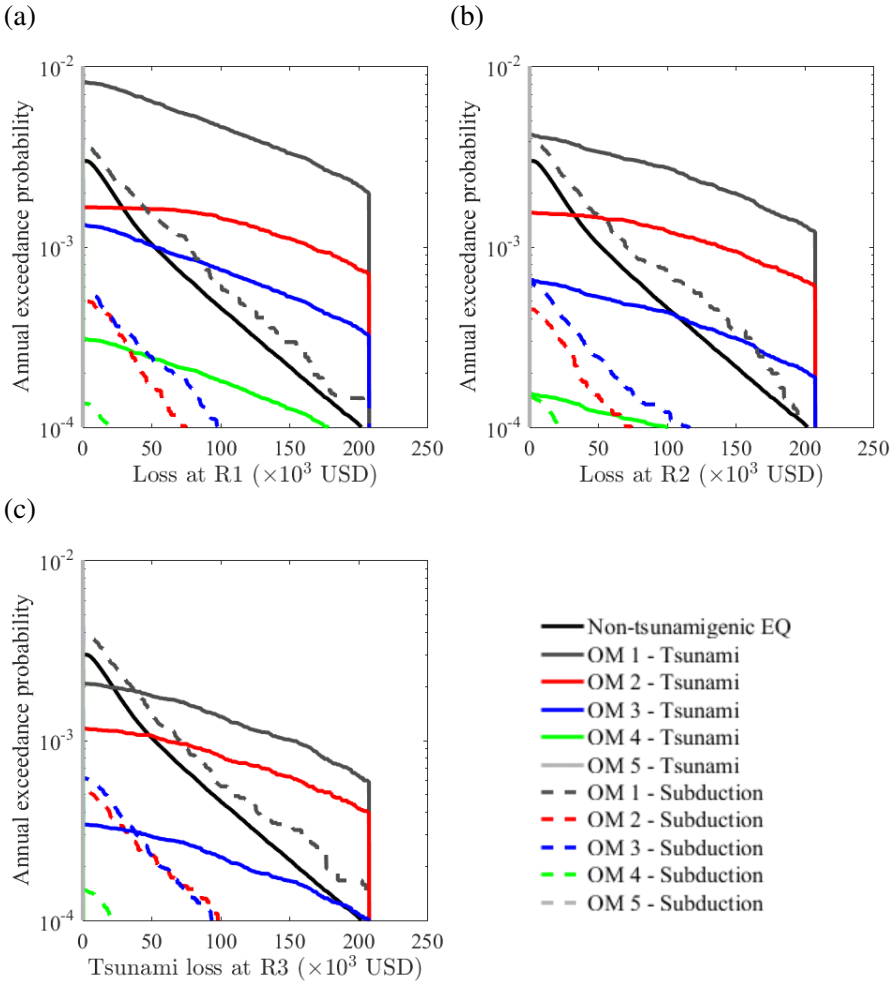

Figure 5.16 Annual EP curves for a wooden residential structure at different elevations in Onagawa using 10-m DEM: (a) R1, (b) R2, and (c) R3.

2 which considers only M_w 9.0 events generates the least differences between three locations. At all three locations, the tsunami loss EP curves exceed the EP curves of corresponding subduction earthquakes. Similar to OM 1, a decrease of tsunami risk is seen from R1 to R2 and R3, with the increase of elevation using OM 3 and OM 4. Given almost constant seismic risks and decreased tsunami risks at the three locations, the difference between tsunami risk and seismic risk becomes smaller when the elevation is increased to 6 m at R3. Unlike the results for Sendai, where OM 4 generates almost zero risk above the annual exceedance probability of 10^{-4}, at the three locations in Onagawa, the risks based on OM 4 are not negligible. At R1 and R2, the tsunami risk is higher than the seismic risk from tsunamigenic earthquakes but lower than that of non-tsunamigenic earthquakes when OM 4 is considered, while at R3 the tsunami risk is reduced to almost zero and is exceeded by the seismic risk of tsunamigenic earthquakes.

Similar to the case in Sendai, the seismic and tsunami risks in Onagawa given by OM 5 are zero.

The tsunami insurance pure premium rates based on the five occurrence models are shown in Table 5.13, using the 10-m DEM. The relative differences caused by the recurrence models are similar to the results for Sendai. From the normalised rates with respect to R1 (see Table 5.14), for OM 1, OM 3, OM 4, and OM 5, the rates at R1 are almost twice as large as the rates at R2 and the rates at R3 are reduced to about 28% of the rates at R1. For OM 2 the differences in rates among the three locations are smaller, and the rates at P2 and P3 are only 13% and 40% lower than that at R1, respectively. OM 2 only considers the extreme M_w 9.0 events and Onagawa is prone to high inundation depths, so when the tsunami run-up is high, a higher elevation may not result in less building damage than a lower elevation because the building tends to collapse anyway.

Table 5.13 Tsunami insurance pure premium rate for wood structures with different elevations by considering different earthquake occurrence models (per 1000 insured value).

Location	Elevation	OM 1	OM 2	OM 3	OM 4	OM 5
R1	2 m	4.7689	1.3269	0.7657	0.1829	0.0371
R2	4 m	2.6257	1.1571	0.4138	0.0957	0.0199
R3	6 m	1.3419	0.8051	0.2228	0.0536	0.0097

Table 5.14 Tsunami insurance pure premium rates normalised by rates at R1 by considering different earthquake occurrence models.

Location	Elevation	OM 1	OM 2	OM 3	OM 4	OM 5
R1	2 m	1.00	1.00	1.00	1.00	1.00
R2	4 m	0.55	0.87	0.54	0.52	0.53
R3	6 m	0.28	0.60	0.29	0.29	0.26

Influence of structural types and flow velocity on tsunami insurance premium rate

By adopting OM 3 as a representative earthquake occurrence model, the tsunami insurance rates distinguishing structural types are shown in Table 5.15. Wooden structures

have the highest premium rates, followed by steel and masonry structures, and the lowest is RC structures. The comparison between the rates neglecting and considering flow velocity reveals the underestimation of tsunami risk without considering the influence of flow velocity. It can be seen in Table 5.16 that more than 30% increases in rates are caused by considering flow velocity, regardless of structural types and locations.

Table 5.15 Tsunami insurance pure premium rate at different elevations based on OM 3 using different intensity measures (per 1000 insured value).

Location	IM - Depth				IM - Depth and Velocity			
	RC	Steel	Wood	Masonry	RC	Steel	Wood	Masonry
R1	0.6684	0.7354	0.7657	0.7134	0.7410	0.7843	0.8456	0.8233
R2	0.3364	0.3818	0.4138	0.3734	0.3733	0.4046	0.4475	0.4216
R3	0.1855	0.2099	0.2228	0.2057	0.2061	0.2221	0.2406	0.2288

Table 5.16 Relative differences of rates neglecting and considering flow velocity in Table 5.15.

Location	RC	Steel	Wood	Masonry
R1	0.10	0.06	0.10	0.15
R2	0.10	0.05	0.08	0.12
R3	0.11	0.05	0.07	0.11

Influence of DEM resolution on tsunami premium rate

Since the elevation in Onagawa changes abruptly, this makes the local tsunami risk in Onagawa very sensitive to DEM resolution. The DEM of low resolution is more likely to cause substantial errors in elevation assigned to locations close to one another. The assigned elevations based on a coarse DEM can be significantly different from what it is, resulting in an inaccurate estimation of local tsunami risk (Chapter 3). Although the 50-m DEM has the second finest resolution, it still cannot capture the realistic elevations at R2 and R3, giving 1.92 m for R2 and 3.26 m for R3, while it is 3.81 m and 6 m, respectively, according to the 10-m resolution DEM (see Table 3.5). Even worse accuracy of local elevation is resulted from the 150-m and 450-m DEMs. Particularly, the 450-m resolution cannot provide elevations close to the realistic values for any of the three locations. Consequently, the errors caused by using inaccurate elevation

models result in unreliable local tsunami insurance rates, as can be found in Table 5.17. Compared to the rates using the 10-m DEM, the rates given by the other three coarser DEMs are higher at all three locations. A coarser DEM results in higher rates for the Onagawa case. Taking R1 as an example, the rates given by the 50-m, 150-m, and 450-m DEMs are 1.5, 2.4, and 3.1 times greater than the rate given by the 10-m DEM.

Table 5.17 Tsunami insurance pure premium rate at different elevations based on OM 3 (1000 value).

Location	10 m	50 m	150m	450m
R1	0.7657	1.1675	1.8246	2.3665
R2	0.4138	0.8880	1.9368	2.3953
R3	0.2228	0.5367	2.0917	2.3897

In addition to the higher rates caused by the coarser DEMs, in Onagawa a coarser DEM also tends to overestimate the rate for a location with lower elevation while overestimate the rate for a location with higher elevation. Consequently, the coarser DEM makes the insurance rates more uniform across locations with different elevations. As shown in Table 5.17, for the 10-m resolution case, the insurance rate drops by 45% and 72% from R1 to R2 and R1 to R3, respectively, while the rates become almost the same when the grid size is increased to 150 m or 450 m . Even for the second finest DEM of 50 m, the rate at R3 is only 55% lower than the rate at R1, while this difference based on the 10-m DEM is more than 70%. It needs to be mentioned that the disparity in pure premium rate at single locations does not necessarily happen in the total regional tsunami loss, because a building portfolio includes buildings at various locations. Therefore, the rate differentiation by elevation is viable only when tsunami risk calculation is able to accurately capture the differences in elevation using a fine DEM.

5.5 Multi-hazard insurance rate-making

Tsunamis share the same source and occurrence rate with the triggering earthquakes. Given the dependency of tsunamis on the mega-thrust subduction earthquakes, this section investigates the insurance rate-making for both earthquake and tsunami loss coverage using the same catastrophe model. The seismic risk is affected not only by

tsunamigenic earthquakes but also by non-tsunamigenic earthquakes. Therefore, the earthquake-tsunami insurance pure premium P_{total} is composed of two parts: i) pure premium of nontsunamigenic earthquakes $P_{nontsunamigenic}$ (Section 5.2.2), and ii) pure premium of tsunamigenic earthquakes and tsunamis $P_{tsunamigenic}$. For non-tsunamigenic earthquakes, the seismic intensity pgv is approximated by the Weibull distribution and is simulated though a Monte Carlo simulation given the seismic hazard curve, as demonstrated in Section 5.2.2. By integrating the simulated pgv values with the seismic fragility curves and cost model, the annual loss EP curve of nont-sunamigenic earthquakes is obtained, which is used to calculate $P_{nontsunamigenic}$. On the other hand, $P_{tsunamigenic}$ is calculated based on the multi-hazard loss estimation method (see Section 5.2.4) by considering tsunamigenic earthquakes (Section 5.2.3) and tsunamis as a series of events.

To reflect the influence of occurrence models and the resulted risk by tsunamigenic earthquakes and triggered tsunamis, the loss of tsunamigenic earthquakes is compared with the seismic loss of non-tsunamigenic earthquakes. The tsunamigenic loss is the combined loss for both subduction earthquakes and tsunamis. In this section, earthquake-tsunami risk refers to the combined loss of both ground shaking and tsunami due to tsunamigenic earthquakes, and multi-hazard risk refers to the total of tsunami loss and seismic loss (due to both tsunamigenic and non-tsunamigenic earthquakes). The earthquake-tsunami insurance pure premium rates are calculated based on the cases in Section 5.4, with additional consideration of losses caused by ground shaking.

5.5.1 Sendai

The annual EP curves for the combined loss of tsunamigenic earthquakes and non-tsunamigenic earthquakes in Sendai are displayed in Figure 5.17, reflecting variations of the results in using different occurrence models. Note that the seismic hazard curves obtained from the J-SHIS for calculating loss of non-tsunamigenic earthquakes at four locations are almost identical (i.e. same hazard curve), which leads to the same loss EP curves, while the hazard curves for subduction earthquakes are obtained by applying a GMPE by Morikawa and Fujiwara (2013) and by considering local site conditions (i.e. different Vs_{30}). The EP curve of tsunamigenic earthquakes given by OM 1 exceeds that of non-tsunamigenic earthquakes at P1, and it is close to the EP curves for non-tsunamigenic earthquakes at the other three locations where ground shaking is more

dominant. EP curves of OM 2 and OM 3 intersect with the curve of non-tsunamigenic earthquakes at P1, which indicates lower occurrence rates with higher consequences for those extreme events.

With the decrease of tsunami risk due to the increasing distance from the sea, the tsunamigenic EP curves of OM 2 and OM 3 are below the curve of non-tsunamigenic earthquake. Given OM 3, it can be noticed that for P1 which is the closest from the sea, the earthquake-tsunami risk is comparable with seismic risk of non-tsunamigenic earthquakes, while for other farther locations, the non-tsunamigenic earthquakes remain the greatest threat since the EP curves for tsunamigenic earthquakes are much lower than those for the non-tsunamigenic earthquakes. It can be also noticed that the earthquake-tsunami risk of OM 3 does not decrease from P2 to P4 with increasing distance from the sea. This is because for these locations ground shaking is dominant and the decreasing tsunami risk does not influence the overall risk of tsunamigenic earthquakes. OM 4 generates earthquake-tsunami risks significantly lower than non-tsunamigenic earthquakes at all locations, and OM 5 gives almost zero risk. Figure 5.17 also indicates the relative contributions of risks from ground shaking and tsunami. The increase of distance from the coast decreases the contributions of tsunami risk in total multi-hazard risk. $P_{nontsunamigenic}$ for Onagawa is calculated as 1.06 per 1000 insured based on the J-SHIS bed-rock velocity curve and a typical site amplification factor in Onagawa of 1.47 (see Section 5.2.2), using the same cost model and damage ratios for $P_{tsunamigenic}$. $P_{nontsunamigenic}$ is lower than the standard earthquake insurance rate (1.97 per 1000 insured value) for wood structures in Miyagi Prefecture because $P_{nontsunamigenic}$ is pure premium rate (risk premium P_{risk} and transaction fees $P_{expense}$ are not included).

Table 5.18 $P_{tsunamigenic}$ rate for wood structures in Sendai (per 1000 insured value).

Location	$P_{tsunamigenic}$					P_{total}				
	OM 1	OM 2	OM 3	OM 4	OM 5	OM 1	OM 2	OM 3	OM 4	OM 5
P1	3.33	1.23	0.53	0.12	0.02	4.39	2.28	1.59	1.17	1.08
P2	0.61	0.38	0.10	0.02	0	1.67	1.44	1.15	1.07	1.06
P3	0.97	0.39	0.16	0.03	0	2.02	1.45	1.21	1.09	1.06
P4	0.97	0.30	0.15	0.03	0	2.02	1.35	1.21	1.09	1.06

The corresponding earthquake-tsunami pure premium rates $P_{tsunamigenic}$ and total multi-hazard pure premium rates P_{total} in Sendai are shown in Table 5.18, distinguishing the different locations and occurrence models. P_{total} is the sum of both $P_{tsunamigenic}$ and

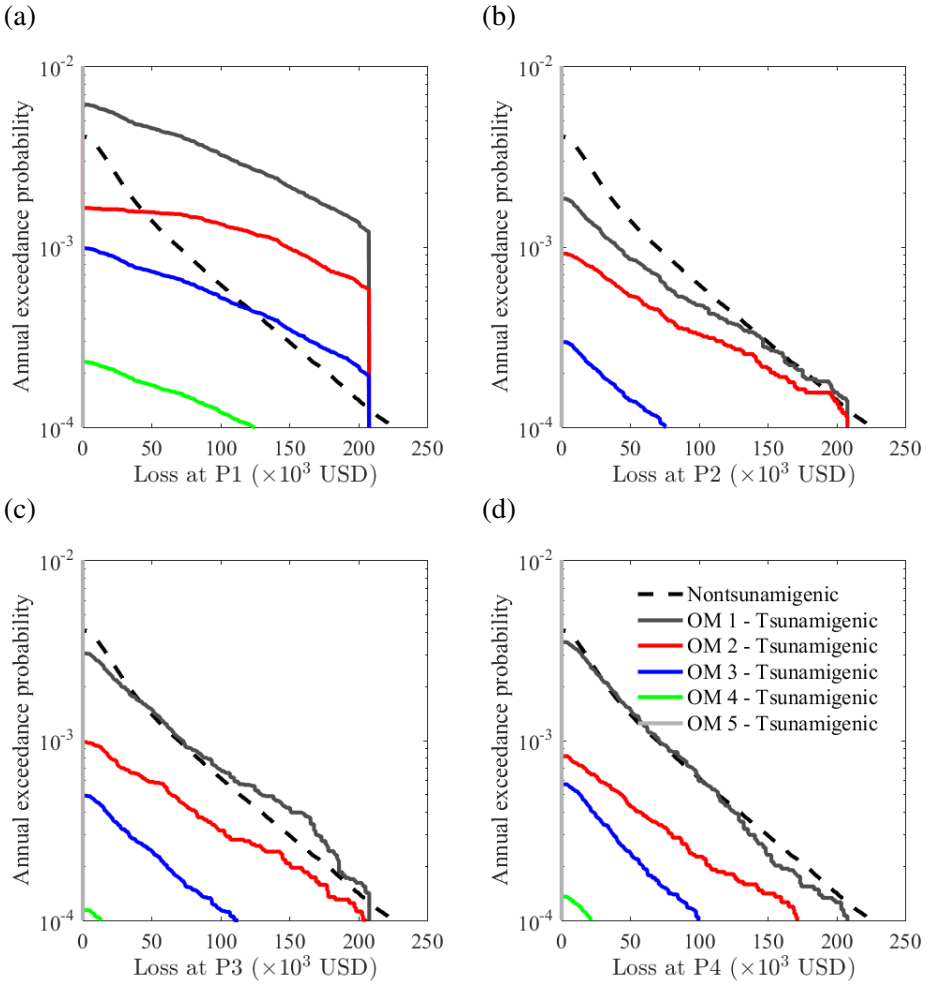

Figure 5.17 Annual EP curves in Sendai for nontsunamigenic earthquakes and tsunamigenic earthquakes for a wooden structure using 10-m DEM: (a) P1, (b) P2, (c) P3, and (d) P4.

Table 5.19 Relative difference of $P_{tsunamigenic}$ and $P_{nontsunamigenic}$ in Sendai.

Location	OM 1	OM 2	OM 3	OM 4	OM 5
P1	2.14	0.16	-0.50	-0.88	-0.98
P2	-0.42	-0.64	-0.90	-0.98	-1.00
P3	-0.08	-0.63	-0.84	-0.97	-1.00
P4	-0.08	-0.71	-0.85	-0.97	-1.00

$P_{nontsunamigenic}$. To quantify the relative importance of tsunamigenic earthquakes and non-tsunamigenic earthquakes, the relative differences of $P_{tsunamigenic}$ and $P_{nontsunamigenic}$ (($P_{tsunamigenic}$ - $P_{nontsunamigenic}$)/$P_{nontsunamigenic}$) are shown in Table 5.19. At P1, which is the most risky location, $P_{tsunamigenic}$ is higher than $P_{nontsunamigenic}$ by more than twice

Table 5.20 Contribution of $P_{tsunamigenic}$ to P_{total} in Sendai.

Location	OM 1	OM 2	OM 3	OM 4	OM 5
P1	0.75	0.53	0.33	0.10	0.01
P2	0.36	0.26	0.08	0.01	0
P3	0.48	0.26	0.13	0.02	0
P4	0.48	0.22	0.12	0.02	0

of $P_{nontsunamigenic}$ given OM 1, while $P_{tsunamigenic}$ is similar to $P_{nontsunamigenic}$ (2% difference) given OM 5, which shows the great uncertainty associated with earthquake recurrence modelling. $P_{tsunamigenic}$ drops to be lower than $P_{nontsunamigenic}$ when the distance from the sea increases to 1 km at P2, regardless of the recurrence model. The contributions of $P_{nontsunamigenic}$ to P_{total} distinguishing distances from the sea are shown in Table 5.20, and a reduced contribution can be seen from OM 1 to OM 5. When a recurrence model is selected (e.g. OM 3), the contribution of tsunamigenic earthquakes reduces with the increasing distance from the sea. Given OM 3, from P1 to P3, $P_{tsunamigenic}$ decreases from 50% to 14% in terms of $P_{nontsunamigenic}$ to 14% from P1 to P3. $P_{tsunamigenic}$ becomes lower than $P_{nontsunamigenic}$ using OM 3, OM 4 and OM 5 for all four locations.

Excluding P1 given OM 1 and OM 2, $P_{tsunamigenic}$ at all locations are lower than $P_{nontsunamigenic}$ regardless of earthquake recurrence model. For all recurrence models which consider multiple earthquake magnitudes, the multi-hazard pure premium rates at P3 and P4 considering only tsunamigenic earthquakes are the same, because they are more than 1.5 km far from the coast and ground shaking is more influential. Consequently, earthquakes are dominant at P4 and the combined earthquake-tsunami risk is higher than its tsunami risk. P2 has have a reduced rate compared to P1, but the difference of $P_{tsunamigenic}$ between P1 and P2 is smaller than the difference of tsunami insurance premium rates due to the contribution of ground shaking. The selection of recurrence model for subduction earthquakes has a significant influence on the contribution of $P_{tsunamigenic}$ in P_{total}. When a recurrence model is selected, which gives a lower occurrence rate, the contribution of tsunami risk in the multi-hazard insurance rate is lower, and hence, the influence of distance from the coastline becomes less significant. Taking P1 as an example, $P_{tsunamigenic}$ composes 33% of P_{total} using OM 3, while $P_{tsunamigenic}$ only contributes to 10% of P_{total} given OM 4.

5.5.2 Onagawa

Similar to Sendai, the loss curves of tsunamigenic earthquakes and non-tsunamigenic earthquakes using different occurrence models are compared in Figure 5.18. The EP curves of nontsunamigenic earthquakes in Onagawa are slightly lower than that in Sendai because Onagawa has a firmer site condition and the typical site amplification factor for Onagawa is lower than Sendai. Since tsunami is dominant at all three locations, the earthquake-tsunami EP curves are similar to tsunami EP curves in Figure 5.16. The recurrence model has a significant influence on the relative importance of tsunamigenic events. The EP curves for tsunamigenic earthquakes given by OM 1 are above those for non-tsunamigenic earthquakes at all three locations. The tsunamigenic EP curves of OM 2 and OM 3 intersect with the curves for non-tsunamigenic earthquake (dashed lines) regardless of the elevation. However, the differences among three locations using OM 2 which only considers M_w 9.0 events are significantly lower than those recurrence models that consider multiple magnitudes. Given OM 3, the intersection points of the EP curves of tsunamigenic earthquakes and non-tsunamigenic earthquakes become lower with the increase of elevation, and at R3 the EP curve of tsunamigenic earthquakes is almost below that of non-tsunamigenic earthquakes. For OM 4, the EP curves of tsunamigenic earthquakes are below the counterparts for non-tsunamigenic earthquakes at all three locations, and the differences increase with the rising elevation.

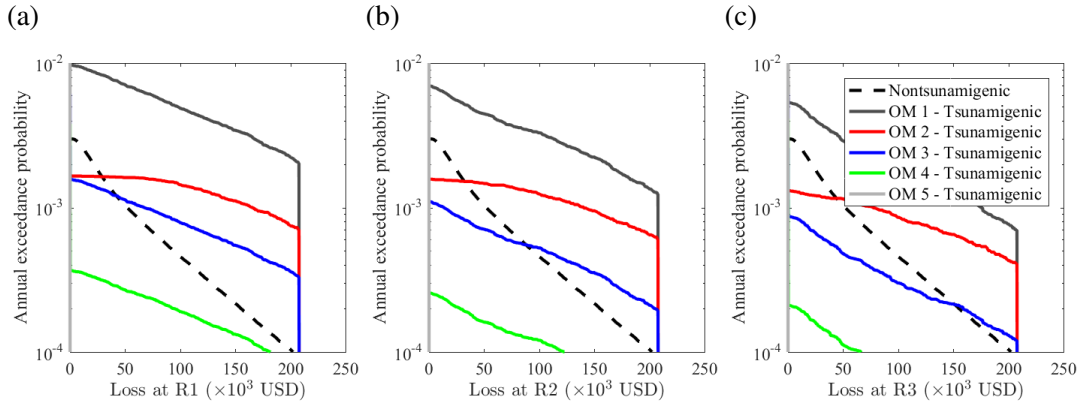

Figure 5.18 Annual EP curves in Onagawa for nontsunamigenic earthquakes and tsunamigenic earthquakes for a wooden structure using 10-m DEM: (a) R1, (b) R2, and (a) R3.

The corresponding insurance pure premiums rates are shown in Table 5.21, and the relative differences of $P_{tsunamigenic}$ and $P_{nontsunamigenic}$ are calculated in Table 5.22. Table 5.22 quantifies the relative importance of tsunamigenic earthquakes and non-

Table 5.21 $P_{tsunamigenic}$ rate for wood structures in Onagawa (per 1000 insured value).

Location	$P_{tsunamigenic}$					P_{total}				
	OM 1	OM 2	OM 3	OM 4	OM 5	OM 1	OM 2	OM 3	OM 4	OM 5
R1	5.21	1.32	0.83	0.20	0.03	5.98	2.10	1.61	0.97	0.81
R2	3.37	1.17	0.53	0.12	0.02	4.15	1.95	1.31	0.90	0.80
R3	2.18	0.85	0.36	0.08	0.01	2.96	1.63	1.14	0.86	0.79

Table 5.22 Relative difference of $P_{tsunamigenic}$ and $P_{nontsunamigenic}$ in Onagawa.

Location	OM 1	OM 2	OM 3	OM 4	OM 5
R1	5.85	0.73	0.09	-0.73	-0.96
R2	3.43	0.53	-0.30	-0.84	-0.97
R3	1.86	0.11	-0.52	-0.89	-0.98

Table 5.23 Contribution of $P_{tsunamigenic}$ to P_{total} in Onagawa.

Location	OM 1	OM 2	OM 3	OM 4	OM 5
R1	0.87	0.62	0.51	0.20	0.03
R2	0.81	0.60	0.40	0.13	0.02
R3	0.73	0.52	0.31	0.09	0.01

tsunamigenic earthquakes. It is clear that the importance of $P_{tsunamigenic}$ is higher than Sendai given the same recurrence model. Compared to Sendai, the high tsunami risk in Onagawa also leads to higher contributions of $P_{tsunamigenic}$ in the total multi-hazard premium P_{total}, as indicated by Table 5.23. Given OM 1 and OM 2, in Sendai only at the most risky location P1 (0.5 km from the sea) $P_{tsunamigenic}$ is higher than $P_{nontsunamigenic}$, while in Onagawa this is applicable at all three locations even at the highest location R3 (elevation of 6 m). Due to high tsunami risks, all three locations have higher $P_{tsunamigenic}$ than $P_{nontsunamigenic}$ which is 0.76 per 1000 insured value, using OM 1 and OM 2. For all recurrence models considered, $P_{tsunamigenic}$ becomes smaller with the increase of elevation, while in Sendai at certain distances from the sea where seismic risk becomes dominant, the increase of site-to-coast distance does not reduce $P_{tsunamigenic}$.

It can be found in Table 5.23 and Table 5.21 that the contribution of tsunamigenic events largely depends on the selected recurrence model, and when the contribution of $P_{tsunamigenic}$ to P_{total} is low the elevation has little influence on P_{total}. A reduced contribution of $P_{tsunamigenic}$ is seen from OM 1 to OM 5 with a decreased occurrence rate. As shown in Table 5.22, at R1 $P_{tsunamigenic}$ is higher than $P_{nontsunamigenic}$ by almost

a factor of 6 of $P_{nontsunamigenic}$ using OM 1, while $P_{tsunamigenic}$ is only 73% higher than $P_{nontsunamigenic}$ using OM 2. When OM 5 which gives the lowest occurrence rate is used, P_{total} is similar for all three locations, while a significant decrease of P_{total} is seen from R1 to R3 using OM 1. The increase of elevation reduces the contribution of tsunami risk to P_{total}. Taking OM 3 for example, the contribution of $P_{tsunamigenic}$ is 52% of P_{total} at R1, and this percentage is reduced to 42% and 32% at R2, and R3, respectively. The occurrence rate is dependent on the selected recurrence model for tsunamigenic earthquakes, and it determines the weight of $P_{tsunamigenic}$ in P_{total}, which is related to the importance of elevation for multi-hazard rate-making.

5.6 Summary and conclusions

A new multi-hazard earthquake-tsunami insurance rate-making method was developed in this chapter by considering both earthquakes (tsunamigenic and non-tsunamigenic) and tsunamis. This method bridged the gap in the current multi-hazard earthquake-tsunami catastrophe modelling that seismic risk and tsunami risk are modelled separately without considering the link between them, since shaking and tsunami are caused by the common earthquake sources and their occurrence rates. Treating mega-thrust subduction earthquakes as a series of hazards, effects due to the uncertain earthquake occurrence were investigated by considering multiple time-dependent recurrence models with different model parameters. The pure premium rates were calculated by incorporating the influence of several key attributes on tsunami rate-making, including the elevation data resolution (Chapter 3), the building location (i.e. coastal topography, distance from the coast, and elevation), flow velocity (Chapter 4), structural type, and earthquake recurrence models. The main findings of this chapters are:

- There is great uncertainty in tsunami risk due to the selection of earthquake recurrence models. For a given insurance portfolio of buildings, the tsunami pure premium rate can range from zero to more than 4 per 1000 insured value (note: the commercial earthquake insurance standard rate is 1.97 per 1000 insured value including risk premium and expenses) due to the uncertain tsunami occurrence rate.
- For the fair pricing of tsunami insurance, the distance from the coast and land elevation should be taken into account. The increase of distance from the coastline

and increase of elevation significantly reduce the tsunami insurance premium. However, the influence of location attributes depends on the DEM resolution. A coarser DEM is less able to distinguish the geographical differences and tends generate more uniform (and probably biased) premium rates for different locations.

- In Sendai on plain coast, using the 10-m DEM, the rate drops by more than 85% when the distance from the coast increases from 0.5 km to 1.2 km, and the rate is reduced to only 4% of that when the distance is 2 km, while when the 450-m DEM is used the rates are almost uniform, independent of different distances from the coast. Therefore, when a coarse DEM is used for insurance underwriting for a building portfolio on a plain coast, it tends to give more conservative tsunami loss estimation due to incapability of capturing the decreasing tsunami hazard with the increase of distance to the coast. Households at locations farther from the coast with less tsunami risk will end up paying the same premium as those at more dangerous locations.

- In Onagawa on ria coast, which has a rapidly changing land elevation, the local tsunami risk and rate-making is more sensitive to DEM resolution than Sendai. Given the 10-m DEM and the same distance to the coast, the rates for location of 4 m and 6 m are reduced to only about 55% and 28% of that for location of 2 m. The coarser DEM is more likely to assign wrong elevations to particular locations, which results in wrong tsunami risk and rates. When the model grid size is too large for the spatial expansion of building portfolio, the simulated inundation can be biased and unrealistic; this was the case when the 150-m and 450-m are used for Onagawa.

- For tsunami insurance, it is suggested that the finest available DEM be used for rate differentiation, and a suitable rate-differentiation scheme is devised to offer fair premium rates commensurate with actual tsunami risks at insured properties. Uncertainty due to the selection of recurrence models of tsunamigenic earthquakes should also be considered for insurance rate-making.

- For earthquake-tsunami multi-hazard insurance, the relative importance of risk from crustal earthquakes, subduction earthquakes and tsunamis greatly depends on the selected recurrence model for tsunamigenic earthquakes. In addition, the location of a building affects the contributions of these risks. The influence of location is weakened when the contribution of tsunami risk to multi-hazard risk is

low. Locations at different distances from the sea or different elevations, can have similar multi-hazard premium rates but various tsunami insurance premium rates.

Chapter 6

Conclusions and Outlook

6.1 Summary

The objectives of this thesis are to improve the understanding of uncertainties in tsunami catastrophe modelling, entailing components of hazard (event generation and intensity distribution), vulnerability (probabilistic damage given the intensity measures), exposure/building portfolio, and financial loss. The main contribution of this study is that major sources of uncertainty are identified and quantified for tsunami loss estimation. To achieve the goal of the thesis, a case study of two building portfolios located with different geographical features in Miyagi Prefecture, Japan has been discussed. The investigated uncertainties include: i) earthquake source characterisation, ii) DEM resolution, iii) building location (i.e. coastal topography, distance from the coastline, and elevation), iv) selection of tsunami intensity measure (i.e. inundation depth, flow velocity, and momentum flux), v) earthquake recurrence model, and v) dependency of tsunamis on subduction earthquakes. A full tsunami catastrophe modelling is carried out by adopting a stochastic tsunami risk assessment approach. Based on the findings with regard to these uncertainties, a multi-hazard earthquake-tsunami insurance rate-making methodology is proposed and is applied to rate differentiation problem for fair insurance pricing by considering structural and location attributes of insured buildings/properties. Prior to investigations of the above-mentioned issues, Chapter 2 reviews the importance of catastrophe modelling and identified the research gaps in tsunami catastrophe modelling.

For evaluating the uncertainty in earthquake source characterisation, a stochastic tsunami loss estimation method was proposed in Chapter 3 and was employed as the

basic framework throughout the thesis. The novelty of this method is that it considers a wide range of possible earthquake slip models with varied geometry and slip parameters, by using scaling relationships (Goda et al., 2014a, 2016). The approach was implemented for mega-thrust subduction earthquakes, such as the 2011 Tohoku tsunami. Unlike the deterministic or scenario-based tsunami hazard assessment, the new probabilistic tsunami risk assessment (PTRA) results in a set of tsunami hazard maps at different probability levels and is capable of showing the rich hazard and risk information through various visualisation methods. For a given region, both the regional tsunami hazard maps of hundreds of stochastic tsunami scenarios obtained using different intensity measures (inundation depth, flow velocity, or momentum flux) and the probability hazard/risk curve for a specific location can be produced. The variation of tsunami loss estimated caused by stochastic earthquake slip models is able to reflect how the uncertainty in earthquake source characterisation propagates into tsunami risk.

6.2 Conclusions

Based on the stochastic tsunami catastrophe modelling method and focusing on the financial loss, the thesis is composed of three main parts.

Chapter 3 investigated the influence of elevation resolution and building location. DEMs of four resolutions (450-m, 150-m, 50-m, and 10-m) are implemented and compared. The location of a building is characterised by the coastal topography (plain coast represented by Sendai or ria coast represented by Onagawa), distance to the sea, and land elevation. The main conclusions are:

- For tsunami loss estimation, the DEM resolution has greater effects at local level than at regional level. The influence is particularly significant for risk assessment of individual buildings. The regional loss is less sensitive compared to the local loss partly because the coarser DEM tends to underestimate the tsunami intensity at some places, while overestimate it at some other places.
- When the fine elevation data of 10 m resolution are not available, the 50-m DEM gives reasonably good loss estimation results at regional level in Sendai on a plain coast, with less than 10% differences compared to the 10-m resolution case. However, the 50-m DEM is still unable to capture the local variations especially in Onagawa on a ria coast where the elevation changes abruptly. The 150-m and

450-m DEMs are highly unreliable for both Sendai and Onagawa, which can give a dramatically higher loss. Using a coarser DEM tends to underestimate the tsunami loss for areas closer to the sea but overestimate it for farther places. Therefore, differences caused by using a coarse DEM also depend on the locations of buildings in the portfolio. In addition, the tsunami risk at single locations is more sensitive to DEM resolution than regional tsunami losses. When land elevation changes over a small scale, a greater difference is caused by using a coarser DEM.

- Locations closer to the sea have significantly higher tsunami risk than farther locations, particularly for building located within 0.5 km m from the sea. For example, the tsunami risk reduced from 0.5 km to 1 km is much more than the risk reduced from 1 km to 1.5 km. Locations with higher elevation have less tsunami risk, however, the importance of land elevation also depends on the DEM resolution because the coarse DEM is not able to capture the difference of elevation correctly.

- These findings are useful for understanding the basis risk when only DEM of certain resolution is available and facilitate the selection of appropriate DEM resolution depending on the size and location of the building portfolio. For example, using the finest elevation data may not be necessary for loss estimation of a large region because of the significantly increased computation time.

Chapter 4 explored the importance of considering flow velocity and momentum as IM in addition to inundation depth, and the main conclusions are:

- RC buildings are the most sensitive structure type to flow velocity, followed by steel and masonry. Wood structures are not sensitive to consideration of velocity for tsunami loss estimation.

- The importance of flow velocity for tsunami depends on the combination of inundation depth and flow velocity. Generally, flow velocity is important for tsunami waves with relatively low depth and high velocity. The combinations of inundation and flow velocity vary at different locations and need to be determined based on tsunami simulations. For tsunami of low level of inundation (i.e. inundation less than 3 m and velocity less than 3 m/s) on plain coast, flow velocity is not important for steel, wood and masonry structures. Buildings located close to the sea (e.g. less than 1 km) tend to be more sensitive to the consideration of flow velocity because they tend to experience the fastest tsunami waves.

- The importance of flow velocity for regional tsunami loss depend on the tsunami inundation scale and spatial distribution of buildings, because flow velocity is more important for locations close to the sea where higher flow velocity will be experienced. Flow velocity makes more significant differences for a building portfolio in which the majority of buildings are located close to sea (e.g. less than 1 km).

- The improvement by considering momentum flux in addition to inundation depth and flow velocity is limited. At a regional level, the differences caused by either flow velocity or momentum is not significant and thus inundation depth is more suitable for use as it is more convenient to measure while the flow velocity and momentum flux data are very limited in post-event surveys.

Chapter 5 looked into the uncertainty in occurrence rates of mega-thrust subduction earthquakes, and proposed a comprehensive multi-hazard earthquake-tsunami insurance rate-making method by distinguishing structural type, distance from the sea, and lane elevation. The main conclusions are:

- There is great uncertainty in tsunami risk due to the selection of different recurrence models. The uncertainty in occurrence rate of subduction earthquakes is higher than that of crustal earthquakes, because the long return period tends to result in a lack of historical data. The uncertainty comes from not only the selection of probability distribution (e.g. lognormal, Weibull, or BPT) but also the determination of model parameters (i.e. return period and *cov*). Using different earthquake recurrence models, the tsunami insurance pure premium rate can range from zero to twice higher than the commercial earthquake insurance standard rate in Japan.

- Location attributes (i.e. coastal topography, distance from the sea, and land elevation) are suggested to take into account for differentiating tsunami insurance premium rates. However, the differentiation largely depends on the accuracy of DEM for tsunami simulations. On plain coast (e.g. Sendai), a coarser DEM tends to overestimate the rates at locations relatively far from the coastline, which results in more uniform tsunami insurance premium rates. When a coarse DEM is used for insurance underwriting of a building portfolio on a plain coast, it tends to give more conservative and more uniform tsunami risk across the region. The

location farther from the coast with less tsunami risk ends up paying the same premium as those most risky locations if a coarse DEM is used. In Onagawa (ria coast), the tsunami insurance premium rate is more sensitive to DEM resolution than Sendai. Given 10-m DEM and a similar distance from the coastline, the rate for locations of 4 m and 6 m elevation are reduced to only about 55% and 28% of that for location of 2 m. The coarser DEM is more likely to assign wrong elevations for ria coast due to the rapidly changing elevation, and results in wrong tsunami risk and rates. The 150-m and 450-m DEMs are not suggested to use for ria coast.

- The occurrence rates predicted by the recurrence model for subduction earthquakes have major influences on the relative importance of risk from tsunamigenic events and non-tsunamigenic earthquakes. The location of building affects the contributions of these risks as well. In a tsunami-prone area, the seismic risk is almost uniform, while the tsunami risk varies significantly. As a result, locations with different distances from the sea or different elevations, can have similar multi-hazard premium rates but various tsunami risks. For the earthquake-tsunami multi-hazard insurance, the importance of location attributes also depends on occurrence rate of tsunamigenic earthquakes. A low occurrence rate of tsunamis reduces the contribution of tsunamigenic events, and thus weakened the influence of location.

- The finest DEM is suggested to use for tsunami insurance rate differentiation, and a certain discount can be offer to properties farther from the coast or with a higher elevation. Multiple possible recurrence models can be applied for insurance rate-making to view the range of loss or applied in a logic tree approach, to deal with the uncertainty of occurrence rate.

6.3 Future research

Focusing on tsunami catastrophe modelling for insurance purposes, the work presented in this thesis can be extended in other directions. Several ideas for future research include:

- Heterogeneous slip models have been developed as more advanced approach than the standard uniform slip models. The tsunami hazard intensity may be

significantly underestimated when uniform slip models are adopted (Muhammad and Goda, 2018), and differences caused by using heterogeneous and uniform slip models have not been thoroughly understood. Therefore, an investigation of influence of earthquake source model complexity (i.e. uniform slip model and heterogeneous slip model) for tsunami loss estimation can be conducted.

- The sensitivity of tsunami modelling to surface roughness needs to be investigated, including micro-roughness and macro-roughness. The influence of macro-roughness is not considered in this thesis. Surface roughness is assigned uniformly depending on the category of land use (i.e. agricultural, ocean/water, forest vegetation, low-density residential, moderate-density residential, or high-density residential).

- Only Sendai and Onagawa are used as representatives of plain coast and ria coast. More locations along the north-east coast of the Tohoku region of Japan need to be considered to draw more general conclusions with regards to the effect of coastal topography.

- In the multi-hazard earthquake-tsunami loss estimation and rate-making method developed in this thesis, the earthquake damage and tsunami damage are assessed separately using seismic fragility functions and tsunami fragility functions, respectively. The underlying empirical data for developing those fragility models are not consistent (i.e. not collected from the same events and not in the same region). The limitation of adopting such an approach is due to the lack of earthquake-tsunami fragility functions which consider the accumulation of damage from earthquake loading and tsunami loading in sequence. For example, empirical earthquake-tsunami fragility surfaces based on the 2011 Tohoku earthquake and tsunami can be developed using both tsunami IM (e.g. inundation depth) and seismic IM (e.g. pgv) through multinomial regression analysis. Besides, analytical earthquake-tsunami fragility functions can be developed through structural analysis by loading earthquake forces and tsunami forces in sequence.

- In the multi-hazard insurance rate-making method, existing hazard information of crustal earthquake is obtained from the J-SHIS. There is significant uncertainty involved due to the missing information about underlying methods (e.g. how seismic intensity is predicted). For the consistency of data and methodology, a comprehensive probabilistic seismic hazard assessment should be carried out by considering both subduction earthquakes and crustal earthquakes.

- The multi-hazard loss estimation can be implemented for designing the trigger mechanism of parametric catastrophe bonds for mega-subduction earthquakes and triggered tsunamis. Goda et al. (2019) designed a CAT-in-a-box trigger with intensity-based index trigger mechanisms using a new seafloor observation network S-net off the Tohoku-Hokkaido coast of Japan, which contains both seismic and tsunami recording stations. Their method can be extended to include seismic effects as well.

References

Abaimov, S. G., Turcotte, D. L., Shcherbakov, R., Rundle, J. B., Yakovlev, G., Goltz, C., and Newman, W. I. (2008). Earthquakes: Recurrence and interoccurrence times. *Pure and Applied Geophysics*, 165(3-4):777–795.

AIR (2013). Seismic Risk Assessment Must Include Tsunami. https://www.air-worldwide.com/Publications/AIR-Currents/2013/Introducing-The-Industry's-First-Fully-Probabilistic-Tsunami-Model/. Accessed: 2018-04-01.

Akaike, H. (1974). A new look at the statistical model identification. *IEEE Transactionson Automatic Control*, 19(6):716–723.

Ammon, C. J., Lay, T., Kanamori, H., and Cleveland, M. (2011). A rupture model of the 2011 off the Pacific coast of Tohoku Earthquake. *Earth, Planets and Space*, 63(7):693–696.

Anagnos, T. and Kiremidjian, A. S. (1988). A review of earthquake occurrence models for seismic hazard analysis. *Probabilistic Engineering Mechanics*, 3(1):3–11.

Annaka, T., Satake, K., Sakakiyama, T., Yanagisawa, K., and Shuto, N. (2007). Logic-tree approach for probabilistic tsunami hazard analysis and its applications to the Japanese coasts. In *Pure and Applied Geophysics*, volume 164, pages 577–592.

Barani, S. and Spallarossa, D. (2017). Soil amplification in probabilistic ground motion hazard analysis. *Bulletin of Earthquake Engineering*, 15(6):2525–2545.

Blaser, L., Krüger, F., Ohrnberger, M., and Scherbaum, F. (2010). Scaling relations of earthquake source parameter estimates with special focus on subduction environment. *Bulletin of the Seismological Society of America*, 100(6):2914–2926.

Bommer, J. J., Douglas, J., Scherbaum, F., Cotton, F., Bungum, H., and Fah, D. (2010). On the selection of ground-motion prediction equations for seismic hazard analysis. *Seismological Research Letters*, 81(5):783–793.

Borrero, J. C. (2005). Field survey of northern Sumatra and Banda Aceh, Indonesia after the tsunami and earthquake of 26 December 2004. *Seismological Research Letters*, 76(3):312–320.

Braun, A. (2016). Pricing in the Primary Market for Cat Bonds: New Empirical Evidence. *Journal of Risk and Insurance*, 83(4):811–847.

Burbidge, D., Cummins, P. R., Mleczko, R., and Thio, H. K. (2008). A probabilistic tsunami hazard assessment for Western Australia. *Pure and Applied Geophysics*, 165(11-12):2059–2088.

Charvet, I., Ioannou, I., Rossetto, T., Suppasri, A., and Imamura, F. (2014a). Empirical fragility assessment of buildings affected by the 2011 Great East Japan tsunami using improved statistical models. *Natural Hazards*, 73(2):951–973.

Charvet, I., Macabuag, J., and Rossetto, T. (2017). Estimating tsunami-induced building damage through fragility functions: critical review and research needs. *Frontiers in Built Environment*, 3:36.

Charvet, I., Suppasri, A., and Imamura, F. (2014b). Empirical fragility analysis of building damage caused by the 2011 Great East Japan tsunami in Ishinomaki city using ordinal regression, and influence of key geographical features. *Stochastic Environmental Research and Risk Assessment*, 28(7):1853–1867.

Charvet, I., Suppasri, A., Kimura, H., Sugawara, D., and Imamura, F. (2015). A multivariate generalized linear tsunami fragility model for Kesennuma City based on maximum flow depths, velocities and debris impact, with evaluation of predictive accuracy. *Natural Hazards*, 79(3):2073–2099.

Console, R., Murru, M., Falcone, G., and Catalli, F. (2008). Stress interaction effect on the occurrence probability of characteristic earthquakes in Central Apennines. *Journal of Geophysical Research: Solid Earth*, 113(8):1–18.

Construction Research Institute (2011). *Japan building cost information*. Tokyo.

Cramer, C. H., Petersen, M. D., Cao, T., Toppozada, T. R., and Reichle, M. (2000). A time-dependent probabilistic seismic-hazard model for California. *Bulletin of the Seismological Society of America*, 90(1):1–21.

Cummins, J. D. (2008). CAT bonds and other risk-linked securities: state of the market and recent developments. *Risk Management and Insurance Review*, 11(1):23–47.

Cummins, J. D. and Mahul, O. (2004). The demand for insurance with an upper limit on coverage. *Journal of Risk and Insurance*, 71(2):253–264.

Cummins, J. D. and Weiss, M. A. (2009). Convergence of insurance and financial markets: Hybrid and securitized risk-transfer solutions. *Journal of Risk and Insurance*, 76(3):493–545.

Dao, M. H. and Tkalich, P. (2007). Tsunami propagation modelling - a sensitivity study. *Natural Hazards and Earth System Science*, 7:741–754.

Davies, G., Horspool, N., and Miller, V. (2015). Tsunami inundation from heterogeneous earthquake slip distributions: Evaluation of synthetic source models. *Journal of Geophysical Research: Solid Earth*, 120(9):6431–6451.

De Risi, R. and Goda, K. (2016). Probabilistic earthquake–tsunami multi-hazard analysis: application to the Tohoku region, Japan. *Frontiers in Built Environment*, 2:25.

De Risi, R., Goda, K., Yasuda, T., and Mori, N. (2017). Is flow velocity important in tsunami empirical fragility modeling? *Earth-Science Reviews*, 166:64–82.

Dias, W. P. S., Yapa, H. D., and Peiris, L. M. N. (2009). Tsunami vulnerability functions from field surveys and Monte Carlo simulation. *Civil Engineering and Environmental Systems*, 26(2):181–194.

Dong, W. and Grossi, P. (2005). Insurance portfolio management. In *Catastrophe modeling: a new approach to managing risk*. New York: Springer.

Douglas, J. and Edwards, B. (2016). Recent and future developments in earthquake ground motion estimation. *Earth-Science Reviews*, 160:203–219.

Ellsworth, W. L., Matthews, M., and Nadeau, R. (1999). A physically based earthquake recurrence model for estimation of long-term earthquake probabilities.

FEMA (2012). Guidelines for design of structures for vertical evacuation from tsunamis.

Fewtrell, T. J., Bates, P. D., Horritt, M., and Hunter, N. M. (2008). Evaluating the effect of scale in flood inundation modelling in urban environments. *Hydrological Processes*, 22(26):5107–5118.

Field, E. H., Dawson, T. E., Felzer, K. R., Frankel, A. D., Gupta, V., Jordan, T. H., Parsons, T., Petersen, M. D., Stein, R. S., Weldon, R. J., and Wills, C. J. (2009). Uniform California earthquake rupture forecast, version 2 (UCERF 2). *Bulletin of the Seismological Society of America*, 99(4):2053–2107.

Field, E. H. and Jordan, T. H. (2015). Time-dependent renewal-model probabilities when date of last earthquake is unknown. *Bulletin of the Seismological Society of America*, 105(1):459–463.

Fitzenz, D. D. and Nyst, M. (2015). Building time-dependent earthquake recurrence models for probabilistic risk computations. *Bulletin of the Seismological Society of America*, 105(1):120–133.

Franco, G. (2010). Minimization of trigger error in cat-in-a-box parametric earthquake catastrophe bonds with an application to Costa Rica. *Earthquake Spectra*, 26(4):983–998.

Fraser, S., Raby, A., Pomonis, A., Goda, K., Chian, S. C., Macabuag, J., Offord, M., Saito, K., and Sammonds, P. (2013). Tsunami damage to coastal defences and buildings in the March 11th 2011 M_w 9.0 Great East Japan earthquake and tsunami. *Bulletin of Earthquake Engineering*, 11:205–239.

Fraser, S. A., Power, W. L., Wang, X., Wallace, L. M., Mueller, C., and Johnston, D. M. (2014). Tsunami inundation in Napier, New Zealand, due to local earthquake sources. *Natural Hazards*, 70(1):415–445.

Fritz, H., Borrero, J., Synolakis, C., and Yoo, J. (2006). 2004 Indian Ocean tsunami flow velocity measurements from survivor videos. *Geophysical Research Letters*, 33(24).

Frohlich, C. and Wetzel, L. R. (2007). Comparison of seismic moment release rates along different types of plate boundaries. *Geophysical Journal International*, 171(2):909–920.

Fujii, Y. and Satake, K. (2007). Tsunami source of the 2004 Sumatra-Andaman earthquake inferred from tide gauge and satellite data. *Bulletin of the Seismological Society of America*, 97(1A):S192–S207.

Fujii, Y., Satake, K., Sakai, S., Shinohara, M., and Kanazawa, T. (2011). Tsunami source of the 2011 off the Pacific coast of Tohoku Earthquake. *Earth, Planets and Space*, 63(7):815–820.

Fukutani, Y., Suppasri, A., and Imamura, F. (2015). Stochastic analysis and uncertainty assessment of tsunami wave height using a random source parameter model that targets a Tohoku-type earthquake fault. *Stochastic Environmental Research and Risk Assessment*, 29(7):1763–1779.

Garavaglia, E., Guagenti, E., Pavani, R., Petrini, L., Garavaglia, E., Guagenti, E., Pavani, R., and Renewal, L. P. (2010). Renewal models for earthquake predictability. *Journal of Seismology*, 14(1):79–93.

García, D., Wald, D. J., and Hearne, M. G. (2012). A global earthquake discrimination scheme to optimize ground-motion prediction equation selection. *Bulletin of the Seismological Society of America*, 102(1):185–203.

Geist, E. L. (2002). Complex earthquake rupture and local tsunamis. *Journal of Geophysical Research B: Solid Earth*, 107(5).

Geist, E. L. and Parsons, T. (2006). Probabilistic analysis of tsunami hazards. *Natural Hazards*, 37(3):277–314.

Geist, E. L. and Parsons, T. (2011). Assessing historical rate changes in global tsunami occurrence. *Geophysical Journal International*, 187(1):497–509.

Gibson, R., Habib, M. A., and Ziegler, A. (2014). Reinsurance or securitization: The case of natural catastrophe risk. *Journal of Mathematical Economics*, 53:79–100.

Goda, K. (2015a). Effects of seabed surface rupture versus buried rupture on tsunami wave modeling: A case study for the 2011 Tohoku, Japan, earthquake. *Bulletin of the Seismological Society of America*, 105(5):2563–2571.

Goda, K. (2015b). Seismic risk management of insurance portfolio using catastrophe bonds. *Computer-Aided Civil and Infrastructure Engineering*, 30(7):570–582.

Goda, K. and De Risi, R. (2017). Probabilistic tsunami loss estimation methodology: Stochastic earthquake scenario approach. *Earthquake Spectra*, 33(4):1301–1323.

Goda, K. and De Risi, R. (2018). Multi-hazard loss estimation for shaking and tsunami using stochastic rupture sources. *International Journal of Disaster Risk Reduction*, 28:539–554.

Goda, K., Franco, G., Song, J., and Radu, A. (2019). Parametric Catastrophe Bonds for Tsunamis: CAT-in-a-Box trigger and intensity-based index trigger methods. *Earthquake Spectra*, 35(1):113–136.

Goda, K., Mai, P. M., Yasuda, T., and Mori, N. (2014a). Sensitivity of tsunami wave profiles and inundation simulations to earthquake slip and fault geometry for the 2011 Tohoku earthquake. *Earth, Planets and Space*, 66(1):1–20.

Goda, K. and Song, J. (2016). Uncertainty modeling and visualization for tsunami hazard and risk mapping: a case study for the 2011 Tohoku earthquake. *Stochastic Environmental Research and Risk Assessment*, 30(8):2271–2285.

Goda, K., Wenzel, F., and Daniell, J. (2014b). Insurance and reinsurance models for earthquake. In Beer, M., Patelli, E., Kougioumtzoglou, I., and Au, I. S.-K., editors, *Encyclopedia of Earthquake Engineering*. Springer.

Goda, K., Yasuda, T., Mori, N., and Maruyama, T. (2016). New scaling relationships of earthquake source parameters for stochastic tsunami simulations. *Coastal Engineering Journal*, 58(3):1–40.

Gomberg, J., Belardinelli, M. E., Cocco, M., and Reasenberg, P. (2005). Time-dependent earthquake probabilities. *Journal of Geophysical Research: Solid Earth*, 110(5):1–12.

González, Á., Gómez, J. B., and Pacheco, A. F. (2006). Updating seismic hazard at Parkfield. *Journal of Seismology*, 10(2):131–135.

González, F. I., Geist, E. L., Jaffe, B., Kânoğlu, U., Mofjeld, H., Synolakis, C. E., Titov, V. V., Areas, D., Bellomo, D., Carlton, D., Horning, T., Johnson, J., Newman, J., Parsons, T., Peters, R., Peterson, C., Priest, G., Venturato, A., Weber, J., Wong, F., and Yalciner, A. (2009). Probabilistic tsunami hazard assessment at Seaside, Oregon, for near-and far-field seismic sources. *Journal of Geophysical Research: Oceans*, 114(11):1–19.

Goto, C., Ogawa, Y., and Shuto, N. (1997). Numerical method of tsunami simulation with the leap-frog scheme.

Gray, R. J. and Pitts, S. M. (2012). *Risk modelling in general insurance: From principles to practice*. Cambridge University Press.

Grezio, A., Babeyko, A., Baptista, M. A., Behrens, J., Costa, A., Davies, G., Geist, E. L., Glimsdal, S., González, F. I., Griffin, J., Harbitz, C. B., LeVeque, R. J., Lorito, S., Løvholt, F., Omira, R., Mueller, C., Paris, R., Parsons, T., Polet, J., Power, W., Selva, J., Sørensen, M. B., and Thio, H. K. (2017). Probabilistic tsunami hazard analysis: Multiple sources and global applications. *Reviews of Geophysics*, 55:1158–1198.

Griffin, J., Latief, H., Kongko, W., Harig, S., Horspool, N., Hanung, R., Rojali, A., Maher, N., Fuchs, A., Hossen, J., Upi, S., Edi Dewanto, S., Rakowsky, N., and Cummins, P. (2015). An evaluation of onshore digital elevation models for modeling tsunami inundation zones. *Frontiers in Earth Science*, 3:1–16.

Grossi, P. and Kunreuther, H. (2005). *Catastrophe modeling: a new approach to managing risk*. Springer, New York.

Gusman, A. R., Tanioka, Y., Sakai, S., and Tsushima, H. (2012). Source model of the great 2011 Tohoku earthquake estimated from tsunami waveforms and crustal deformation data. *Earth and Planetary Science Letters*, 341:234–242.

Gutenberg, B. and Richter, C. (1956). Magnitude and energy of earthquakes. *Annals of Geophysics*, 9(1):1–15.

Hagendorff, B., Hagendorff, J., Keasey, K., and Gonzalez, A. (2014). The risk implications of insurance securitization: The case of catastrophe bonds. *Journal of Corporate Finance*, 25:387–402.

Hanks, T. C. and Kanamori, H. (1979). A moment magnitude scale. *Journal of Geophysical Research B: Solid Earth*, 84(B5):2348–2350.

Hayashi, S. and Koshimura, S. (2013). The 2011 Tohoku tsunami flow velocity estimation by the aerial video analysis and numerical modeling. *Journal of Disaster Research*, 8(4):561–572.

Hayashi, S., Narita, Y., and Koshimura, S. (2013). Developing tsunami fragility curves from the surveyed data and numerical modeling of the 2011 Tohoku earthquake tsunami (in Japanese). *Journal of Japan Society of Civil Engineers (Coastal Engineering)*, 69:1–5.

Hayes, G. P. (2011). Rapid source characterization of the 2011 Mw 9.0 off the Pacific coast of Tohoku earthquake. *Earth, Planets and Space*, 63(7):529–534.

Headquarters for Earthquake Research Promotion (HERP) (2013). Investigations of future seismic hazard assessment.

Heidarzadeh, M. and Kijko, A. (2011). A probabilistic tsunami hazard assessment for the Makran subduction zone at the northwestern Indian Ocean. *Natural Hazards*, 56(3):577–593.

Heidarzadeh, M., Muhari, A., and Wijanarto, A. B. (2018). Insights on the source of the 28 September 2018 Sulawesi tsunami, Indonesia based on spectral analyses and numerical simulations. *Pure and Applied Geophysics*, 176:25–43.

Hosmer, D. W., Lemeshow, S., and Sturdivant, R. X. (2013). *Applied Logistic Regression*. John Wiley & Sons.

Iinuma, T., Hino, R., Kido, M., Inazu, D., Osada, Y., Ito, Y., Ohzono, M., Tsushima, H., Suzuki, S., and Fujimoto, H. (2012). Coseismic slip distribution of the 2011 off the Pacific Coast of Tohoku Earthquake (M9. 0) refined by means of seafloor geodetic data. *Journal of Geophysical Research: Solid Earth*, 117(B7).

Imamura, F., Muhari, A., Mas, E., Pradono, M. H., Post, J., and Sugimoto, M. (2012). Tsunami disaster mitigation by integrating comprehensive countermeasures in Padang city, Indonesia. *Journal of Disaster Research*, 7(1):48–64.

Ioualalen, M., Asavanant, J., Kaewbanjak, N., Grilli, S. T., Kirby, J. T., and Watts, P. (2007). Modeling the 26 December 2004 Indian Ocean tsunami: Case study of impact in Thailand. *Journal of Geophysical Research: Oceans*, 112(7):1–21.

Japan Cabinet Office (2013). Residential disaster damage accreditation criteria operational guideline.

Kaczmarska, J., Jewson, S., and Bellone, E. (2018). Quantifying the sources of simulation uncertainty in natural catastrophe models. *Stochastic Environmental Research and Risk Assessment*, 32(3):591–605.

Kagan, Y. Y. and Jackson, D. D. (2013). Tohoku earthquake: a surprise? *Bulletin of the Seismological Society of America*, 103(2B):1181–1194.

Kaiser, G., Scheele, L., Kortenhaus, A., Løvholt, F., Römer, H., and Leschka, S. (2011). The influence of land cover roughness on the results of high resolution tsunami inundation modeling. *Natural Hazards and Earth System Science*, 11(9):2521–2540.

Kajitani, Y., Chang, S. E., and Tatano, H. (2013). Economic Impacts of the 2011 Tohoku-oki earthquake and tsunami. *Earthquake Spectra*, 29(S1):S457–S478.

Kanamori, H. (1972). Mechanism of tsunami earthquakes. *Physics of the Earth and Planetary Interiors*, 6(5):346–359.

Kawahara, M., Takeuchi, N., and Yoshida, T. (1978). Two step explicit finite element method for tsunami wave propagation analysis. *International Journal for Numerical Methods in Engineering*, 12(2):331–351.

Kazama, M. and Noda, T. (2012). Damage statistics (Summary of the 2011 off the Pacific coast of Tohoku earthquake damage). *Soils and Foundations*, 52(5):780–792.

Koshimura, S. and Kayaba, S. (2010). Tsunami fragility inferred from the 1993 Hokkaido Nansei-oki earthquake tsunami disaster. *Journal of Japan Association for Earthquake Engineering*, 10(3):87–101.

Koshimura, S., Oie, T., Yanagisawa, H., and Imamura, F. (2009). Developing fragility functions for tsunami damage estimation using numerical model and post-tsunami data from Banda Aceh, Indonesia. *Coastal Engineering Journal*, 51(03):243–273.

Kunreuther, H. (1996). Mitigating disaster losses through insurance. *Journal of Risk and Uncertainty*, 12:171–187.

Kunz, M., Grêt-Regamey, A., and Hurni, L. (2011). Visualization of uncertainty in natural hazards assessments using an interactive cartographic information system. *Natural Hazards*, 59(3):1735–1751.

Kusaka, A., Ishida, H., Torisawa, K., Doi, H., and Yamada, K. (2015). Vulnerability functions in terms of ground motion characteristics for wooden houses evaluated by use of earthquake insurance experience. *AIJ Journal of Technology and Design*, 21(48):527–532.

Kuzak, D. and Larsen, T. (2005). Use of catastrophe models in insurance rate making. In Grossi, P. and Kunreuther, H., editors, *Catastrophe modeling: a new approach to managing risk*. Springer, New York.

Lakdawalla, D. and Zanjani, G. (2012). Catastrophe bonds, reinsurance, and the optimal collateralization of risk transfer. *Journal of Risk and Insurance*, 79(2):449–476.

Lalonde, D. (2005). Risk financing. In *Catastrophe modeling: a new approach to managing risk*, page 31. New York: Springer.

Latcharote, P., Suppasri, A., Yamashita, A., Adriano, B., Koshimura, S., Kai, Y., and Imamura, F. (2017). Possible failure mechanism of buildings overturned during the 2011 Great East Japan tsunami in the town of Onagawa. *Frontiers in Built Environment*, 3.

Lavallée, D., Liu, P., and Archuleta, R. J. (2006). Stochastic model of heterogeneity in earthquake slip spatial distributions. *Geophysical Journal International*, 165(2):622–640.

Lay, T., Ammon, C. J., Kanamori, H., Xue, L., and Kim, M. J. (2011). Possible large near-trench slip during the 2011 M_w 9.0 off the Pacific coast of Tohoku Earthquake. *Earth, Planets and Space*, 63(7):687–692.

Le Billon, P. and Waizenegger, A. (2007). Peace in the wake of disaster? Secessionist conflicts and the 2004 Indian Ocean tsunami. *Transactions of the Institute of British Geographers*, 32(3):411–427.

Lee, C. P. and Tsai, Y. B. (2005). A study of recurrence models of earthquakes in Taiwan. *Terrestrial, Atmospheric and Oceanic Sciences*, 16(1):251–271.

Leelawat, N., Suppasri, A., Charvet, I., and Imamura, F. (2014). Building damage from the 2011 Great East Japan tsunami: quantitative assessment of influential factors. *Natural Hazards*, 73(2):449–471.

Leelawat, N., Suppasri, A., Charvet, I., Kimura, T., Sugawara, D., and Imamura, F. (2015). A study on influential factors on building damage in Kesennuma, Japan from the 2011 Great East Japan Tsunami. *Engineering Journal*, 19(3):105–116.

Lipa, B., Isaacson, J., Nyden, B., and Barrick, D. (2012). Tsunami arrival detection with high frequency (HF) radar. *Remote Sensing*, 4(5):1448–1461.

Løvholt, F., Pedersen, G., Bazin, S., Kühn, D., Bredesen, R. E., and Harbitz, C. (2012). Stochastic analysis of tsunami runup due to heterogeneous coseismic slip and dispersion. *Journal of Geophysical Research: Oceans*, 117(C3).

Lynett, P. and Liu, P. L. (2011). Numerical simulation of complex tsunami behavior. *Computing in Science and Engineering*, 13(4):50–57.

Macabuag, J., Rossetto, T., Ioannou, I., Suppasri, A., Sugawara, D., Adriano, B., Imamura, F., Eames, I., and Koshimura, S. (2016). A proposed methodology for deriving tsunami fragility functions for buildings using optimum intensity measures. *Natural Hazards*, 84(2):1257–1285.

MacEachren, A. M., Robinson, A., Hopper, S., Gardner, S., Murray, R., Gahegan, M., and Hetzler, E. (2005). Visualizing geospatial information uncertainty: What we know and what we need to know. *Cartography and Geographic Information Science*, 32(3):139–160.

Mai, P. M. and Beroza, G. C. (2002). A spatial random field model to characterize complexity in earthquake slip. *Journal of Geophysical Research: Solid Earth*, 107(B11).

Mai, P. M. and Thingbaijam, K. K. S. (2014). SRCMOD: an online database of finite-fault rupture models. *Seismological Research Letters*, 85(6):1348–1357.

Mariani, M. and Amoruso, P. (2016). The effectiveness of catastrophe bonds in portfolio diversification. *International Journal of Economics and Financial Issues*, 6(4):1760–1767.

Maruyama, Y., Kitamura, K., and Yamazaki, F. (2013). Tsunami damage assessment of buildings in Chiba Prefecture , Japan using fragility function developed after the 2011 Tohoku-Oki Earthquake. In *Safety, Reliability, Risk and Life-Cycle Performance of Structures & Infrastructures*, pages 4237–4244.

Matthews, M. V., Ellsworth, W. L., and Reasenberg, P. A. (2002). A brownian model for recurrent earthquakes. *Bullentin of the Seismological Society of America*, 92(6):2233–2250.

McCloskey, J., Antonioli, A., Piatanesi, A., Sieh, K., Steacy, S., Nalbant, S., Cocco, M., Giunchi, C., Huang, J., and Dunlop, P. (2008). Tsunami threat in the Indian Ocean from a future megathrust earthquake west of Sumatra. *Earth and Planetary Science Letters*, 265(1):61–81.

Melgar, D., LeVeque, R. J., Dreger, D. S., and Allen, R. M. (2016). Kinematic rupture scenarios and synthetic displacement data: An example application to the Cascadia subduction zone. *Journal of Geophysical Research: Solid Earth*, (121):6658–6674.

Midorikawa, S., Ito, Y., and Miura, H. (2011). Vulnerability functions of buildings based on damage survey data of earthquake after the 1995 Kobe Earthquake. *Journal of Japan Association for Earthquake Engineering*, 11(4):34–47.

Mitchell-Wallace, K., Foote, M., Jones, M., and Hillier, J. (2017). *Natural catastrophe risk management and modelling: a practitioner's guide*. John Wiley & Sons.

MLIT (2014). Survey of tsunami damage condition. http://www.mlit.go.jp/toshi/toshi-hukkou-arkaibu.html. Accessed: 2016-03-01.

Montalva, G. A., Bastías, N., and Rodriguez-Marek, A. (2017). Ground-motion prediction equation for the Chilean subduction zone. *Bulletin of the Seismological Society of America*, 107(2):901–911.

Mori, N., Cox, D. T., Yasuda, T., and Mase, H. (2013). Overview of the 2011 Tohoku earthquake tsunami damage and its relation to coastal protection along the Sanriku coast. *Earthquake Spectra*, 29(S1):127–143.

Mori, N., Takahashi, T., and The Tohoku Earthquake Tsunami Joint Survey Group (2012). Nationwide post event survey and analysis of the 2011 Tohoku earthquake tsunami. *Coastal Engineering Journal*, 54(01):1250001.

Mori, N., Takahashi, T., Yasuda, T., and Yanagisawa, H. (2011). Survey of 2011 Tohoku earthquake tsunami inundation and run-up. *Geophysical Research Letters*, 38(7):L00G14.

Morikawa, N. and Fujiwara, H. (2013). A new ground motion prediction equation for Japan applicable up to M9 mega-earthquake. *Journal of Dsaster Research*, 8(5):878–888.

Mueller, C., Power, W., Fraser, S., and Wang, X. (2015). Effects of rupture complexity on local tsunami inundation: Implications for probabilistic tsunami hazard assessment by example. *Journal of Geophysical Research: Solid Earth*, 120(1):488–502.

Muhammad, A. and Goda, K. (2018). Impact of earthquake source complexity and land elevation data resolution on tsunami hazard assessment and fatality estimation. *Computers and Geosciences*, 112:83–100.

Murata, S., Imamura, F., Katoh, K., Kawata, Y., Takahashi, S., and Takayama, T. (2010). *Tsunami: To survive from tsunami*. World Scientific.

Murotani, S., Satake, K., and Fujii, Y. (2013). Scaling relations of seismic moment, rupture area, average slip, and asperity size for M9 subduction-zone earthquakes. *Geophysical Research Letters*, 40(19):5070–5074.

Naito, C., Cercone, C., Riggs, H. R., and Cox, D. (2013). Procedure for site assessment of the potential for tsunami debris impact. *Journal of Waterway, Port, Coastal, and Ocean Engineering*, 140(2):223–232.

Narita, Y. and Koshimura, S. (2015). Classification of tsunami fragility curves based on regional characteristics of tsunami damage (in Japnese). *Journal of Japan Society of Civil Engineers, Ser.B2 (Coastal Engineering)*, 71(2):I_331–I_336.

Nielson, B. G. and DesRoches, R. (2007). Seismic fragility methodology for highway bridges using a component level approach. *Earthquake Engineering and Structural Dynamics*, 36(6):823–839.

Nomura, S., Ogata, Y., Komaki, F., and Toda, S. (2011). Bayesian forecasting of recurrent earthquakes and predictive performance for a small sample size. *Journal of Geophysical Research: Solid Earth*, 116(4).

Okada, Y. (1985). Surface deformation due to shear and tensile faults in a half-space. *Bulletin of the Seismological Society of Americaociety of America*, 75(4):1135–1154.

Ozawa, S., Nishimura, T., Suito, H., Kobayashi, T., Tobita, M., and Imakiire, T. (2011). Coseismic and postseismic slip of the 2011 magnitude-9 Tohoku-Oki earthquake. *Nature*, 475(7356):373–377.

Pardo-Igúzquiza, E. and Chica-Olmo, M. (1993). The Fourier integral method: an efficient spectral method for simulation of random fields. *Mathematical geology*, 25(2):177.

Park, H. and Cox, D. T. (2016). Probabilistic assessment of near-field tsunami hazards: Inundation depth, velocity, momentum flux, arrival time, and duration applied to Seaside, Oregon. *Coastal Engineering*, 117:79–96.

Park, H., Cox, D. T., and Barbosa, A. R. (2017). Comparison of inundation depth and momentum flux based fragilities for probabilistic tsunami damage assessment and uncertainty analysis. *Coastal Engineering*, 122:10–26.

Park, H., Cox, D. T., Lynett, P. J., Wiebe, D. M., and Shin, S. (2013). Tsunami inundation modeling in constructed environments: A physical and numerical comparison of free-surface elevation, velocity, and momentum flux. *Coastal Engineering*, 79:9–21.

Park, S., van de Lindt, J. W., Cox, D., Gupta, R., and Aguiniga, F. (2012). Successive earthquake-tsunami analysis to develop collapse fragilities. *Journal of Earthquake Engineering*, 16(6):851–863.

Parsons, T., Console, R., Falcone, G., Murru, M., and Yamashina, K. (2012). Comparison of characteristic and Gutenberg-Richter models for time-dependent M 7.9 earthquake probability in the Nankai-Tokai subduction zone, Japan. *Geophysical Journal International*, 190(3):1673–1688.

Parsons, T. and Geist, E. L. (2008). *Tsunami probability in the Caribbean region*, pages 2089–2116. Birkhäuser Basel.

Petrone, C., Rossetto, T., and Goda, K. (2017). Fragility assessment of a RC structure under tsunami actions via nonlinear static and dynamic analyses. *Engineering Structures*, 136:36–53.

Potter, K., Kniss, J., Riesenfeld, R., and Johnson, C. R. (2010). Visualizing summary statistics and uncertainty. In *Computer Graphics Forum*, volume 29, pages 823–832. Wiley Online Library.

Power, W., Downes, G., and Stirling, M. (2007). Estimation of tsunami hazard in New Zealand due to South American earthquakes. *Pure and Applied Geophysics*, 164(2-3):547–564.

Reese, S., Bradley, B. A., Bind, J., Smart, G., Power, W., and Sturman, J. (2011). Empirical building fragilities from observed damage in the 2009 South Pacific tsunami. *Earth-Science Reviews*, 107(1):156–173.

RMS (2012). Cat bonds demystified RMS guide to the asset class.

Sangati, M. and Borga, M. (2009). Influence of rainfall spatial resolution on flash flood modelling. *Natural Hazards and Earth System Science*, 9(2):575–584.

Satake, K. (1995). Linear and nonlinear computations of the 1992 Nicaragua earthquake tsunami. *Pure and Applied Geophysics*, 144(3-4):455–470.

Satake, K., Fujii, Y., Harada, T., and Namegaya, Y. (2013). Time and space distribution of coseismic slip of the 2011 Tohoku earthquake as inferred from tsunami waveform data. *Bulletin of the Seismological Society of America*, 103(2B):1473–1492.

Schäfer, A. M. and Wenzel, F. (2017). TsuPy: Computational robustness in Tsunami hazard modelling. *Computers and Geosciences*, 102:148–157.

Schwarz, G. (1978). Estimating the Dimension of a Model. *The Annals of Statistics*, 6(2):461–464.

Sfahani, M. G., Guan, H., and Loo, Y.-C. (2015). Seismic Reliability and Risk Assessment of Structures Based on Fragility Analysis – A Review. *Advances in Structural Engineering*, 18(10):1653–1669.

Shao, G., Li, X., Ji, C., and Maeda, T. (2011). Focal mechanism and slip history of the 2011 Mw 9.1 off the Pacific coast of Tohoku Earthquake, constrained with teleseismic body and surface waves. *Earth, Planets and Space*, 63(7):559–564.

Shuto, N. (1991). Numerical simulation of tsunamis - Its present and near future. *Natural Hazards*, 4:171–191.

Si, H. and Midorikawa, S. (1999). New attenuation relations for peak ground acceleration and velocity considering effects of fault type and site condition. *Journal of structural and construction engineering*, AIJ(523):63–70.

Somerville, P., Irikura, K., Graves, R. W., Sawada, S., Wald, D. J., Abrahamson, N. A., Iwasaki, Y., Kagawa, N., Smith, N., and Kowada, A. (1999). Characterizing earthquake slip models for the prediction of strong ground motion. *Seismological Research Letters*, 70(1):59–80.

Song, J., De Risi, R., and Goda, K. (2017). Influence of flow velocity on tsunami loss estimation. *Geosciences*, 7(4).

Song, Y. T., Fukumori, I., Shum, C. K., and Yi, Y. (2012). Merging tsunamis of the 2011 Tohoku-Oki earthquake detected over the open ocean. *Geophysical Research Letters*, 39(5).

Strasser, F. O., Arango, M. C., and Bommer, J. J. (2010). Scaling of the source dimensions of interface and intraslab subduction-zone earthquakes with moment magnitude. *Seismological Research Letters*, 81(6):941–950.

Straub, E. (1988). *Non-life insurance mathematics*. Berlin: Springer-Verlag.

Strusińska-Correia, A. (2017). Tsunami mitigation in Japan after the 2011 Tohoku Tsunami. *International Journal of Disaster Risk Reduction*, 22:397–411.

Sugawara, D., Takahashi, T., and Imamura, F. (2014). Sediment transport due to the 2011 Tohoku-oki tsunami at Sendai: Results from numerical modeling. *Marine Geology*, 358:18–37.

Suppasri, A., Charvet, I., Imai, K., and Imamura, F. (2015). Fragility curves based on data from the 2011 Tohoku-Oki tsunami in Ishinomaki City, with discussion of parameters influencing building damage. *Earthquake Spectra*, 31(2):841–868.

Suppasri, A., Koshimura, S., Imai, K., Mas, E., Gokon, H., Muhari, A., and Imamura, F. (2012). Damage characteristic and field survey of the 2011 Great East Japan Tsunami in Miyagi Prefecture. *Coastal Engineering Journal*, 54(1):1250005–1–125005–30.

Suppasri, A., Koshimura, S., and Imamura, F. (2011). Developing tsunami fragility curves based on the satellite remote sensing and the numerical modeling of the 2004 Indian Ocean tsunami in Thailand. *Natural Hazards and Earth System Science*, 11(1):173–189.

Suppasri, A., Mas, E., Charvet, I., Gunasekera, R., Imai, K., Fukutani, Y., Abe, Y., and Imamura, F. (2013). Building damage characteristics based on surveyed data and fragility curves of the 2011 Great East Japan tsunami. *Natural Hazards*, 66(2):319–341.

Sykes, L. R. and Menke, W. (2006). Repeat times of large earthquakes: Implications for earthquake mechanics and long-term prediction. *Bulletin of the Seismological Society of America*, 96(5):1569–1596.

Synolakis, C., Liu, P., Carrier, G., and Yeh, H. (1997). Tsunamigenic sea-floor deformations.

Tanaka, N., Onai, A., and Kondo, K. (2015). Fragility curve of different damage of wooden building due to tsunami based on tsunami fluid force and its moment. *Journal of Japan Society of Civil Engineers (Coastal Engineering)*, 71(1):1–11.

Tang, L., Titov, V. V., and Chamberlin, C. D. (2009). Development, testing, and applications of site-specific tsunami inundation models for real-time forecasting. *Journal of Geophysical Research: Oceans*, 114(12):1–22.

Tanioka, Y. and Satake, K. (1996). Tsunami generation by horizontal displacement of ocean bottom. *Geophysical Research Letters*, 23(8):861–864.

Titov, V., Rabinovich, A. B., Mofjeld, H. O., Thomson, R. E., and Gonzalez, F. I. (2005). The global reach of the 26 December 2004 Sumatra tsunami. *Science*, 309(5743):2045–2048.

Toda, S. and Stein, R. S. (2018). Why aftershock duration matters for probabilistic seismic hazard assessment. *Bulletin of the Seismological Society of America*, 108(3):1414–1426.

Wells, D. D. L. and Coppersmith, K. J. K. (1994). Empirical relationships among magnitude, rupture length, rupture width, rupture area and surface displacements. *Bulletin of the Seismological Society of America*, 84(4):974–1002.

Wiebe, D. M. and Cox, D. T. (2014). Application of fragility curves to estimate building damage and economic loss at a community scale: a case study of Seaside, Oregon. *Natural Hazards*, 71(3):2043–2061.

Woessner, J., Farahani, R. J., Williams, C., Porto, N. M., Masuda, M., Dollarhide, E., and Bingi, S. (2018). Tsunami Risk for insurance protfolios in Japan. In *16th European Conference on Earthquake Engineering*, pages 1–12, Thessaloniki.

Wu, H., Masaki, K., Irikura, K., and Kurahashi, S. (2016). Empirical fragility curves of buildings in northern Miyagi prefecture during the 2011 off the pacific coast of Tohoku earthquake. *Journal of Disaster Research*, 11(6):1253–1270.

Yamaguchi, N. and Yamazaki, F. (2001). Estimation of strong motion distribution in the 1995 Kobe earthquake based on building damage data. *Earthquake Engineering and Structural Dynamics*, 30(6):787–801.

Yamazaki, Y., Lay, T., Cheung, K. F., Yue, H., and Kanamori, H. (2011). Modeling near-field tsunami observations to improve finite-fault slip models for the 11 March 2011 Tohoku earthquake. *Geophysical Research Letters*, 38(7):L00G15.

Yeh, H. (2007). Tsunami load determination for on-shore structures. In *Proceedings of the Fourth International Conference on Urban Earthquake Engineering*, pages 415–422.

Yeh, H., Barbosa, A. R., Ko, H., and Cawley, J. (2014). Tsunami loadings on structures: Review and analysis. *Coastal Engineering Proceedings*, 1(34):1–13.

Yeh, H., Sato, S., and Tajima, Y. (2013). The 11 March 2011 East Japan earthquake and tsunami: tsunami effects on coastal infrastructure and buildings. *Pure and Applied Geophysics*, 170(6-8):1019–1031.

Yoshikawa, H. and Goda, K. (2013). Financial seismic risk analysis of building portfolios. *Natural Hazards Review*, 15(2):112–120.

Zakharova, O., Hainzl, S., Lange, D., and Enescu, B. (2017). Spatial variations of aftershock parameters and their relation to geodetic slip models for the 2010 Mw8.8 Maule and the 2011 Mw9.0 Tohoku-oki earthquakes. *Pure and Applied Geophysics*, 174(1):77–102.